Electromagnetic Position Estimation Using High-Magnetic-Permeability Materials: Design, Modeling, and Applications

A DISSERTATION
SUBMITTED TO THE FACULTY OF THE
UNIVERSITY OF MINNESOTA
BY

Heng Wang

IN PARTIAL FULFILLMENT OF THE REQUIREMENTS
FOR THE DEGREE OF
DOCTOR OF PHILOSOPHY

Professor Rajesh Rajamani

July 2021

Acknowledgements

First and foremost, I would like to express my sincere gratitude to my advisor Professor Rajesh Rajamani for his endless support and guidance throughout the past several years of my doctoral study at the University of Minnesota. As a great advisor, professorial researcher, and mentor, he has provided me with invaluable inspiration and advice. Without his patience and encouragement, I would have never completed the research work presented in this dissertation. His passion and creativity in research, hardworking nature, and positive mindset impressed me in the past years, and will motivate me constantly in my future life.

I am grateful to Prof. Ryan Caverly, Prof. Kim Stelson, and Prof. Zongxuan Sun for their valuable feedback and help by serving on my preliminary exam and PhD defense committees.

I especially thank Prof. Shuangyi Wang at Institute of Automation, Chinese Academy of Sciences for his generosity in hosting me as a visiting student in his lab to complete a key part of the dissertation regarding medical robotics. Without his kind support, I would have never finished my research work under the situation of the COVID-19 pandemic.

My further gratitude extends to Lee Alexander for his help in developing multiple prototypes and test rigs, and Mike Gust who brought the opportunity of the CNH project.

I would also like to thank all my past and current colleagues in the lab: Dr. Yan Wang, Dr. Peng Peng, Dr. Song Zhang, Dr. Mahdi Ahmadi, Dr. Ryan Madson, Dr. Ye Zhang, Dr. Woongsun Jeon, Dr. Corey Cruttenden, Zhenming Xie, Greg Johnson, Hamidreza Movahedi, and Dingyi Gu. It has been a pleasure to work alongside them. I would like to thank my roommates and best friends in the United States: Dr. Yiru Wang, Dr. Huan Yang, Zonghu Han, Rui Luo, Dr. Pengyue Wang, Mian Wang, Dr. Bin Kong, and Xingxuan

Huang, who have provided me with help and support both academically and personally.

Finally, I would express my sincere appreciation to my parents and brother for their unconditional love and support. This dissertation would not have been accomplished without their encouragement. I would also thank my girlfriend, Saisai Wang, for her persistent company with patience and love over the past few years towards this dissertation.

This research was supported in part by the National Science Foundation (NSF) under Grant CMMI 1562006, Case New Holland Industrial Inc., and Institute of Automation, Chinese Academy of Sciences.

Dedication

To My Parents, Lianzhen Gao and Guoliang Wang

Abstract

This doctoral dissertation proposes and demonstrates a novel electromagnetic position sensing principle based on the use of alternating magnetic fields and on the use of passive high-magnetic-permeability metal located on the moving object. Position estimation systems robust to ambient ferromagnetic disturbances are developed based on this sensing principle for a range of applications, including: (1) 1-D position estimation system for piston position measurement in linear actuators; (2) Angular position estimation system for rotational motion of mechanical links; (3) 3-D position estimation for transluminal medical robots. Furthermore, an active position sensing system based on current control is designed for achieving better estimation performance with electromagnetic sensing that also minimizes the power consumption of the electromagnet.

Many existing position sensing systems require either line-of-sight access to the concerned object (e.g. optical sensing systems), intrusive installation (e.g. magnetostrictive sensors), or need physical connection to the object (e.g. potentiometers), which limit their applications or result in poor durability. The new electromagnetic position estimation system developed in this dissertation provides a non-intrusive, non-contacting, easy to install, and low-cost position sensing system. Unlike permanent magnet-based sensors, the new sensing system also does not suffer from errors due to magnetic disturbances caused by surrounding ferromagnetic objects. This is because selective sensing of the amplitude of an alternating magnetic field at a specific operating frequency eliminates the influence of ambient low-frequency magnetic disturbances.

Since an electromagnet is used as the magnetic field source for the position sensing system, active real-time control of the current of the electromagnet to ensure adequate magnetic sensitivity at all positions while reducing power consumption is another aspect studied in the research. Since the current control depends on the unknown position to be estimated, the problem is a coupled active control and estimation problem. A nonlinear observer is designed to simultaneously ensure stable position estimation and optimal current profile tracking.

The research presented involves analytical and numerical modeling of the magnetic

sensing system and design of stable estimation algorithms for a challenging nonlinear position estimation problem. The specific technical contributions of the dissertation are:

1. Development and verification of a novel passive position sensing principle based on high-magnetic-permeability metal.
2. Hardware development for signal processing of alternating magnetic fields to achieve position estimation immune to ferromagnetic disturbance. Disturbance rejection performance is characterized for each of the three types of applications. Nonlinear estimation algorithms are implemented for position estimation.
3. Development and experimental evaluation of 1-D position estimation system for linear actuators. Analytical modeling of the sensing principle for 1-D position estimation.
4. Development, numerical modeling, and experimental evaluation of angular position estimation system for rotational motion.
5. Development, modeling, and experimental evaluation of 3-D position estimation system for localization of transluminal medical robots.
6. Development of electromagnetic position estimation system using active current control for more accurate and energy-efficient position measurement. A nonlinear observer for simultaneous active control and estimation is designed based on Lyapunov theory.

Experimental evaluation is pursued for all three types of position measurement applications. The 1-D position estimation system is shown to provide an accuracy of 1% over a stroke length of 20 cm for a non-ferrous actuator with the possibility to further enlarge the stroke length by daisy-chained additional sensors. However, its accuracy deteriorates significantly if the actuator is ferrous and the mu-metal is located completely inside a ferrous body. The angular position measurement sensor is shown to provide an accuracy of 1 degree over a range of $\pm$ 60 degrees in an off-joint configuration and an accuracy of 2 degrees over a full range of 360 degrees in an on-joint configuration. Finally, a 3-D position estimation system is evaluated on a trans-esophageal endoscopic robot wherein an RMS accuracy of 5 mm and a maximum error bounded within 9 mm are achieved.

The new sensing principle developed and demonstrated in this project can be the foundation that leads to practically useful position estimation systems for a wide range of industrial, transportation and biomedical applications in the future.

Table of Contents

List of Tables

List of Figures

Citations of Published Work

Some portions of this thesis have appeared in the following publications:

Journal Publications:

1) H. Wang, and R. Rajamani, "A Remote Position Sensing Method Based on Passive High Magnetic Permeability Thin Films," *Sensors and Actuators A: Physical,* vol. 295, pp. 217-223, 2019.
2) H. Wang, R. Madson and R. Rajamani, "Electromagnetic Position Measurement System Immune to Ferromagnetic Disturbances", *IEEE Sensors Journal*, vol. 19, no. 21, pp. 9662-9671, July 2019.
3) H. Wang, A. Zemouche, and R. Rajamani, "Nonlinear Observer for Electromagnetic Position Estimation Using Active Current Control," submitted to *Mechanical Systems and Signal Processing*, 2021.

Conference Publications:

1) H. Wang, and R. Rajamani, "Electromagnetic Position Estimation Using Active Current Control and Nonlinear Observer," in *Proceedings of the 2020 American Control Conference (ACC)*, Denver, CO, USA, 2020.

Patent:

H. Wang, R. Rajamani, and R. Madson, "Position Sensing System with an Electromagnet," U.S. Patent 10837802, Granted on November 17, 2020.

Chapter 1

Introduction

This dissertation is devoted to proposing and demonstrating a novel position sensing principle based on the use of high-magnetic-permeability materials and an electromagnet. Based on the same electromagnetic position sensing principle, prototypes of position estimation systems are designed with thorough analytical and numerical modeling, and validated using experiments for a series of real-world applications:

1) 1-D position measurement for linear actuators;
2) Angular position measurement for rotational joints;
3) 3-D position measurement for flexible transluminal medical robots and robotic capsules.

The new position sensing system enables a non-contacting, non-intrusive, and low-cost position measurement solution that does not require powered or wired components on moving objects and can reject disturbances from surrounding foreign ferromagnetic objects. In addition, a related active electromagnetic position sensing framework is established based on nonlinear observer design for enhancement of measurement accuracy, extension of sensing range, and conservation of power consumption.

1.1 Position Measurement

Position is a fundamental kinematic variable that describes the spatial relation of an

object in mechanical motion with respect to some origin. Position sensing is of vital significance for monitoring, fault diagnostics, feedback control, and automation in various industrial [1], vehicular [2], aerospace [3] and biomedical [4] applications. Position measurement is performed in various scales ranging from positioning of a spacecraft or satellite in outer space, to localization of autonomous vehicles on open roadways, to human indoor positioning, to positioning of micro-robots inside of a human body. The scope of this dissertation is limited to the constrained 1-D linear or angular position measurement in mechanical systems such as actuators and rotational joints, and unconstrained 3-D position measurement of transluminal medical robots, both of which have a short range of motion within 1 meter.

Existing short-range position measurement methods can be classified as potentiometer based, optical, ultrasonic, magnetic and radio frequency (RF) wave based methods. Potentiometer based position sensors [5] are widely used for linear and angular position measurement due to their very low cost. The wiper of the potentiometer is connected to the moving object through physical contact and it divides the voltage between two terminals, giving a voltage signal proportional to its position. Another widely used linear position sensor is the linear variable differential transformer (LVDT) consists of one primary coil and two secondary coils. The alternating current in the primary coil induces a voltage in each secondary coil proportional to the displacement of the ferrous core connecting to the moving object. The problem with potentiometers and LVDTs is the contacting operation that results in significant wear under fatigue loads over long-term use.

Optical position sensing can be categorized as active methods and passive methods. In passive methods, the natural optical features of the moving object or the surrounding environment are directly extracted and measured by an image sensor for positioning using 3-D vision techniques. Monocular cameras [6], stereo cameras [7], or RGB-D cameras [8] can be used for visual positioning. Passive optical methods based on visible light sensing can provide abundant semantic information of the target object apart from the position information, making it suitable for monitoring applications. However, the passive optical methods highly depend on illumination conditions and fail to work in darkness. Besides, if the target object has a uniform appearance, the passive optical methods fail to extract useful

optical features for positioning. Although fiducial markers like ArUco markers can be attached to the target object for positioning, it may not be practical for applications in dirty environments where the markers are easily stained. In active optical position measurement systems, a light source is integrated into the sensor to actively emit light signals to enhance position measurement. The active light emission has multiple purposes. In the reflective marker-based position tracking systems [9], infrared (IR) light is illuminated on reflective markers attached to the target object and the markers are measured by multiple infrared cameras for position measurement. In the laser gauging sensors for 1-D linear position measurement [10], and time-of-flight (ToF) cameras [11] and light detection and ranging (LiDAR) sensors [12] for 3-D position measurement and reconstruction, light signals (often lasers in the infrared spectrum) are emitted from a light source on the sensor to the target object and the time it takes the light beam to be reflected back to the sensor is measured to determine the depth and position of the object. In optical encoders for angular position measurement [13], an IR beam is transmitted through an optical disk encoded with discrete slits and the angle information is derived from the optical pattern received by the IR sensor on the other side of the disk. Active optical methods do not depend on external illumination conditions and can be used in dark environments. Furthermore, active optical methods normally have a higher position measurement accuracy than passive methods with inaccurate feature extraction of the target object. However, there are some common limitations for all optical position sensing methods. First, optical position measurement methods require a line-of-sight access to the target object and thus suffer from occlusion issues in some applications. For example, external cameras cannot be used for localization of medical robots operating inside of the human body. Second, the performance of optical position sensing methods is significantly impaired in harsh environments with smoke, dust, and non-transparent liquids, which attenuate and even block the light transmission towards the receiver.

Ultrasound sensors with a working frequency above 20 kHz has been used for 1-D linear position measurement [14] of telescopic boom structure on a crane loader and 3-D position measurement of mobile robots [15]. Ultrasound positioning can be categorized as time-of-flight (ToF) based and received-signal-strength (RSS) based methods. In ToF

based methods, ultrasound transmitters and receivers and used, where the time between the ultrasound emission and receiving is calculated for position measurement. Some ToF based ultrasound positioning systems [16] (e.g. sonars) have integrated ultrasound transmitters and receivers located close to each other, where ultrasound wave is emitted from a transmitter, echoed back from the moving target, and sensed by the receiver located near the transmitter. Another ToF based method [17] adopts separated transmitter and receiver, where the transmitter is attached to the target object and receivers are placed around for localization of the target. In RSS based methods [18], the position of the target can be estimated from the strength of the received ultrasound signal, which is modeled as a function of the propagation distance of the ultrasound wave considering the power loss due to the spherical divergence and atmospheric absorption. The problem with the ultrasound position sensing is that it still requires line-of-sight operation, which may not be available in certain applications. In addition, both the speed and intensity of ultrasound wave are influenced by atmospheric conditions like temperature and air turbulence [15], resulting in position measurement errors using either ToF or RSS based ultrasound methods.

Radio frequency (RF) wave is electromagnetic wave with frequency lower than that of infrared light. In RF based position measurement systems, a RF tag is attached to the moving object to transmit RF wave and multiple RF readers are placed around to measure either the strength of the received signal or the time-of-flight, from which the position of the target can be estimated. The RF based position measurement methods have been applied to human indoor navigation [19] and localization of endoscopic capsule robots [20][21]. However, the measured RSS and ToF cannot be accurately related to the traveled distance if RF is transmitted in non-homogeneous or highly attenuating medium such as a human body.

Magnetic fields can penetrate most of non-ferromagnetic materials and thus magnetic position measurement methods do not need line-of-sight operation, making it suitable for positioning medical devices inside of the human body. In addition, magnetic sensing methods can perform well in harsh environments with dust and liquids. Although the magnetic field attenuates rapidly with distance from the magnetic source, the spatial distribution of the magnetic field is stable, not depending on atmospheric conditions like

temperature, pressure and air convection. Many magnetic position estimation methods have been developed by exploring the spatial distribution of the magnetic field around a magnetic source. Previously, magnetic position sensing was achieved using Hall-effect sensors and eddy current sensors with a measurement range of only a few millimeters. With the development of magnetic sensors (e.g. tunnel magneto-resistive (TMR) sensors) with increased sensitivity and reduced cost, the position measurement accuracy of magnetic sensing based methods is improved and the measurement range can be extended to tens of centimeters. Various types of magnetic position sensing systems are introduced in the next section.

1.2 Position Measurement Using Magnetic Fields

It is well known that a compass has been used as a navigation tool since ancient times in voyages across the sea to find the orientation of the north pole of the earth. Magnetometers, which measure the earth magnetic field, are also used in ground vehicles and aircrafts for determination of orientation. Apart from indication of orientation using the earth's magnetic field, the magnetic field of various magnetic sources have also been explored for position measurement. In this section, some common magnetic field sources for position sensing are introduced and typical position estimation systems based on magnetic field measurement near these magnetic sources are briefly discussed with their respective advantages and drawbacks.

1.2.1 Magnetic Field Sources for Position Measurement

Since magnetism originates from two possible sources, i.e. electric current and spin magnetic moments of elementary particles, magnetic field sources for position measurement are categorized as magnetic materials with magnetism from microscopic magnetic moments, and electromagnets with magnetism from electric current.

In a broad sense, any material has some sort of magnetism. Materials can be classified into five categories due to their different magnetic behaviors under the presence of external magnetizing magnetic field: diamagnetic, paramagnetic, ferrimagnetic, ferromagnetic, and antiferromagnetic. Only ferrimagnetic and ferromagnetic materials (e.g. Fe, Co, Ni, and

their alloys) exhibit significant magnetism with large intensity of magnetization under external magnetic field while the other types of materials show negligible magnetization.

Magnetic permeability μ, i.e. the ratio of the total magnetic field flux density B to the exerted external magnetic field H that magnetizes the material, is used to characterize the measure of magnetization of the material by a certain external magnetic field. Magnetic permeability for different types of materials are summarized below [22]:

1) Vacuum: $\mu = 1$;
2) Diamagnetic: μ is slightly smaller than 1, e.g. copper with $\mu = 0.999994$;
3) Paramagnetic and antiferromagnetic: μ is slightly larger than 1, e.g. air (paramagnetic) with $\mu = 1.00000037$;
4) Ferromagnetic and Ferrimagnetic: μ is tremendously larger than 1, e.g. iron (ferromagnetic, 99.8% pure) with $\mu = 5000$.

It is noted that ferromagnetic materials show the highest capability of magnetization and can form a strong magnetic field around them once magnetized. Ferromagnetic materials can be further classified as "soft" materials that can be magnetized but not tend to stay magnetized without presence of the external magnetic field, and "hard" materials that will remain magnetized even without the external magnetic field. Since it is required for the magnetic field source in position sensing applications to maintain a stable magnetic field around it, hard ferromagnetic materials (e.g. permanent magnets) are usually used as desired magnetic field sources. Some soft ferromagnetic materials with high magnetic permeability (e.g. mu-metal with $\mu = 50000$), which can be easily magnetized and demagnetized with low coercivity, can be explored to function as sensitive medium targets in magnetic position measurement as is proposed in this dissertation, though not suitable to serve as magnetic field sources.

Another kind of magnetic field source is the electromagnet. Electromagnets are normally made by winding electric wires around some soft ferromagnetic core. Compared with permanent magnets, an electromagnets has the flexibility to adjust its magnetic strength by varying its current and to generate an alternating magnetic field by using an alternating current input, though a continuous current needs to be supplied to the electromagnet to maintain the magnetism.

1.2.2 Position Measurement Using Earth's Magnetic Field

The magnetic field around the earth is generated by the molten iron and nickel in the external core of the earth. Approximately, the earth's magnetic field can be represented by a magnetic dipole tilted with a small angle with respect to the rotational axis of the earth. Some animals in migration can derive their global position from the intensity and inclination angle of the earth magnetic field [23][24]. Inspired by animals using magnetic navigation, the spatial variation of geomagnetic magnetic field has been explored for positioning of underwater vehicles [25]. With the disturbance from the ferromagnetic vehicle body modeled and compensated, the measured geomagnetic field is matched to a geomagnetic map stored in a database with high accuracy and resolution for position determination. Since the earth's magnetic field only changes with large variation of geographical location, geomagnetic field based positioning can only be used for applications with large ranges of motion like aircraft and submarine localization.

1.2.3 Position Measurement Using Non-Magnet Ferromagnetic Objects

Many objects are fully or in part made from ferromagnetic materials such as hand tools, cars, industrial machines, etc. These ferromagnetic objects with residual magnetization will form a magnetic field as a function of distance from them. The 1-D and 2-D position of a vehicle can be estimated for imminent collision prediction by modeling the magnetic field of the vehicle as a function of vehicle-specific parameters and the position around the vehicle [26][27][28]. The piston position of a free piston engine has been estimated from the inherent magnetic field of the ferromagnetic piston [29]. In indoor environments, multiple ferromagnetic objects like metallic desks, pipes and electric appliances can disturb the originally uniform geomagnetic field and result in magnetic field variation in the room. The magnetic field variation is surveyed into a magnetic map stored in a database and then 3-D position of a target object can be determined by taking magnetic field measurements and matching to the magnetic map of the room [30]. The position measurement method using an existing ferromagnetic object only needs magnetic sensors and a model of the magnetic field distribution of the objects without the requirement of installation of any permanent magnets or electromagnets. However, the residual magnetization of existing

ferromagnetic objects is much lower than that of a permanent magnet. Thus, the position measurement accuracy is limited by the weak magnetic field. In addition, since the magnetic field model depends on the magnetization intensity and geometry of the ferromagnetic objects, a specific model has to be built for each application involving a different ferromagnetic object.

1.2.4 Position Measurement Using Permanent Magnets

Permanent magnets are desired magnetic sources for position measurement applications due to their strong and stable magnetization. A permanent magnet of small size can be embedded in the target object as a magnetic source and the position of the target can be estimated from magnetic field measurements with one or multiple magnetic sensors located nearby. Linear position measurement systems have been developed to estimate the piston position of pneumatic and hydraulic actuators by embedding a permanent magnet in the piston [31][32]. A permanent magnet is attached to the tongue to find its position and orientation for speech-related applications using neural network model of the magnetic field [33]. A permanent magnet based position measurement system has also been developed to localize an endoscopic capsule robot using a magnetic dipole model and an online optimization method [34]. Positions of multiple permanent magnets can be tracked simultaneously with low latency using analytical magnetic field gradient [35]. Since the permanent magnet is a passive element that does not require power or wiring, it is easy to install on the target and the volume and power consumption of the tracked devices can be reduced using this passive position measurement method. Furthermore, a permanent magnet can be well modeled as a magnetic dipole if the magnetic field is measured at a distance from the magnet way larger than the size of the magnet. The use of a magnetic dipole model enables simultaneous estimation of the magnetization parameters of the magnet and its position, which simplifies calibration of the magnetic field model. The problem with the permanent magnet based systems is that it suffers from errors due to magnetic disturbance from foreign ferromagnetic objects, though some algorithms has been proposed to compensate for the disturbance magnetic field [31].

1.2.5 Position Measurement Using Electromagnets

Electromagnets have the flexibility to adjust their magnetic strength by varying the current supply and to generate non-static magnetic field such that a simple induction coil can be used to measure the magnetic field. Most electromagnet based position measurement systems consist of one or multiple transmitting coils to generate the magnetic field and a induction sensing coil attached to the target to measure the magnetic field for position determination. An electromagnetic position tracking system has been developed with multiple coils excited simultaneously with different frequencies for localization of a capsule robot [36]. In another electromagnetic tracking system, multiple transmitting coils are excited sequentially for tip position measurement and shape sensing of a flexible continuum robot [37]. Some electromagnetic position tracking methods employ rotating transmitting coils or sensing coils and closed-form analytical solutions of the target position from magnetic field measurements[38][39]. Since electromagnetic position sensing systems use a sensing coil that measures the inducted electromotive force by the transmitted alternating magnetic field, surrounding ferromagnetic objects with low-frequency motion do not have influence on the measurement. However, wiring and power supply for the sensor on the moving target are required in electromagnetic position measurement systems, which is especially undesired for positioning of endoscopic capsule robots that need to save space and power for surgical and diagnostic operations.

1.3 A New Position Sensing Principle Using High-Magnetic-Permeability Materials

It was discussed in the previous section that a permanent magnet based position measurement system has only a passive element attached to the moving target object but suffers from foreign ferromagnetic disturbances. The electromagnet based system can reject ferromagnetic disturbances but requires powered or wired components on the moving target. Therefore, there is a need to develop a new type of magnetic position measurement system with no powered components on the moving target and meanwhile immune to ferromagnetic disturbances. Motivated by this objective, a new magnetic

position sensing principle is proposed in this dissertation using an electromagnet that generates an alternating magnetic field, and high-magnetic-permeability soft ferromagnetic materials attached to the moving target. Both the electromagnet and magnetic sensors are separated and located stationarily near the working region of the moving target. The high-magnetic-permeability element (e.g. mu-metal) is magnetized with different intensity at different spatial locations with respect to the electromagnet and becomes an intermediate magnet inducing the magnetic field variation measured by the magnetic sensors for position sensing. The proposed position sensing principle is fundamentally different from existing magnetic position sensing methods which utilize the spatial distribution of magnetic field around a magnetic field source. Instead, the new position sensing principle utilizes the magnetic field variation induced by a soft magnetic medium.

The Mu-metal is employed as the high-magnetic-permeability soft ferromagnetic element in the proposed new position sensing system. Mu-metal is mainly composed of 80% Ni, 15% Fe, and small amount of Mo, Mn, and Si, and named by the symbol of magnetic permeability μ due to its very high magnetic permeability ($10^4 - 10^5$) after annealing treatment. Mu-metal has been mainly used as magnetic shielding material to cover magnetic disturbance sources like power cables [40] or to enclose electronic devices sensitive to external magnetic disturbance [41]. In addition, mu-metal has also been used as magnetic flux concentrator in microscale for sensitivity enhancement of magnetic sensors [42]. However, mu-metal has never been explored as a sensitive element for magnetic position sensing applications.

Two features of mu-metal contribute to the function of the proposed position sensing principle. First, mu-metal is a kind of "soft" ferromagnetic material, which means it has low coercivity during magnetization and can be easily magnetized. When an alternating magnetic field at a specific frequency (e.g. 100 Hz) from an electromagnet is used in the position sensing system for rejection of disturbance from foreign ferromagnetic objects with low-frequency motion, the magnetization of mu-metal is also alternating in the alternating magnetic field due to its soft magnetic property with low coercivity. The mu-metal behaves like a magnet with alternating north and south poles at the same frequency as that of the alternating magnetic field from the electromagnet. Thus, the alternatingly

magnetized mu-metal can further exert an additional alternating magnetic field whose amplitude varies with the relative position of the mu-metal with respect to the electromagnet. Second, the mu-metal has a very high magnetic permeability, resulting in a strong magnetization in external magnetic field. Therefore, the magnetic field generated by the mu-metal with strong magnetization is sufficiently high and thereafter measured by magnetic sensors for position sensing. The two features of mu-metal, i.e. low coercivity and high permeability make it a desired sensitive medium for electromagnetic position sensing.

In summary, the proposed new position sensing principle requires only a passive mu-metal element attached to the moving target without powered or wired components on it. Furthermore, the position sensing system is immune to ferromagnetic disturbance owing to the use of an alternating magnetic field from the electromagnet. With these two features, the proposed position sensing principle can be transferred to a broad range of real-world applications that will be presented in this dissertation in detail.

1.4 Estimation Algorithms for Magnetic Position Sensing

In magnetic position measurement systems, the position of the target is determined either from the spatial distribution of magnetic field around a magnetic source, or from the magnetic variation caused by a magnetic medium as proposed in this dissertation. In either position sensing method, the magnetic field model as a function of the position is highly nonlinear. Therefore, a nonlinear state estimation algorithm is required to compute the position from raw magnetic measurements. In this section, two classes of estimation algorithms, i.e. Bayes filter based methods and LMI-based nonlinear observer design, are introduced.

1.4.1 Bayes filter based methods

Bayes filter is a widely used stochastic framework for position estimation. Based on the Markov assumption that future states depend only on the present state rather than past states, Bayes filter is implemented in two steps: state propagation using a dynamic model and state update using a measurement model. In general, both the dynamic model and

measurement model are represented by probability density functions (PDF) in a Bayes filter, as given by (1-1)

$$\begin{aligned} x_k &\sim p(x_k|x_{k-1}) \\ y_k &\sim p(y_k|x_k) \end{aligned} \tag{1-1}$$

where x_k is the state to be estimated and y_k is the measurement at time step k. First, *a priori* estimate is obtained by the state propagation step using the dynamical model as given by (1-2) [43].

$$p(x_k|y_{1:k-1}) = \int p(x_k|x_{k-1})p(x_{k-1}|y_{1:k-1})dx_{k-1} \tag{1-2}$$

where $y_{1:k-1}$ the sequence of measurements up to the time step of $k-1$. Then *a posteriori* estimate of the state is obtained in the measurement update step using Bayes' rule, as given by (1-3)

$$p(x_k|y_{1:k}) = \frac{p(y_k|x_k)p(x_k|y_{1:k-1})}{\int p(y_k|x_k)p(x_k|y_{1:k-1})dx_k} \tag{1-3}$$

Bayes filter can be implemented in various ways with different computational efficiency and accuracy of approximation. The Kalman filter is a famous Bayes filter for optimal state estimation of a linear system with the Gaussian process and measurement noise. However, since the measurement model in magnetic position sensing systems is usually, if not always, highly nonlinear, the Kalman filter cannot be directly used.

A relaxed form of the Kalman filter, extended Kalman filter (EKF), does not require linearity for dynamic model and measurement model. In EKF, the nonlinear functions in the model are approximated by linearization at the current state estimate. Due to its simplicity of implementation and high computational efficiency, EKF has been used in many magnetic position measurement applications [27] [29]. However, the performance of EKF is limited due to the inaccurate approximation by simple linearization, especially when the nonlinearity of the system is severe.

An unscented Kalman filter (UKF) can improve the estimation performance using an unscented transformation to approximate the change of mean and covariance of the random state estimate over the nonlinear transformation. With improved estimation accuracy and moderate computational effort, UKF has been used for linear magnetic position estimation

problems involving large nonlinearities in measurement model [31][32].

The particle filter (PF) is a nonlinear Bayes filtering technique that approximate posterior probability distribution of states conditional on available measurements using a finite number of random samples (particles). PF does not require the process and measurement noise to be Gaussian. PF can reach very high estimation accuracy for systems with significant nonlinearities by using a sufficient number of particles but at a cost of increased computational effort. PF has been used to improve the dynamic accuracy of electromagnetic position tracking [44].

1.4.2 LMI-based Nonlinear Observer Design

Linear Matrix Inequality (LMI) based nonlinear observer design is another state estimation method. While the Bayes filter based method is formulated in the stochastic framework modeling the dynamic process and measurements as random processes, LMI based observer design is formulated in a deterministic framework. The goal of observer design is to determine the feedback gain such that the state estimate can asymptotically converge to the true state. Based on the Lyapunov stability theory, the determination of observer gain is usually formulated as solving an LMI. An LMI in the variable $x \in \mathbb{R}^n$ has the form [45]:

$$F(x) = F_0 + x_1 F_1 + \cdots + x_n F_n \leq 0 \tag{1-4}$$

where $F_0 \in \mathbb{R}^{m\times m}, \cdots, F_n \in \mathbb{R}^{m\times m}$ are symmetric matrices, and $x = [x_1, x_2, \ldots, x_n]^T$. Though optimal estimation is not ensured, there are two advantages of the LMI based observer design method over the Bayes filter method. First, the oberver gain is obtained offline by solving the LMI so the computational effort of real-time implementation of the estimator is lower than that of the Bayes filter. Second, the global stability of the state estimator is guarranteed in observer design while the Bayes filter potentially diverges in the presence of significant nonlinearies. Nonlinear observers have been developed to estimate the piston positon of a pneumatic actuator from the nonlinear magnetic field model with bounded Jocobians [46][47]. A nonlinear observer with switched gain has also been developed for magnetic position sensing involving a non-monotonic measurement model [48]. In these applications, the magnetic field model of the magnetic source is fixed and is

not actively controlled to vary with the target positon.

In this dissertation, an active sensing problem for magnetic position measurement is solved using nonlinear observer design. In the electromagnetic position estimation system, the magnetic strength of the electromagnet is actively controlled by varying its current input to follow an optimal profile to enhance position estimation performance, especially in the region with low magnetic sensitivity, in an energy efficient way. It is noted that current control depends on the unknown position to be estimated, and stable and optimal position estimation depends on accurate tracking of the optimal current profile in return. Therefore, a challenging problem with coupled control and state estimation is involved, where the failure of either current control or position estimation might cause the instability of the other one. In this dissertation, a nonlinear observer is designed for the active electromagnetic position estimation system to ensure the global stability of both current control and position estimation.

1.5 Thesis Contributions

The primary research contributions of this dissertation are as follows:

1) Development of a novel position sensing principle based on the use of an electromagnet and high-magnetic-permeability materials: High-magnetic-permeability materials (e.g. mu-metal) are used as the magnetic medium that is magnetized by the magnetic field from the electromagnet with a magnetization intensity dependent on the relative position of the mu-metal. The magnetic field induced by the magnetized mu-metal is measured for position sensing. The proposed position sensing principle using passive high-magnetic-permeability materials enables a non-contacting, non-intrusive, low-cost position measurement solution that does not require wiring and power supply to the moving object and can reject ferromagnetic disturbances by using an alternating magnetic field.
2) Development of a 1-D piston position estimation system for linear actuators: Based on the proposed position sensing principle, a linear position estimation system is developed for non-ferrous hydraulic and pneumatic actuators with a mu-metal

element attached to the moving piston, and an electromagnet and magnetic sensors located outside of the stationary cylinder. An analytical model is developed to investigate the sensing mechanism. The linear position sensing system is experimentally validated to have a 1% accuracy. The performance of the estimation system degrades significantly, however, when the actuator is ferrous and the mu-metal object is completely enclosed by a ferrous body.

3) Development of a nonlinear observer for active electromagnetic position estimation system using current control: In the basic linear electromagnetic sensing system, the magnetic field distribution of an electromagnet is measured for position estimation but the magnetic sensitivity decreases sharply with the distance. To solve the low-sensitivity problem in the large-distance region, an active sensing system is developed by optimal control of the current input to the electromagnet over the measurement range. The challenging problem of coupled current control and position estimation is tackled by nonlinear observer design. The active position sensing system is experimentally validated to be stable with a measurement accuracy of 1% over the whole stroke length of 20 cm.
4) Development of an angular position estimation system for rotational joints: The mu-metal based position sensing principle is applied to develop angular position estimation systems to measure the angle of mechanical joints on off-road vehicles for automatic operation. Assisted by numerical modeling, two configurations are designed with optimization of the sensor placement scheme and geometry of the mu-metal. An off-joint configuration can achieve a measurement error under 1 degree but fails to cover the full 360-degree measurement range. An on-joint configuration is validated to have a measurement error under 2 degrees over the 360-degree range.
5) Development of a 3-D position estimation system for flexible transluminal medical robots: The mu-metal position sensing principle is applied to develop a 3-D position estimation system for localization of flexible transluminal medical robots for feedback control and autonomous navigation. Only a passive mu-metal element is attached to the robot moving inside of the human body, and the electromagnet

and magnetic sensors are located outside of the body. Wireless 3-D position sensing is achieved without requirement of line-of-sight access, which is desired for localization of transluminal robots. Extensive experiments are conducted to validate the 3-D position estimation system on a trans-esophageal ultrasound robot.

Chapter 2

One-dimensional Linear Position Estimation

2.1 Introduction

Linear position measurement is becoming increasingly important for hydraulic, pneumatic and electrical actuators used in industrial machines and in off-road vehicles such as agricultural and construction machines. In such actuators, the ability to measure the piston position enables automation, more accurate operation and intelligent solutions that reduce manual effort on the part of human operators. The work presented in this chapter is motivated by the need to develop a reliable and robust linear position estimation system for such actuators.

Traditional position sensors for such actuators, like linear variable differential transformers (LVDTs) [49] and potentiometers [50], have contacting operation, need to be installed between the moving piston and the actuator housing, and are thus subject to fatigue loads that can cause failure. Laser and sonar sensors [50] require line-of-sight access to the piston while such line-of-sight access is often not available on piston-cylinder actuators. A popular magnetostrictive sensor, which is often used in such actuators, requires drilling a blind bore hole down nearly the entire length of the piston rod for installation of a magnetostrictive wave guide, thus involving significant installation costs

and potentially causing damage to the structure of the piston rod [49]. Therefore, the above limitations demonstrate the need to develop a new type of position measurement system for 1-D linear actuators that is non-intrusive, non-contacting, easy to install, and low cost. Magnetic-sensing based position measurement system is thus promising to meet the above needs.

Magnetic sensors have previously been used for small range position measurement by measuring the magnetic field near a magnet. The most popular sensors for position sensing in such applications are hall-effect [51][52] and eddy current sensors [53]–[55]. However, these sensors only allow for small distances between the magnet and sensor. An array of magnets or an array of these sensors can be used together for position estimation when a long range of motion is desired [56][57]. Recently, it has also been shown that magnetic sensors can achieve longer range position estimation by measuring the magnetic field strength near a magnet and using nonlinear models of the magnetic field as a function of position [29][31][58]. This type of sensor does not require contact or line of sight with the object being measured. However, the disadvantage of magnetic sensors during large range motion is that magnetic disturbances can cause significant error in position estimation. Such magnetic disturbances arise not only from magnets but also from regular steel and ferromagnetic objects in the surrounding environment of the sensor.

In this chapter, a novel sensing principle based on the use of an alternating electromagnetic field and a high-magnetic-permeability metal (i.e. mu-metal) is proposed for non-contacting measurement of the position of a linearly moving object such as the piston in a linear stage or on industrial linear actuators. The main idea of the new sensing principle is to use the mu-metal attached to the moving object as the medium to change the local magnetic field from the magnetic source (i.e. the electromagnet) measured by the magnetic sensors. In the developed linear position estimation system, only one or more pieces of passive mu-metal films are attached to the surface of the piston and thus no powered objects need to be attached to the moving object, making the system durable, non-intrusive and easy to install. Furthermore, due to the use of an electromagnet, an alternating source magnetic field at a specific high frequency can be utilized to differentiate from the low-frequency disturbances from nearby ferromagnetic objects, resulting in a position

sensing system robust to ferromagnetic disturbances. This feature of the new position sensing system solves the problem of being sensitive to adjacent ferromagnetic disturbances that has plagued many other magnetic-sensing-based position measurement systems. With all the features and advantages above, the newly developed 1-D linear position measurement system presented in this chapter could enable a new generation of low cost "smart actuators".

This chapter is organized as follows: In Section 2.2, a basic electromagnetic linear position estimation system without the use of mu-metal is demonstrated. In Section 2.3, the novel mu-metal based electromagnetic position estimation system is presented. Its sensing principle is intuitively explained first and then a rigorous analytical model is shown to reveal the underlying physics of the sensing mechanism. Then the sensor signal processing is shown in Section 2.4 to demonstrate how the ferromagnetic disturbance rejection is achieved. Since the magnetic field measurement varies with the position of the moving object nonlinearly, a nonlinear estimation algorithm needs to be used to estimation the position, which is presented in Section 2.5. Experimental results are shown and discussed for both the basic embodiment and the mu-metal based position sensing system in Section 2.6. Its performance of ferromagnetic disturbance rejection is described in Section 2.7. Finally, the chapter is concluded in Section 2.8.

2.2 Preliminary Electromagnetic Position Estimation System

Before showing the novel mu-metal based position sensing system, a precursor position estimation system based on the direct measurement of magnetic field from an electromagnet is presented first. Its advantages and shortcomings are briefly discussed, which motivate the development of the mu-metal based system.

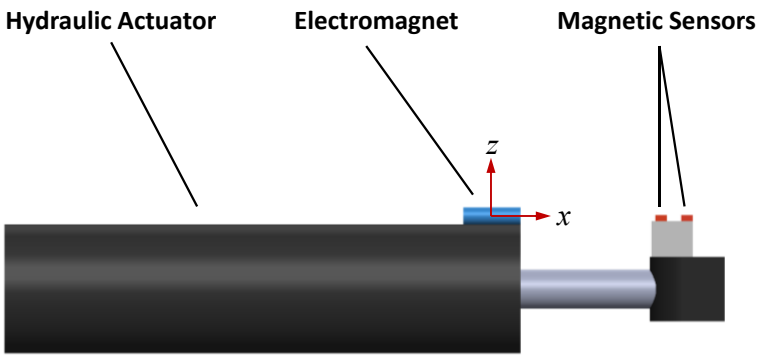

Figure 2-1 System schematic of the preliminary electromagnetic position measurement system without mu-metal.

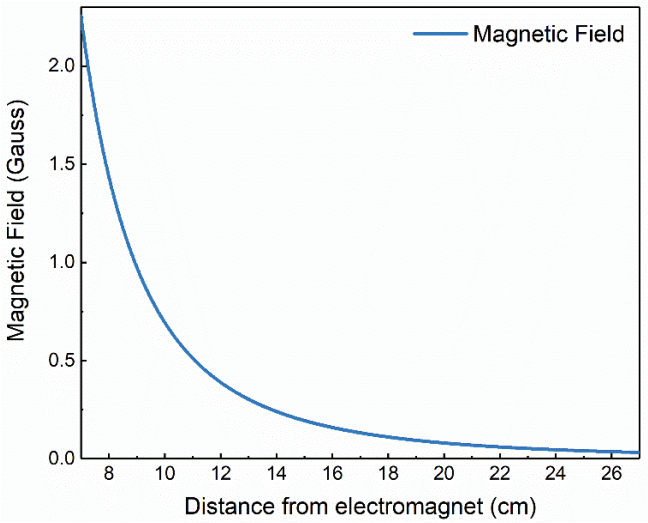

Figure 2-2 Magnetic field distribution along the central axis of the electromagnet

The preliminary position measurement system is composed of an electromagnet on the static cylinder and magnetic sensors on the moving object consisting of the piston rod, as shown in Figure 2-1. The sensors are located at the external end of the moving piston rod. Since power needs to be supplied to both the electromagnet and the sensors, power supply (or a battery) is required to the moving object in this preliminary sensor embodiment.

The magnetic field distribution along the central axis of the electromagnet can be described assuming the relationship for a solenoid as given by equation (2-1) [59]:

$$B_x = \frac{\lambda \mu_0 NI}{2l}\left[\frac{\frac{l}{2}-x}{\sqrt{\left(x-\frac{l}{2}\right)^2 + {R_\mathrm{e}}^2}} + \frac{\frac{l}{2}+x}{\sqrt{\left(x+\frac{l}{2}\right)^2 + {R_\mathrm{e}}^2}}\right] \tag{2-1}$$

where B_x is the magnetic flux density along the central axis, x is the distance of the sensors from the electromagnet along its central axis, l is length of the electromagnet, R_e is radius of the electromagnet, μ_0 is the magnetic permeability of vacuum, N is number of wire turns of the electromagnet, I is the supplied current and λ is a coefficient related to the magnetic permeability and shape of the ferrous core of the electromagnet. The variation of the magnetic field amplitude along the central axis of the electromagnet is illustrated in Figure 2-2. It can be seen that the measured magnetic field decreases monotonically as the sensor moves away from the electromagnet. If the magnetic field were an alternating sinusoidal field, then the amplitude would similarly vary monotonically with distance, which would provide an opportunity for position estimation based on measured magnetic field. Only the x-axis magnetic field is utilized for this basic electromagnetic position estimation system because the y-axis and z-axis magnetic field remain zero because the magnetic sensors are placed right on the central axis of the cylindrical electromagnet.

This preliminary electromagnetic position estimation system has a very simple structure and is easy to install on existing linear actuators. It is non-intrusive and non-contacting, sharing the same advantages with other magnetic-sensing-based position sensors. In addition, due to the use of an electromagnet instead of a permanent magnet as the magnetic source, high-frequency alternating magnetic field can be generated for position sensing to reject low-frequency ferromagnetic disturbances. The method of signal processing to achieve disturbance rejection will be discussed later in Section 2.4. With this said, the preliminary system still falls short in several ways. First of all, it is seen in Figure 2-2 that the magnetic field and magnetic sensitivity (absolute value of derivative of the magnetic field variation) both decrease rapidly with piston position. Since the position estimation accuracy highly depends on the sensitivity of the magnetic field to position, it is expected that the position estimation performance deteriorates when the piston moves far from the electromagnet. A good solution is to use active control of the current input to the electromagnet in order to have an optimal current distribution along the stroke length

so that sufficient magnetic sensitivity over the entire stroke is ensured in an energy efficient way. This active sensing strategy for electromagnetic position estimation is discussed in detail in Chapter 3 of this dissertation. Another shortcoming of the preliminary electromagnetic position measurement system is the need to power a moving object. Due to the wiring or battery charging for electronic parts on the moving object, the system becomes complicated and the durability is impaired. For example, a bad connection or even a wire break could happen. Therefore, this motivates the development of the novel electromagnetic position estimation system based on the use of high-magnetic-permeability materials (mu-metal), which keeps the feature of disturbance rejection enabled by the alternating magnetic field generated from the electromagnet but does not require any powered or wired electronic parts on the moving object (e.g. the piston). Instead, only passive mu-metal is attached to the moving object.

2.3 Electromagnetic Position Estimation System Using High-Magnetic-Permeability Materials

This section is organized as follows: In Section 2.3.1, the structure of the mu-metal based electromagnetic position estimation system is presented and its sensing principle is intuitively explained. Then an analytical model is provided to describe the physics of the sensing principle in Section 2.3.2. Finally, a brief analysis of the sensitivity of the linear position sensing system is provided in Section 2.3.3.

2.3.1 Structure and Sensing Principle

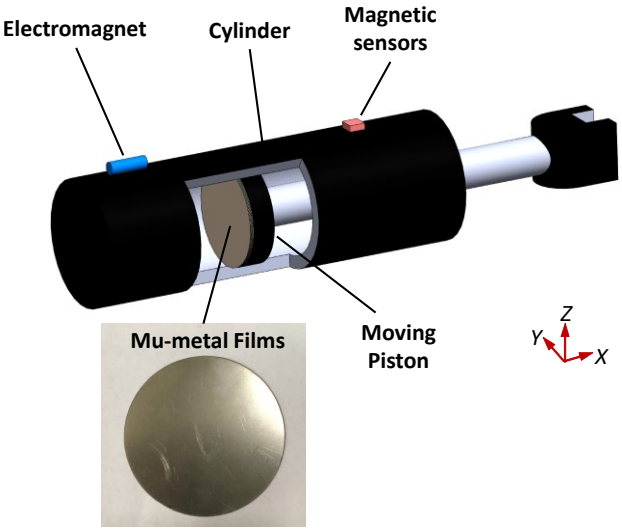

Figure 2-3 Schematic of the mu-metal based electromagnetic position sensing system.

A schematic of the mu-metal based position measurement system is shown in Figure 2-3. The position measurement system again includes an electromagnet, which generates the alternating magnetic field, and a 3-axis magnetic sensor. The sensor is approximately located co-axial to the electromagnet with only a slight offset in *z*-axis. Both the electromagnet and the sensors are located on the stationary cylinder, which effectively simplifies the power supply to them. In addition, a thin stack of mu-metal films is attached to the piston head. Mu-metal is a type of nickel-iron soft ferromagnetic alloy with very high magnetic permeability, which allows it to be readily magnetized by external magnetic fields. The measured magnetic field by the sensor includes two components: (1) the magnetic field from the electromagnet; (2) the magnetic field from the mu-metal magnetized by the electromagnet. Note the magnetic field from the magnetized mu-metal is also alternating if the original magnetic field source, i.e. the electromagnet, is alternating. The first component does not vary with the piston position due to the constant distance between the electromagnet and the sensor, so it cannot be utilized for position sensing. However, the second component changes with the piston position because magnetization intensity and orientation of the mu-metal depends on the local magnetic field from the electromagnet and the latter changes when the mu-metal together with the piston is at

different distances from the electromagnet. In other words, the mu-metal can be viewed as a "magnet" with variable intensity and orientation that varies with the location of the piston. Further, the distance between the sensor and mu-metal varies with the piston position.

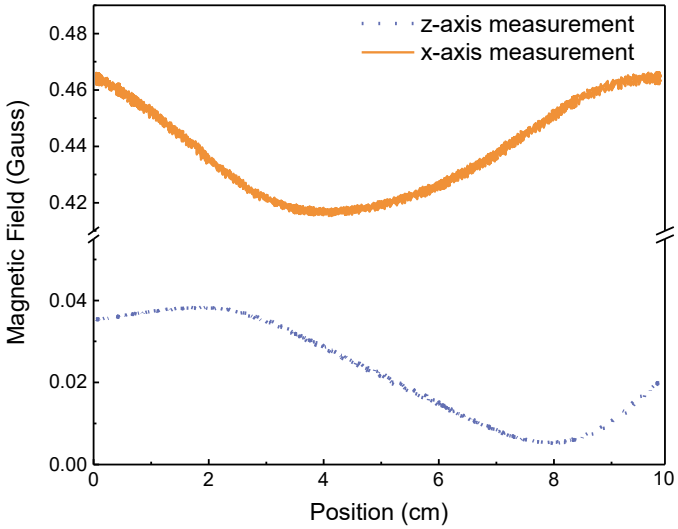

Figure 2-4 Experimental magnetic measurement model of the mu-metal based position sensing system.

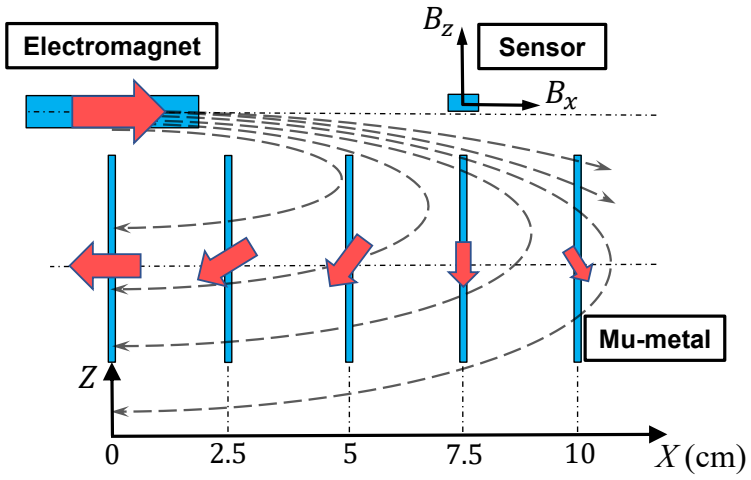

Figure 2-5 Intuitive analysis of the sensing principle of the mu-metal based position sensing system.

The experimentally measured magnetic field as a function of piston position is shown in Figure 2-4 for a measurement range of 10 cm. It is noted that both of the *x*- and *z*-axis magnetic field curves have an inverted bell shape with minimums at 3.5 cm and 8 cm, respectively. An intuitive explanation of the sensing principle can be obtained from Figure

2-5, where the electromagnet and mu-metal plates are both lumped into equivalent magnets with their magnetic fields represented by red arrows. As the piston position changes, the size and direction of red arrows on it represent the intensity and orientation of the magnetic field on it. The magnetic field lines of the electromagnet in a quarter of the cross section is plotted in dashed lines. The mu-metal stack is magnetized into equivalent magnets with different intensities and orientations at different locations with respect to the electromagnet and thus presents a varying effect on the magnetic field at the sensor location. Based on the configuration shown in Figure 2-5, the direct magnetic field at the sensor location from the electromagnet are in positive x and z direction since the sensor is slightly off the center line of the electromagnet in the z-axis.

The magnetic field of the mu-metal stack at the sensor location in x-axis is explained as follows. When the mu-metal stack is right below the electromagnet, the magnetization direction is in the $-x$ direction and thus the mu-metal plates exert a large field in $-x$ direction at the sensor location. As the mu-metal moves along the x direction until $x = 7.5$ cm where the sensor is located, the magnetization direction deflects off the x-axis and gets aligned with the z-axis. Also, magnetization intensity decreases because the mu-metal moves away from the electromagnet. Both of the above cause less contribution from mu-metal to the x-axis field at the sensor location. However, the distance between the sensor and the mu-metal is reduced, which has a favorable effect on the field contribution from mu-metal. From 0 to 3.5 cm, the latter spatial effect dominates, due to which the field in x-axis at sensor location from mu-metal increases and the total field in x-axis decreases accordingly since the fields from electromagnet and mu-metal are opposite. From 3.5 to 7.5 cm, the magnetization effect dominates, which makes the x-axis field from the mu-metal decrease and thus the total x-axis field recovers back. As the mu-metal continues to move and passes the sensor, the magnetization direction deflects such that mu-metal contributes positively to the field in x-axis, which accounts for the further elevated magnetic field from 7.5 to 10 cm.

The magnetic field of the mu-metal stack at the sensor location in z-axis is explained as follows. As the mu-metal moves from 0 to 7.5 cm, the magnetization direction is deflected and gets aligned with the z-axis gradually, and the distance between the sensor

and the mu-metal decreases, which causes more contribution from the mu-metal to the *z*-axis field at the sensor location. Again, the magnetization intensity decreases, which has an adverse effect on the contribution from mu-metal to *z*-axis field. Since the former effect dominates, the field from the mu-metal in *z*-axis increases and accordingly the total field decreases because the *z*-axis fields from electromagnet and mu-metal are in opposite direction. After the mu-metal passes the sensor, the magnetization direction deflects away from the *z*-axis and the mu-metal moves further away from both the electromagnet and the sensor. All these factors lead to a decreasing contribution from the mu-metal to the *z*-axis field, which makes the total field in the z-axis increase and then recover back.

2.3.2 Analytical Modeling

An analytical model of the measured magnetic field at the sensor as a function of piston position is derived in this section to quantitatively reveal the underlying physics of the mu-metal based position sensing principle. This is done by modeling the magnetic field at the sensor as the sum of the magnetic field from the electromagnet and the magnetized mu-metal. Then the analytical model is verified by comparison with experimental results.

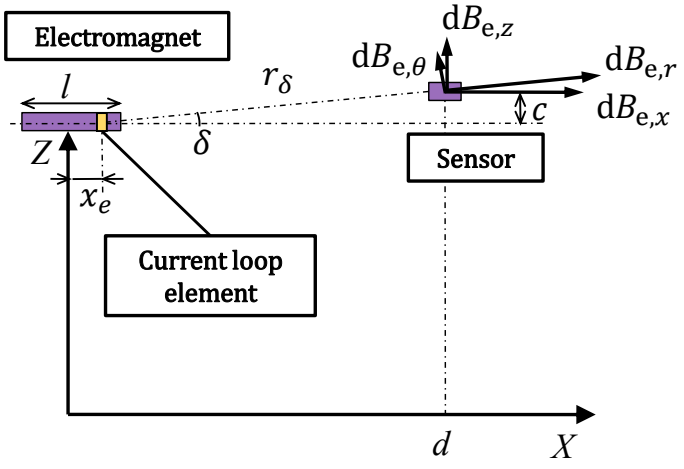

(a) Magnetic field of electromagnet

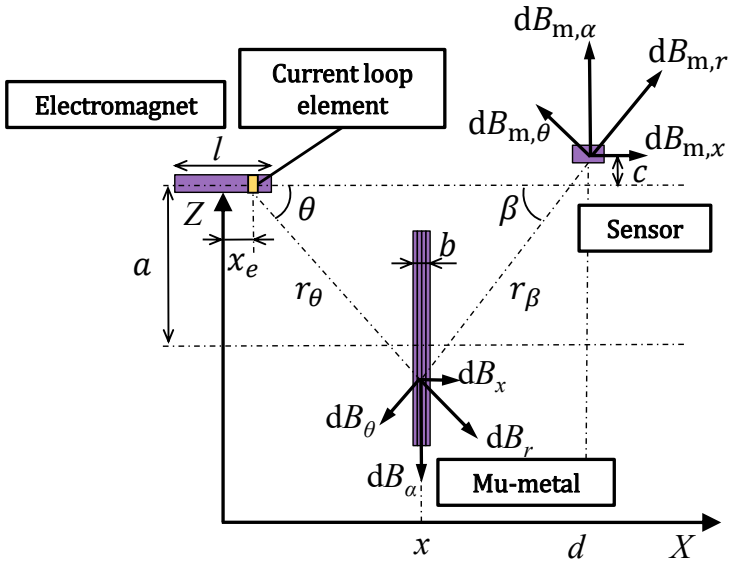

(b) Magnetic field of mu-metal (front view)

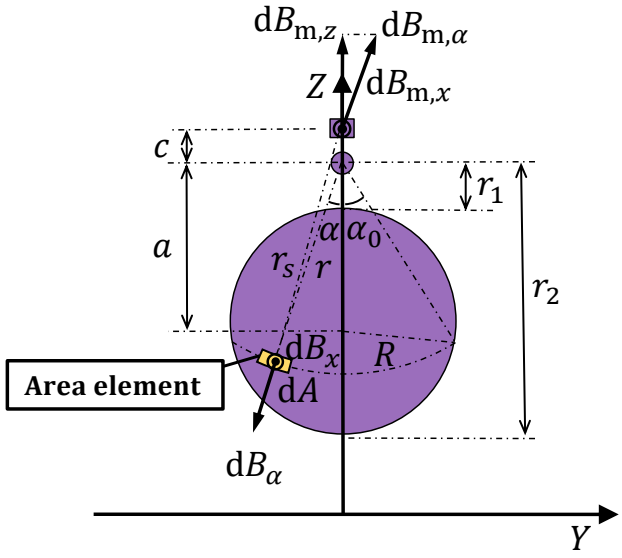

(c) Magnetic field of mu-metal (side view)

Figure 2-6 Analytical modeling of measured magnetic field from the electromagnet and mu-metal.

As shown in Figure 2-6 (a), the electromagnet is modeled as a series of stacked current loops that can be considered as magnetic dipoles with individual magnetic moments. The magnetic field of an individual current loop element in both radial and tangential direction, i.e. $\mathrm{d}B_{\mathrm{e},r}$ and $\mathrm{d}B_{\mathrm{e},\theta}$, is given by

$$m = nI\mathrm{d}x_{\mathrm{e}} \cdot (\pi {R_{\mathrm{e}}}^2) \tag{2-2}$$

$$\mathrm{d}B_{\mathrm{e},r} = \frac{\mu_0 m}{2\pi r_\delta^3}\cos\delta$$

$$\mathrm{d}B_{\mathrm{e},\theta} = \frac{\mu_0 m}{4\pi r_\delta^3}\sin\delta$$

where the subscript "e" represents "electromagnet", m is the effective magnetic moment of the current loop, n is the wire turns per unit length, I is the supply current of the electromagnet, $\mathrm{d}x_\mathrm{e}$ is the length of the current loop element, R_e is the radius of the electromagnet, μ_0 is the magnetic permeability in vacuum, and δ and r_δ are polar coordinates of the concerned location, which are given by

$$\begin{aligned} r_\delta &= \frac{c}{\sin\delta} \\ \delta &= \tan^{-1}\frac{c}{d - x_\mathrm{e}} \end{aligned} \tag{2-3}$$

where c is the offset of the sensor from the electromagnet in z-axis. Then the measured magnetic field of the current loop element is obtained by projecting $\mathrm{d}B_{e,r}$ and $\mathrm{d}B_{e,\theta}$ onto x- and z-axis.

$$\begin{aligned} \mathrm{d}\overrightarrow{B_\mathrm{e}} &= \begin{bmatrix} \mathrm{d}B_{\mathrm{e},x} \\ \mathrm{d}B_{\mathrm{e},z} \end{bmatrix} \\ &= \begin{bmatrix} \cos\delta & -\sin\delta \\ \sin\delta & \cos\delta \end{bmatrix} \begin{bmatrix} \mathrm{d}B_{\mathrm{e},r} \\ \mathrm{d}B_{\mathrm{e},\theta} \end{bmatrix} \end{aligned} \tag{2-4}$$

Therefore, the magnetic field of the electromagnet at the sensor location is computed by integrating (2-4) over the total length of the electromagnet. This integral is given by

$$\overrightarrow{B_\mathrm{e}} = \int_{\substack{\text{Length of} \\ \text{electromagnet}}} \mathrm{d}\overrightarrow{B_\mathrm{e}} \tag{2-5}$$

where $\overrightarrow{B_\mathrm{e}}$ is the magnetic field from the whole electromagnet in x- and z- axis, d is the distance of the sensors from the electromagnet along its central axis, l is length of the electromagnet, N is number of wire turns of the electromagnet, and λ is a coefficient related to the magnetic permeability and shape of the ferrous core of the electromagnet. It is noted that $\overrightarrow{B_\mathrm{e}}$ is not a function of the piston position x and thus not involved in position sensing.

The other magnetic field component measured by the sensors is from the magnetized mu-metal thin films. The schematic of the analytical modeling for the magnetic field of mu-metal films is shown in Figure 2-6 (b) and (c). The magnetic field of an element of the mu-metal film with area $\mathrm{d}A$ magnetized by the current loop element with length $\mathrm{d}x_{\mathrm{e}}$ is computed first and then the total magnetic field of the mu-metal film is obtained by integrating the element field over the whole area of the mu-metal film and whole length of the electromagnet. It is assumed that more than 1 layer of mu-metal film (i.e. a stack of films) can be utilized.

The magnetic field from the current loop element at the location of the element of the mu-metal film, i.e. $\mathrm{d}B_r$ and $\mathrm{d}B_\theta$, serves as the magnetization source and is obtained by equation (2-2) with the polar coordinates replaced by r_θ and θ.

$$r_\theta = \frac{r}{\sin\theta}$$
$$\theta = \tan^{-1}\frac{r}{x - x_{\mathrm{e}}} \tag{2-6}$$

where r is distance between central axis of electromagnet and the mu-metal element. Due to the multi-layer structure of mu-metal films, the magnetization of mu-metal laminations is anisotropic. Magnetization is much easier within the plane of each mu-metal film than in the perpendicular direction because of the small air gaps with low permeability between adjacent mu-metal films. According to [60], the effective relative magnetic permeability in perpendicular and in-plane direction is given by

$$\mu_x \approx \frac{1}{1-p}$$
$$\mu_\alpha \approx p\mu_r \tag{2-7}$$

where p is the proportion of mu-metal volume in total volume of mu-metal laminations (≈ 0.98), μ_r is the relative permeability of mu-metal material ($\approx 10^5$). It is noted that $\mu_x \ll \mu_\alpha$ based on the calculation of (2-7). According to the ideal magnetization model given by [42], the magnetization of element mu-metal films in perpendicular and in-plane directions is given by

$$\mathrm{d}M_x = \frac{\mu_x - 1}{[1 + N_x(\mu_x - 1)]\mu_0}\mathrm{d}B_x \tag{2-8}$$

$$\mathrm{d}M_\alpha = \frac{\mu_\alpha - 1}{[1 + N_\alpha(\mu_\alpha - 1)]\mu_0}\mathrm{d}B_\alpha$$

where N_x and N_α are demagnetizing factors in each corresponding direction. $\mathrm{d}B_x$ and $\mathrm{d}B_\alpha$ are external field components from the current loop element by projecting $\mathrm{d}B_r$ and $\mathrm{d}B_\theta$ onto perpendicular and in-plane directions, which are expressed by

$$\begin{bmatrix}\mathrm{d}B_x \\ \mathrm{d}B_\alpha\end{bmatrix} = \begin{bmatrix}\cos\theta & -\sin\theta \\ \sin\theta & \cos\theta\end{bmatrix}\begin{bmatrix}\mathrm{d}B_r \\ \mathrm{d}B_\theta\end{bmatrix} \tag{2-9}$$

Then the mu-metal elements are considered as two orthogonal dipoles with magnetization of $\mathrm{d}M_x$ and $\mathrm{d}M_\alpha$ and their magnetic field at the sensor location is computed as

$$\begin{gathered}
\mathrm{d}B_{\mathrm{m},r} = \frac{\mu_0 \mathrm{d}M_x \cdot b\mathrm{d}A}{2\pi r_\beta^3}\cdot\cos\beta + \frac{\mu_0 \mathrm{d}M_y \cdot b\mathrm{d}A}{2\pi r_\beta^3}\cdot\cos(\frac{\pi}{2}+\beta) \\
\mathrm{d}B_{\mathrm{m},\theta} = \frac{\mu_0 \mathrm{d}M_x \cdot b\mathrm{d}A}{4\pi r_\beta^3}\cdot\sin\beta + \frac{\mu_0 \mathrm{d}M_y \cdot b\mathrm{d}A}{4\pi r_\beta^3}\cdot\sin(\frac{\pi}{2}+\beta) \\
\begin{bmatrix}\mathrm{d}B_{\mathrm{m},x} \\ \mathrm{d}B_{\mathrm{m},\alpha}\end{bmatrix} = \begin{bmatrix}\cos\beta & -\sin\beta \\ \sin\beta & \cos\beta\end{bmatrix}\begin{bmatrix}\mathrm{d}B_{\mathrm{m},r} \\ \mathrm{d}B_{\mathrm{m},\theta}\end{bmatrix} \\
\mathrm{d}B_{\mathrm{m},z} = \mathrm{d}B_{\mathrm{m},\alpha}\cdot\cos\alpha \\
\beta = \tan^{-1}\frac{r_s}{d-x} \\
r_\beta = \frac{r_s}{\sin\beta} \\
r_s = \sqrt{r^2 + c^2 + 2rc\cos\alpha}
\end{gathered} \tag{2-10}$$

where b and $\mathrm{d}A$ are thickness and area of the element mu-metal laminations, respectively, and the subscript "m" represents "mu-metal". The total magnetic field of the magnetized mu-metal films is given by the following integral

$$\begin{aligned}
\overrightarrow{B_{\mathrm{m}}}(x) &= \int_{\substack{\text{Length of}\\ \text{electromagnet}}} \iint_{\substack{\text{Area of}\\ \text{mu-metal}}} \mathrm{d}\overrightarrow{B_{\mathrm{m}}} \\
&= \int_{-\frac{l}{2}}^{\frac{l}{2}}\int_{a-R}^{a+R}\int_0^{\alpha_0} 2\overrightarrow{B_0}(x,r,\alpha,x_{\mathrm{e}})\mathrm{d}A\mathrm{d}x_{\mathrm{e}} \\
\alpha_0 &= \cos^{-1}\frac{r^2 + a^2 - R^2}{2ar}
\end{aligned} \tag{2-11}$$

where $\mathrm{d}\overrightarrow{B_\mathrm{m}} = [\mathrm{d}B_{\mathrm{m},x} \quad \mathrm{d}B_{\mathrm{m},z}]^\mathrm{T}$, $\mathrm{d}A = r\mathrm{d}\alpha\mathrm{d}r$, and $\overrightarrow{B_0}$ is the magnetic field of per unit area mu-metal magnetized by per unit length of electromagnet. The numerical integration is carried out to obtain the total magnetic field of mu-metal films. Note that only the *x*- and *z*- axis components of the magnetic field are considered here because *y*- axis component is always zero due to the symmetric structure of the system.

The total magnetic field measured by the magnetic sensors is the sum of above two magnetic field components as given by

$$\overrightarrow{B_\mathrm{s}}(x) = \overrightarrow{B_\mathrm{e}} + \overrightarrow{B_\mathrm{m}}(x) \tag{2-12}$$

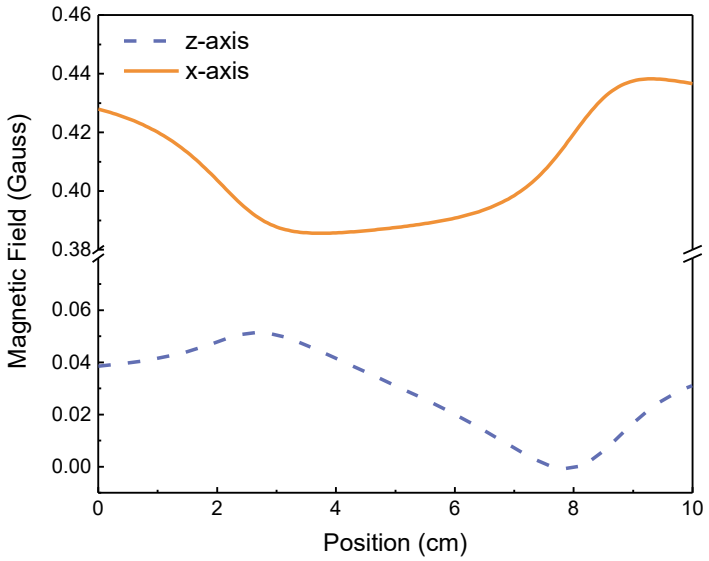

Figure 2-7 Analytical magnetic measurement model of the mu-metal based position sensing system.

This analytical magnetic model as a function of piston position is depicted in Figure 2-7. Compared with the experimental model shown in Figure 2-4, It is observed that the measured magnetic field in both *x*- and *z*-axis varies non-linearly and non-monotonically with the piston position. The analytical model shares approximately the same qualitative variation patterns with the experimental results, which validates the assumptions made in the derivation of the analytical model. In both models, as the piston moves, the magnetic field in *x*-axis decreases to the minimum value at around 3 cm and then increases gradually. The magnetic field in *z*-axis starts to increase slightly, then drops to the minimum value at around 8 cm, and finally increases again. Further, it can be seen that the peak-to-peak variation is approximately 0.05 Gauss for the x axis and 0.045 Gauss for the z axis in both

the experimental data and analytical model. The minor quantitative disagreement between analytical and experimental results may be attributed to the inadequate modeling of the anisotropic aspects of the magnetization and demagnetizing factor of mu-metal films.

2.3.3 Analysis of Sensitivity

It is required to have sufficient sensitivity between the measured magnetic field and the position change of the mu-metal in order to estimate the unknown position. As shown in Figure 2-7, the magnetic field in both *x*- and *z*-axis varies nonlinearly and non-monotonically, which means there must be some regions of position where the magnetic sensitivity deteriorates. These regions are around the maximums and minimums of the magnetic field measurements. However, the extremums for *x*-axis magnetic field and *z*-axis magnetic field are separated in different positions. While the magnetic sensitivity is low for one axis measurement, that of the other axis measurement is sufficient to guarantee the functioning of the position estimation algorithm.

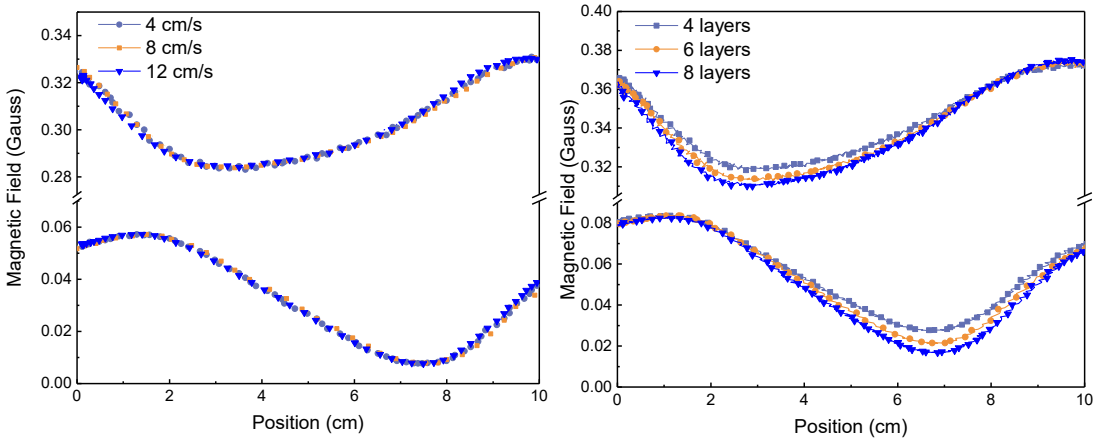

(a) **(b)**

Figure 2-8 Influence of (a) piston speed and (b) thickness of mu-metal films on magnetic sensitivity

The influence of two factors, i.e. the speed of piston motion and the thickness of mu-metal films, on the sensitivity of the position sensing system is investigated. It is shown in Figure 2-8 (a) that piston speed has a negligible effect on the magnetic field within a speed range of 4 cm/s to 12 cm/s. Therefore, piston speed does not influence the sensitivity of the position sensing system. Magnetic field variations with piston position with different layers

of mu-metal films are shown in Figure 2-8 (b). Each layer of mu-metal film is 0.25 mm thick. As the mu-metal film stack become thicker, the magnetic field variation become more significant, which leads to larger sensitivity of the position sensing system. Thus, it is beneficial to use more mu-metal layers to get more accuracy.

2.4 Sensor Signal Processing

It was mentioned earlier in this Chapter that the use of an electromagnet in the position measurement system enables the use of an alternating magnetic field instead of a DC magnetic field. The alternating magnetic field at a specific high frequency could differentiate from the low-frequency disturbances from nearby ferromagnetic objects in the frequency domain, which offers the possibility of ferromagnetic disturbance rejection. This section will describe the method of sensor signal processing in detail.

Since the electromagnet is supplied with alternating current, the direct analog sensor readings are also alternating signals. Multiple steps of signal processing are required to extract the amplitude of the alternating signal from which position can be estimated robust to ambient ferromagnetic disturbances. A flow chart of signal processing and the electronics used in the position estimation system is shown in Figure 2-9. An alternating magnetic field at 100 Hz is generated by supplying an alternating voltage to the electromagnet. This frequency is sufficiently high compared to the frequency of piston motion, whose bandwidth is lower than 10 Hz. The magnetic sensors on the piston read an alternating magnetic field offset by a bias value that depends on the magnetic field of the earth and of the immediate surroundings of the system. In order to remove the influence of the static magnetic field due to the surroundings, the measured magnetic field is high-pass filtered using an RC circuit (cutoff frequency $f_c = 20$ Hz). The cutoff frequency of the high-pass filter can be adjusted to accommodate the expected range of disturbance frequencies in the actual field application. For this research, it is assumed that the motion of ambient ferromagnetic objects is at frequencies much lower than 20 Hz. A purely oscillatory voltage signal with no bias is then obtained after the high pass filter which is amplified using an instrumental amplifier (INA2126) and then supplied to an RMS

measurement chip (AD637). The RMS measurement chip provides a voltage proportional to the amplitude of the magnetic field at the 100 Hz frequency, i.e. $B_{\mathrm{RMS}} = \frac{1}{\sqrt{2}} B_{\mathrm{amp}}$, where B_{RMS} is the RMS value of the filtered and amplified alternating magnetic field, and B_{amp} is its amplitude. This voltage is then low-pass filtered (cutoff frequency $f_c = 15$ Hz) and fed to a 16-bit analog-to-digital converter (ADS1115). The digitized magnetic field measurements are then read by the microprocessor and an extended Kalman Filter based position estimation algorithm is implemented.

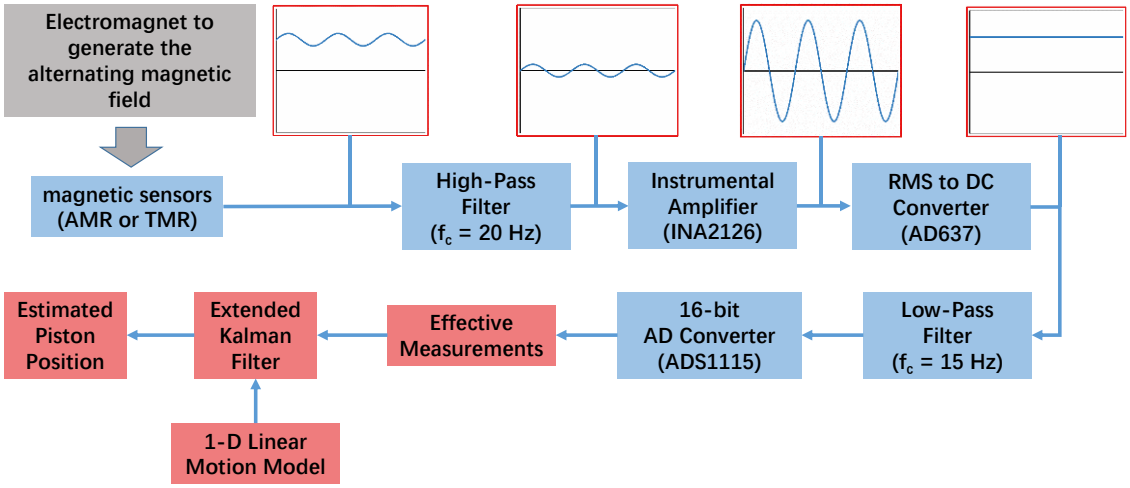

Figure 2-9 Flow chart of magnetic signal processing.

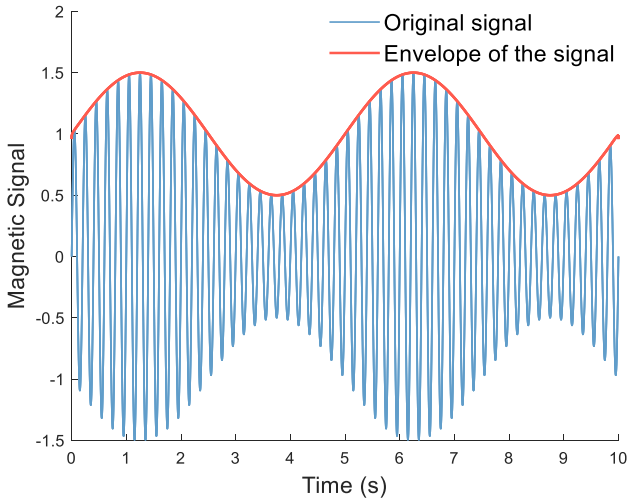

Figure 2-10 Extraction of the dynamic amplitude of the alternating magnetic field.

As the mu-metal moves with the piston, the amplitude of alternating magnetic field varies, as is shown in Figure 2-10. The objective of the signal processing is thus to extract the dynamic amplitude of the alternating magnetic measurements at the pre-determined 100 Hz frequency. The 100 Hz frequency of the electromagnet is high enough to be above the bandwidth of frequencies in which the piston or disturbing ferromagnetic objects move. Low frequency components such as ferromagnetic disturbances and constant magnetic fields like the earth's magnetic field are removed when the raw magnetic sensor outputs are passed through the high-pass filter with a cut-off frequency of 20 Hz.

2.5 Position Estimation Algorithm

A nonlinear state estimation algorithm is required to fuse the motion model with measurements from multiple magnetic sensors because the magnetic measurement model is nonlinear with respect to the piston position. The Extended Kalman filter (EKF) is therefore employed here because it is suitable for this real-time application due to its simplicity of implementation and high computational efficiency. The states to be estimated are given by

$$X = [x_p \quad v_p \quad a_p]^{\mathrm{T}} \tag{2-13}$$

where x_p, v_p and a_p are the piston position, velocity and acceleration, respectively. A 1-D linear kinematic model with constant acceleration assumption is employed to propagate the states and the magnetic measurements are used to update the estimates. The process noise, which is associated with the uncertainty of the acceleration, is assumed to be zero mean Gaussian noise with given covariance Q. The measurement noise is also assumed to be zero mean Gaussian noise with constant covariance R. R is obtained by computing the sample variance of the experimental magnetic sensor measurement data and Q is estimated approximately based on the potential maximum acceleration of motion. The kinematic model and measurement model are listed below [61]:

$$\begin{aligned} X_{\mathrm{k}} &= \Phi X_{\mathrm{k-1}} + G w_{\mathrm{k-1}} \\ y_{\mathrm{k}} &= h(X_{\mathrm{k}}) + n_{\mathrm{k}} \\ n_{\mathrm{k}} &\sim N(0, R) \end{aligned} \tag{2-14}$$

$$w_{\mathrm{k}} \sim N(0, Q)$$

where

$$\Phi = \begin{bmatrix} 1 & \mathrm{d}t & \frac{\mathrm{d}t^2}{2} \\ 0 & 1 & \mathrm{d}t \\ 0 & 0 & 1 \end{bmatrix}, G = \begin{bmatrix} \frac{\mathrm{d}t^2}{2} \\ \mathrm{d}t \\ 1 \end{bmatrix}, Q = {\sigma_a}^2, \quad R = \begin{bmatrix} {\sigma_{s1}}^2 & 0 \\ 0 & {\sigma_{s2}}^2 \end{bmatrix} \tag{2-15}$$

and where $\mathrm{d}t$ is the sampling time. y represents magnetic measurements from one or more magnetic sensors. w and n are process noise and measurement noise, respectively. Subscript k is the time step index. For both the preliminary position sensing system and the mu-metal based position sensing system, two sensors are used so ${\sigma_{s1}}^2$ and ${\sigma_{s2}}^2$ are measurement variance associated with two magnetic sensors and it is assumed that there is no correlation between different sensor measurements. ${\sigma_a}^2$ is the variance of acceleration. $h(\cdot)$ is the nonlinear measurement model. The EKF estimation algorithm is listed below [62]:

$$\hat{X}_{\mathrm{k}}^{-} = \Phi \hat{X}_{\mathrm{k\text{-}1}}^{+} \tag{2-16}$$

$$P_{\mathrm{k}}^{-} = \Phi P_{\mathrm{k}-1}^{+} \Phi^{\mathrm{T}} + G Q G^{\mathrm{T}} \tag{2-17}$$

$$H_{\mathrm{k}} = \left.\frac{\partial h}{\partial X}\right|_{\hat{X}_{\mathrm{k}}^{-}} \tag{2-18}$$

$$K_{\mathrm{k}} = P_{\mathrm{k}}^{-} {H_{\mathrm{k}}}^{\mathrm{T}} (H_{\mathrm{k}} P_{\mathrm{k}}^{-} {H_{\mathrm{k}}}^{\mathrm{T}} + R)^{-1} \tag{2-19}$$

$$\hat{X}_{\mathrm{k}}^{+} = \hat{X}_{\mathrm{k}}^{-} + K_{\mathrm{k}} \left[y_{\mathrm{k}} - h\left(\hat{X}_{\mathrm{k}}^{-}\right) \right] \tag{2-20}$$

$$P_{\mathrm{k}}^{+} = (I - K_{\mathrm{k}} H_{\mathrm{k}}) P_{\mathrm{k}}^{-} \tag{2-21}$$

where P is the covariance of states and K is the Kalman gain. The initial P is set to be a diagonal matrix with potential maximum position, velocity and acceleration during motion in its diagonal entries. For example, the initial P could be set to be

$$P = \begin{bmatrix} 20^2 & 0 & 0 \\ 0 & 2^2 & 0 \\ 0 & 0 & 10^2 \end{bmatrix} \tag{2-22}$$

Superscript "+" and "-" represents a posteriori estimates and a priori estimates for a certain time step, respectively. I is the identity matrix with proper dimensions. To sum up, piston position, velocity and acceleration are estimated from magnetic field measurements in real

time using a nonlinear state estimation algorithm (EKF). Generally, this algorithm can deal with measurements from multiple sensors. For both sensor embodiments proposed in this chapter, two sensor signals are adopted for position estimation. Since the magnetic disturbance is already eliminated by analog signal processing electronics, no special disturbance rejection algorithms need to be implemented during position estimation.

2.6 Experimental Results

In this section, the results of experimental characterization of both the preliminary electromagnetic position measurement system and the mu-metal based electromagnetic position measurement system are presented and discussed.

2.6.1 Experimental Results of the Preliminary System

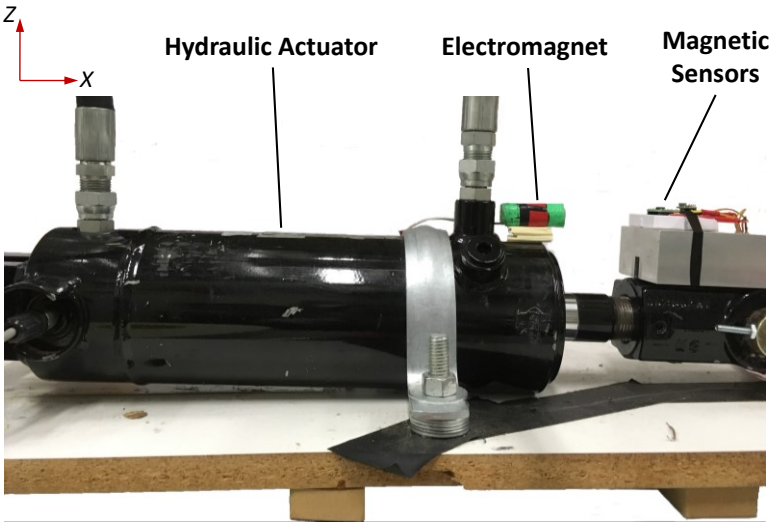

Figure 2-11 Experimental setup of the preliminary system.

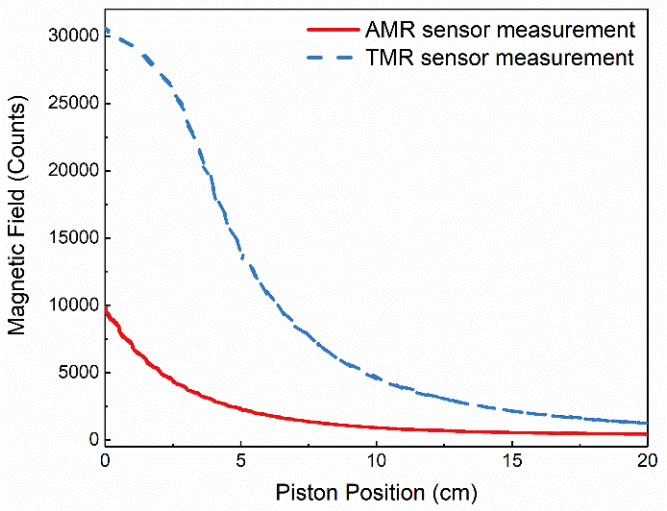

Figure 2-12 Experimental measurement model for the preliminary position measurement system.

The experimental setup for the preliminary position sensing system is shown in Figure 2-11. A hydraulic actuator with stroke length of 20 cm is used for experimental testing. The actuator is made of steel with a 3.50 cm diameter piston rod and an 8.84 cm diameter piston head. An electromagnet made by wrapping copper wires around a 0.6 cm diameter × 4.5 cm steel core is mounted on the head end of the cylinder. An alternating current of 560 mA (peak to peak value) is supplied to the electromagnet to generate an alternating magnetic field around it. Two magnetic sensors are placed on the external end of the piston rod and the distance between them is approximately 1.5 cm. One of the sensors is an anisotropic magneto-resistance (AMR) sensor (HMC1001) with a sensitivity of 3 mV/V/Oe and the other sensor is a tunnel magneto-resistance (TMR) sensor (TMR2003) with a larger sensitivity of 6 mV/V/Oe. Only the AMR sensor with low sensitivity is used for position estimation when the sensors are near the electromagnet because the TMR sensor with high sensitivity gets saturated there due to the high magnetic field. However, both sensors are employed when the sensors are far enough from the electromagnet because the high sensitivity of the TMR sensor enhances the accuracy of position estimation when the piston extends far out along its stroke. The necessity of this sensor fusion strategy can be illustrated by the measurement model shown in Figure 2-12. It is seen that the TMR sensor signal get saturated under 4 cm and the AMR sensor lose sensitivity when position is above 15 cm. Note that the distance of the TMR sensor from the electromagnet is 7 cm when the

piston is fully withdrawn into the cylinder and that is defined as the origin of the piston position for this system. The reference sensor for comparison is an expensive magneto-strictive position sensor of high accuracy that is embedded in the core of the piston rod of the hydraulic actuator.

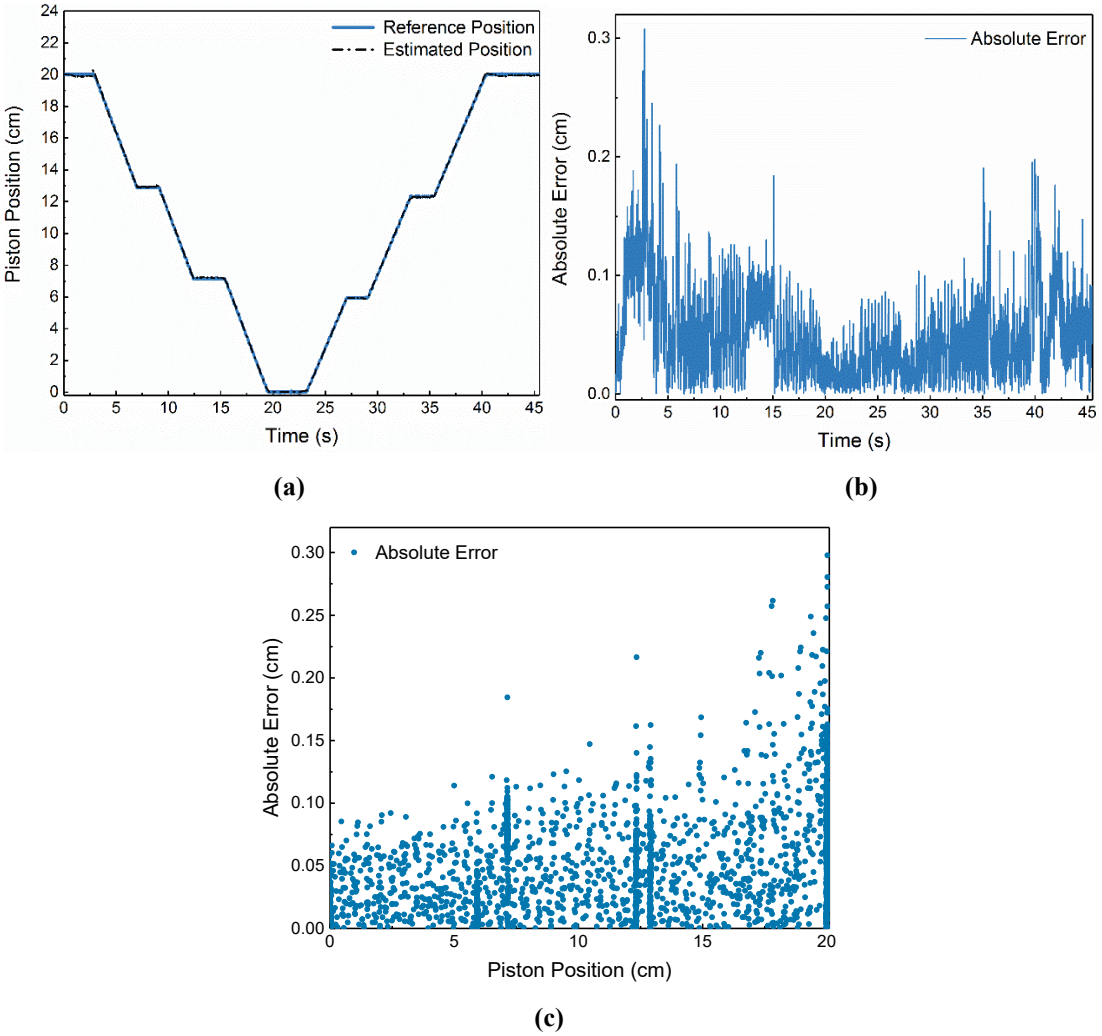

Figure 2-13 Position estimation results of the preliminary system (a) Position estimates compared to Magnetostrictive sensor measurements. (b) Absolute estimation error over time. (c) Absolute estimation error as a function of position.

The piston position can be estimated using the estimation algorithms given by (2-16) – (2-21), together with the signal processing hardware described earlier in Section 2.4. An example of the position estimation results for one test is shown in Figure 2-13. Figure 2-13 (a) shows both the position estimates of the new estimation system and the position measured by the expensive reference sensor. It is seen that the position estimates appear

to track the reference signal very closely. The estimation error (defined by taking the absolute value of the difference between the new position estimates and the reference sensor measurements) is seen in Figure 2-13 (b) to have a maximum value of 0.3 cm, which corresponds to a max error of less than 1.5% for this 20 cm stroke cylinder. The variation of estimation error with position is also plotted in Figure 2-13 (c) and it shows that the error increases with piston position due to a decrease of magnetic measurement sensitivity with distance. The theoretical variance of position estimates can be obtained by (2-17) and (2-21), which are found to be 0.012 cm, 0.030 cm and 0.073cm at positions 5 cm, 10 cm and 15 cm, respectively. It is noted that the variance increases with the piston position as expected.

2.6.2 Experimental Results of the Mu-metal Based System

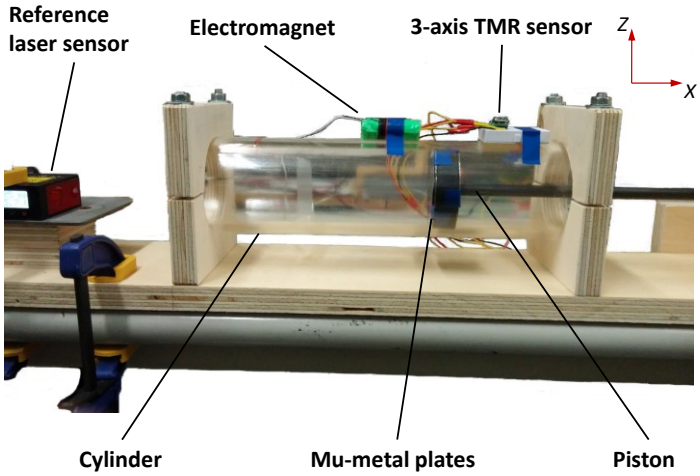

Figure 2-14 Experimental setup of the mu-metal based electromagnetic position sensing system

The experimental setup is shown in Figure 2-14. A 3-D printed plastic piston-cylinder system was fabricated to test the position measurement system. The diameters of the piston rod and piston head are 0.960 cm and 6.330 cm, respectively. The length of the cylinder is 30 cm but the position measurement system is only tested for a stroke length of 10 cm on either side of the electromagnet. The mu-metal plates are fixed to the piston head. The electromagnet used in this system is the same as that for the basic electromagnetic position measurement system. The electromagnet is supplied with an alternating current of 560 mA (peak to peak value) again. Since the variation of measured magnetic field with piston

position is small, a 3-axis analogue TMR sensor (TMR2305M) with high sensitivity of 25 mV/V/Oe is used in this position measurement system. The sensor is mounted statically on the cylinder to measure the magnetic field. The sensor is aligned with the electromagnet in *x*- and *z*-axis with no offset in *y*-axis. Therefore, the measured magnetic field from the electromagnet and mu-metal plates only includes *x* and *z* components and the magnetic field in *y*-axis is always zero because the geometric structure of the position measurement system is axisymmetric about *xz*-plane and the piston only moves in *x*-axis. Hence, only *x* and *z*-axis measurements are adopted for position estimation. An expensive laser sensor is employed as the reference position sensor for comparison. The left cap of the cylinder is removed to allow the laser beam to go through and shine on the piston for reference position measurement.

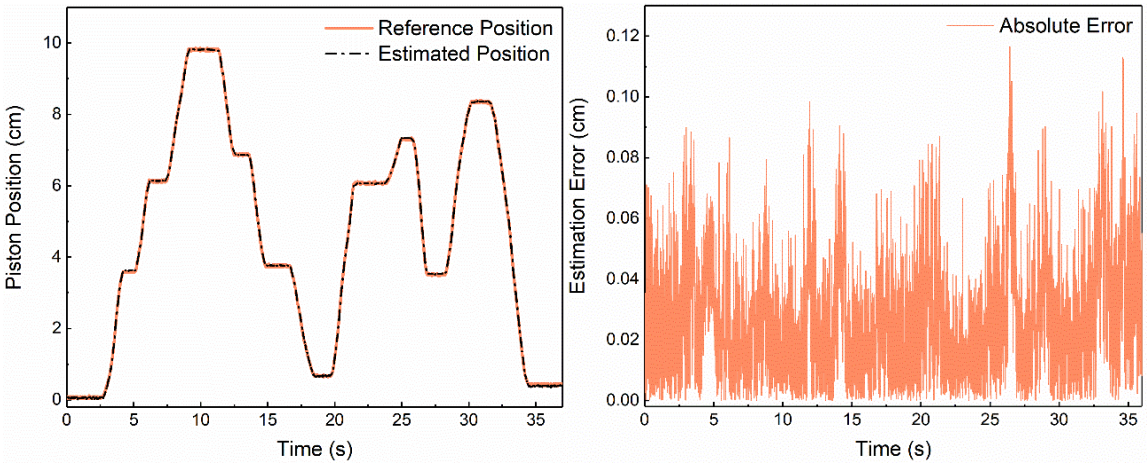

(a) **(b)**

Figure 2-15 Position estimation results of the mu-metal based system. (a) Position estimates compared to laser sensor measurements. (b) Absolute estimation error.

For accurate position estimation, the measurement model $h(\cdot)$ in equation (2-14) is obtained by fitting a Fourier series to the experimental data shown in Figure 2-4Figure 2-15. It is seen that the measurement model is non-monotonic and highly nonlinear. In experiments, a sampling rate of 133 Hz is adopted for robust position estimation since the piston moves at a much lower frequency. Note that the raw 100 Hz signals are not read directly by the data acquisition system and the output of the RMS chip is read instead.

The position measurement results with no foreign ferromagnetic disturbance are shown

in Figure 2-15. It is shown that the position estimates from magnetic sensing tracks the reference position from the expensive laser sensor well with a maximum absolute error of 0.12 cm, which amounts to a maximum 1.2 % error over the entire 10 cm range of motion. It is observed from Figure 2-15 (b) that there exist several peaks of position error. These peaks of position error happen when the piston undergoes a rapid start or stop. This is because the assumption of constant acceleration does not hold for the situation of fast dynamics. However, the accuracy of the position estimation even with these errors is within 1.2%, which is satisfactory for this specific application. Therefore, the proposed novel sensing principle based on passive high permeability mu-metal thin films has been experimentally validated and found to work very accurately for position sensing on linear actuators.

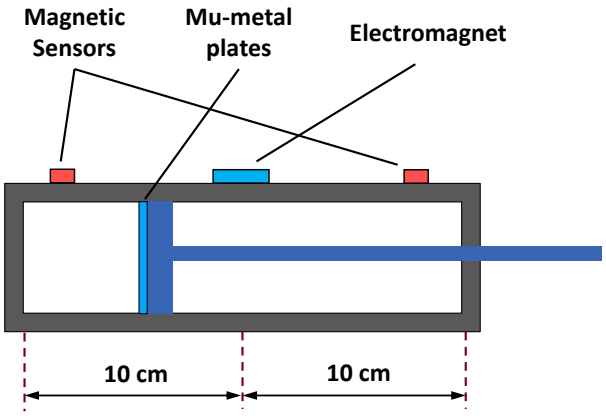

Figure 2-16 Schematic of extension of sensing range.

Although the position measurement system has only been tested on one side of the electromagnet with a sensing range of 10 cm, it can be easily modified to measure the piston position over a range of 20 cm. As is shown in Figure 2-16, one magnetic sensor each can be placed on each side of the electromagnet and the nearest set of sensors with respect to the piston can be used for position estimation. Since the position measurement system with one set of sensors is experimentally shown to accurately measure the piston position in a range of 10 cm with 1.2 mm maximum error, it should be able to measure the position over a range of 20 cm without significant increase of absolute error when equipped with two sensors in symmetric locations. Therefore, the maximum error with respect to the total sensing range can be decreased below 1%.

2.7 Performance Evaluation of Disturbance Rejection

Both the preliminary and the mu-metal based position measurement system are experimentally evaluated for their immunity to foreign ferromagnetic disturbance. A 250 mm long and 25 mm wide steel wrench is used as the disturbance source. It is ferromagnetic and has a strong inherent magnetic field. It is brought near the sensor at some time instant and kept there later.

2.7.1 Disturbance Rejection Results of the Preliminary System

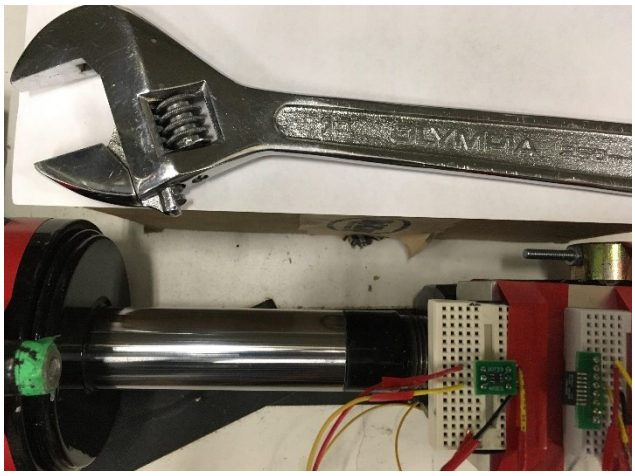

Figure 2-17 Wrench configurations for disturbance rejection characterization of the preliminary system.

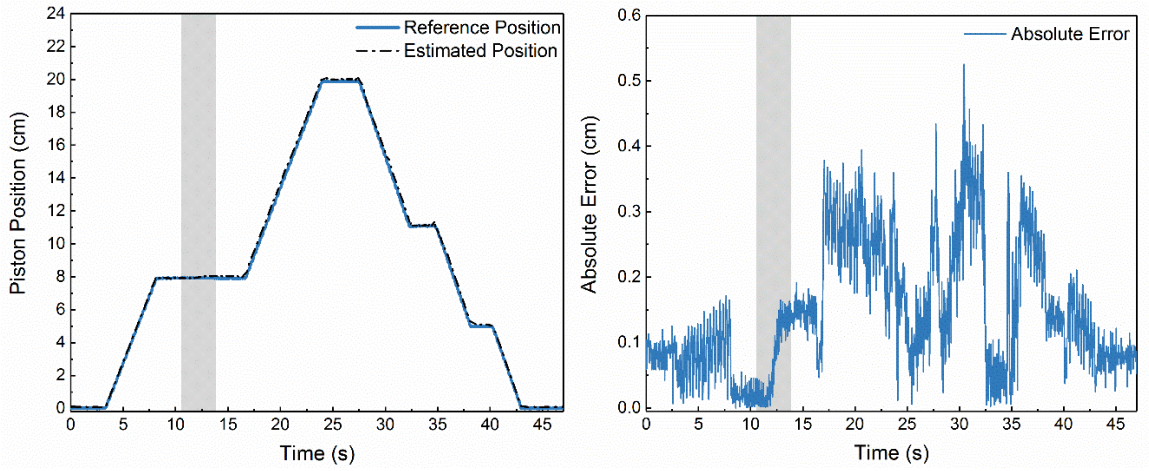

(a) **(b)**

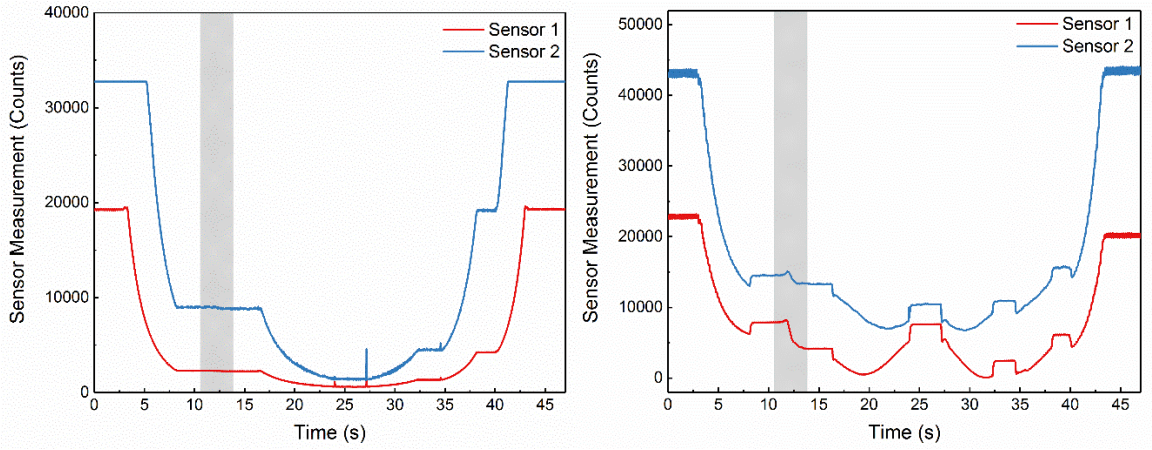

Figure 2-18 Disturbance rejection performance for the preliminary system. (a) Position estimation results. (b) Estimation error. (c) Effective measurements after high pass filter (d) Measurements before high pass filter.

Figure 2-17 shows the wrench configuration of the disturbance rejection test for the preliminary system. Figure 2-18 (a) and (b) show the position estimation results. The shaded rectangle represents the time at which the disturbance is introduced. It is seen that there is no significant increase of position measurement error when disturbance is introduced. The large estimation error from 18 s to 38 s happens when the sensors move far from the electromagnet, where the magnetic field is weak and thus the sensitivity is low. The maximum measurement error is 0.5 cm, which corresponds to 2.5% of stroke. The position measurement system in this paper is superior to the system proposed by [31] using a disturbance rejection algorithm, which had 10% maximum error. In addition, the disturbance rejection performance is robust and effective no matter the piston moves or not while the disturbance rejection performance of the system in [31] deteriorates when the piston is stationary. This indicates that the fundamental elimination of ferromagnetic disturbance in the frequency domain is a more effective strategy to improve the accuracy and robustness of the position sensing system compared with the method using an algorithm to detect and estimate the disturbance.

Figure 2-18 (c) and (d) give the raw measurements before high pass filter and the effective measurements after the high pass filter, respectively. It is seen that the raw magnetic field measurements are affected significantly as the wrench is brought close to

the sensors with a tremendous static signal change of several thousand counts. However, the effective amplitude measurements at 100 Hz are only slightly changed. For the raw measurements, the sudden changes outside the rectangle are related to turning the motor on/off. The signal variation patterns are slightly different between raw measurements and effective measurements from 20 s to 30 s because the raw measurements undergo different low frequency disturbance components as the piston moves to different locations.

2.7.2 Disturbance Rejection Results of the Mu-metal Based System

Figure 2-19 shows two configurations of the wrench with respect to the cylinder and position sensing system in the test for disturbance rejection.

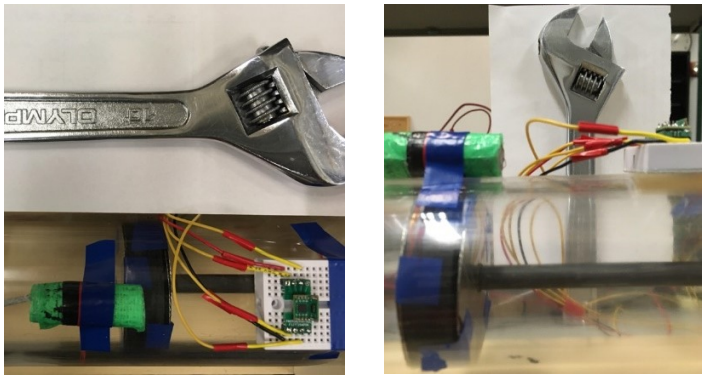

(a) **(b)**

Figure 2-19 Wrench configurations for disturbance rejection characterization of the mu-metal based system. (a) Wrench parallel to the cylinder. (b) Wrench perpendicular to the cylinder.

The disturbance rejection performance when the wrench is placed along the cylinder is shown Figure 2-20, where the shaded rectangle represents the time at which the disturbance is introduced. It is seen that the position estimates track the true position well even under the ferromagnetic disturbance and the maximum estimation error is 0.22 cm, which amounts to 2.2% error. This error is slightly larger than that of the nominal position estimation with no disturbance by 1%. This minor deterioration of estimation accuracy is due to the fact that the measured alternating magnetic field is shifted to the nonlinear region of the sensors by the ferromagnetic disturbance.

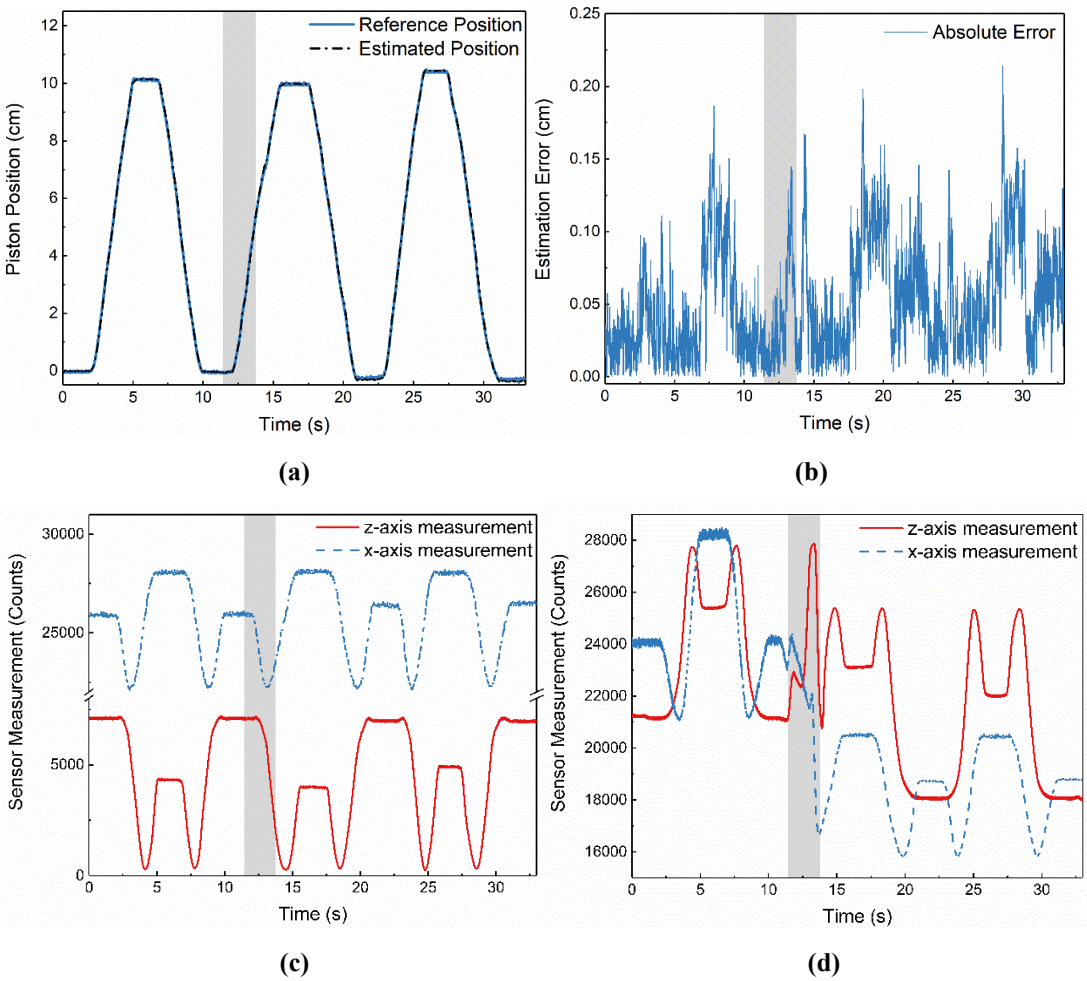

Figure 2-20 Disturbance rejection performance with wrench parallel to the cylinder for mu-metal based system. (a) Position estimation results. (b) Estimation error. (c) Effective measurements after high pass filter (d) Measurements before high pass filter.

Figure 2-20 (c) and (d) shows the effective measurements and raw measurements, respectively. Note that both measurements before and after high pass filter are the RMS value of the corresponding amplified signals instead of the raw alternating signals. It is seen that that the effective measurements almost remain the same when the disturbance is introduced, even while the raw measurements are changed significantly. The ferromagnetic disturbance introduced is about 0.038 Gauss in x-axis and 0.014 Gauss in z-axis. Therefore, the signal processing in this position measurement system successfully eliminates the influence of the ferromagnetic disturbance.

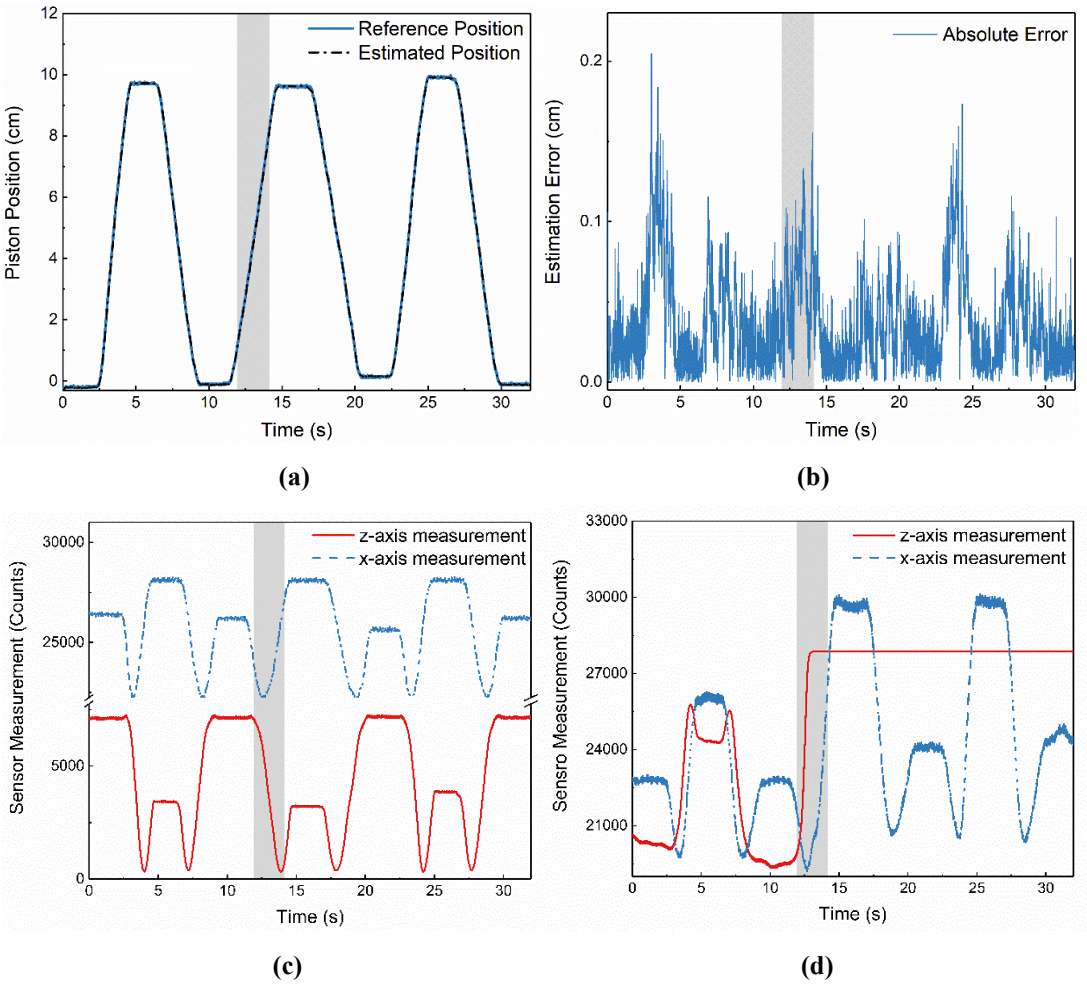

Figure 2-21 Disturbance rejection performance with wrench perpendicular to the cylinder for mu-metal based system. (a) Position estimation results. (b) Estimation error. (c) Effective measurements after high pass filter (d) Measurements before high pass filter.

The disturbance rejection performance when the wrench is placed perpendicular to the cylinder is shown in Figure 2-21. It can be seen in Figure 2-21 (a) that the ferromagnetic disturbance has minor influence on the position measurement system with no significant increase of estimation error. The maximum error is shown to be 0.21 cm, which amounts to 2.1% error. The estimation error in this disturbance configuration is approximately the same as that for the configuration with wrench parallel to the cylinder. Figure 2-21 (c) and (d) shows the effective measurements and raw measurements, respectively. Again, the effective measurements used for position estimation do not change much when the disturbance is introduced after the signal processing while the raw sensor measurements in

fact undergo significant disturbance from the ferromagnetic wrench. It is noted in Figure 2-21 (d) that the z-axis measurements increase to a constant level after the disturbance is introduced, which is attributed to the saturation of the instrumental amplifier. The ferromagnetic disturbance introduced is about 0.016 Gauss in x-axis and more than 0.040 Gauss in z-axis.

2.8 Conclusions

This chapter presented an electromagnet-based position measurement system for industrial actuators which offers significant advantages compared to traditional position measurement systems such as potentiometers or LVDTs. These advantages include low cost, non-contacting operation, easy installation and robustness to ferromagnetic disturbances.

In the preliminary embodiment of the sensor, the electromagnet was located on the stationary actuator housing while the sensor was mounted on the moving piston rod. The sensing principle relied on alternating magnetic fields and a model of amplitude variation with actuator position. Signal processing electronics and estimation filters were developed to estimate position with an accuracy of better than 1% of total stroke. Additionally, the position estimation system was able to reject disturbances from foreign magnetic objects and provide good accuracy even in the presence of disturbances.

The disadvantage of the first embodiment is the need to supply power to the electronics on a moving piston rod. A second embodiment that eliminates this disadvantage was then developed. The second embodiment located both the electromagnet and the powered sensor on the stationary housing. A stack of high magnetic permeability mu-metal films was located on the moving piston. Due to its high magnetic permeability, a significant fraction of the magnetic field measured by the sensor was coupled through the mu-metal on the piston of the actuator. Hence, as the piston position changed, the magnetic field measured by the sensor changed with piston position. This constituted the sensing principle for a new non-contacting and non-powered position measurement system with high sensitivity. Experimental results on a non-ferrous actuator showed that the mu-metal based position

sensor embodiment could also provide 1% accuracy in position measurement, could reject the influence of disturbances from magnetic objects and could measure positions for a stroke length up to 20 cm. Longer stroke length can be handled using additional daisy-chained sensors.

The developed position measurement system in this chapter represents a fundamental new position sensing technology that requires no power supply to the moving object and offers unique advantages compared to other existing one-dimensional linear position measurement methods. A limitation of the developed position estimation system is that it cannot be used on ferrous actuators in which the mu-metal is located entirely inside a ferrous enclosure.

Chapter 3

Nonlinear Observer for Active Electromagnetic Position Estimation

3.1 Introduction

In the last chapter, a preliminary electromagnetic position measurement system was developed based on the use of an electromagnet as the magnetic field source. Though it requires power for the sensors located on a moving object and thus is less desirable in long-term use compared with the high-magnetic-permeability mu-metal based system, it is still a practical solution for many applications due to its simple structure and easy installation on existing linear actuators. Apart from the issue of requiring power on a moving object, the preliminary system suffers from a low-magnetic-sensitivity problem towards the end of the stroke. The magnetic sensitivity here refers to the absolute value (or the squared value) of the derivative of magnetic field with respect to the position. Figure 3-1 shows the distribution of the axial magnetic field and the magnetic sensitivity of a cylindrical electromagnet. It is seen that the magnetic field decreases rapidly with the position and asymptotically converges to zero. Considering the magnetic sensitivity plotted in the logarithm scale in the figure, the magnetic sensitivity decreases even faster with position, which leads to a significant deterioration of estimation accuracy. This decrease of position estimation accuracy can be observed in Figure 2-13 (c), where the position estimation error

increases from 0.1 cm at a position of 0 cm to 0.3 cm at the position of 20 cm. Normally, position estimation accuracy for industrial actuators needs to be within 1%. A 0.3 cm absolute error at the end of the stroke amounts to a 1.5% relative error for an actuator with a stroke length of 20 cm. Therefore, there is a clear need to address the estimation error and keep it under 1% across the whole stroke length of the actuator.

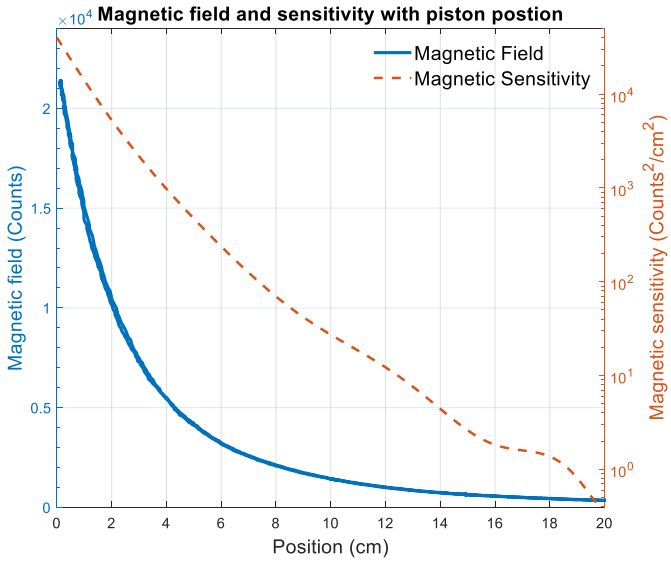

Figure 3-1 Variation of magnetic field and magnetic sensitivity with position for the preliminary electromagnetic measurement system.

In fact, the above issue exists generally for all positioning systems whose working principle is based on exploiting the spatial distribution of a single magnetic field source including permanent magnets. Thanks to the use of an electromagnet as a magnetic field source, there is a remedy to the problem of inadequate magnetic sensitivity at positions far from the magnetic source because of the flexibility of tuning magnetic intensity for an electromagnet by varying its current input. The larger the intensity of the electromagnet, the larger the magnetic sensitivity at a specific position. Basically, the current input to the electromagnet can be dynamically increased as the piston and magnetic sensor move far away from the electromagnet to maintain a sufficient magnetic sensitivity and thus a sufficient estimation accuracy for the whole stroke length. This active sensing strategy can bring the following advantages for the electromagnet-based position sensing systems:

1) For applications with a fixed position measurement range, the active sensing strategy can improve the estimation accuracy especially for the region far from the

electromagnet.

2) For applications without a fixed position measurement range, the active sensing strategy can extend the sensing range to regions where the sensitivity is too low.
3) The current input to the electromagnet can be adjusted to be lower near the electromagnet to prevent saturation of the magnetic sensor.
4) For applications with demanding requirements of energy efficiency such as wearable sensors, the active sensing strategy can strike a balance between energy efficiency and esitmation accuracy by optimizing the distribution of current input to the electromagnet across the measurement range.

In this chapter, the active sensing strategy is implemented and evaluated on an electromagnetic piston position estimation system for a 1-D linear actuator. However, the active sensing strategy can also be applied to 2-D or 3-D electromagnetic position measurement applications. It should be noted that the disturbance rejection function by using an alternating magnetic field proposed in last chapter can still be preserverd when implementing the active sensing strategy, where the amplitude of the alternating current is varied according to different positions.

The concept of active sensing has been used in many applicaitons of state estimation. Usually, some parameters of the sensing system are actively controlled to achieve improved estimation of states. The trajectory of a mobile robot with positioning sensors can be actively planned to improve the accuracy of robot localization and map building, resulting in a active simultaneous localizaiton and mapping (SLAM) system [63]. The motion of a ummaned arial vehicle (UAV) with limited sensing capability is actively controlled to follow a specific trajectory for enhanced observability in estimation of both of the orientaiont of the UAV and the flow field states [64]. In some active sensing system, the active control of sensor parameters or sensor input is implemented online through the model predictive control (MPC) framework, where the parameters are optimized in a fixed look-ahead time window and only the first control input is executed at the current time step. However, the MPC framework fails to provide a globally optimal strategy for sensor parameter control due to its local optimization in a limited time window. Furthermore, most active sensing systems use a Kalman filter based method for state estimation, which is only

locally stable for nonlinear systems. Since the sensor parameter input control and state estimation are coupled, the deterioration of either of the sensor control or state estimation will result in the worsening and even divergence of the other. Therefore, there is clear need to build a framework for active sensing that ensures globally stable and optimal state estimation.

This chapter is devoted to establishing such an active estimation framework using Lyapunov theory based nonlinear observer desgin for simultaneous current input control of the electromagnet and piston position estimation of the linear actuator. Experimental results show that both the current control and the positoin estimation are stable, and the position measurement accuracy is improved by maintaining the estimation error below 1% along the whole stroke length in an energy efficient way.

This chapter is organized as follows: In Section 3.2, the principle of the active electromagnetic position estimation system is presented. Then the technical challenges with the design of the active sensing system are described in Section 3.3. The nonlinear observer design for the active sensing system is shown with a rigorous proof in Section 3.4 and the optimization method for the current profile of the electromagnet is given in Section 3.5. Extensive experimental results and presented and discussed in Section 3.6 and the chapter is concluded in Section 3.7.

3.2 Principle of Active Electromagnetic Position Estimation

The principle of electromagnetic position estimation system using active current control is elaborated in this section. In this chapter, the position estimation system is designed and tested for linear actuator applications although it could be possibly extended to other 2-D or 3-D electromagnet-based position sensing applications in the future.

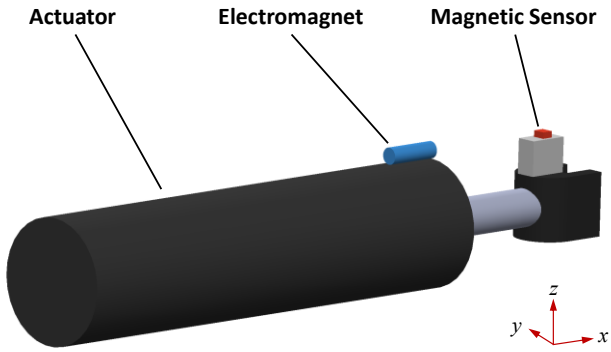

Figure 3-2 System schematic of the active electromagnetic position estimation system.

As is shown in Figure 3-2, the active electromagnetic position estimation system shares exactly the same major components with the preliminary electromagnetic position estimation system proposed in Chapter 2, with an electromagnet on the stationary cylinder and a magnetic sensor on the moving external piston rod. To reject disturbances from ferromagnetic objects, an alternating current with fixed amplitude and fixed frequency can be supplied to the electromagnet to generate an alternating magnetic field. The measured magnetic signal is high-pass filtered to remove low-frequency ferromagnetic disturbances such that only the amplitude of the measured signal at the desired frequency is extracted for position sensing. However, the amplitude of the alternating current needs to vary based on piston position in the active position estimation system.

For the basic system with a constant current input, it is seen in Figure 3-1 that the magnetic field and magnetic sensitivity (absolute value of derivative of the magnetic field variation) both decrease rapidly with piston position. Since the position estimation accuracy highly depends on the sensitivity of the magnetic field to position, it is expected that the position estimation performance deteriorates when the piston moves far from the electromagnet. One way to reduce the large estimation error at the far end of the stroke is to increase the current input to the electromagnet. Nevertheless, this method lowers the estimation error for the whole stroke length although the estimation error when the sensor is near the electromagnet (e.g. $x < 5$ cm) may already meet the error specification requirement even without boosting the current. Therefore, it is a waste of energy to have high current supply when the piston with the sensor moves close to the electromagnet. In

addition, the magnetic sensor might be saturated when it moves near the electromagnet if the electromagnet has too high an intensity. Therefore active control of the current input to the electromagnet is adopted in this dissertation in order to have an optimal current distribution along the stroke length so that the position estimation accuracy over the entire stroke is improved in an energy efficient way.

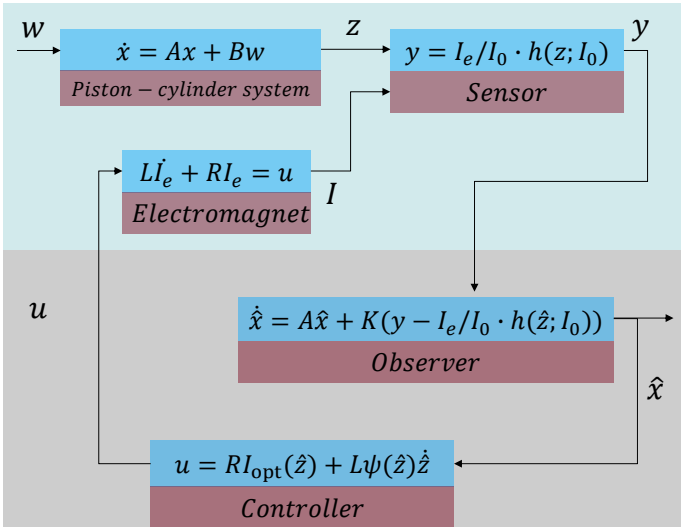

Figure 3-3 Diagram of working principle of electromagnetic position estimation system with active current control.

Figure 3-3 shows a flow chart schematic of the active position estimation system. The dynamics of the piston of an industrial actuator can be represented by kinematics as moving under some unknown jerk w. x is the state vector of kinematic states, namely position, velocity, and acceleration:

$$x = [z \quad \dot{z} \quad \ddot{z}]^{\mathrm{T}} \tag{3-1}$$

The electromagnet is modeled as a resistor R and an inductor L in series. The current supply to the electromagnet is controlled by a voltage, which is governed by the first order dynamics shown in the diagram. Under the specific current supply to the electromagnet, the magnetic field at the current piston position is measured for state estimation. It is assumed that the magnetic field, for a position fixed, is proportional to the current supply. $h(z; I_0)$ is the magnetic field variation with position under some constant nominal current I_0. A nonlinear state observer is designed to achieve stable estimation of the position. Then the voltage input for current control is determined based on an offline designed optimal

current profile $I_{\mathrm{opt}}(z)$ and the immediate position estimates $\hat{z}$. The optimal current profile is designed offline, which defines how to allocate the current supply to the electromagnet along the stroke length to achieve both energy efficient and accurate estimation.

3.3 Technical Challenges with Active Position Estimation

To achieve an optimal current distribution along the stroke of the linear actuator, a trajectory optimization problem needs to be formulated and solved offline to consider the piston motion over the whole measurement range. The current profile to track is defined as $I_{\mathrm{opt}}(z)$, which is a function of position. For optimization of the current profile, a reasonable objective function is the magnetic sensitivity averaged over the whole measurement range. To simplify the analysis, an implicit assumption is made here that the piston has uniform probability to move across the whole measurement range such that the average magnetic sensitivity represents the overall position estimation performance well.

Besides the need of a well-defined formulation of the current profile optimization problem, the active sensing system involves a fundamental coupled current control and position estimation problem. It requires accurate tracking of the desired current profile but the current profile $I_{\mathrm{opt}}(z)$ itself depends on position that is unknown and needs to be estimated. Hence, inaccurate position estimation would lead to a bad voltage input to the electromagnet, which in turn causes the actual current input to deviate from the optimal current profile. The failure of optimal current tracking will further deteriorate position estimation. This inter-coupling between current control and position estimation poses a significant challenge to the stability of the whole system. As a result, we resort to Lyapunov stability theory to design a nonlinear observer to ensure the global stability of both position estimation and optimal current tracking.

3.4 Nonlinear Observer Design

Since the magnetic field measurement depends on piston position in a nonlinear relation, and also on current supply to the electromagnet, a nonlinear state observer needs to be designed to obtain asymptotically stable estimates of the kinematic states. While the

control law is designed to make the true current track an optimal profile which depends on position, the position itself is not measured and is being estimated. Hence the goal is to estimate both position and decide on the voltage input so that the true current supply I_{e} converges to the optimal current input dependent on the true position $I_{\mathrm{opt}}(z)$.

3.4.1 System Model

The piston motion is modeled as a constant-acceleration motion with unknown jerk input:

$$\dot{x} = Ax + Bw \tag{3-2}$$

where x is the vector of kinematic states of piston motion as defined by (3-1) and w is the unknown jerk noise input. A and B are defined as follows:

$$A = \begin{bmatrix} 0 & 1 & 0 \\ 0 & 0 & 1 \\ 0 & 0 & 0 \end{bmatrix}, B = \begin{bmatrix} 0 \\ 0 \\ 1 \end{bmatrix} \tag{3-3}$$

The unknown jerk is considered to be zero in a deterministic estimation framework, or as zero mean Gaussian noise in a stochastic framework. The electromagnet is modeled as a resistor and an inductor in series with first order dynamics:

$$L\dot{I}_{\mathrm{e}} + RI_{\mathrm{e}} = u \tag{3-4}$$

where L and R are equivalent inductance and resistance, respectively. I_{e} and u are current and voltage of the electromagnet, respectively. The magnetic sensing model is given by

$$y_i = \frac{I_{\mathrm{e}}}{I_0} \cdot h_i(z; I_0) \tag{3-5}$$

where $i = 1,2, \dots, m$ and m is the number of sensors used, y_i is the magnetic field measurement from the i-th sensor, I_0 is some constant nominal current, and $h_i(z; I_0)$ is the nonlinear magnetic model at I_0 as shown in Figure 3-1. It is noted that the magnetic field is proportional to the current supply to the electromagnet at fixed position, which can be seen from (3-5). To achieve accurate modeling of the magnetic field of the electromagnet, $h_i(z; I_0)$ is obtained by fitting 9th order polynomials to the experimental data collected under I_0. Let $\alpha(I_e) = \frac{I_{\mathrm{e}}}{I_0}$, then

$$y_i = \alpha(I_{\mathrm{e}}) h_i(C_i x) \tag{3-6}$$

$$y = \alpha(I_e)h(Cx) = [y_1, y_2, \dots, y_m]^T$$

Since the nonlinear function h_i depends only on position z, C_i is given by

$$\begin{aligned} C_i &= [1 \quad 0 \quad 0] \\ C &= [C_1^T, C_2^T, \dots, C_m^T]^T \end{aligned} \tag{3-7}$$

Therefore, $z = C_i x$. In the theoretical formulation of observer design, multiple sensors ($m \geq 1$) are allowed while only one sensor is actually used in experiments.

3.4.2 Current Control System

Let $\psi(z) = \frac{\partial I_{\text{opt}}(z)}{\partial z}$. The following simple control law is implemented with the goal to make the true current I_e track the optimal current profile $I_{\text{opt}}(z)$:

$$u = RI_{\text{opt}}(\hat{z}) + L\psi(\hat{z})\dot{\hat{z}} \tag{3-8}$$

where $\hat{z}$ is the piston position estimate. The challenge here is that we have to use the estimated position $\hat{z}$ in the control law. Substituting (3-8) into (3-4), we find

$$\frac{L}{R}\dot{I}_e + I_e = I_{\text{opt}}(\hat{z}) + \frac{L}{R}\psi(\hat{z})\dot{\hat{z}} \tag{3-9}$$

Normally, the time constant $\frac{L}{R}$ is relatively small, which causes I_e to track $I_{\text{opt}}(\hat{z})$ at steady state. However, the goal is to ensure I_e to track $I_{\text{opt}}(z)$. This requirement is fulfilled by the following observer design.

3.4.3 Observer Design

Let the observer be given by

$$\dot{\hat{x}} = A\hat{x} + K\alpha(I_e)(h(Cx) - h(C\hat{x})) \tag{3-10}$$

where K is the observer gain to be designed later. Let the error states be $\tilde{x} = x - \hat{x}$. Then the estimation error dynamics will be

$$\dot{\tilde{x}} = A\tilde{x} - K\alpha(I_e)(h(Cx) - h(C\hat{x})) \tag{3-11}$$

It is assumed that the current I_e is measured or known from the electromagnet model (3-4).

Assumption 1: The following bound holds:

$$\left\| I_{\text{opt}}(z) - I_{\text{opt}}(\hat{z}) \right\|_2 \leq \gamma \|z - \hat{z}\|_2 \tag{3-12}$$

for all z, $\hat{z}$.

Assumption 2: The following bounds hold:

$$|\dot{z}| \leq \dot{z}_{max},$$
$$\|\psi(z) - \psi(\hat{z})\|_2 \leq \gamma_\psi \|z - \hat{z}\|_2, \text{ and} \tag{3-13}$$
$$\|\psi(z)\| \leq \delta_\psi$$

for all z, $\hat{z}$. These assumptions are reasonable because $I_{\text{opt}}(z)$ and its derivative $\psi(z)$ are both bounded and Lipschitz functions.

Let $M = diag(M_1, M_2, \ldots M_m)$ be a diagonal matrix with lower bounds M_i and let $N = diag(N_1, N_2, \ldots N_m)$ be a diagonal matrix with upper bounds N_i on the derivatives $\frac{\partial h_i}{\partial (C_i x)}$ of the magnetic field output functions.

Theorem 1: If the observer gain matrix K is chosen such that the following linear matrix inequality (LMI) is always satisfied

$$\begin{bmatrix} F & G & 0 \\ G^T & -\epsilon I & 0 \\ 0 & 0 & -\frac{R\rho}{2L} + \rho \end{bmatrix} < 0 \tag{3-14}$$

with

$$P > 0,\ \rho > 0, \epsilon > 0,$$
$$F = A^T P + PA - \epsilon \frac{C^T M^T N C + C^T N^T M C}{2} + \frac{R\rho}{2L}\gamma^2 E_{11} + \frac{\rho}{2}\gamma_\psi^2 (\dot{z}_{max})^2 E_{11} + \frac{\rho}{2}\delta_\psi^2 E_{22},$$
$$G = -PK\alpha(I_e) + \epsilon \frac{C^T M^T + C^T N^T}{2}, \tag{3-15}$$
$$E_{11} = \begin{bmatrix} 1 & 0 & 0 \\ 0 & 0 & 0 \\ 0 & 0 & 0 \end{bmatrix} \text{ and } E_{22} = \begin{bmatrix} 0 & 0 & 0 \\ 0 & 1 & 0 \\ 0 & 0 & 0 \end{bmatrix},$$

then the state estimates converge to the real states and I_e converges to $I_{\text{opt}}(z)$.

Proof: Consider the following Lyapunov function candidate

$$V = \tilde{x}^T P \tilde{x} + \frac{1}{2}\rho [I_e - I_{\text{opt}}(z)]^2 \tag{3-16}$$

Taking the time derivative gives

$$\begin{aligned} \dot{V} = {} & \tilde{x}^T (A^T P + PA)\tilde{x} - \tilde{x}^T PK\alpha(I_e)[h(Cx) - h(C\hat{x})] \\ & - [h(Cx) - h(C\hat{x})]^T K^T P \tilde{x} \alpha(I_e) + \rho [I_e - I_{\text{opt}}(z)]\{\dot{I}_e - \psi(z)\dot{z}\} \end{aligned} \tag{3-17}$$

Let $\tilde{h}(x,\hat{x}) = h(Cx) - h(C\hat{x})$. Then, in matrix form,

$$\dot{V} = [\tilde{x}^T \quad \tilde{h}^T]\begin{bmatrix} A^TP + PA & -PK\alpha(I_e) \\ -K^TP\alpha(I_e) & 0 \end{bmatrix}\begin{bmatrix}\tilde{x}\\ \tilde{h}\end{bmatrix} + \rho[I_e - I_{opt}(z)]\{\dot{I}_e - \psi(z)\dot{z}\} \tag{3-18}$$

According to the differential mean value theorem, there exists $\bar{z}_i$ in the interval between z and $\hat{z}$ such that the output function difference is

$$\begin{aligned}\tilde{h}(x,\hat{x}) &= \begin{Bmatrix} \vdots \\ h_i(C_ix) - h_i(C_i\hat{x}) \\ \vdots \end{Bmatrix} \\ &= diag\left\{\frac{\partial h_1}{\partial(C_1x)}\Big|_{z=\bar{z}_1}, \dots, \frac{\partial h_m}{\partial(C_mx)}\Big|_{z=\bar{z}_m}\right\}(Cx - C\hat{x})\end{aligned} \tag{3-19}$$

Then, using the lower and upper Jacobian bounds of $\frac{\partial h_i}{\partial(C_ix)}$ in equation (3-19), the following inequality in matrix form (18) can be obtained, as described in [48].

$$V_1 = \begin{bmatrix}\tilde{x}\\ \tilde{h}\end{bmatrix}^T \begin{bmatrix} \frac{C^TM^TNC + C^TN^TMC}{2} & -\frac{C^TM^T + C^TN^T}{2} \\ -\frac{MC + NC}{2} & I \end{bmatrix}\begin{bmatrix}\tilde{x}\\ \tilde{h}\end{bmatrix} \le 0 \tag{3-20}$$

Using the S-Procedure Lemma [45], $\dot{V} < 0$ if and only if $\dot{V} < \epsilon V_1$ for some $\epsilon > 0$, yields the LMI (3-21).

$$\begin{aligned}&\begin{bmatrix}\tilde{x}\\ \tilde{h}\end{bmatrix}^T \begin{bmatrix} A^TP + PA - \epsilon\frac{C^TM^TNC + C^TN^TMC}{2} & -PK\alpha(I_e) + \epsilon\frac{C^TM^T + C^TN^T}{2} \\ -K^TP\alpha(I_e) + \epsilon\frac{MC + NC}{2} & -\epsilon I \end{bmatrix}\begin{bmatrix}\tilde{x}\\ \tilde{h}\end{bmatrix} \\ &+\rho\left[I_e - I_{opt}(z)\right]\left\{-\frac{R}{L}I_e + \frac{R}{L}I_{opt}(\hat{z}) + \psi(\hat{z})\dot{\hat{z}} - \psi(z)\dot{z}\right\} < 0\end{aligned} \tag{3-21}$$

Let

$$Q = \begin{bmatrix} A^TP + PA - \epsilon\frac{C^TM^TNC + C^TN^TMC}{2} & -PK\alpha(I_e) + \epsilon\frac{C^TM^T + C^TN^T}{2} \\ -K^TP\alpha(I_e) + \epsilon\frac{MC + NC}{2} & -\epsilon I \end{bmatrix} \tag{3-22}$$

Then $\dot{V} - \epsilon V_1$ can be written as equation (3-23).

$$\begin{aligned}\dot{V} - \epsilon V_1 = \begin{bmatrix}\tilde{x}\\ \tilde{h}\end{bmatrix}^T Q \begin{bmatrix}\tilde{x}\\ \tilde{h}\end{bmatrix} - \frac{R\rho}{L}\left[I_e - I_{opt}(z)\right]^2 - \frac{R\rho}{L}\left[I_e - I_{opt}(z)\right]\left[I_{opt}(z) - I_{opt}(\hat{z})\right] \\ -\rho\left[I_e - I_{opt}(z)\right]\{[\psi(z) - \psi(\hat{z})]\dot{z} + \psi(\hat{z})\dot{\tilde{z}}\}\end{aligned} \tag{3-23}$$

Using $-2ab \le a^2 + b^2$, and using $\left[I_{opt}(z) - I_{opt}(\hat{z})\right]^2 \le \gamma^2 \tilde{z}^2$, $[\psi(z) - \psi(\hat{z})]^2 \le \gamma_\psi{}^2 \tilde{z}^2$, $\psi(\hat{z})^2 \dot{\hat{z}}^2 \le \delta_\psi{}^2 \dot{\hat{z}}^2$, and $|\dot{z}| \le \dot{z}_{max}$ from Assumption 1 and 2, the inequality (3-24) can be obtained.

$$\begin{aligned}\dot{V} - \epsilon V_1 \le & \begin{bmatrix}\tilde{x}\\ \tilde{h}\end{bmatrix}^T Q \begin{bmatrix}\tilde{x}\\ \tilde{h}\end{bmatrix} - \frac{R\rho}{L}\left[I_{\mathrm{e}} - I_{\mathrm{opt}}(z)\right]^2 + \frac{R\rho}{2L}\left[I_{\mathrm{e}} - I_{\mathrm{opt}}(z)\right]^2 + \frac{R\rho}{2L}\gamma^2\tilde{z}^2 \\ & + \frac{\rho}{2}\left[I_{\mathrm{e}} - I_{\mathrm{opt}}(z)\right]^2 + \frac{\rho}{2}\gamma_{\psi}^2(\dot{z}_{max})^2\,\tilde{z}^2 + \frac{\rho}{2}\left[I_{\mathrm{e}} - I_{\mathrm{opt}}(z)\right]^2 + \frac{\rho}{2}\delta_{\psi}^2\dot{\tilde{z}}^2\end{aligned} \tag{3-24}$$

It is known that

$$\tilde{z}^T\tilde{z} = \{[1 \quad 0 \quad 0]\tilde{x}\}^T[1 \quad 0 \quad 0]\tilde{x} = \tilde{x}^T\begin{bmatrix}1 & 0 & 0\\ 0 & 0 & 0\\ 0 & 0 & 0\end{bmatrix}\tilde{x} \tag{3-25}$$

and

$$\dot{\tilde{z}}^T\dot{\tilde{z}} = \{[0 \quad 1 \quad 0]\tilde{x}\}^T[0 \quad 1 \quad 0]\tilde{x} = \tilde{x}^T\begin{bmatrix}0 & 0 & 0\\ 0 & 1 & 0\\ 0 & 0 & 0\end{bmatrix}\tilde{x} \tag{3-26}$$

Let $E_{11} = \begin{bmatrix}1 & 0 & 0\\ 0 & 0 & 0\\ 0 & 0 & 0\end{bmatrix}$ and $E_{22} = \begin{bmatrix}0 & 0 & 0\\ 0 & 1 & 0\\ 0 & 0 & 0\end{bmatrix}$. Then, the inequality can be written as the form of (3-27)

$$\begin{aligned}\dot{V} - \epsilon V_1 \le & \begin{bmatrix}\tilde{x}\\ \tilde{h}\end{bmatrix}^T Q \begin{bmatrix}\tilde{x}\\ \tilde{h}\end{bmatrix} - \frac{R\rho}{L}\left[I_{\mathrm{e}} - I_{\mathrm{opt}}(z)\right]^2 + \frac{R\rho}{2L}\left[I_{\mathrm{e}} - I_{\mathrm{opt}}(z)\right]^2 + \frac{R\rho}{2L}\gamma^2\tilde{x}^T E_{11}\tilde{x} \\ & + \frac{\rho}{2}\left[I_{\mathrm{e}} - I_{\mathrm{opt}}(z)\right]^2 + \frac{\rho}{2}\gamma_{\psi}^2(\dot{z}_{max})^2\,\tilde{x}^T E_{11}\tilde{x} + \frac{\rho}{2}\left[I_{\mathrm{e}} - I_{\mathrm{opt}}(z)\right]^2 + \frac{\rho}{2}\delta_{\psi}^2\tilde{x}^T E_{22}\tilde{x}\end{aligned} \tag{3-27}$$

Its matrix form is shown in (3-28).

$$\begin{aligned}&\dot{V} - \epsilon V_1 \le \\ &\begin{bmatrix}\tilde{x}\\ \tilde{h}\\ I_e - I_{opt}(z)\end{bmatrix}^T \begin{bmatrix} A^TP + PA - \epsilon\dfrac{C^TM^TNC + C^TN^TMC}{2} + \dfrac{R\rho}{2L}\gamma^2E_{11} + \dfrac{\rho}{2}\gamma_{\psi}^2(\dot{z}_{max})^2 & -K^TP\alpha(I_e) + \epsilon\dfrac{MC + NC}{2} & 0\\ -PK\alpha(I_e) + \epsilon\dfrac{C^TM^T + C^TN^T}{2} & -\epsilon I & 0\\ 0 & 0 & -\dfrac{R\rho}{2L} + \rho\end{bmatrix}\begin{bmatrix}\tilde{x}\\ \tilde{h}\\ I_{\mathrm{e}} - I_{\mathrm{opt}}(z)\end{bmatrix}\end{aligned} \tag{3-28}$$

Hence $\dot{\mathrm{V}} < 0$ if the matrix inequality in equation (3-14) is satisfied. ■

Solving LMI (3-14): Note that $\alpha(I_e)$ in (3-14) depends on current I_{e}. However, the current is bounded with $\alpha(I_{\mathrm{e,min}}) \le \alpha(I_{\mathrm{e}}) \le \alpha(I_{\mathrm{e,max}})$, where $I_{\mathrm{e,min}}$ and $I_{\mathrm{e,min}}$ are the minimum and maximum admissible current. Let the LMI in (13) be $\Phi(\alpha(I_{\mathrm{e}}); K) < 0$. Therefore, if the observer gain K can be found such that the following two LMIs in (3-29) are satisfied simultaneously,

$$\begin{aligned} \Phi(\alpha(I_{\mathrm{e,min}}); K) < 0 \\ \Phi(\alpha(I_{\mathrm{e,max}}); K) < 0 \end{aligned} \tag{3-29}$$

Then from convexity principles, there exists $\beta \in [0,1]$ such that

$$\begin{aligned} \Phi(\alpha(I_{\mathrm{e}}); K) &= \Phi(\beta\alpha(I_{\mathrm{e,min}}) + (1-\beta)\alpha(I_{\mathrm{e,max}}); K) \\ &= \beta\Phi(\alpha(I_{\mathrm{e,min}}); K) + (1-\beta)\Phi(\alpha(I_{\mathrm{e,max}}); K) < 0, \text{ for all } \alpha(I_{\mathrm{e}}) \end{aligned} \tag{3-30}$$

3.5 Optimization of Current Profile of the Electromagnet

Although the nonlinear observer has been designed to ensure state estimates to track true states and true current to track a desired current profile, the optimal desired current profile needs to be designed such that there is an optimal trade-off between estimation accuracy and energy efficiency.

3.5.1 Optimization Problem Formulation

The position estimation accuracy highly depends on the magnetic field sensitivity with respect to position, which is set as the performance measure to be maximized, as shown in Equation (3-31).

$$S = \left(\frac{I_{\mathrm{e}}}{I_0} \cdot \frac{\partial h(z; I_0)}{\partial z}\right)^2 \tag{3-31}$$

where S is the squared magnetic sensitivity at the position z under the current supply I_{e}. If it is assumed that the true current tracks the optimal current profile perfectly with the observer designed in Section 3.4, the magnetic sensitivity can be rewritten as

$$S(z) = \left(\frac{I_{\mathrm{opt}}(z)}{I_0} \cdot \frac{\partial h(z; I_0)}{\partial z}\right)^2 \tag{3-32}$$

Then the objective of optimization is to maximize the magnetic sensitivity. It is noted that the higher the current supply, the higher the magnetic sensitivity. However, it is desired to

save energy while achieving sufficient estimation accuracy. Therefore, an average power consumption constraint is added. Hence the optimization problem can be formulated as

$$\begin{aligned} \max_{I_{\mathrm{opt}}(z)} J &= \int_0^{L_\mathrm{s}} w(z)S(z)\mathrm{d}z \\ \text{subject to } P &= \tfrac{1}{L_\mathrm{s}}\textstyle\int_0^{L_\mathrm{s}} I_{\mathrm{opt}}(z)^2 R\mathrm{d}z \\ P &< P_{\mathrm{limit}} \\ I_\mathrm{L} &< I_{\mathrm{opt}}(z) < I_\mathrm{U} \\ \frac{\partial I_{\mathrm{opt}}(z)}{\partial z} &\geq 0 \end{aligned} \tag{3-33}$$

where L_s is the stroke length of the actuator (e.g. 20 cm in this specific application), P is the average power consumption across the stroke length, P_{limit} is the average power limit, and I_L and I_U are lower and upper bound of the admissible current value. The last constraint enforces the current profile to increase monotonically with position because larger current is desired for larger position due to lower sensitivity there. $w(z)$ is a weighting function, which needs to weight more on large positions since the magnetic sensitivity is very low there and should be improved particularly. Here, an exponential weighting function is used as given by

$$\begin{aligned} w(z) &= Ae^{\beta z} \\ \int_0^{L_\mathrm{s}} w(z)\mathrm{d}z &= 1 \end{aligned} \tag{3-34}$$

where $A = 0.008$ and $\beta = 0.15$.

3.5.2 Direct Collocation Method

Although the optimization problem has been formulated, it remains to provide a representative form for $I_{\mathrm{opt}}(z)$, which defines how the desired current varies with piston position. One way to represent this function is to choose some basis functions, e.g. sinusoidal or polynomial functions, and then optimize the weight parameters. The disadvantage of this method is that the certain function form can limit the degrees of freedom of the current profile, which results in suboptimal solutions. In this paper, a trajectory optimization method, namely direct collocation method, is used instead for current profile optimization [65]. Instead of taking a specific function form, the current profile is represented by a set of N discrete collocation points: $I_0, I_1, \ \ldots, I_k, \ \ldots, I_N$ across

the domain of interest $z \in [0, 20]$ uniformly, the values of which are to be optimized. The trapezoidal collocation method is used in this paper, where the current profile values between two adjacent collocation points are interpolated by linear splines and thus the current profile is a piecewise linear function. In trapezoidal collocation, the objective function and the power consumption constraint, appearing as an integral in this problem, are approximated by the summation of trapezoid quadrature. After the transcription, the optimization problem (3-33) can be reformulated as a nonlinear programming problem, as given by (3-35).

$$\max_{I_0 \dots I_N} J = \sum_{k=0}^{N-1} \frac{1}{2} \cdot \Delta z_k \cdot [w(z_k) S(z_k, I_k) + w(z_{k+1}) S(z_{k+1}, I_{k+1})]$$

subject to

$$P = \frac{1}{L_s} \sum_{k=0}^{N-1} \frac{1}{2} \cdot \Delta z_k \cdot [I_k^2 R + I_{k+1}^2 R] \tag{3-35}$$

$$P < P_{\text{limit}}$$

$$I_L < I_k < I_U, \quad k = 0,1, \dots, N$$

$$I_k \leq I_{k+1}$$

The implementation of this optimization problem is fulfilled using the OptimTraj library in Matlab [66].

3.6 Experimental Results

3.6.1 Experimental Setup

Figure 3-4 shows the experimental setup of the active electromagnetic position estimation system. A plastic piston-cylinder system was made to simulate the linear motion of industrial actuators. The diameters of the piston rod and piston head are 0.960 cm and 6.330 cm, respectively. The stroke length of the piston is 20 cm. An electromagnet made by wrapping copper wires around a 0.6 cm diameter × 4.5 cm steel core is mounted on the stationary test stand together with the cylinder. A Tunnel Magneto-resistance (TMR) sensor (TMR 2305M, MultiDimension Technology Co., Ltd) is located on the moving handle connected to the piston rod and aligned with the central axis of the electromagnet. The sensor measures the magnetic field along the moving direction of piston. An accurate

laser sensor (L-GAGE LE550) is employed for reference position measurement. The alternating current at 100 Hz is supplied to the electromagnet, the amplitude of which is controlled by a 10-bit digital potentiometer (X9119). Note that the potentiometer controls the voltage of the low-power signal from the waveform generator before this controlled signal is amplified by the power amplifier for the electromagnet current supply. Hence, there is negligible power loss in this voltage division control method.

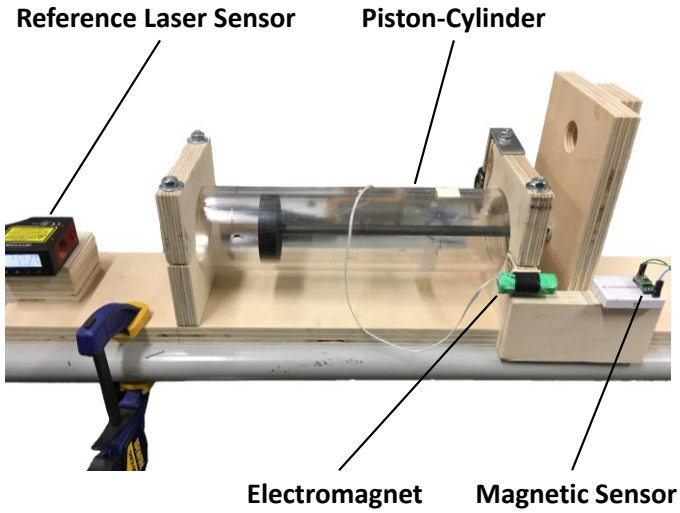

Figure 3-4 Experimental setup of active electromagnetic position estimation system with current control.

Since the current supply to the electromagnet is alternating, the measured magnetic field is also alternating. Since the frequency of piston motion and ambient ferromagnetic disturbances is normally lower than 10 Hz, the 100 Hz alternating magnetic signal is first high-pass filtered using an RC circuit with cutoff frequency of 20 Hz. Then this purely oscillatory signal is amplified by an instrumental amplifier (INA2126), which is further converted to a DC voltage signal proportional to the amplitude by the RMS-to-DC converter (AD637). This DC signal is finally fed to a 16-bit analog-to-digital converter (ADS1115) to generate the digital magnetic measurements, which are read by an Arduino Uno microcontroller and further transmitted to a computer for state estimation. With this signal processing, the selective sensing of the amplitude of the alternating magnetic field from the electromagnet is achieved such that no low-frequency disturbance would influence the position estimation. The digital potentiometer is controlled by the

microcontroller through the I2C bus. The position estimate is computed in the computer by the nonlinear state observer designed in section 3.4 and the control signal is computed based on the optimal current profile evaluated at the most recent position estimate. The estimation and control process are synchronized at a frequency of 50 Hz.

3.6.2 Position Estimation Results

Figure 3-5 Nominal constant current, constant current with doubled power, and optimal current profile with doubled power.

Two sets of experiments were performed to show the superiority of the active position estimation system. In the first set of experiments, one experiment was first performed to show the position estimation performance with a nominal constant current supply to the electromagnet. Then two ways of enhancing the estimation accuracy were implemented, i.e. boosting the constant current and active control of current, both of which doubled the power consumption compared to the case with the nominal current supply. For the case of active current control, the average power across the stroke length, as shown in (3-33), is used as its power consumption statistic. The current profiles for the three cases are shown in Figure 3-5. Note that the unit for current is counts/Ohm since the voltage is represented by the position of potentiometer, the total number of levels of which is 1024 counts (10-bit). The 1X power in the nominal constant current case means 0.27 W. It is seen that the

constant current with 2X power is $\sqrt{2}$ times of the nominal current. The optimal current profile increases monotonically with position as designed. Particularly, the current supply increases with accelerating slope at the end of the stroke length, which is desired for improving the poor magnetic sensitivity there. On the other hand, the current in the optimal profile is lower than the constant current with the same power consumption below 12.5 cm to save energy because the magnetic sensitivity is sufficient in this region for accurate position estimation even with lower current.

The position estimation results for the three cases are shown in Figure 3-6. It is seen that the position estimation error is well below the 1% bound when position is under 15 cm and the largest estimation error happens at the end of the stroke for all 3 cases. However, by simply increasing the constant current supply, the largest error cannot be bounded within the 1% limit that is normally required by industrial actuators. The estimation error drops below 1% only for the system using active current control.

Figure 3-7 shows that the current tracks the desired current $I_{\text{opt}}(z)$ well with 2% accuracy. The good current tracking and position estimation verifies the stability results of the designed nonlinear observer.

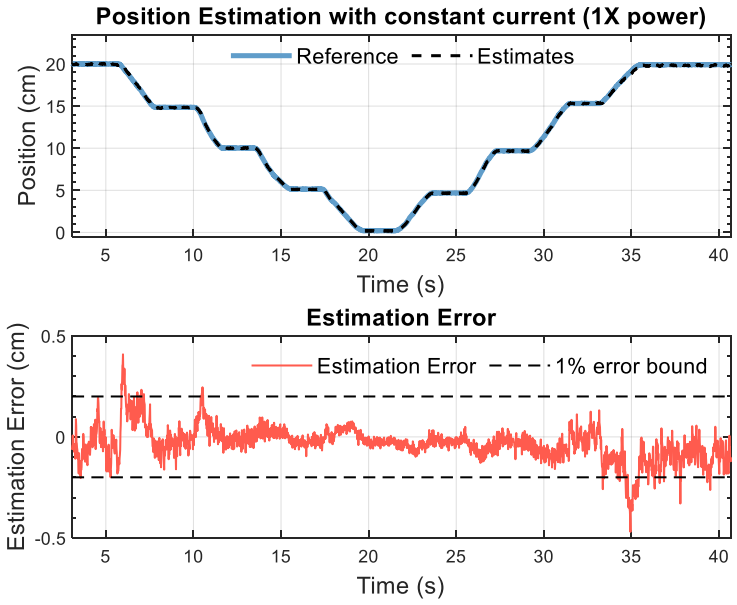

(a)

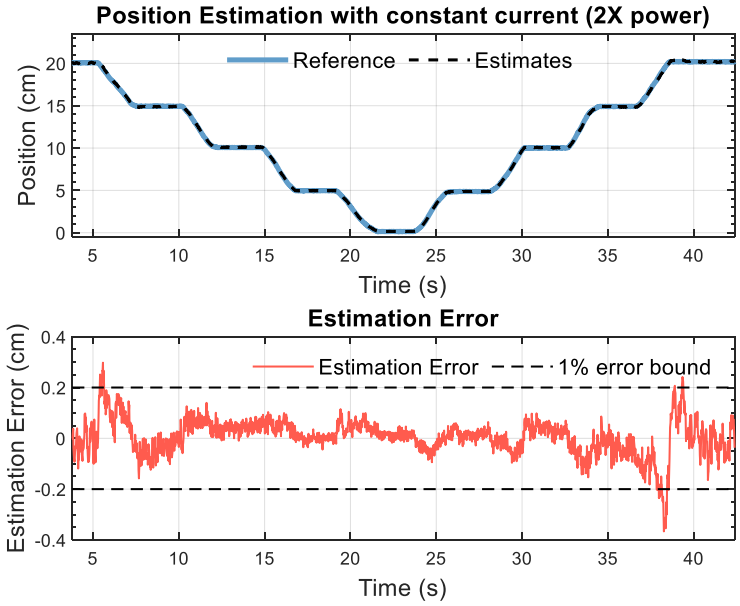

(b)

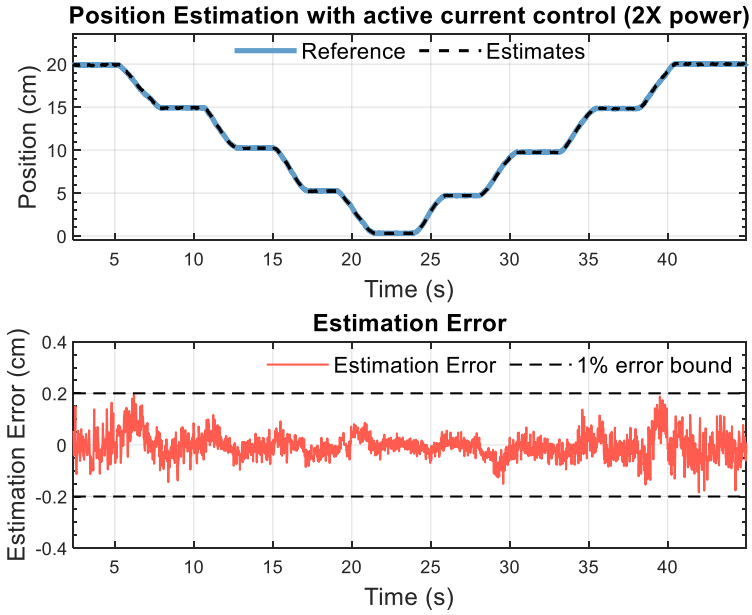

(c)

Figure 3-6 Position estimation results. (a) nominal constant current with 1x power. (b) constant current with 2x power. (c) active current control with 2x power.

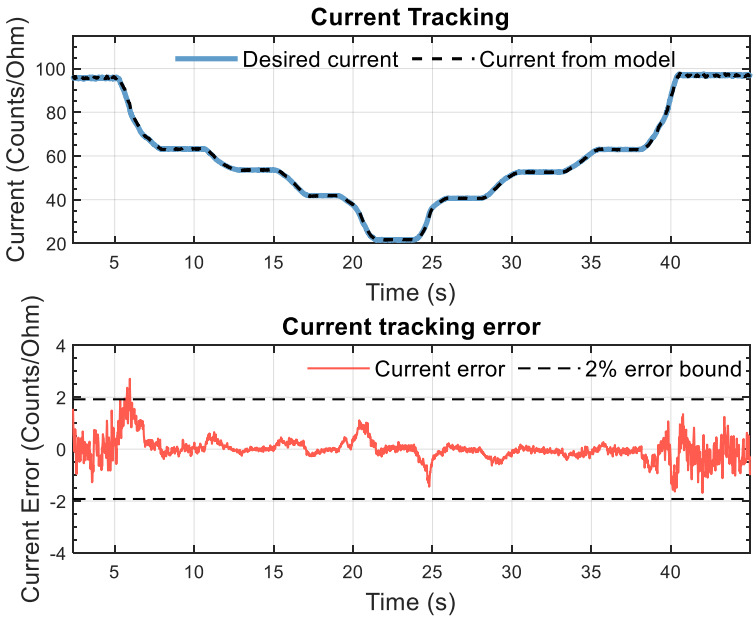

Figure 3-7 Current tracking performance of the active current control.

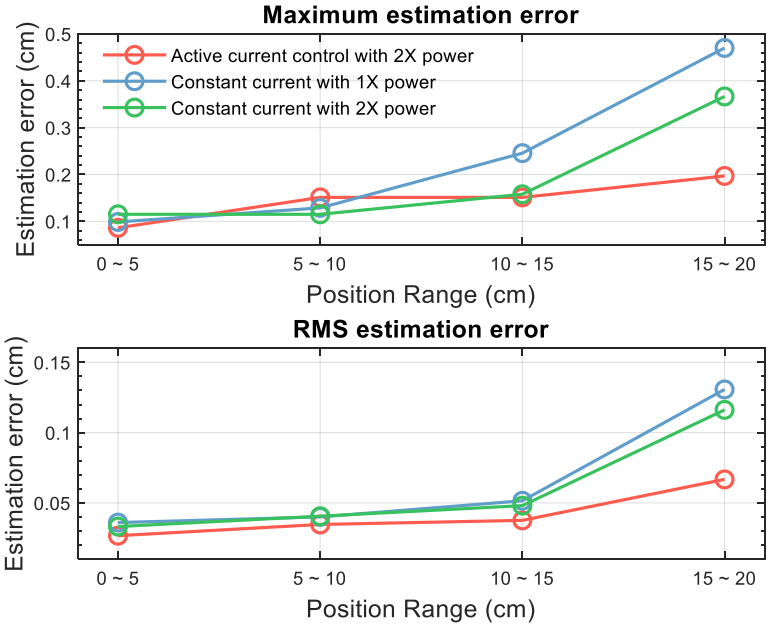

Figure 3-8 Position estimation error statistics for cases with constant current and active current control.

Estimation error statistics are summarized in Figure 3-8. The 20 cm sensing range is divided into four regions with equal length. The maximum error and RMS error are computed for each region for the three cases. Note that the average power consumption is

the same with the boosted constant current and active current control so their estimation performance is comparable. For all three cases, the estimation error increases with piston position due to the decrease of magnetic sensitivity. It is seen that boosting the constant current hardly reduces the maximum error and RMS error under 10 cm since the sensitivity is already very high in this region with the nominal current with 1X power. In the 15 ~ 20 cm position range, the maximum error drops from 0.47 cm with nominal constant current to 0.37 cm with the boosted constant current, and to 0.20 cm with active current control. The RMS error drops from 0.13 cm to 0.12 cm with the boosted constant current, and to 0.07 cm with active current control. The active current control decreases both maximum error and RMS error by around 50%. Therefore, with the same average power consumption, the active current control outperforms boosting the constant current in terms of improving the estimation accuracy for the low sensitivity region without significant loss of accuracy in the high-sensitivity region.

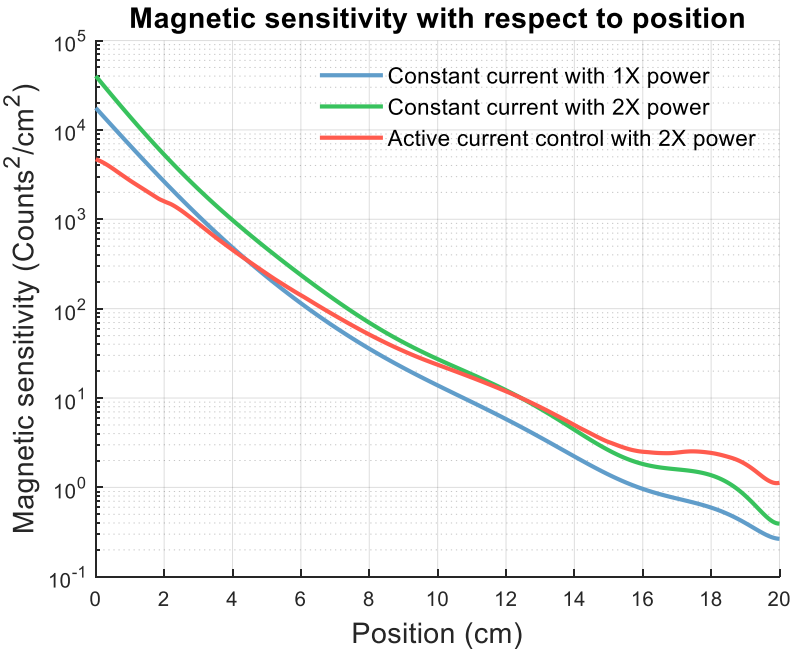

Figure 3-9 Magnetic sensitivity distribution over position

It is shown in Figure 3-9 that the magnetic sensitivity with respect to position is improved all through the stroke length by boosting the constant current. However, by active current control, the sensitivity is particularly enhanced for the far distance region with weak magnetic sensitivity, which leads to the superior estimation performance there.

A second set of experiments compares the position estimation performance using the optimal current profile with that of two extreme cases, i.e. constant current supply with maximum and minimum value of the optimal current profile. The current profiles are shown in Figure 3-10.

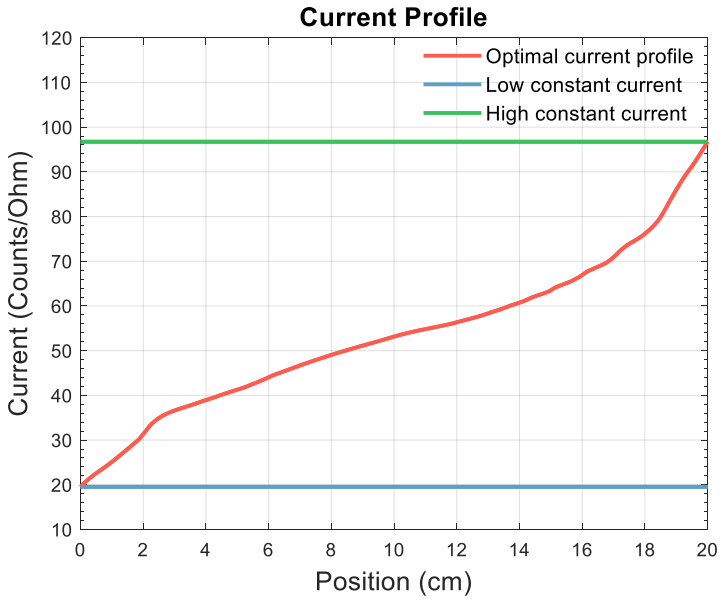

Figure 3-10 Optimal current profile and constant current supply with maximum and minimum value of the optimal current profile.

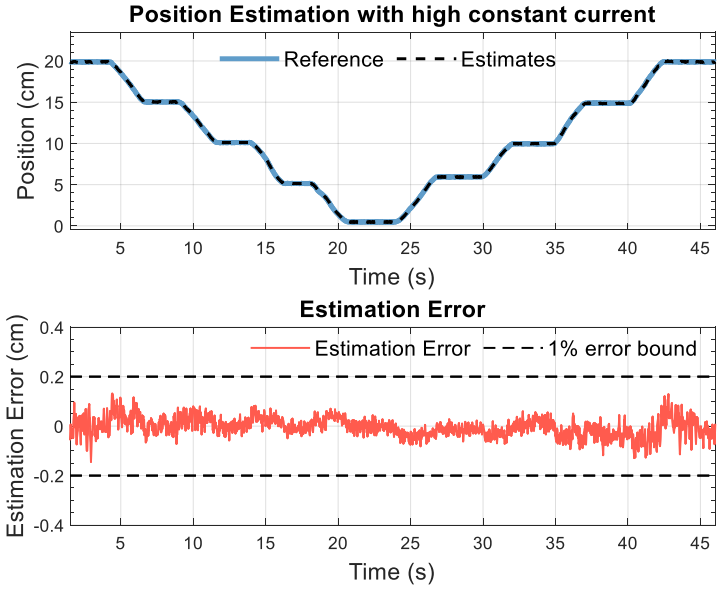

(a)

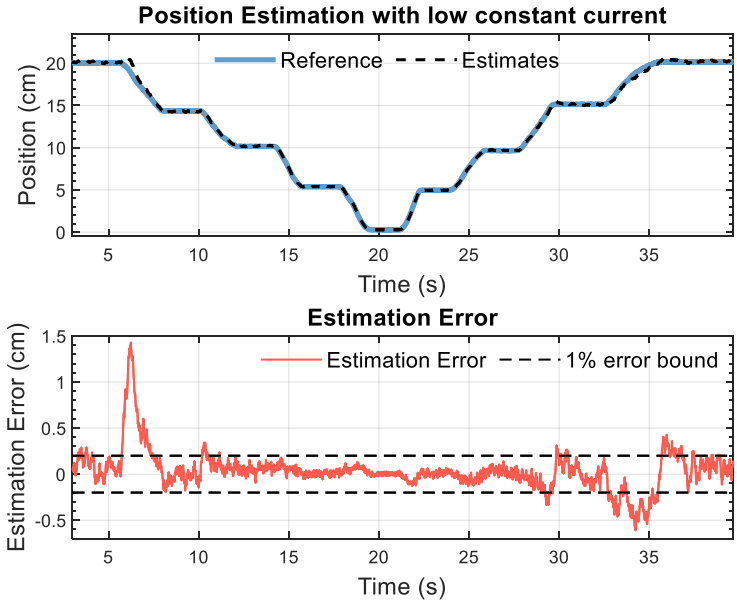

(b)

Figure 3-11 Position estimation results. (a) high constant current. (b) low constant current.

The position estimation results with high and low constant current are illustrated in Figure 3-11. The estimation result of active current control can be found in Figure 3-6 (c). It is observed that the estimation error is well below the 1% error bound with high constant current while in the other extreme case with low constant current, large error peak appears due to low magnetic sensitivity, especially when the piston with sensor is far from the electromagnet. The error statistics are shown in Figure 3-12. The low constant current case has much larger maximum and RMS estimation error than that of active current control and high constant current, particularly at the far end of the stroke length, due to the extremely low magnetic sensitivity. Therefore, too low constant current supply is not acceptable for electromagnetic position estimation. Although the high constant current is larger than the optimal current profile all along the stroke length, it does not show significantly smaller estimation error. However, the power consumption in the case of high constant current is 2.88 times of that of applying the optimal current profile. Hence, considering both estimation accuracy and energy efficiency, the active current control method is the best approach towards electromagnetic position sensing.

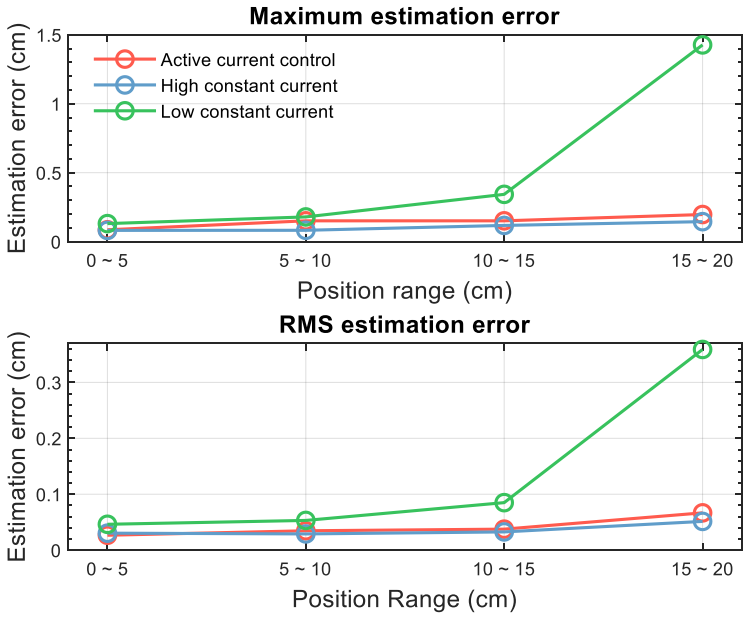

Figure 3-12 Position estimation error statistics for cases with active current control, and high and low constant current.

3.7 Conclusions

This chapter proposed an active electromagnetic position estimation system for linear actuators. The current supply to the electromagnet is actively controlled to track an optimal current profile, by which accurate position estimation can be achieved with high energy efficiency for the entire 20 cm stroke length of the actuator. In the optimal current profile, the current supply increases with position monotonically. The high current at far positions can enhance the weak magnetic sensitivity there while the low current at near positions, where the sensitivity is sufficiently high, can avoid wastage of energy. Furthermore, this active electromagnetic position estimation can also be used to extend the sensing range in an energy efficient way. A nonlinear state observer is designed to ensure both asymptotically stable position estimation and current tracking using the estimated position.

Experimental results show that the active estimation system outperforms the constant current system with the same amount of power consumption with an estimation error less than 1% achieved over the range of 20 cm. It is also shown that it is not efficient to increase the estimation accuracy just by using very high constant current (maximum value of the

optimal current profile), because then the energy consumption is nearly tripled. This active position estimation scheme can in the future also be applied to 2-D or 3-D electromagnetic position estimation problems although it is developed only for a 1-D linear actuator in this chapter. In addition, the active sensing strategy proposed in this chapter solved a challenging problem involving coupled state estimation and optimal sensor parameter control, providing guidelines for the design of similar active sensing systems for a broader range of applications.

Chapter 4

Angular Position Estimation

4.1 Introduction

Rotational motion is pervasive in various mechanical systems like automobiles, robotic manipulators and paper production machines, as is shown in Figure 4-1. For example, multiple mechanisms and sub-systems with rotational motion are involved in an automobile such as steering wheel, accelerator/brake pedal, and crankshaft, etc. Accurate angular position sensing can enable real-time monitoring of the end-effector position, feedback control of the system, and fault diagnostics of the machine, resulting in a higher level of automation and intelligent operation of the system.

(a)

(b)

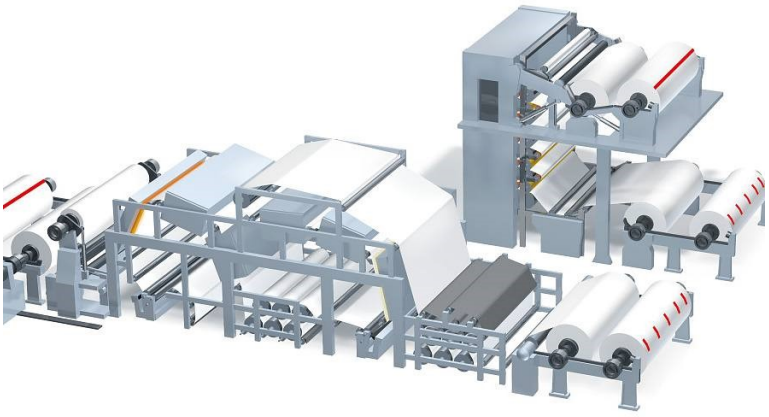

(c)

Figure 4-1 Examples of rotational motion and potential applications of angle measurement. (a) a robotic manipulator with multiple rotational joints [67]. (b) steering wheel on an automobile [68]. (c) paper production involving multiple rollers [69].

In this chapter, angular position measurement for rotational joints on off-road vehicles such as track loaders and excavators is addressed using the mu-metal based electromagnetic position sensing technique. As is shown in Figure 4-2, a track loader has multiple rotational joints, whose angle will change as the hydraulic actuators move. The next-generation off-road vehicles require autonomous operation in tasks like loading and excavating. Thus, the bucket position needs to be estimated for real-time feedback. Though the end-effector position can be estimated from individual piston positions of hydraulic actuators using methods like what is proposed in Chapter 2, some of the hydraulic actuators have a stroke length beyond the measurement range of the mu-metal based linear position sensors. If multiple electromagnets and magnetic sensors are used in a daisy-chain configuration for the extension of measurement range, the cost of the position measurement system is significantly increased. As an alternative, the measurement of joint angles instead of the linear piston position results in a low-cost solution with a simple structure to estimate the end-effector position if the length of mechanical links between joints are fixed and known.

Figure 4-2 A track loader involving multiple rotational joints (shown in blue boxes) (TV380 track loader, ©2020 *CNH Industrial America LLC*. [70]).

There are multiple existing angle sensing solutions. Potentiometers are widely used inexpensive angle sensors. However, they have to be installed between rotational machine parts with contacting operation, which leads to wear over long-term use and failure due to fatigue loads. Inertial sensors (accelerometers and gyroscopes) can be inexpensive and they are non-contacting and easy to install [71]. The limitation of inertial sensors is that they cannot measure the horizontal angle (yaw angle). Optical encoders are contactless sensors with high resolution and can provide high-accuracy angle measurement [13]. However, they are not robust in harsh environments with dust or liquid, which could potentially contaminate the optical encoder disk and affect the light transmission. Magnetic-sensor based solutions [72], on the other hand, can provide reasonably accurate angle measurements with lower costs than optical encoders. Most of such sensors are composed of a single permanent magnet bar or a magnetically poled ring and a magnetic sensor (Hall-effect, Anisotropic Magnetoresistive (AMR), or Giant Magnetoresistive (GMR) sensor). The angle information can be derived from the measured variation of the local magnetic field due to rotation of the part. The drawback of these permanent-magnet angle sensing systems is that they suffer from ambient ferromagnetic disturbances and need to be installed at the rotational joint. Therefore, it is meaningful to develop a low-cost magnetic-field-sensing based angular position measurement system immune to ferromagnetic disturbances. In this chapter, a high-permeability-material (mu-metal) based

electromagnetic angular position estimation system is developed for the measurement of joint angles of mechanisms on off-road vehicles and this system can be extended to general angle measurement with easy modification.

The outline of this chapter is listed below. In Section 4.2, the sensor signal processing and estimation algorithm are discussed briefly. Then two configurations of the mu-metal based angular position estimation systems are demonstrated in Section 4.3 and Section 4.4, respectively. For each configuration, the design and modeling of the system is presented, the experimental results are discussed, and the performance of ferromagnetic disturbance rejection is evaluated. The chapter is concluded in Section 4.5.

4.2 Signal Processing and Estimation Algorithm

The angular position sensing system has the same major components as the 1-D linear position sensing system, namely an electromagnet, a magnetic sensor, and a mu-metal element as the sensing medium. The electromagnet and magnetic sensor are located on one mechanical link while the mu-metal is on the other link that rotates around the common joint. The motion of magnetized mu-metal incurs a variation of magnetic field in the neighboring region, which is picked up by the magnetic sensor for angle sensing. Similar to the mu-metal based 1-D linear position estimation system, the use of an electromagnet enables the use of an alternating magnetic field at a certain frequency, which results in separation from low-frequency disturbances from adjacent ferromagnetic objects in the frequency domain. Therefore, instead of using the immediate alternating magnetic measurements, the sensor signal is first high-pass filtered using an RC circuit and then sent to an instrumental amplifier for signal amplification. Finally, the amplitude of the purely oscillatory signal is extracted using an RMS measurement chip. Finally, the RMS signal (proportional to the amplitude of the alternating signal) is read by an analog-to-digital converter and transmitted to a microcontroller as effective magnetic measurements. The effective magnetic measurements are fused with a constant acceleration motion model using an extended Kalman filter for angular position estimation. The scheme of signal

processing is shown in Figure 2-9 with the linear motion model replaced by an angular motion model.

Since the magnetic measurement varies with rotation angle in a nonlinear fashion, a nonlinear state estimation algorithm needs to be implemented for angle estimation. Again, similar to the linear position estimation, the extended Kalman filter (EKF) is used for the angular position estimation application. The estimation algorithm is given by equations (2-16) to (2-21) in Chapter 2. The state to be estimated is

$$X = [\theta \quad \omega \quad \alpha]^{\mathrm{T}} \tag{4-1}$$

where θ is the joint angle, ω is the angular velocity, and α is the angular acceleration. The magnetic measurement model $h(\cdot)$ in EKF is shown in Section 4.3 and 4.4 for each specific configuration of angle sensing system. The model is in a mathematical form of Fourier series (4-2) by fitting the experimental measurements for accurate angle estimation.

$$y = c + \sum_{i=1}^{n} a_i \sin(iw\theta) + b_i \cos(iw\theta) \tag{4-2}$$

where θ is the joint angle and y is the magnetic field measurement. a_i, b_i, and c are model parameters.

4.3 Angular Position Estimation System with Off-joint Configuration

4.3.1 Sensing Principle

Since the angular position estimation system is primarily designed for the joint angle measurement of mechanism employed on an off-road vehicle (e.g. a track loader), it is better to have a simple installation on existing vehicles. Therefore, an off-joint configuration is designed to meet the need of this application. In this configuration, as shown in Figure 4-3, the electromagnet, magnetic sensors, and the mu-metal element are all placed at a small distance away from the joint. Because the angle sensor is not located exactly on the joint like a ring encoder, it is called the “off-joint” configuration.

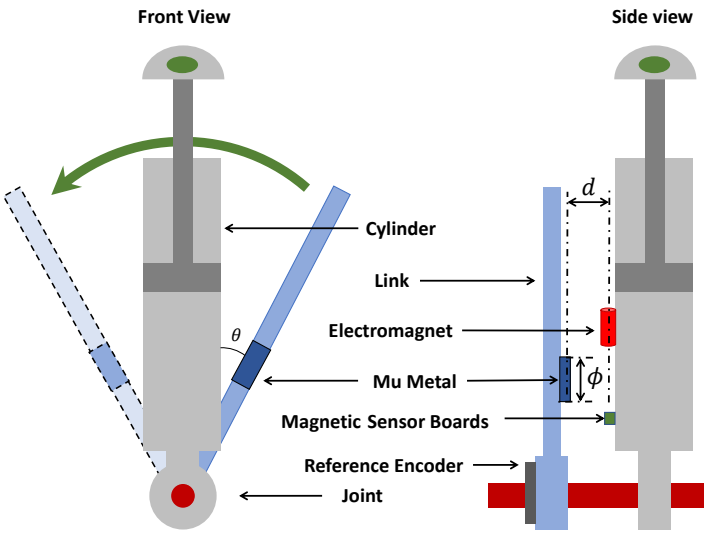

Figure 4-3 Schematic of the mu-metal based angle sensing system with off-joint configuration.

It is noted that the electromagnet and the magnetic sensor are located on one mechanical part and the mu-metal element is located on the other mechanical part with relative rotation to the first part around the joint. Though one mechanical part is shown as a hydraulic cylinder in the schematic, it is not necessarily the case and can be any mechanical structure on the vehicle. When the mechanical link rotates, the mu-metal passes by the electromagnet and the magnetic sensor, which incurs a change of magnetic permeability in the neighboring region around the magnetic sensor. As a result, the measured magnetic field varies with the rotation angle. The exact measurement model will be shown in the next section. The angular position can be estimated from the nonlinear magnetic measurement model using a nonlinear estimation algorithm like EKF.

4.3.2 Design and Modeling

To achieve a low-cost and simple angle measurement system while obtaining sufficiently high accuracy, different configurations of sensor placement are designed and tested for the off-joint configuration. As is shown in Figure 4-4, three configurations of sensor placement are proposed, namely (1) a single sensor with x-axis measurement; (2) dual sensors at the same location with x-axis and z-axis measurement; (3) spatially separated dual sensors with x-axis measurement. It is noted that the mechanical link with the mu-metal on it can rotate to both sides of the cylinder, all of the sensor placement

schemes are designed symmetrically with respect to the center line of the cylinder to maximize the measurement range on both sides of the cylinder.

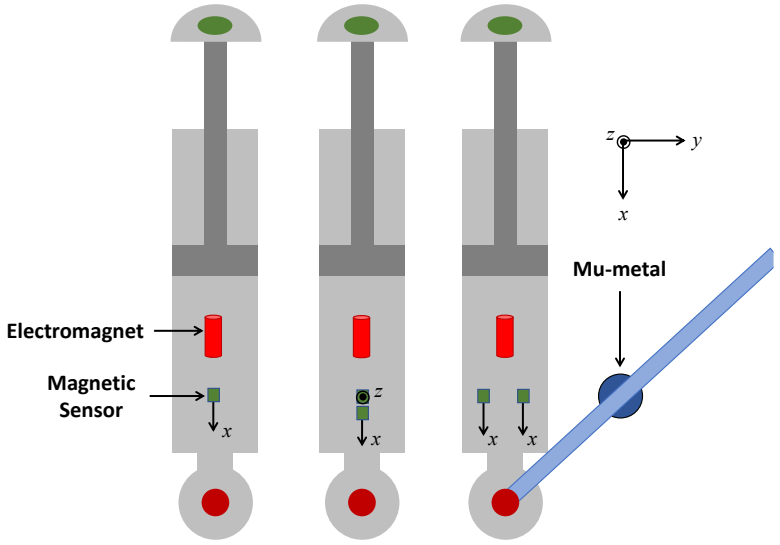

Figure 4-4 Design of sensor placement for the off-joint angle measurement system.

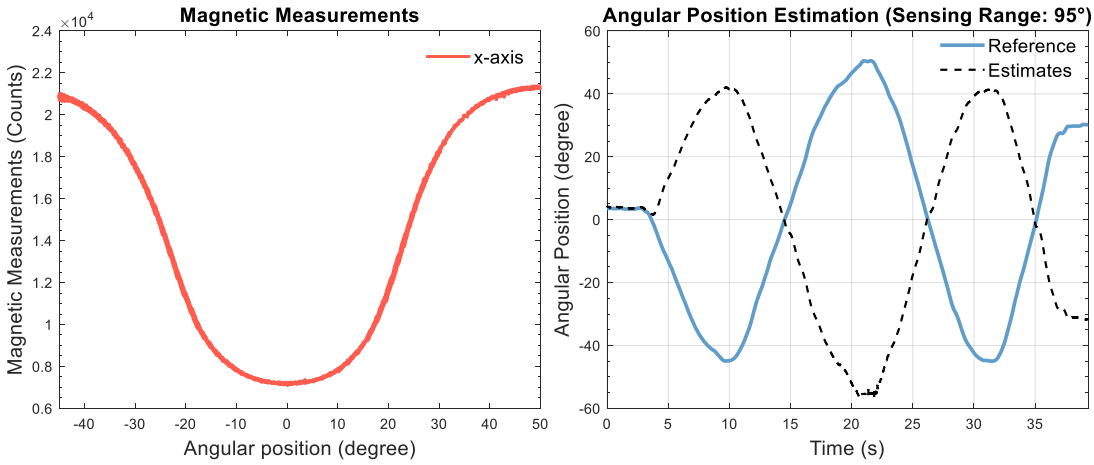

(a) **(b)**

Figure 4-5 (a) Magnetic measurement model and (b) angular position estimation using single sensor with x-axis measurements.

The single sensor configuration is the simplest one with only one magnetic sensor used. Figure 4-5 (a) shows the magnetic measurement variation caused by the angular motion of the mu-metal. It is shown that the magnetic field variation is symmetric with the center line of the system. Note that the zero angular position is set to be the position when the mechanical link with the mu-metal element coincides with the hydraulic cylinder. The

magnetic variation is in an inverted bell shape with one minimum point at the zero position, where the angular position is unobservable. This can be verified by the experimental results shown in Figure 4-5 (b), where angle estimates deviate from the true position when the mu-metal passes by the zero position because the estimation system cannot differentiate the symmetric magnetic measurements around zero position. In the range of -10 to 10 degrees, the magnetic measurement is not very sensitive to the angle position change and thus cannot provide accurate angle estimates even if the divergence issue is overcome. In addition, the magnetic sensitivity is only sufficient for the range of -50 to 50 degrees as the magnetic field flattens beyond 50 degrees away from the zero position in both sides. Therefore, the single sensor placement cannot be adopted.

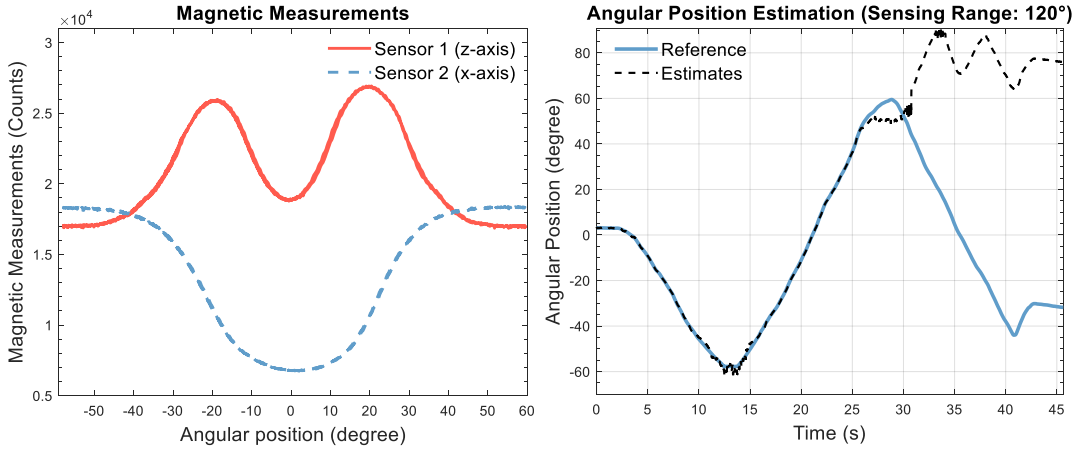

Figure 4-6 (a) Magnetic measurement model and (b) angular position estimation using dual sensors at the same location with x-axis and z-axis measurements.

The second sensor placement design uses two sensors at the same location measuring both *x*- and *z*-axis magnetic field. Its magnetic measurement model is given by Figure 4-6 (a). It is seen that both *x*-axis and *z*-axis measurement are symmetric with zero position, which still poses an issue of unobservability at zero position. The advantage is that the added *z*-axis measurement is more sensitive to angular position than the *x*-axis measurement around the zero position, which might prevent divergence of position estimation at zero position for the specific experimental test shown in Figure 4-6 (b). However, the magnetic sensitivity is low beyond the range of -50 to 50 degrees for both *x*- and *z*- axis measurement, resulting in inaccurate estimates and even divergence of position

estimation.

The third sensor placement scheme is to use two sensors separated on the two sides of the electromagnet so as to maximize the coverage of both sides of the cylinder. Figure 4-7 shows the magnetic field variation caused by the mu-metal movement. It is seen that the magnetic field model is in a skewed inverted bell shape for both sensors with the minimum point occurring at the location of the sensor. The separation of two sensors in space leads to the separation of positions of ambiguity, making at least one magnetic measurement sensitive at any angular position in the measurement range. Therefore, the divergence issue is successfully prevented using this sensor placement design. Furthermore, it is noted that the magnetic measurements are sensitive to the angle position up to the range of -60 to 60 degrees, which is slightly broader than the previous two configurations of sensor placement. Hence, considering its potential of stable and accurate estimation of angular position, the configuration of spatially separated dual sensors is adopted for the off-joint angle estimation system. Extensive experimental results for this configuration will be shown in Section 4.3.3.

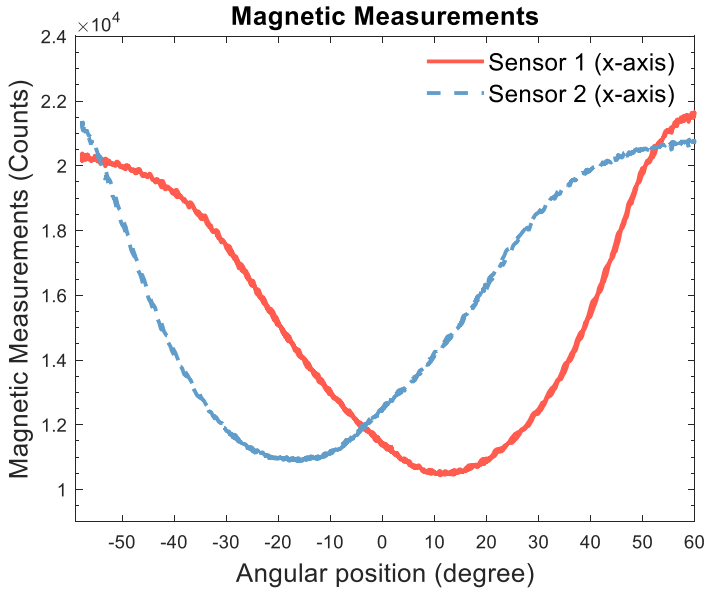

Figure 4-7 Magnetic measurement model using spatially separated dual sensors with x-axis measurements.

The experimental measurement model is obtained as shown in Figure 4-7, where the magnetic field varies with the angular position nonlinearly and non-monotonically.

Although it can be directly used for position estimation, a deeper understanding of this magnetic field pattern and how it is influenced by the magnetized mu-metal is beneficial to the system design and optimization in the future. Thanks to the development of the computational tools of multi-physics modeling, the magnetic field of the angle sensing system can be numerically modeled and analyzed using the software of COMSOL. In the following part, the numerical modeling using COMSOL reveals the physics of how the magnetic field distribution of the electromagnet is influenced by the sensing medium of mu-metal element.

In the numerical simulation, the finite element method (FEM) is adopted to subdivide the whole region of interest into smaller parts called finite elements. For each finite element, the governing equation of physics, originally as partial differential equations (PDE), are approximated by simpler algebraic equations with proper boundary conditions. Then the set of element algebraic equations are combined into a large system of equations solved using some numerical linear algebra method. The advantage of FEM is that it can solve problems involving complex geometries and materials with non-uniform properties. If the region is meshed into sufficiently fine subdomains and the material properties are well modeled, the accuracy of numerical simulation can be ensured. Thus, many real-world experiments can be replaced by numerical simulation for validation and design of a prototype, saving costs of time and money.

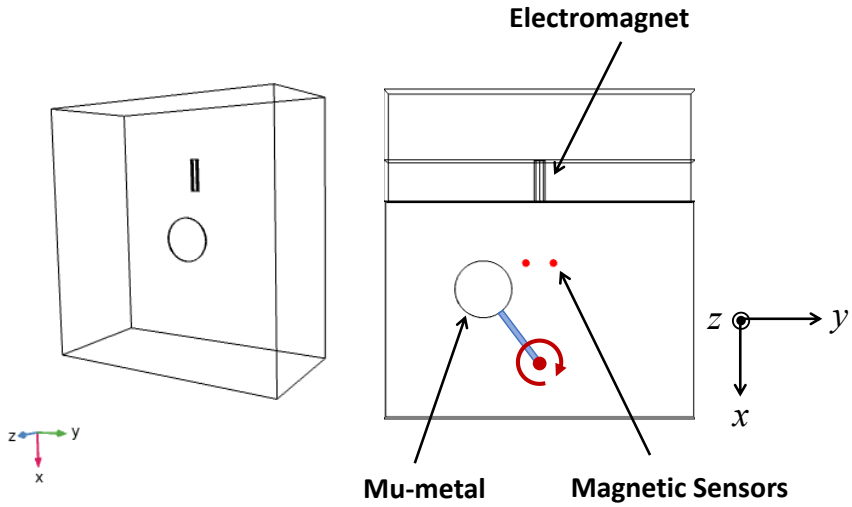

Figure 4-8 Geometric model for numerical simulation of the off-joint angle sensing system.

For the specific problem of modeling of a magnetic angle sensing system involving high-magnetic-permeability materials, the magnetic field (i.e. magnetic field flux density) distribution around the electromagnet and mu-metal element need to be computed. The magnetic field variation at the sensor locations caused by the mu-metal rotation need to be particularly investigated. Although an alternating magnetic field is generated by the electromagnet, its frequency (100 Hz) is still in the low-frequency regime, at which the wave-like behavior of the electromagnetic field is negligible and thus the steady-state modeling using a constant magnetic field can well approximate the average behavior of the original alternating magnetic field. Since an electromagnet (a coil carrying current) is involved, the steady-state magnetic field can be described using the following governing equation [73]

$$\nabla \times \left(\mu^{-1} \nabla \times \vec{A}\right) = \vec{J} \tag{4-3}$$

where μ is the magnetic permeability, $\vec{A}$ is the magnetic vector potential, and $\vec{J}$ is the electric current density. In the numerical simulation, $\vec{A}$ is solved to compute the magnetic flux density $\vec{B}$ using

$$\vec{B} = \nabla \times \vec{A} \tag{4-4}$$

The geometric model is shown in Figure 4-8, where the region of interest is set to be a cube enclosing the electromagnet and the circular mu-metal plates. In simulation, the mu-metal rotates to pass by magnetic sensors. The location of magnetic sensors is marked as red dots in the figure. The meshed region for computation using FEM is shown in Figure 4-9, where the region of electromagnet and mu-metal and the neighboring area are meshed finer than the rest of the domain for better accuracy of simulation because the magnetic property changes significantly at the boundary of different materials.

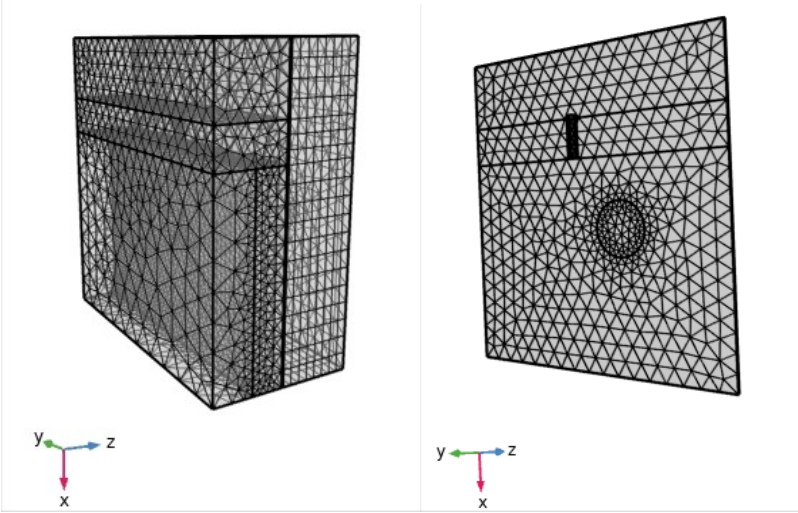

Figure 4-9 Meshed region for numerical simulation using FEM.

Figure 4-10 shows the distribution of magnetic field in *x*-axis in the cross section where the sensors are located when the mu-metal element rotates to different angles. The mu-metal plates are shown as a black circle while the two magnetic sensors are shown as black dots. The electromagnet is marked as a white rectangle. The separated dual sensors are also adopted as the sensor placement configuration in numerical simulation for comparison with its experimental results. Note that the mu-metal plate is above the plane with the depicted magnetic field (i.e. the plane where the electromagnet and sensors are located). It is observed that the magnetic field at the sensor location is impaired when the mu-metal is passing by the sensor. It is because the magnetic field is concentrated to the mu-metal element and thus deflected away from the sensor location due to the much higher magnetic permeability of mu-metal than the surrounding air. This effect explains the pattern of magnetic field variation with the angular position of mu-metal obtained by numerical simulation, as shown in Figure 4-11. As the mu-metal element passes by each sensor from above, the magnetic field decreases first and then goes up with the minimum point appearing when the mu-metal plate is right above the sensor. In comparison with the experimental magnetic measurement model shown in Figure 4-7, the numerical model follows the same pattern of variation with respect to the rotation angle of mu-metal. Therefore, the numerical simulation is verified to be an effective tool of magnetic sensing system. The position sensing system can be analyzed and optimized using numerical

simulation before prototyping and experimental test.

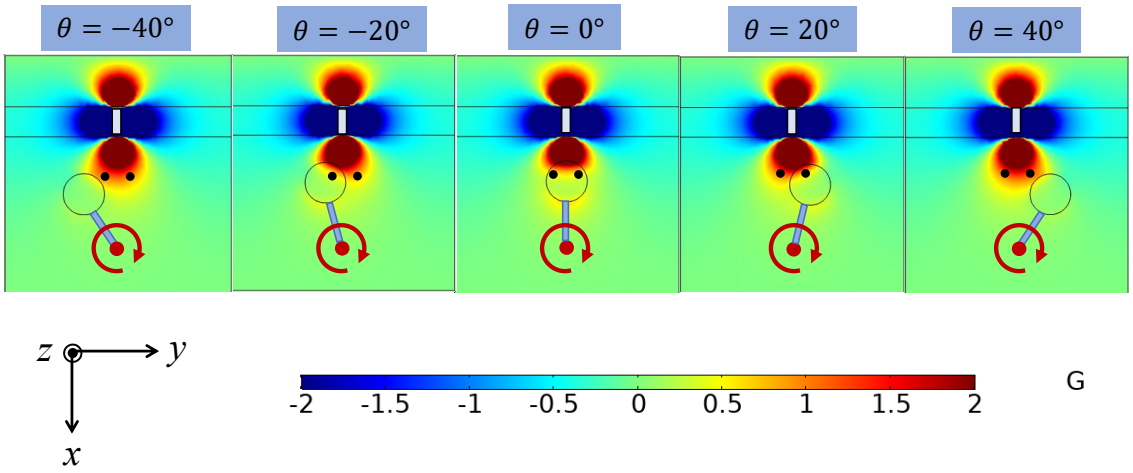

Figure 4-10 Magnetic field distribution with rotation of mu-metal in the off-joint configuration from numerical modeling.

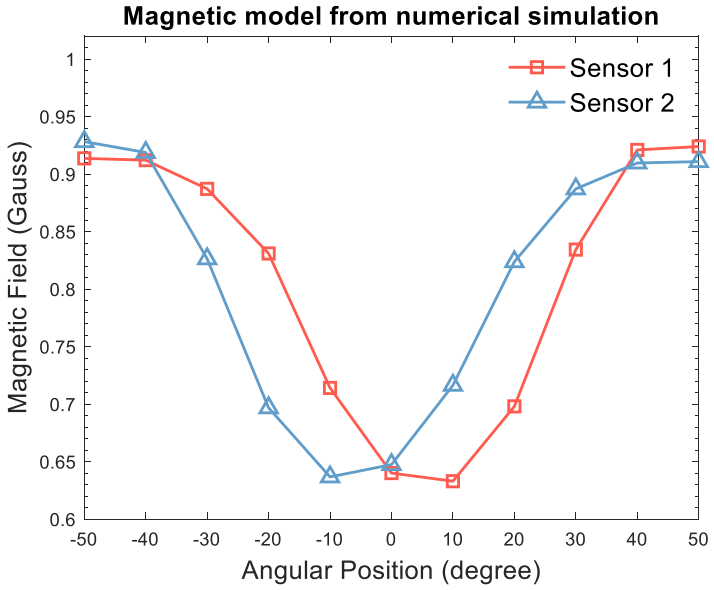

Figure 4-11 Numerical magnetic measurement model for the off-joint angle sensing system.

4.3.3 Experimental Results

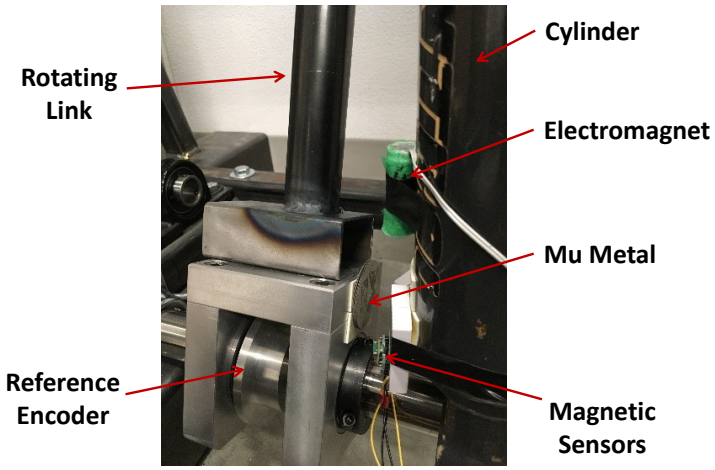

Figure 4-12 Test rig of angular position estimation system with off-joint configuration.

Figure 4-12 shows the test rig of the angle estimation system with off-joint configuration. An expensive magnetic encoder (RLS MBAD01_08) with high accuracy of 0.05 degree is mounted on the joint as reference. The hydraulic cylinder is fixed while a steel lever can rotate around the joint, making the mu-metal plates passing by the sensors. The lever can rotate to both sides of the cylinder. The mu-metal element used here is a stack of thin circular plates with the thickness of 0.25 mm. The mu-metal plates are attached to the rotating steel lever while the electromagnet and the magnetic sensors are fixed to the stationary hydraulic cylinder. The alternating magnetic field is generated by the electromagnet to achieve ferromagnetic disturbance rejection. The method of sensor signal processing and estimation algorithms is used as given by Section 4.2.

The first set of experiments are performed to evaluate the influence of mu-metal plate size on the angle estimation performance. The mu-metal plates with a diameter of 4.60 cm and 6.20 cm are tested respectively. 8 layers of mu-metal plates are used for both sizes. For each size of mu-metal plates, the estimation system is tested for three different measurement ranges (i.e. $\pm 50°$, $\pm 55°$, and $\pm 60°$) to explore the limit of effective measurement.

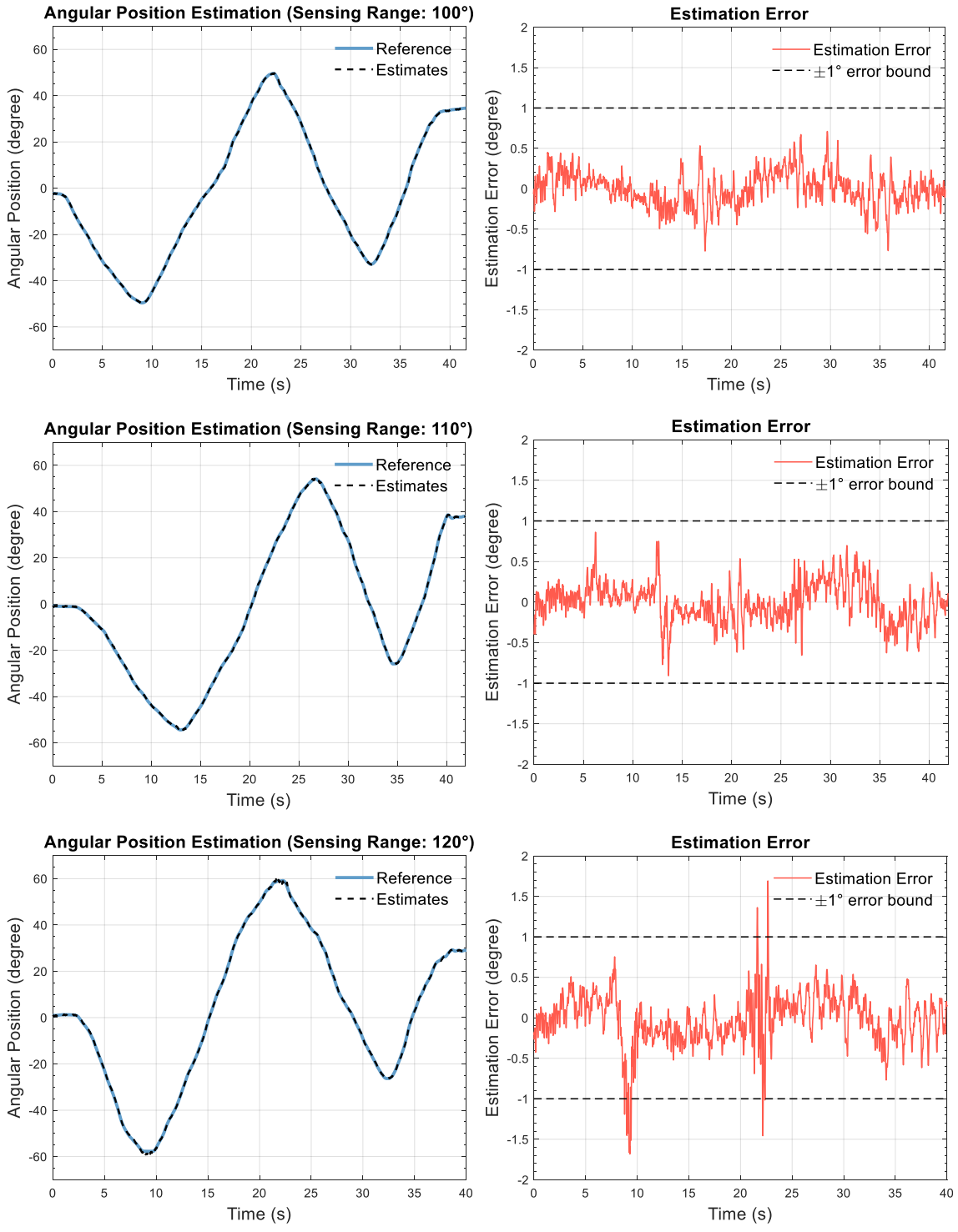

Figure 4-13 Angular position estimation results with mu-metal plates with a diameter of 4.60 cm for different measurement ranges.

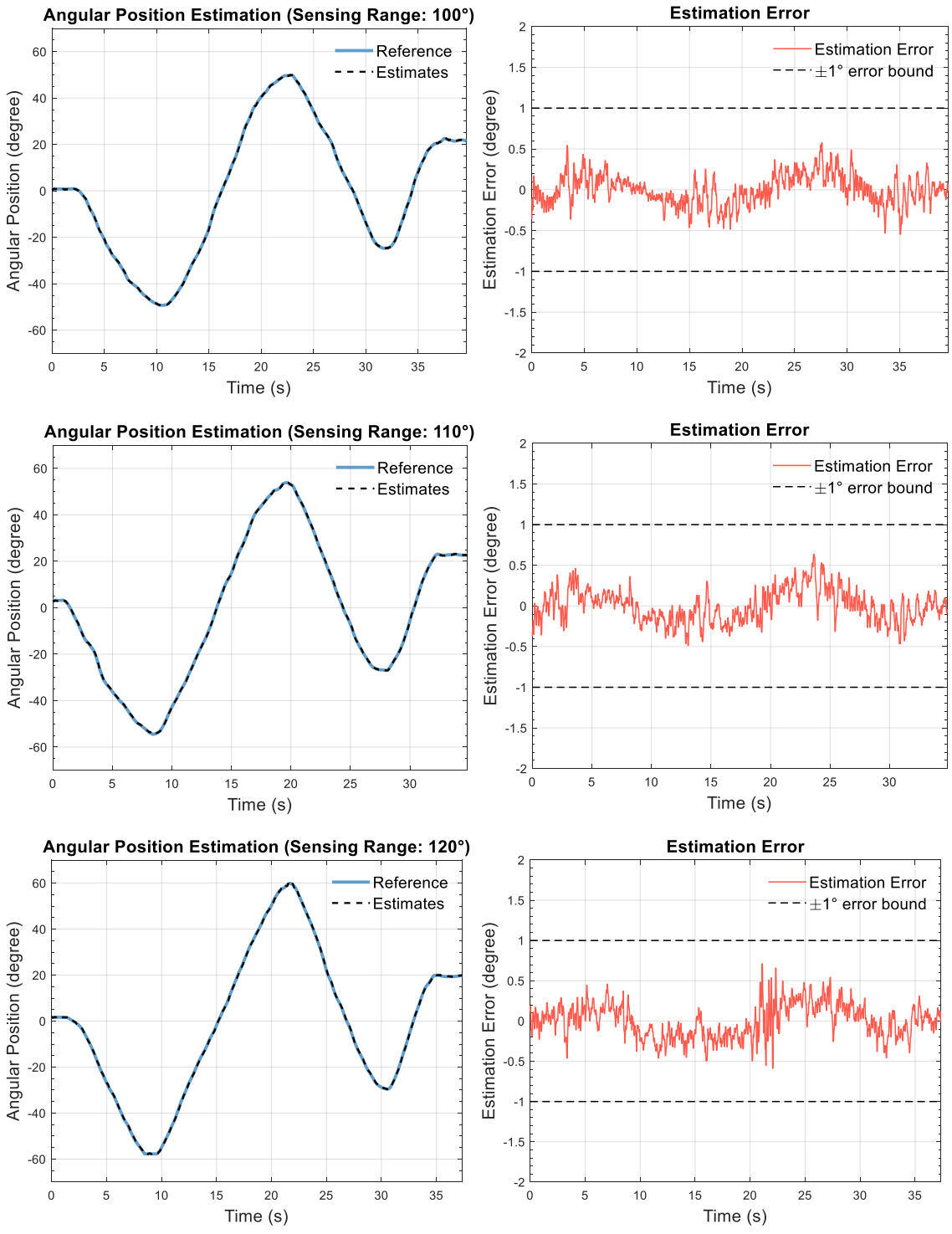

Figure 4-14 Angular position estimation results with mu-metal plates with a diameter of 6.20 cm for different measurement ranges.

The angular position estimation results using the mu-metal plates with a diameter of

4.60 cm are shown in Figure 4-13. It is shown that the position can be estimated with an accuracy of less than 1 degree up to the measurement range of $\pm 55°$. When the mu-metal rotates beyond $\pm 55°$, the estimation error can exceed 1.5 degrees. Figure 4-14 shows the angle estimation results using the mu-metal plates with a diameter of 6.20 cm. Compared with the case with smaller mu-metal plates, the position estimation error can be bounded within 1 degree up to $\pm 60°$. This can be explained by the fact that larger mu-metal element can incur stronger influence on the local magnetic field measured by magnetic sensors. The root-mean-square (RMS) error and maximum error are summarized in Table 4-1. It is seen that the RMS error and maximum error increases as the mechanical link rotates to larger angles, which can be explained by the fact that the magnetic sensitivity decreases when the mu-metal moves far from the magnetic sensors and the electromagnet, as shown in Figure 4-7. In addition, it is observed from the table that the RMS error for the case of ϕ = 6.20 cm is about 0.2 degree up to the measurement range of $\pm 60°$ while that for the case of ϕ = 4.60 cm reaches 0.32 degree. The Maximum error for the case of ϕ = 6.20 cm is 0.71 degree and that for the case of ϕ = 4.60 cm is 1.69 degree up to the measurement range of $\pm 60°$. If the design specification of estimation accuracy is set to be less than 1 degree for maximum error, which is a typical measurement accuracy for applications of off-road vehicles, the size of ϕ = 6.20 cm meets the requirement. If the design specification can be released, smaller sizes of mu-metal plates can also be used.

Table 4-1 Angular position estimation error for different measurement ranges

Measurement Range (degree)	Max. Error (degree)		RMS Error (degree)	
	ϕ = 4.60 cm	ϕ = 6.20 cm	ϕ = 4.60 cm	ϕ = 6.20 cm
100 (-50 ~ 50)	0.71	0.57	0.21	0.18
110 (-55 ~ 55)	0.86	0.63	0.24	0.20
120 (-60 ~ 60)	1.69	0.71	0.32	0.21

A second set of experiments are performed to evaluate the influence of axial distance (denoted as d as shown in Figure 4-3) between the mu-metal plates and the electromagnet/magnetic sensor on the performance of the angular position estimation system. This is also the axial distance between two mechanical parts with relative rotation,

which varies with different applications. Therefore, it is meaningful to investigate the influence of this distance on the position estimation accuracy. The experiments are conducted again for mu-metal plates with 8 layers and with sizes of ϕ = 6.20 cm and ϕ = 4.60 cm. Figure 4-15 shows the magnetic variation with the angular position for different axial distances with ϕ = 6.20 cm. It is seen that the magnitude of magnetic variation decreases as the axial distance become larger. Quantitatively, the magnitude of magnetic variation (i.e. the absolute difference between the maximum and minimum of the magnetic field) for d = 3.5 cm is only 1/5 of that for d = 1.5 cm. It is expected that the position estimation accuracy is impaired by larger axial distances since the position estimation performance highly depends on magnetic sensitivity.

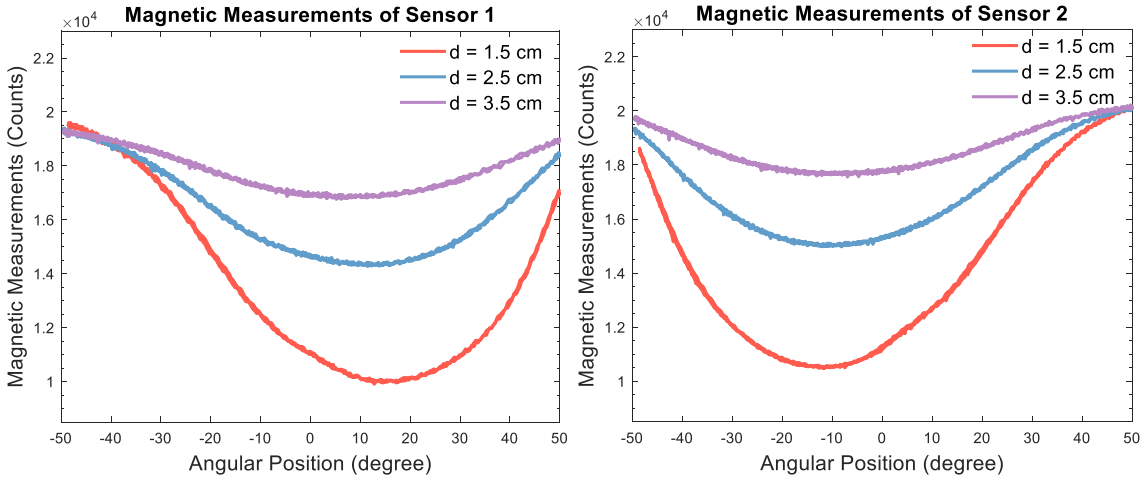

Figure 4-15 Magnetic measurement model for different axial distances.

Figure 4-16 shows angular position estimation results with different axial distances when mu-metal size is ϕ = 4.60 cm. It is observed that if the axial distance is less than 2.5 cm, the estimation error will be well bounded within 1 degree. If the axial distance becomes 3.5 cm, the maximum error is beyond 2 degrees. This deterioration of position estimation accuracy can be well explained by the measurement model shown by Figure 4-15. Figure 4-17 shows angular position estimation results with different axial distances when mu-metal size is ϕ = 6.20 cm. Again, the position estimation error is well below 1 degree if the axial distance is under 2.5 cm. When the axial distance goes up to 3.5 cm, the estimation error can increase up to more than 2 degrees. Therefore, it is better to keep the axial distance

under 2.5 cm when installing the angle sensing system to mechanical structures.

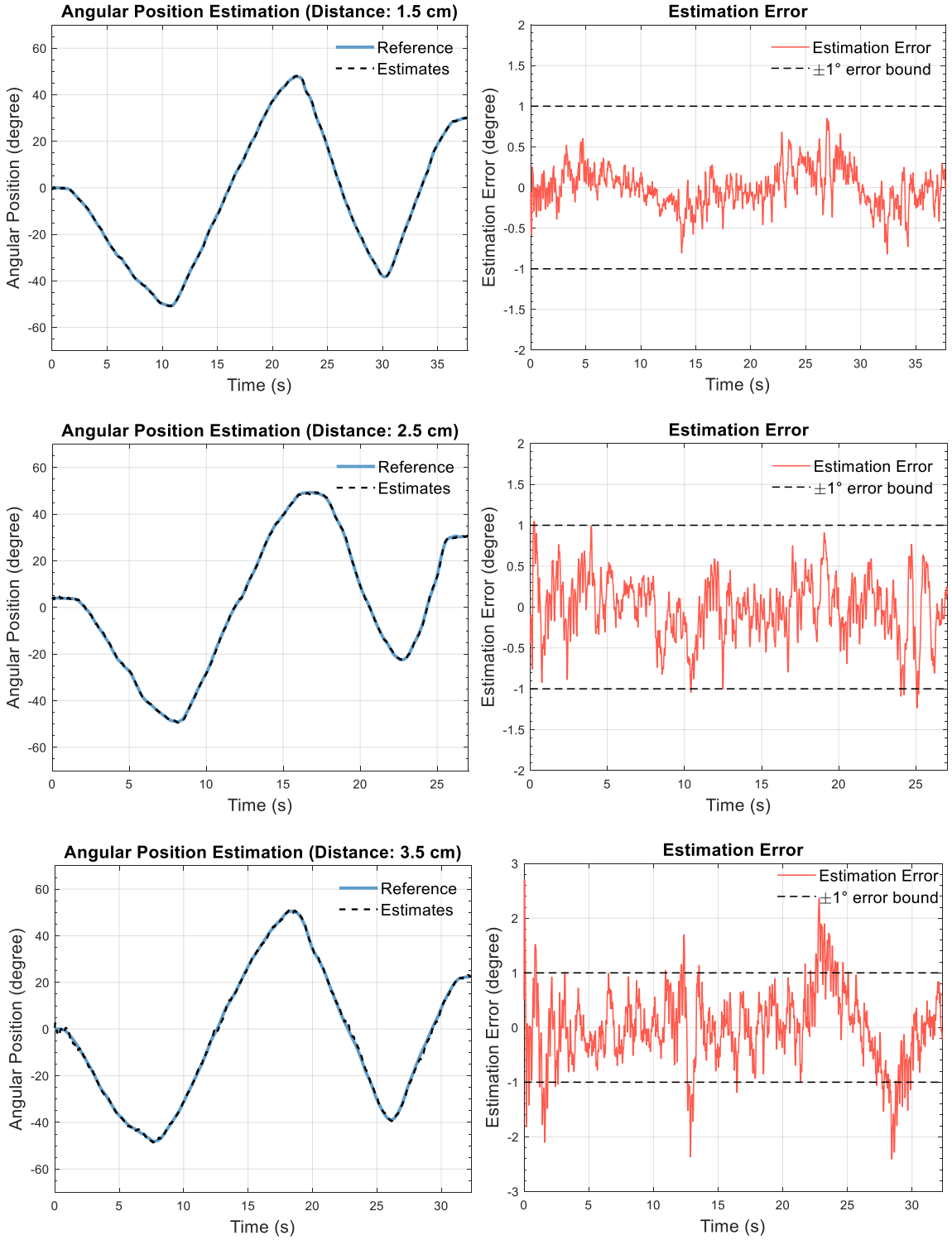

Figure 4-16 Angular position estimation results with mu-metal plates with a diameter of 4.60 cm for different axial distances.

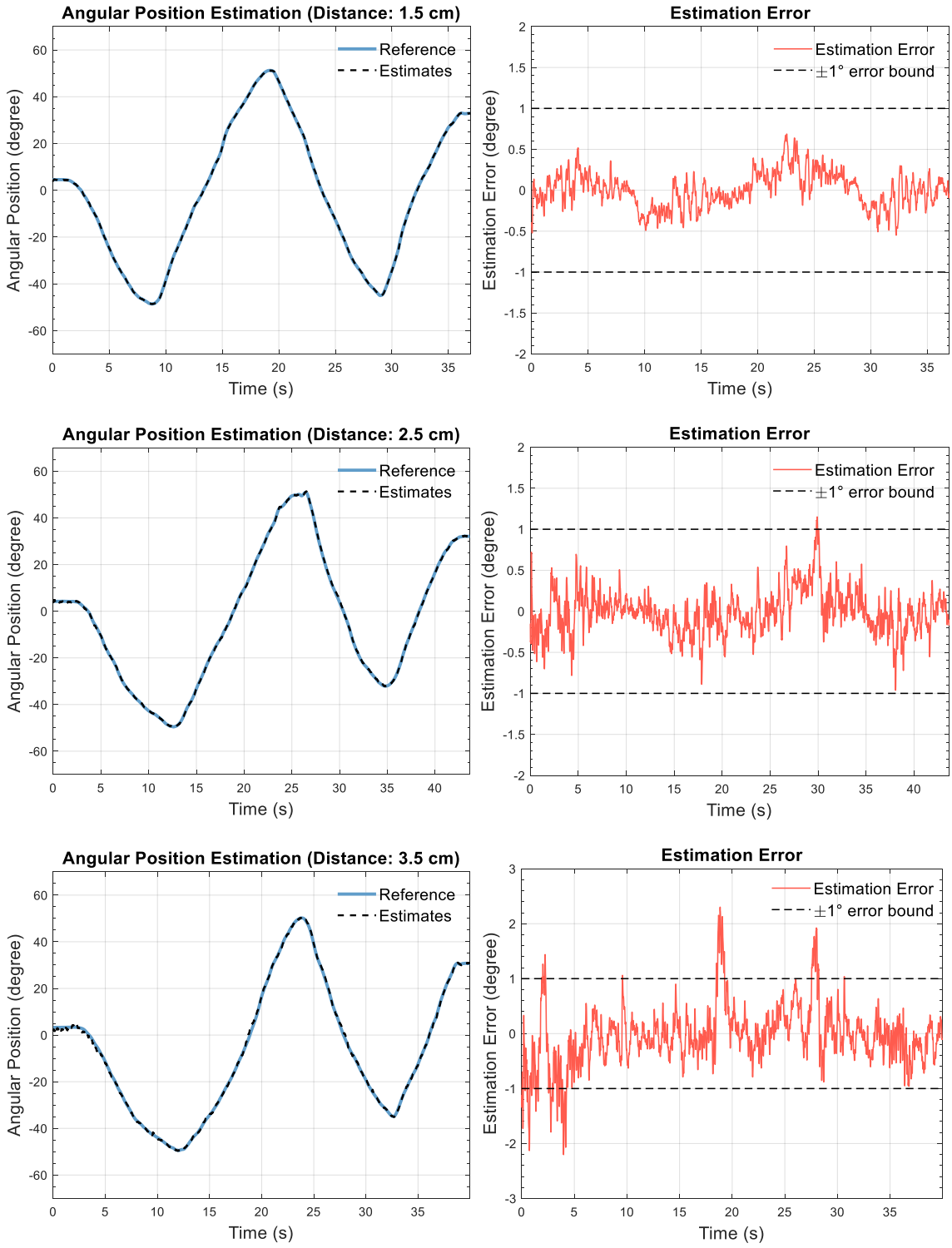

Figure 4-17 Angular position estimation results with mu-metal plates with a diameter of 6.20 cm for different axial distances.

Table 4-2 summarizes the error statistics of angular position estimation for different axial distances. It is seen that the RMS error and maximum error increase as the axial distance becomes larger. As the axial distance increases from 2.5 cm to 3.5 cm, the maximum error and RMS error nearly doubles due to the sharp decrease of magnetic sensitivity to the angular position. The RMS error associated with the smaller mu-metal size is slightly larger than that of the large mu-metal size. This is because larger mu-metal element can provide stronger magnetic field variation.

Table 4-2 Angular position estimation error for different axial distances

Axial Distance (cm)	Max. Error (degree)		RMS Error (degree)	
	ϕ = 4.60 cm	ϕ = 6.20 cm	ϕ = 4.60 cm	ϕ = 6.20 cm
1.5	0.85	0.69	0.24	0.21
2.5	1.03	1.15	0.37	0.27
3.5	2.70	2.30	0.67	0.54

4.3.4 Performance of Disturbance Rejection

It is claimed that the angular position estimation system has the capability of ferromagnetic disturbance rejection enabled by the use of the alternating magnetic field and related signal processing techniques. Its performance of disturbance rejection is evaluated in this section.

Figure 4-18 Evaluation of disturbance rejection performance for the off-joint angle measurement system.

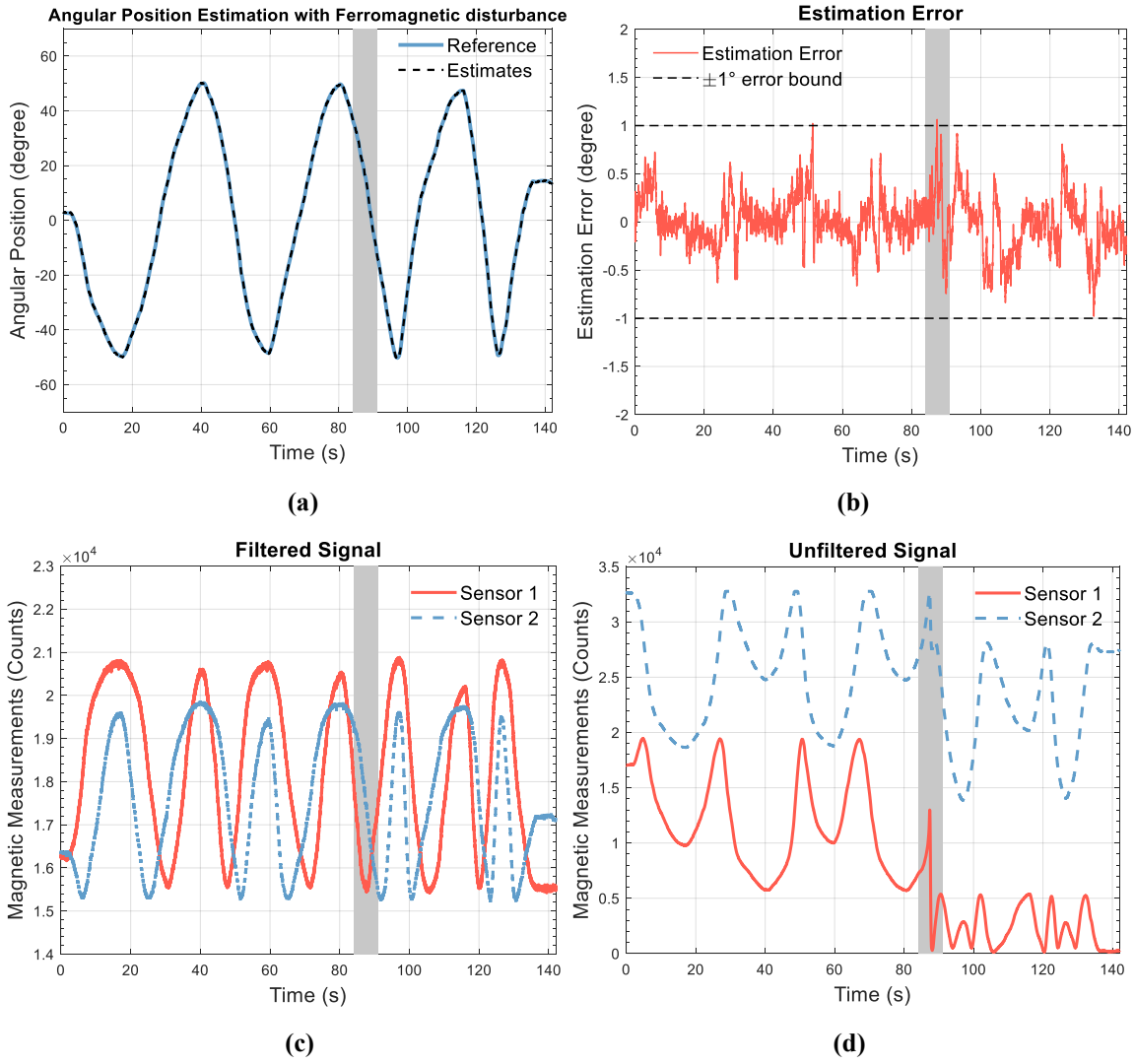

Figure 4-19 Disturbance rejection performance of mu-metal based angular position estimation system with off-joint configuration. (a) Position estimation results. (b) Estimation error. (c) Effective measurements after high pass filter (d) Measurements before high pass filter.

A wrench made of steel is used as the source of ferromagnetic disturbance as shown in Figure 4-18. To test the disturbance rejection performance of the angle estimation system, the wrench is placed near the sensing system when the joint angle is being measured. The angular position estimation results are shown in Figure 4-19. The shaded rectangle represents the occasion when the wrench is placed near the sensing system. It is shown that the estimation error is kept approximately within 1 degree even after the disturbance of wrench is introduced. The maximum error is 1.02 degree, which amounts to about 1% relative error for the measurement range of -50 ~ 50 degree. The RMS error is 0.27 degree.

Figure 4-19 (c) and (d) shows the filtered and unfiltered magnetic signal under the influence of ferromagnetic disturbance. It is observed that the unfiltered raw measurement experiences significant shift when the disturbance is introduced while the filtered signal almost keeps the original pattern. This validates the effectiveness of the use of the alternating magnetic field and related signal processing techniques for ferromagnetic disturbance rejection.

4.4 Angular Position Estimation System with On-joint Configuration

4.4.1 Sensing Principle

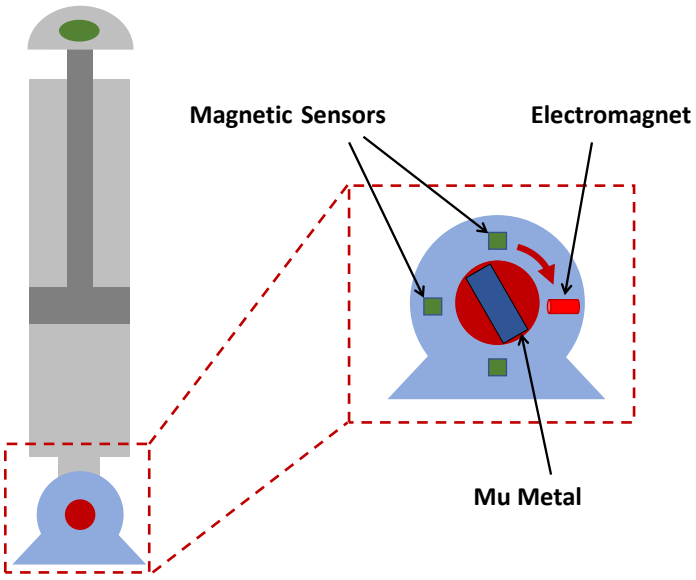

Figure 4-20 Schematic of mu-metal based angular position estimation system with on-joint configuration.

The angle estimation system with off-joint configuration presented in Section 4.3 can provide position estimation accuracy below 1 degree for the measurement range of 60 degrees on either side of the electromagnet. However, this off-joint configuration suffers from the problem of limited angle sensing range because the electromagnet, magnetic sensors and mu-metal are all installed away from the joint. When the mu-metal rotates far from the electromagnet and magnetic sensors, it cannot significantly influence the

magnetic field at the location of the magnetic sensors, resulting in failure of angle estimation. In some applications, the joint angle needs to be measured over a large range and even over the range of full 360 degrees, where the off-joint configuration does not work. Therefore, a new angular position estimation system with on-joint configuration is proposed in this chapter to achieve the full 360-degree angle measurement. The schematic of the on-joint configuration is shown in Figure 4-20. Different from the off-joint configuration with all the sensing components on rotating mechanical structures away from the joint, the sensing components of the on-joint configuration are placed right around the joint. The electromagnet and magnetic sensors are located on the outer housing of the joint while the mu-metal element is placed on the rotating shaft of the joint. When the mu-metal rotates to have different orientation with respect to the electromagnet, it is magnetized with different intensity and orientation and thus exerts different influence on the magnetic field around the joint, which is sensed by magnetic sensors for angle estimation.

4.4.2 Design and Modeling

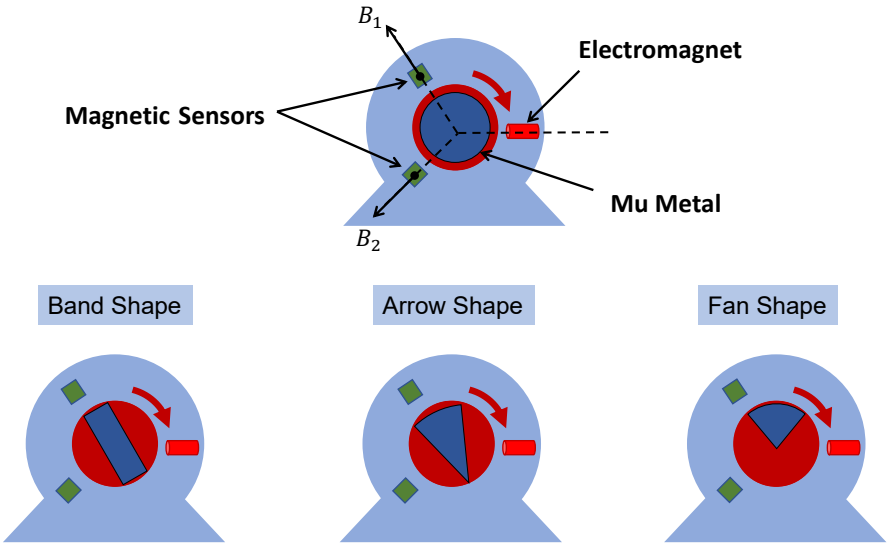

Figure 4-21 Design of mu-metal geometry for the on-joint angle measurement system.

The challenge of the angle sensing system with on-joint configuration to obtain a unique magnetic field distribution for each angle of the mu-metal rotation in order to realize the full coverage of 360-degree sensing range. Therefore, the design of the geometry of the

mu-metal element is crucial since it is the simplest way to result in unique magnetic distribution over the 360-degree range. To achieve non-repetition of magnetic field over the 360-degree, the geometry of the mu-metal element needs to be designed to have an asymmetric shape. As is shown in Figure 4-21, if the mu-metal element is in the perfect circular shape like what is used in the off-configuration system, it cannot cause any magnetic field variation when it rotates since it is a rotationally symmetric geometry. Hence the mu-metal with circular shape cannot be used for angle sensing. Other shapes shown in Figure 4-21 are be considered in design of the mu-metal geometry, namely the band shape, arrow shape, and fan shape. Two sensors are used to measure the magnetic field in the radial direction for all three shapes of mu-metal. Two magnetic sensors and the electromagnet are separated uniformly around the shaft with the angle between any two components being 120 degrees. The diameter of the shaft is 30 mm. Since the method of numerical simulation has been proved to model the magnetic field of the angle sensing system with off-joint configuration with reasonable accuracy, it is used here to model the influence of mu-metal element with different geometries on the magnetic field measurement to find out the best mu-metal shape for the angle sensing system with on-joint configuration.

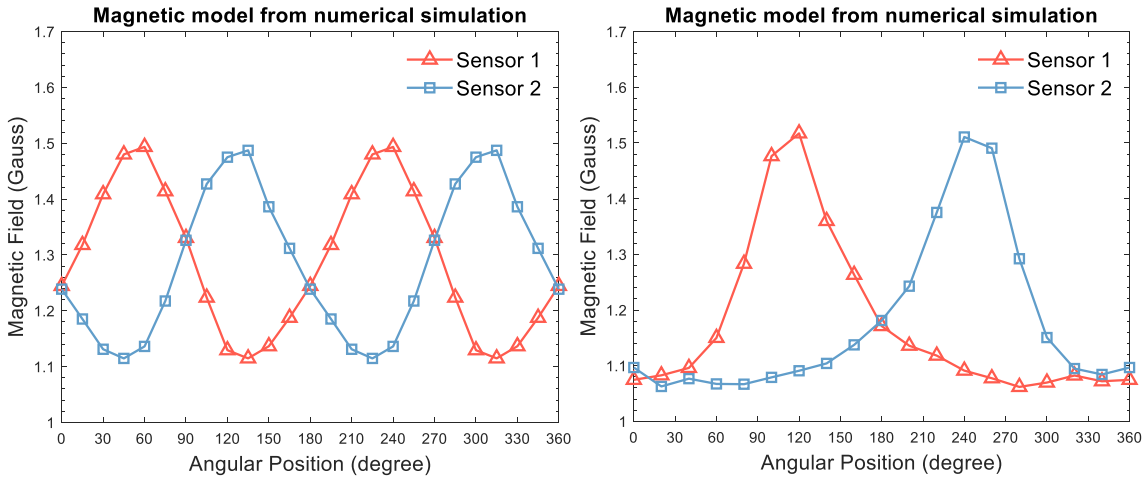

Figure 4-22 Magnetic variation with rotation angle from numerical simulation for mu-metal element in (a) band shape and (b) fan shape.

The first shape considered is the band shape with a width of 10 mm. The magnetic field variation caused by band-shape mu-metal rotation is shown in Figure 4-22 (a). The range

of variation is shown to be about 0.4 Gauss. However, the magnetic field measured by either sensor repeat itself every 180 degrees since the band shape repeats the same configuration with respect to the electromagnet and magnetic sensors when it rotates 180 degrees. Therefore, this fundamental ambiguity between two 180-degree regions makes band shape not applicable for full 360-degree angle sensing.

The fan-shape mu-metal seems to be promising for 360-degree angle sensing since it has an asymmetric shape. The fan shape considered here is a partial circle with a central angle of 80 degrees. Its numerical magnetic model is given in Figure 4-22 (b). The range of variation is about 0.45 Gauss. It is observed that there is a unique magnetic field measurement for each rotation angle over the range of 360 degrees. However, the magnetic sensitivity with rotation angle is extremely low for both sensors in the range of 0 ~ 40 and 320 ~ 360 degrees, amounting to a consecutive 80-degree insensitive region. The insensitive region is where the fan-shape mu-metal rotates away from both magnetic sensors and towards the electromagnet so there is negligible influence of mu-metal on the magnetic field at locations of magnetic sensors. Therefore, the arrow-shape mu-metal is proposed as a "mixture" of band shape and fan shape. The arrow-shape mu-metal considered here is manufactured by cutting off two segments from the full circle, with the left part having an angle of circumference of 40 degrees. Unlike the two equal ends of the band shape, the arrow shape has one small end and another large end. When the large end rotates away from magnetic sensors towards the electromagnet, the small end ("arrow head") points to the side of magnetic sensors, eliminating large insensitive region. Figure 4-23 (a) shows the numerical magnetic model for the angle sensing system with arrow-shape mu-metal. The range of magnetic field variation is 0.9 Gauss, which is twice of that of the fan shape, making the angle sensing system with arrow-shape mu-metal more sensitive overall. The numerical results agree with the experimental model shown in Figure 4-23 (b) in terms of overall variation pattern and locations of extremum points. The experimental model shows fewer insensitive locations than the numerical results, which favors angle estimation using the arrow-shape mu-metal. The minor mismatch between the numerical and experimental model might be attributed to inaccurate modeling of magnetic property of the mu-metal in the numerical simulation.

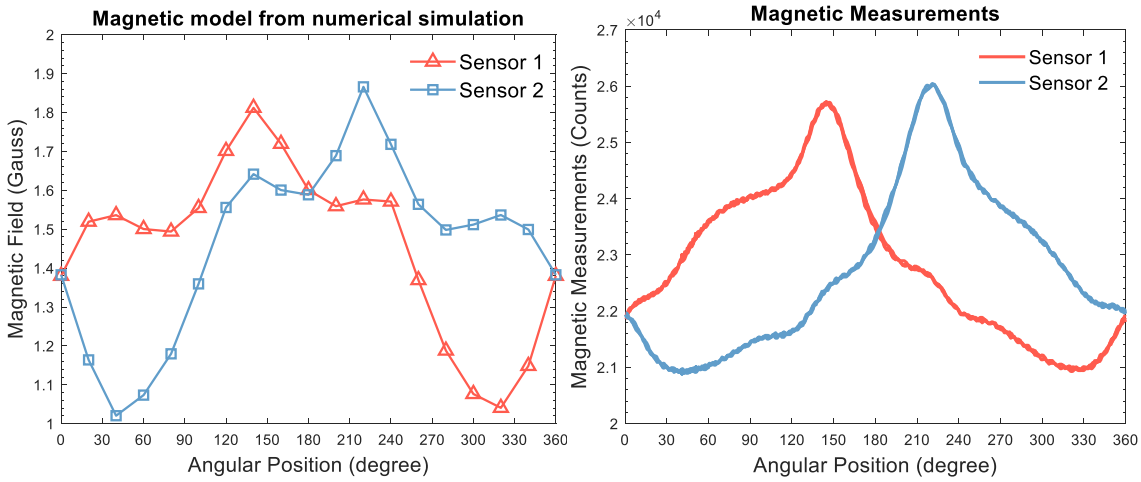

Figure 4-23 Magnetic variation with rotation angle of mu-metal in arrow shape. (a) Numerical simulation results. (b) Experimental results.

The magnetic field distribution under the influence of rotating arrow-shape mu-metal at six angular positions with a 60-degree spacing is illustrated in Figure 4-24. In the figure, the location of two magnetic sensors are marked as black dots, the arrow-shape mu-metal is shown as white triangles, and the electromagnet is shown as white bars. Note that the magnetic field shown here is in the Cartesian coordinate frame while the actual magnetic field measurement is taken in the radial direction of the shaft for position estimation, which is a combination of projected B_x and B_y. It is observed that the local magnetic field around the mu-metal element is re-distributed by the presence and rotation of the high-magnetic-permeability mu-metal. Due to the asymmetric design of the mu-metal geometry, the magnetic field distribution is uniquely formed for each individual angle of the mu-metal rotation over the 360-degree range. For example, the distribution of B_x around the mu-metal is different at $\theta = 0°$, when the arrow is pointing downwards, and at $\theta = 180°$, when the arrow is pointing upwards. In the region right below and near the mu-metal, B_x at $\theta = 0°$ is enhanced by the mu-metal with high magnetic permeability for a small area while the amplifying effect for B_x at $\theta = 180°$ is spread to a larger area because of presence of the large end of the arrow-shape mu-metal. Hence, the design of mu-metal geometry is critical for 360-degree absolute angle sensing with on-joint configuration. The arrow shape is expected to provide the best angle estimation performance by preliminary analysis using numerical simulation and is adopted for further experimental validation.

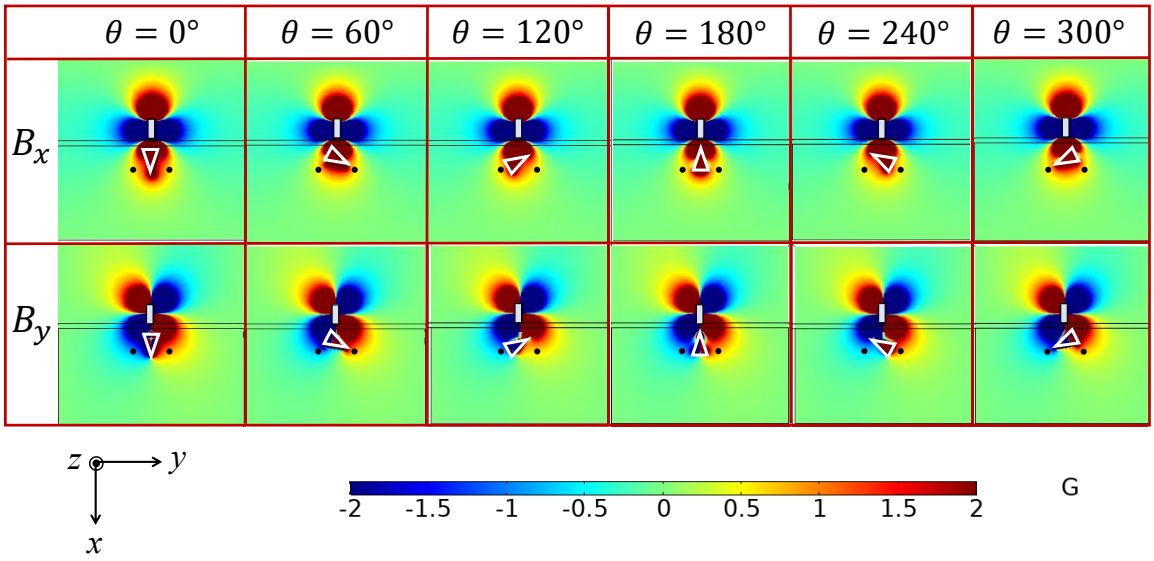

Figure 4-24 Magnetic field distribution with rotation of mu-metal in the on-joint configuration from numerical modeling.

4.4.3 Experimental Results

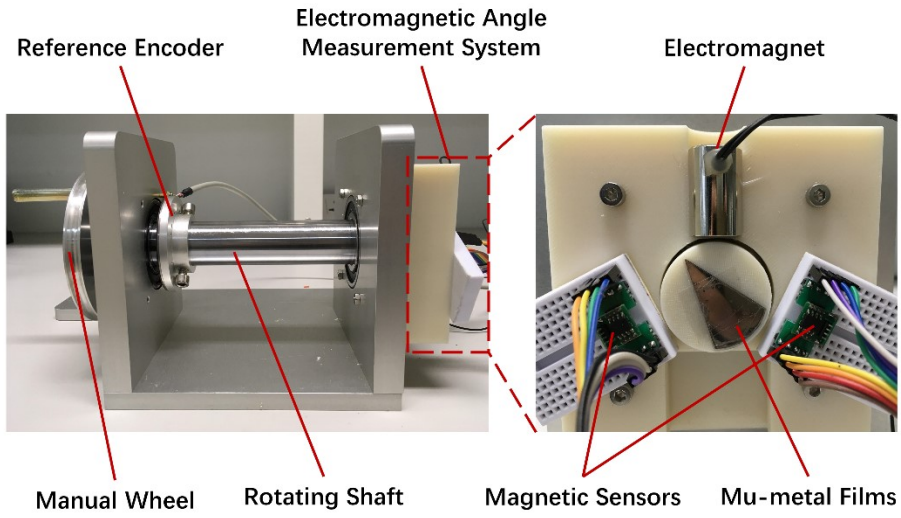

Figure 4-25 Experimental setup of the on-joint angle measurement system.

A test rig is built to experimentally evaluate the mu-metal based angle measurement system with on-joint configuration. A supporting structure made of aluminum is built to hold a rotating shaft with a diameter of 30 mm using bearings. A manual wheel is used to rotate the shaft and a high-accuracy encoder (RLS AksIM-2) is mounted on the shaft for reference. The angle sensing system is installed on one end of the shaft. A stack of 8 layers

of fan-shape mu-metal plates are placed on the surface of shaft end. An electromagnet (ϕ10 mm × 20 mm) and two magnetic sensors (TMR 2305M) are placed around the shaft on the supporting structure with an even arrangement over the circle (i.e. spacing of 120 degree between two components). The magnetic field in the radial direction is measured for angle sensing.

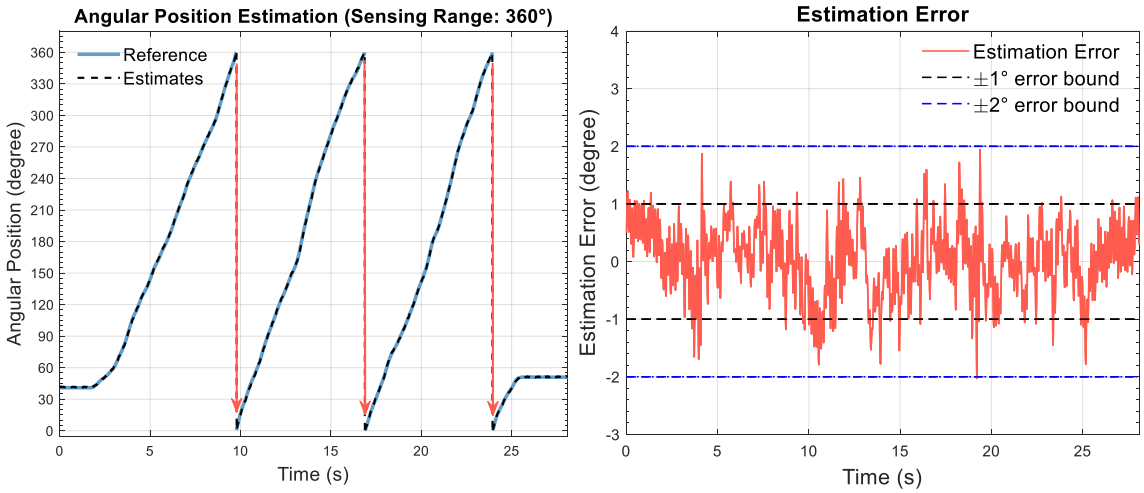

Figure 4-26 Experimental results of angular position estimation with on-joint configuration.

The on-joint angular position estimation system with mu-metal element in arrow shape is experimentally evaluated over the 360-degree range. Figure 4-26 shows that the angle is estimated well in continuous rotation. The estimation error is well below 2 degrees with maximum error of 2.03 degree and RMS error of 0.62 degree. This amounts to a relative maximum error of 0.56% and RMS error of 0.17% for the sensing range of 360 degree.

4.4.4 Performance of Disturbance Rejection

The capability of ferromagnetic disturbance rejection of the angle sensing system with on-joint configuration is validated. Similar to the test with the off-joint configuration, a steel wrench is used as the source of ferromagnetic disturbance, as shown in Figure 4-27. The angle estimation results are shown in Figure 4-28 (a) and (b). The shaded rectangle in the figure marks the time when the wrench is placed near the angle sensing system. The wrench is kept there for the rest of the test. The joint angle can be estimated well using magnetic measurements even under the nearby magnetic disturbance. The introduction of

the disturbance does not cause a significant increase of angle estimation error. The estimation error is mostly bounded within 2-degree range with only occasional spikes up to 3 degrees. The RMS error is 0.82 degree. As shown in Figure 4-28 (d), the unfiltered magnetic measurement is significantly disturbed by the ferromagnetic wrench while the filtered measurement maintains the original pattern of magnetic variation purely caused by the rotation of mu-metal element in Figure 4-28 (c). This experiment verifies that the method of disturbance rejection using alternating magnetic field and proper high-pass filtering works effectively for the mu-metal based angle measurement system with the on-joint configuration.

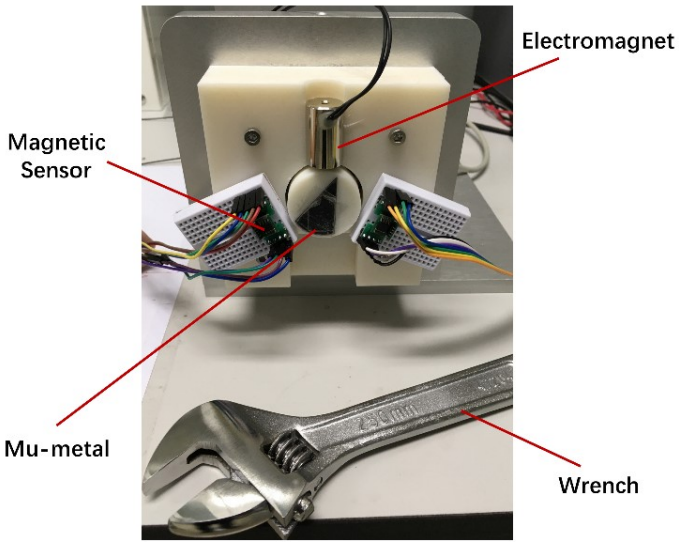

Figure 4-27 Evaluation of disturbance rejection performance for the on-joint angle measurement system.

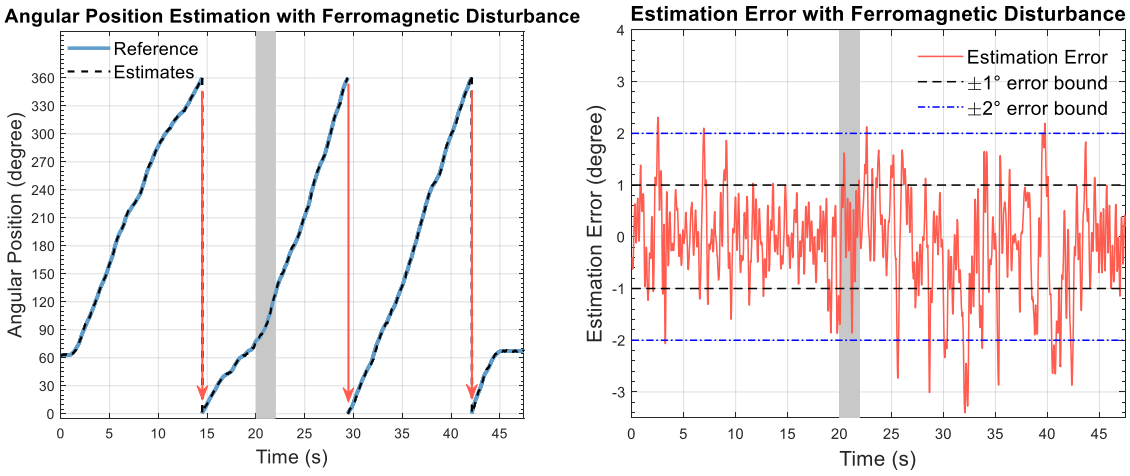

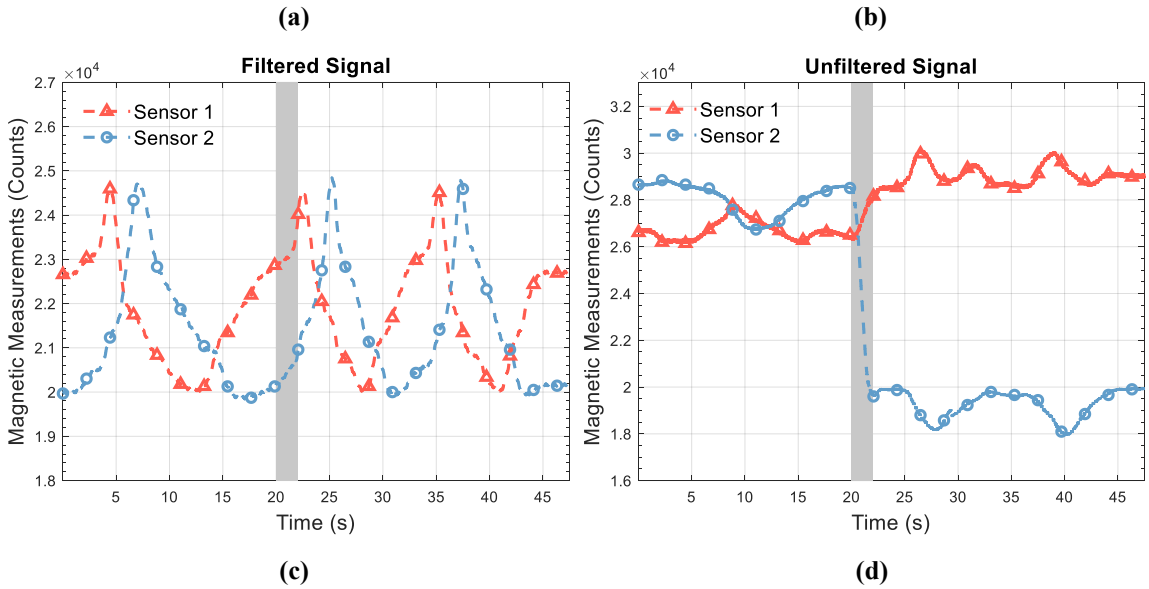

Figure 4-28 Disturbance rejection performance of mu-metal based angular position estimation system with on-joint configuration. (a) Position estimation results. (b) Estimation error. (c) Effective measurements after high pass filter (d) Measurements before high pass filter.

4.5 Conclusions

In this chapter, an angular position estimation system based on the use of an electromagnet and a high-magnetic-permeability metal (mu-metal) is developed to measure the angle of mechanical joints on the mechanisms employed on an off-road vehicle for determination of its end-effector position. In the angular position estimation system, the mu-metal element with high magnetic permeability is attached to the rotating mechanical part and magnetized by the electromagnet to exert an additional magnetic field measured by the magnetic sensors for angle sensing. The use of an alternating magnetic field at a specific high frequency prevents potential low-frequency disturbances from surrounding ferromagnetic objects. Two configurations of the angle sensing system, i.e. off-joint and on-joint configuration, are designed, modeled and experimentally validated.

In the off-joint configuration, major components of the angle sensing system are located off from the joint. The electromagnet and magnetic sensors are mounted on one mechanical part while the magnetic sensors are placed on another mechanical part that rotates around the common joint with respect to the first mechanical part. The angle sensing system with off-joint configuration is designed with several sensor placement schemes, of

which the spatially separated dual sensors works the best to cover the maximum measurement range and maintain magnetic sensitivity at any angle in the measurement range. Numerical simulation shows the variation of magnetic field distribution under the influence of the rotation of mu-metal element. The obtained numerical magnetic measurement model agrees well with the experimental one, which proves that numerical simulation is a reliable tool for design and modeling of such magnetic sensing system. Experimental results show that the angle estimation error is less than 1 degree up to a measurement range of -60 ~ 60 degree if the axial distance along the joint shaft is under 2.5 cm.

To extend the angle measurement range to the full 360 degrees, a second on-joint configuration is proposed. In the on-joint configuration, the electromagnet and magnetic sensors are placed on the housing of the joint around the rotating shaft and the mu-metal element is placed right on the shaft. The geometry of the mu-metal element is designed asymmetrically to incur an aperiodic variation of magnetic field within the 360-degree rotation for unique determination of the joint angle. Numerical simulation shows that the arrow shape of mu-metal element can provide a magnetic measurement model with the best magnetic sensitivity. Experimental results show that a maximum error of 2 degrees and an RMS error of 0.62 degree can be obtained over the 360-degree sensing range. Both the off-joint and on-joint configuration are evaluated experimentally for their performance of ferromagnetic disturbance rejection. It is shown that neither configuration experiences significant deterioration of estimation accuracy when a steel wrench is placed near the sensing system.

Future work includes more sophisticated structural design and optimization of both configurations and experimental validation of the angle sensing system on a real off-road vehicle. Furthermore, the angle sensing system with on-joint configuration can be compactly packaged as a stand-alone absolute angle sensor with general applications.

Chapter 5

Three-dimensional Position Estimation

5.1 Introduction

Non-contacting 3-D position estimation can be widely useful for human motion tracking [74], tip tracking of soft robots [37], and localization of medical devices and surgical tools [75][76]. In human motion tracking, 3-D position of various parts of the human body, e.g. head, fingers, upper and lower limbs, can be measured and analyzed in hospitals for diagnosis of certain diseases [77] or on a daily basis at home for health condition monitoring [78]. In addition, 3-D position measurement of human body motion can be used to ensure or evaluate the effectiveness of physical rehabilitation [79]. In soft robotic manipulators, direct 3-D position estimation of the end-effector is required for feedback motion control due to its high degree-of-freedom of motion and inaccurate modeling of kinematics. Furthermore, the shape sensing of a continuum soft robot can be achieved by position measurement of several discrete points along the robot body and curve fitting of these points [37].

In this dissertation, 3-D position estimation of medical robots or devices moving inside of the human body is considered. Real-time positioning of the medical robot, assisted with pre-procedure magnetic resonance imaging (MRI) or computerized tomography (CT) scans, can guide surgeons directly to the surgical or examination sites without requiring large incisions, reducing complications and side-effects for patients. Furthermore, if the

trajectory of robot motion is pre-planned, autonomous navigation of medical robots can be achieved with 3-D positioning and feedback control, which improves the operation accuracy and safety of the surgery or diagnosis and reduces the efforts of human operators. In addition, 3-D position information of an endoscope can help doctors determine the location of abnormalities once detected [80].

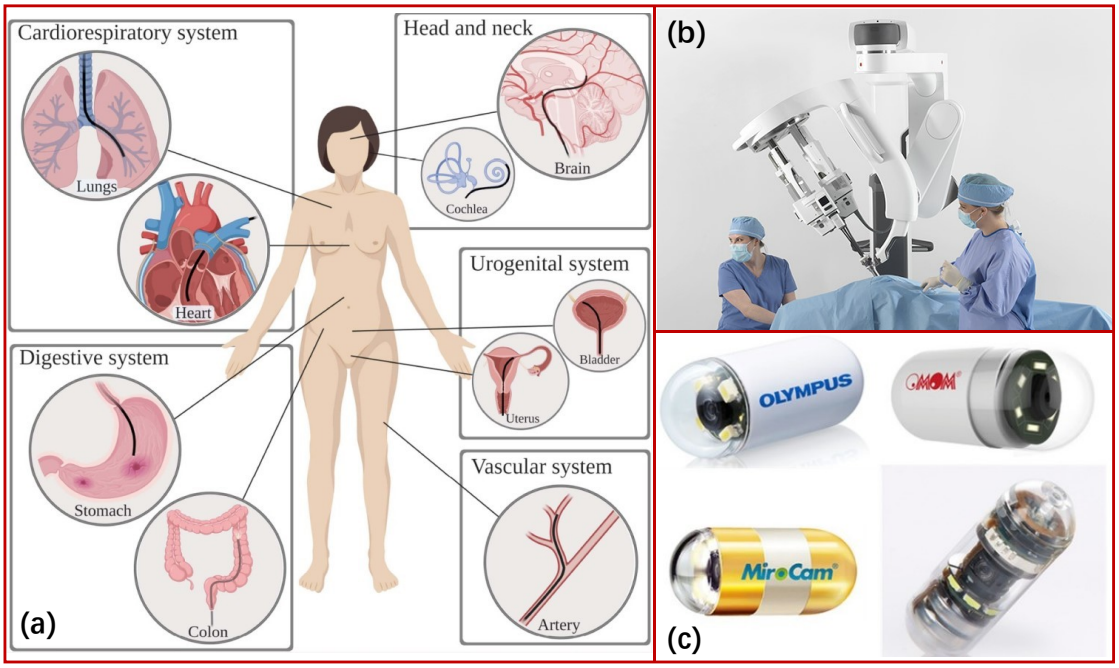

Figure 5-1 Different types of medical robots. (a) Transluminal robot (Reproduced from [81]). (b) Extraluminal robot [82] (Da Vinci robot, ©2021 *Intuitive Surgical, Inc.*). (c) Robotic endoscopic capsules (Reproduced from [80]).

Minimally invasive surgery (MIS) has flourished across many medical disciplines due to its reduced post-operative pain, shortened recovery time and overall cost-effectiveness [83]. Assisted by robotic technology, MIS can be conducted with further reduced skin incisions, by single incision, or by access through natural lumens using flexible robotic structures. Extraluminal medical robots such as laparoscopic robots shown in Figure 5-1 (b), based on rigid links connected by rotational or prismatic joints, can access the targeted sites through one or multiple small extraluminal incisions in abdominal walls [84]. The end-effector position of rigid medical robots can be estimated from angular or linear position of individual joints using accurately modeled forward kinematics. However, its

working space is restricted on a partial sphere with its origin anchored to the trocar. Other drawbacks of rigid medical robots include its counter-intuitive operation due to the fulcrum effect and impaired dexterity due to the loss of wrist articulation. Therefore, transluminal medical robots are developed to navigate through natural tubular anatomies like esophagus, colon, urethra and arteries for diagnostic and therapeutic procedures [81]. Examples of transluminal medical robots are shown in Figure 5-1 (a). Transluminal robots usually have highly compliant and even intrinsically soft structures with high adaptability and conformability to variable environments without damage to the soft tissue. Furthermore, enabled by mechanical, fluidic or magnetic actuation [81], the transluminal robots can navigate to complex targeted sites with high maneuverability and dexterity. However, the end-effector position of flexible transluminal robots cannot be accurately determined from the motion of actuators due to the lack of rigidity between actuators and the end-effector, redundant design and resulting inaccurate kinematic modeling, posing significant challenges for feedback control of the robot. Another kind of medical robots gaining importance in recent years are robotic endoscopic capsules moving in natural lumens of the human body as shown in Figure 5-1 (c). Robotic capsules are untethered and miniaturized with mobility and maneuverability enabled by external driving force like magnetic force [85] or self-propulsion [86]. Compared with tethered transluminal robots, robotic capsules cause less discomfort and pain for patients and does not need sedation [80]. It is noted that direct 3-D positioning is obviously needed for both flexible transluminal robots and untethered robotic capsules for real-time monitoring, control and fully autonomous navigation.

Typical 3-D position estimation or motion tracking systems for medical robots include image-based systems and magnetic tracking systems. Images captured by endoscopes on the robot can be used for positioning by registration with pre-procedure MRI or CT scans [76]. However, image registration is computationally expensive for real-time positioning and an accurate guess of the initial position is required for convergence of the algorithm. Another general problem with optical systems is that they suffer from occlusion issues. X-ray can be adopted to localize the medical robots or devices with high accuracy [85]. Nevertheless, continuous exposure to X-ray does harm to patients so it is not suitable for

real-time positioning. Magnetic tracking systems do not require line-of-sight to detect the robot and involve any harmful radiation. They can be classified as permanent-magnet-based systems [34] and electromagnet-based systems [36][37]. In permanent-magnet-based systems, a magnet is embedded in the medical robot and its position is estimated from magnetic sensor measurements. Permanent-magnet-based systems are suitable for medical applications because the magnet is passive, does not need power supply, and is easy to attach to medical devices. However, it is prone to ferromagnetic disturbances from the surroundings. Electromagnet-based positioning systems use an electromagnet as the magnetic source placed outside of the body transmitting magnetic field pulses, with sensing coils attached to medical robots picking up the signals for position estimation. However, it requires electrical wiring along the tubular robot towards the end-effector inside of the body connecting the sensor for power and signal transmission, making the system complicated and taking up space of the robot that could be reserved for medical purposes. In addition, such delicate wiring can be easily broken with frequent motion and maneuver of the robot. Therefore, it is meaningful to extend the electromagnetic position estimation system based on high-magnetic-permeability materials to applications of 3-D positioning of transluminal continuum and capsule medical robots. In the mu-metal based position estimation system, only the passive mu-metal element is attached to the moving robot with the electromagnet and magnetic sensors placed outside of the body, resulting in a wireless magnetic positioning system immune to ferromagnetic magnetic disturbances.

In this chapter, the mu-metal based 3-D position estimation system is designed and experimentally evaluated on a flexible trans-esophageal robot for ultrasound imaging to demonstrate its function and applicability, though it can be generally used for other flexible transluminal robots or robotic endoscopic capsules. The robotic trans-esophageal echocardiography (TEE) system is shown in Figure 5-2. The TEE robot is designed for remote and automatic ultrasound imaging in cardiac procedures [87][88]. In the robotic TEE system, a flexible commercial TEE probe is embedded in an add-on robot with designed gear-train and belt driving mechanisms, which controls 4-DoF motion of the robot, namely advance/retraction, rotation, and bi-directional bending. 3-D positioning of the ultrasound transducer of TEE robot enables automatic navigation of the robot through

esophagus to pre-planned positions for ultrasound imaging with optimal views. In addition, the absolute positioning of the ultrasound transducer can help register the ultrasound images to pre-procedure CT or MRI scans for real-time multi-modal display of the anatomy with more comprehensive information.

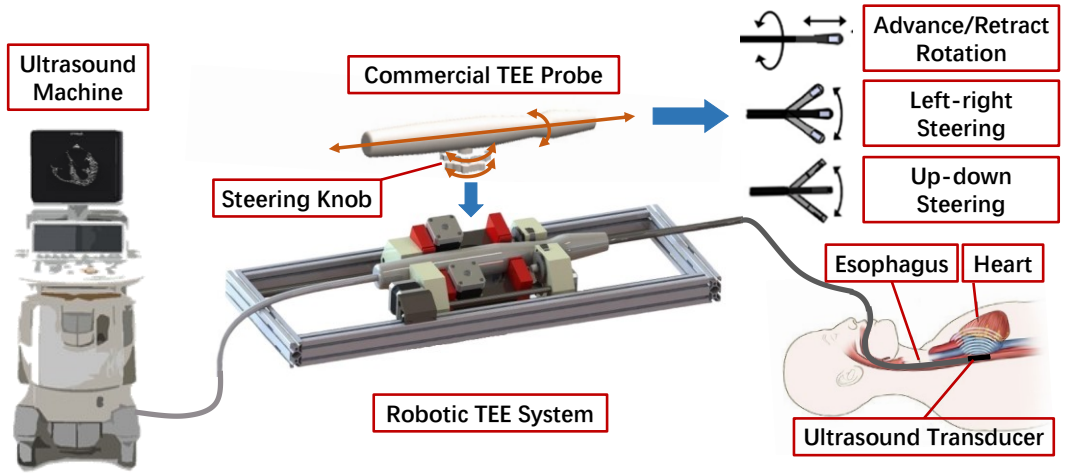

Figure 5-2 Schematic of robotic trans-esophageal echocardiography (TEE) system.

This chapter is organized as follows: The structure of the mu-metal based position estimation system and its sensing principle is presented in Section 5.2. In Section 5.3, the signal processing method and estimation algorithms are described. Then in Section 5.4, extensive experimental results are shown to demonstrate the performance of the proposed mu-metal based 3-D position estimation system for positioning of the distal tip of a flexible TEE robot. Finally, the chapter is concluded in Section 5.5.

5.2 Sensing Principle

Figure 5-3 shows the electromagnetic 3-D positioning system based on mu-metal with high magnetic permeability with the application of positioning the ultrasound transducer of a flexible trans-esophageal robot. Major components of the 3-D positioning system include an electromagnet as the magnetic source, an array of magnetic sensors, and a mu-metal element. The electromagnet and magnetic sensors are placed outside of the body, either fixed on the surface of the human body or held by some mechanical or robotic arm near the region that requires localization of the medical devices. The mu-metal is used as

the sensitive element that exerts influence on the magnetic field for position sensing. It is normally attached to the end-effector (e.g. surgical tools and imaging devices) of a flexible robot and robotic capsules moving inside of the human body, or any spot of a medical robot/device whose 3-D position is of interest.

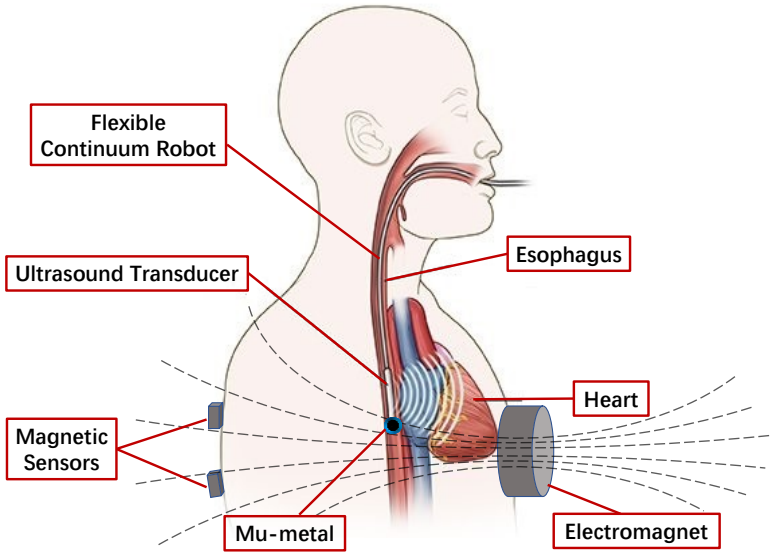

Figure 5-3 Schematic of mu-metal based 3-D position estimation system for transluminal medical robots.

The sensing principle is illustrated in Figure 5-4. The magnetic moment (orientation and intensity of a magnetic object) is shown as red arrows. The magnetic field distribution of the electromagnet is shown as black dashed lines and magnetic field distribution resulting from the magnetized mu-metal is shown as red dashed lines. Since only the 3-D position is estimated in this chapter, the mu-metal is designed to be of the spherical shape, eliminating the influence of its orientation on the magnetic field. The magnetic field measured by the magnetic sensor $\vec{B}_s$ consists of two parts: (1) the magnetic field directly from the electromagnet $\vec{B}_{es}$; (2) the magnetic field from the mu-metal that is magnetized by the electromagnet $\vec{B}_{\mu s}$.

$$\vec{B}_s = \vec{B}_{es} + \vec{B}_{\mu s} \tag{5-1}$$

where the subscript "s" means "sensor", "e" means "electromagnet", and "μ" means "mu-metal". $\vec{B}_{es}$ does not change with the position of mu-metal since it only depends on the

magnetic moment of the electromagnet $\vec{m}_{\mathrm{e}}$ and the relative position between the electromagnet and the magnetic sensor $\vec{r}_{\mathrm{es}}$, both of which do not change in this position sensing system. Therefore, the magnetic field variation at the sensor location only comes from the magnetized mu-metal.

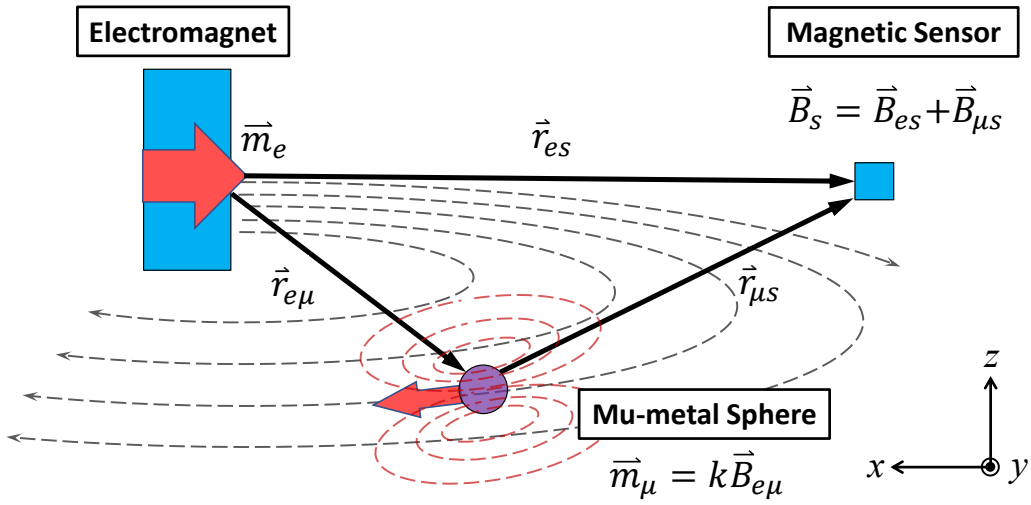

Figure 5-4 Sensing principle of mu-metal based 3-D position estimation system.

The mu-metal is magnetized by the local magnetic field from the electromagnet $\vec{B}_{e\mu}$ given by

$$\vec{B}_{\mathrm{e}\mu} = h_{\mathrm{e}}(\vec{m}_{\mathrm{e}}, \vec{r}_{\mathrm{e}\mu}) \tag{5-2}$$

where $\vec{r}_{\mathrm{e}\mu}$ is the relative position between the electromagnet and the mu-metal, and $h_{\mathrm{e}}(\cdot)$ is a model describing the magnetic field distribution of the electromagnet. The magnetic moment of the magnetized mu-metal $\vec{m}_{\mu}$ depends on the local magnetic field $\vec{B}_{\mathrm{e}\mu}$ at the mu-metal position linearly, as given by

$$\vec{m}_{\mu} = k\vec{B}_{\mathrm{e}\mu} \tag{5-3}$$

where k is the magnetization constant depending on the magnetic permeability μ and demagnetization factor N_{μ} of mu-metal.

$$k = \frac{\mu - 1}{\mu_0(1 + N_{\mu}(\mu - 1))} \cdot \frac{4}{3}\pi r^3 \tag{5-4}$$

where r is the radius of the mu-metal sphere. Since the magnetic moment of the

magnetized mu-metal is determined, its magnetic field at the sensor location can be computed as

$$\vec{B}_{\mu s} = h_{\mu}(\vec{m}_{\mu}, \vec{r}_{\mu s}) \tag{5-5}$$

where $\vec{r}_{\mu s}$ is the relative position between the mu-metal and the magnetic sensor, and $h_{\mu}(\cdot)$ is a model describing the magnetic field distribution of the mu-metal. Substituting (5-2) - (5-3) into (5-5) gives

$$\vec{B}_{\mu s} = h_{\mu}(kh_{e}(\vec{m}_{e}, \vec{r}_{e\mu}), \vec{r}_{\mu s}) \tag{5-6}$$

Since $\vec{r}_{\mu s} = \vec{r}_{es} - \vec{r}_{e\mu}$, the following relation between the magnetic field measurement from the magnetized mu-metal $\vec{B}_{\mu s}$ and the position of mu-metal with respect to the electromagnet $\vec{r}_{e\mu}$ can be obtained as follows:

$$\vec{B}_{\mu s} = h_{\mu}(kh_{e}(\vec{m}_{e}, \vec{r}_{e\mu}), \vec{r}_{es} - \vec{r}_{e\mu}) \tag{5-7}$$

Note that k, $\vec{m}_{e}$, and $\vec{r}_{es}$ are all constants in the system, leaving $\vec{B}_{\mu s}$ a function of the mu-metal position $\vec{r}_{e\mu}$. It is also observed from (5-7) that the magnetic field variation caused by the motion of magnetized mu-metal is two-folded: (1) the relative position of the mu-metal with respect to the electromagnet determines the local magnetizing field and thus the magnetic moment of the mu-metal; (2) the relative position of the mu-metal with respect to the sensor directly influences the measured magnetic field. Therefore, the position of the moving mu-metal can be estimated from the magnetic field measured by stationary sensors if the relating function is well modeled.

5.3 Signal Processing and Estimation Algorithms

5.3.1 Signal Processing Method

As in the previous applications, it is also required that the mu-metal based electromagnetic 3-D position estimation system is immune to ferromagnetic disturbances. Hence, the alternating magnetic field at a certain high frequency is also used in the 3-D position estimation system. The magnetic measurements are high-pass filtered and turned

into the zero-mean oscillating signal. Since the disturbance magnetic fields from earth magnetic field or nearby ferromagnetic objects is at relatively low frequency, they are removed after the high-pass filtering. Then the magnitude of the signal is extracted for position sensing. The signal processing technique of the alternating magnetic field is described in detail in Section 2.4.

5.3.2 Direct Prediction Using Artificial Neural Network

In the linear and angular position estimation systems, the size of the mu-metal element can be made as large as up to a few centimeters so a significant magnetic field variation is caused by the motion of mu-metal. However, for the mu-metal based 3-D position estimation system applied to localization of transluminal medical robots, the size of the mu-metal is strictly limited by the dimension of lumens where the flexible robot travels. For the specific application of trans-esophageal robot positioning considered in this chapter, the largest acceptable size of the mu-metal is about 2 cm and an even smaller size is desired. This size limitation poses a significant challenge of providing reasonable positioning accuracy from the weak magnetic variation. An array of magnetic sensors can be distributed around outside of the body to provide more information for position sensing, improving the positioning accuracy as well as extending the measurement range. Since the magnetic field distribution is highly nonlinear, and multiple measurement outputs and multiple states (three dimensional positions) are involved, it is required that a proper mathematical model sufficiently represents this complex nonlinear relation. An artificial neural network (ANN), consisting of an input layer, an output layer and multiple hidden layers with multiple neurons interconnected between layers, is known for its powerful capability of universal function approximation. Previously, ANN has been employed to predict the position of medical devices from magnetic measurements in permanent-magnet-based position sensing systems [89]. Hence, ANN is adopted here to model the mapping from magnetic field measurements to the 3-D position the mu-metal. As shown in Figure 5-5, a fully-connected feedforward neural network is used with the input of the neural network being magnetic measurements from multiple sensors, and the output of the neural network being the 3-D position of the mu-metal element. In this application, two 3-

axis magnetic sensors are used so there are 6 measurements in total. The number of hidden layers is 5 and the number of neurons in each layer is 16. The output of each neuron in the hidden layer is computed from a nonlinear transformation (i.e. activation function) of weighted sum of outputs from the last layer. The activation function used in this application is the rectified linear unit (ReLU). Before estimating the mu-metal position using ANN, it has to be trained to calibrate model parameters (i.e. weight and bias of each neuron) using magnetic measurements and reference position measurements. Then the mu-metal position can be directly predicted from real-time magnetic measurements using the trained neural network. Since all the model parameters are calibrated offline and no complicated computation like matrix inversion is needed in feedforward prediction, the computational effort for online position estimation is very low using the ANN based direct prediction method. The modeling and training of ANN for electromagnetic 3-D position estimation is implemented using the MATLAB Neural Network Toolbox [90].

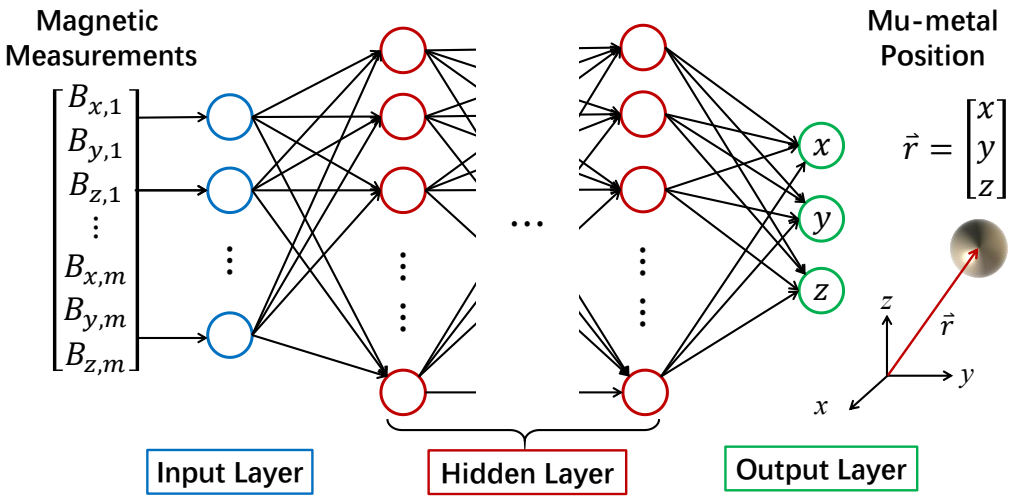

Figure 5-5 Artificial neural network (ANN) for prediction of mu-metal position from magnetic measurements.

5.3.3 Particle Filter with ANN Measurement Model

A problem with the method of direct ANN prediction in last section is that the measurement noise is directly passed through the network to the position estimates. Since the magnetic field variation caused by the motion of mu-metal with small size is very weak, the signal-to-noise ratio (SNR) of magnetic measurements is relatively low, resulting in

large noise level of position estimates. Therefore, a nonlinear filter can be applied to suppress the noise of position estimation by fusing noisy magnetic measurements with some kinematic model. Since the magnetic measurement is a highly nonlinear function of mu-metal position, a particle filter is used to fuse the magnetic measurements and a constant-velocity motion model for accurate position estimation. In the particle-filter-based framework of position estimation, the measurement model is still built with an ANN of the same structure as that used in direct position prediction as shown in last section while the input and output of the neural network is switched, i.e. the input is the position and the output is the magnetic measurements.

The particle filter (PF) is a stochastic nonlinear filtering technique that approximate posterior probability distribution of states conditional on available measurements using a finite number of random samples (particles). In a typical PF, the particles are propagated through the dynamic model and then weighted by the likelihood function, which defines how well the particles match the measurements. Particles with large weight are multiplied and those with small weight are removed in a resampling process to prevent degeneracy. The estimate of the states can be computed as the algebraic average of the resampled particles. Next, the PF-based framework using an ANN measurement model is presented for 3-D position estimation.

The state vector to be estimated is the 3-D position and velocity as given by

$$X = [x \quad y \quad z \quad v_x \quad v_y \quad v_z]^{\mathrm{T}} \tag{5-8}$$

The magnetic measurements are from two 3-axis magnetic sensors as given by

$$y = [B_{x,1} \quad B_{y,1} \quad B_{z,1} \quad B_{x,2} \quad B_{y,2} \quad B_{z,2}]^{\mathrm{T}} \tag{5-9}$$

The constant-velocity kinematic model [61] and the magnetic measurement model are given by

$$\begin{aligned} X_{\mathrm{k}} &= \Phi X_{\mathrm{k-1}} + G w_{\mathrm{k-1}} \\ y_{\mathrm{k}} &= h(X_{\mathrm{k}}) + n_{\mathrm{k}} \\ n_{\mathrm{k}} &\sim N(0, R) \\ w_{\mathrm{k}} &\sim N(0, Q) \end{aligned} \tag{5-10}$$

where

$$\Phi = \begin{bmatrix} 1 & 0 & 0 & \mathrm{d}t & 0 & 0 \\ 0 & 1 & 0 & 0 & \mathrm{d}t & 0 \\ 0 & 0 & 1 & 0 & 0 & \mathrm{d}t \\ 0 & 0 & 0 & 1 & 0 & 0 \\ 0 & 0 & 0 & 0 & 1 & 0 \\ 0 & 0 & 0 & 0 & 0 & 1 \end{bmatrix}, G = \begin{bmatrix} \frac{\mathrm{d}t^2}{2} & 0 & 0 \\ 0 & \frac{\mathrm{d}t^2}{2} & 0 \\ 0 & 0 & \frac{\mathrm{d}t^2}{2} \\ \mathrm{d}t & 0 & 0 \\ 0 & \mathrm{d}t & 0 \\ 0 & 0 & \mathrm{d}t \end{bmatrix},$$

$$Q = \begin{bmatrix} {\sigma_x}^2 & 0 & 0 \\ 0 & {\sigma_y}^2 & 0 \\ 0 & 0 & {\sigma_z}^2 \end{bmatrix}, \tag{5-11}$$

$$R = \begin{bmatrix} {\sigma_{sx1}}^2 & 0 & 0 & 0 & 0 & 0 \\ 0 & {\sigma_{sy1}}^2 & 0 & 0 & 0 & 0 \\ 0 & 0 & {\sigma_{sz1}}^2 & 0 & 0 & 0 \\ 0 & 0 & 0 & {\sigma_{sx2}}^2 & 0 & 0 \\ 0 & 0 & 0 & 0 & {\sigma_{sy2}}^2 & 0 \\ 0 & 0 & 0 & 0 & 0 & {\sigma_{sz2}}^2 \end{bmatrix}$$

It is noted that the unmodeled acceleration w_{k} is assumed to be small and modeled as zero-mean Gaussian and white noise. The measurement noise v_{k} is also modeled as zero-mean Gaussian and white noise. Both the process noise and measurement noise are uncorrelated in different axes of the Cartesian coordinate frame. $h(\cdot)$ is describes the nonlinear relation between the magnetic measurement and the 3-D position to be estimated. In this application, $h(\cdot)$ is modeled by a fully connected neural network with 5 hidden layers with 16 neurons in each layer. The implementation of PF is given below [62]. At the start of the filtering, a set of particles $X_{0,i}^{+}$ $(i = 1, 2, \ldots, N)$ is randomly generated from the probability density function (PDF) $p(X_0)$, which is assumed to be some known Gaussian distribution. The number of particles N is determined as a trade-off between computational cost and estimation accuracy. Then, for time step $k = 1, 2, \ldots \ldots$, the following steps are iterated for position estimation.

1) Perform the time propagation using the kinematic model to generate *a priori* particles $X_{k,i}^{-}$.

$$X_{k,i}^{-} = \Phi X_{k-1,i}^{+} + G w_{k-1,i} \qquad (i = 1, 2, \dots, N) \tag{5-12}$$

$w_{k-1,i}$ is randomly sampled based on the PDF of $w_{\mathrm{k-1}}$.

2) Compute the relative likelihood q_i for each particle $X_{k,i}^{-}$ based on the likelihood function given by

$$p\left(y_k \middle| X_{k,i}^{-}\right) = \frac{1}{\sqrt{(2\pi)^3 |R|}} \exp\left(-\frac{1}{2}\left(y_k - h\left(X_{k,i}^{-}\right)\right)^{\mathrm{T}} R^{-1} \left(y_k - h\left(X_{k,i}^{-}\right)\right)\right) \tag{5-13}$$

The relative likelihood describes how close the predicted measurements evaluated with current propagated particles matches the true measurements.

3) Normalize the relative likelihood q_i such that the sum of q_i equal to one.

$$q_i = \frac{q_i}{\sum_{j=1}^{N} q_j} \tag{5-14}$$

4) Resample a set of *a posteriori* particles $X_{k,i}^{+}$ based on the normalized relative likelihood q_i. The resampling method used here is multinomial resampling given by the following two steps:

   a) Generate a random number r that is uniformly distributed on [0, 1].

   b) Compute the cumulative likelihood $\sum_{m=1}^{j} q_m$ $(j = 1, 2, \dots, N)$, one at a time, until $\sum_{m=1}^{j-1} q_m < r$ and $\sum_{m=1}^{j} q_m > r$. Then set $X_{k,i}^{+} = X_{k,j}^{-}$.

   After the resampling step, the particles with high likelihood is multiplied while those with small likelihood are reduced.

5) Finally, a set of particles $X_{k,i}^{+}$ are obtained according the distribution of PDF $p(X_k|y_k)$. The mean and covariance of the state estimate can be computed as

$$\begin{aligned} \hat{X}_k^{+} &\approx \frac{1}{N} \sum_{i=1}^{N} X_{k,i}^{+} \\ cov(\hat{X}_k^{+}) &\approx \frac{1}{N} \sum_{i=1}^{N} (X_{k,i}^{+} - \hat{X}_k^{+})(X_{k,i}^{+} - \hat{X}_k^{+})^{\mathrm{T}} \end{aligned} \tag{5-15}$$

5.4 Experimental Results

In this section, the mu-metal based electromagnetic 3-D position estimation system is

experimentally validated on a flexible trans-esophageal robot. The position estimation accuracy for two modes of robot motion, i.e. robot insertion and robot maneuver, is presented and discussed by analyzing the magnetic field variation in the 3-D space caused by the mu-metal motion. Finally, the performance of ferromagnetic disturbance rejection is also evaluated for the 3-D positioning system.

5.4.1 Experimental Setup

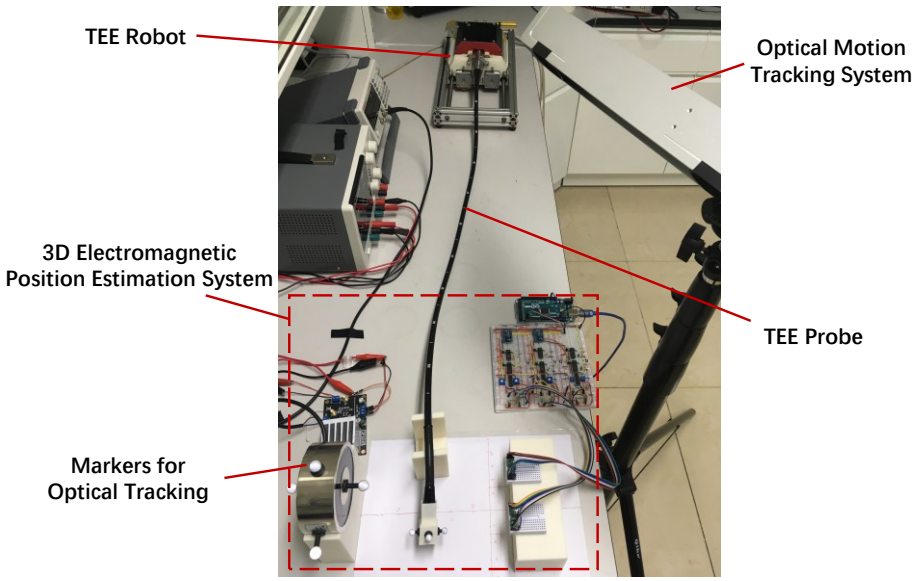

Figure 5-6 Experimental setup of 3D electromagnetic position estimation for a TEE robot.

Figure 5-6 shows the experimental setup of the mu-metal based 3-D electromagnetic position estimation system for localization of the ultrasound transducer of a flexible TEE robot developed by Wang et al [87]. The TEE robot controls the motion of the flexible cable-like probe including advance/retraction, rotation, and bidirectional bending of the distal section with an ultrasound transducer. In the experimental setup, the distal part of the robot is placed in the working region of the electromagnetic 3-D positioning system for experimental test. The mu-metal element is fixed to the distal tip of the robot, whose position is estimated from magnetic measurements. An optical motion tracking system (OptiTrack V120-Trio, *NaturalPoint, Inc.*) with sub-millimeter accuracy is used for reference position measurement. Optical markers are attached to the electromagnet and the mu-metal for optical motion tracking. A closer illustration of the electromagnetic

positioning system and mu-metal installation can be found in Figure 5-7. The dimension of the electromagnet is $\phi 10$ cm $\times$ 4 cm. Two magnetic sensors are located 20 cm away from the electromagnet along the axial direction, making the middle space a working region for robot positioning. For real application, the part of human body where the transluminal robot travels is located between the electromagnet and the magnetic sensors. The raw magnetic measurements are transmitted to the signal processing circuit for denoising and elimination of disturbance signals. Then the effective measurements are output to a PC for position estimation using the algorithms proposed in Section 5.3. The mu-metal sphere is enclosed in a 3D-printed box of a connector that fix the mu-metal on the ultrasound transducer of the TEE robot.

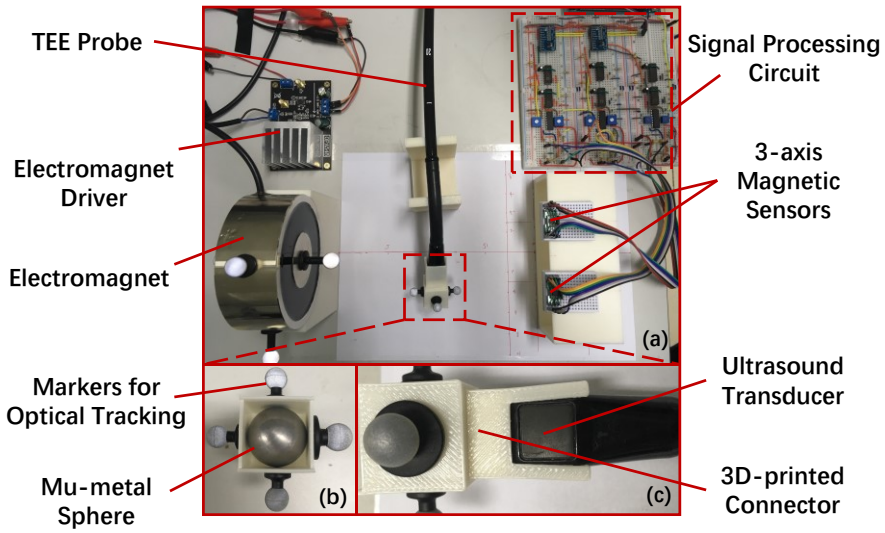

Figure 5-7 (a) Mu-metal based 3D electromagnetic position estimation system (b) Installation of mu-metal sphere (c) Connector between the ultrasound transducer and the mu-metal sphere.

5.4.2 Magnetic Field Response in 3-D Space

Before the experimental results of position estimation are shown, the mu-metal induced magnetic field response in 3-D space is presented in this section to provide an intuitive illustration of the magnetic measurement model. Furthermore, the magnetic field response to the mu-metal displacement also reveals the magnetic sensitivity in different locations of the working region, providing explanation of the position estimation performance shown in the next section.

To obtain the magnetic response in the full 3-D working region, magnetic measurements and reference position of mu-metal are recorded while the mu-metal is held by a robotic manipulator (Han's Robot Elfin5) to sweep through the working region. The experimental setup of the robotic mu-metal sweep is shown in Figure 5-8. The recorded data are also used for training (calibration) of the ANN model of the magnetic field response as a function of mu-metal position.

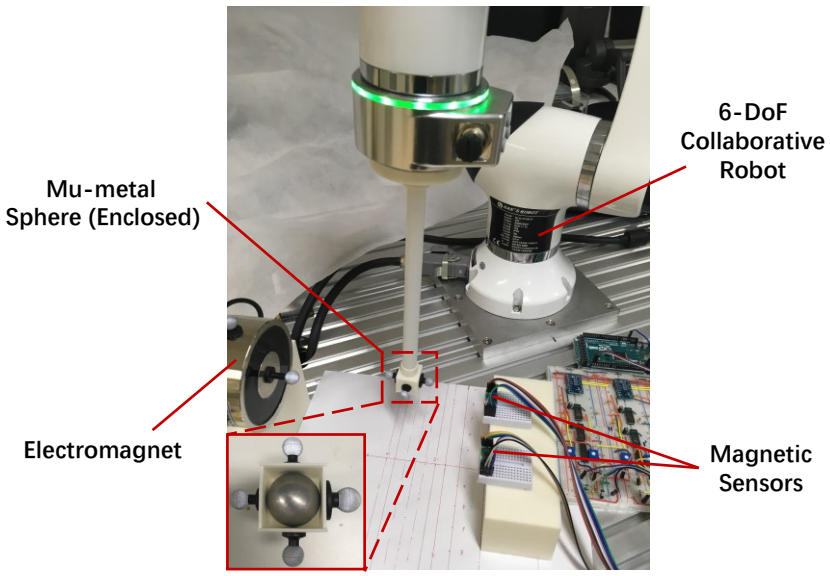

Figure 5-8 Experimental setup for calibration of the magnetic measurement model.

The trajectory of mu-metal motion for magnetic model calibration in the region of interest (ROI) is shown in Figure 5-9. The origin of the global coordinate frame is set to be the center of the electromagnet. The locations of two magnetic sensors are [-200, -30, -35] and [-200, 30, -35] mm, marked by two tri-axis frames with *x*-, *y*- and *z*-axis shown in red, green and blue. It is shown that the trajectory is a collection of lines in *y*-axis with equal spacing of 5 mm in *x*- and *z*-axis direction, spanning a cubic ROI with the dimension of $80 \times 150 \times 100$ mm. It is observed that the ROI spans only the left half of the middle space between the electromagnet and magnetic sensors because the magnetic field response is small in the right half of the space. Therefore, the experiments in this chapter is focused on the ROI shown here for preliminary validation of the mu-metal based 3-D positioning system.

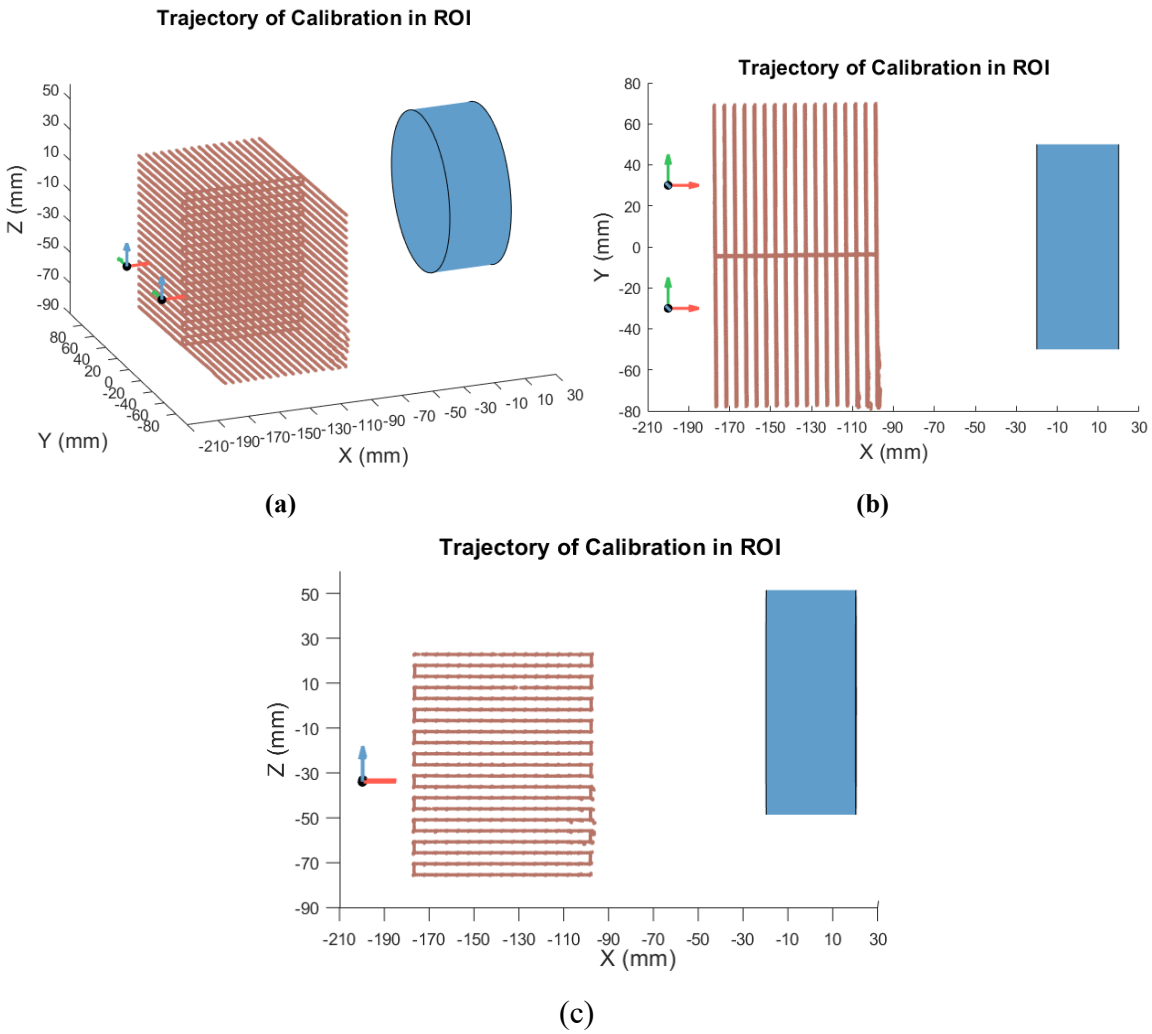

Figure 5-9 Trajectory of mu-metal motion for calibration of magnetic measurement model. (a) 3-D view. (b) *xy*-view. (c) *xz*-view.

Since the mu-metal motion is in 3-D space and magnetic field measurements are also in three orthogonal directions, it is difficult to show the magnetic field response in one figure. Therefore, several slices of sample planes are selected to show the magnetic field response as shown in Figure 5-10. Three vertical planes (parallel to *yz*-plane) and three horizontal planes (parallel to *xy*-plane) are evenly selected in the ROI with a spacing of 30 mm. For each sample plane, all three components of the magnetic field measurements are illustrated in Figure 5-11 and Figure 5-12. Magnetic field variation on both horizontal and vertical plans provides a general picture of mu-metal induced magnetic response in the whole working region. Since the locations of two magnetic sensors are symmetric to the

xz-plane, only the magnetic measurements from the sensor at [-200, -30, -35] (mm) is depicted.

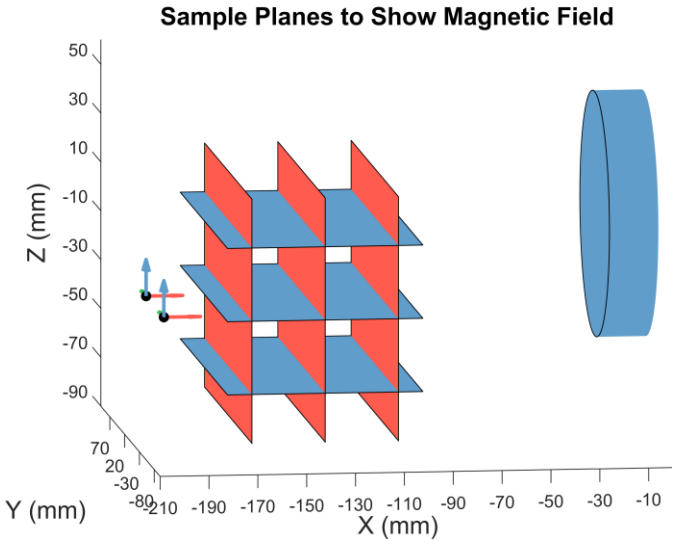

Figure 5-10 Sample planes to show magnetic field response to the mu-metal motion.

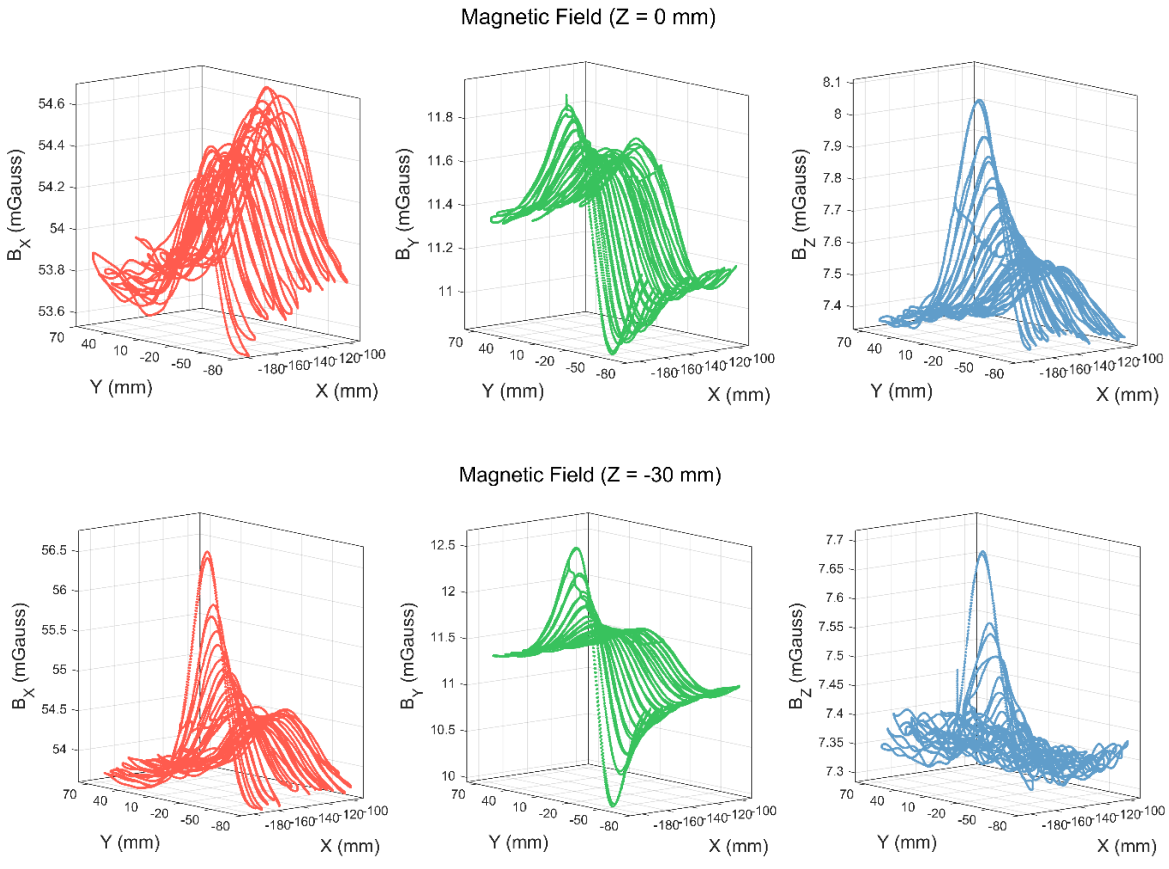

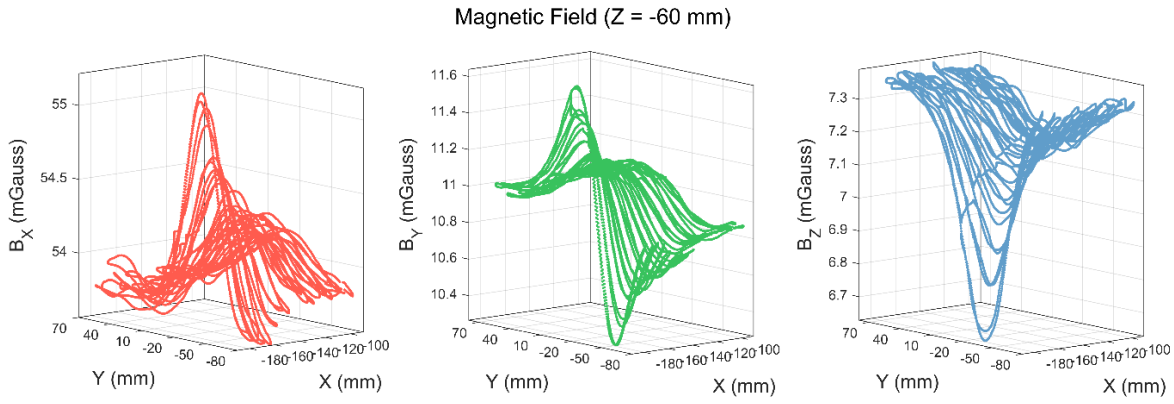

Figure 5-11 Magnetic field response on horizontal planes (parallel to *xy*-plane).

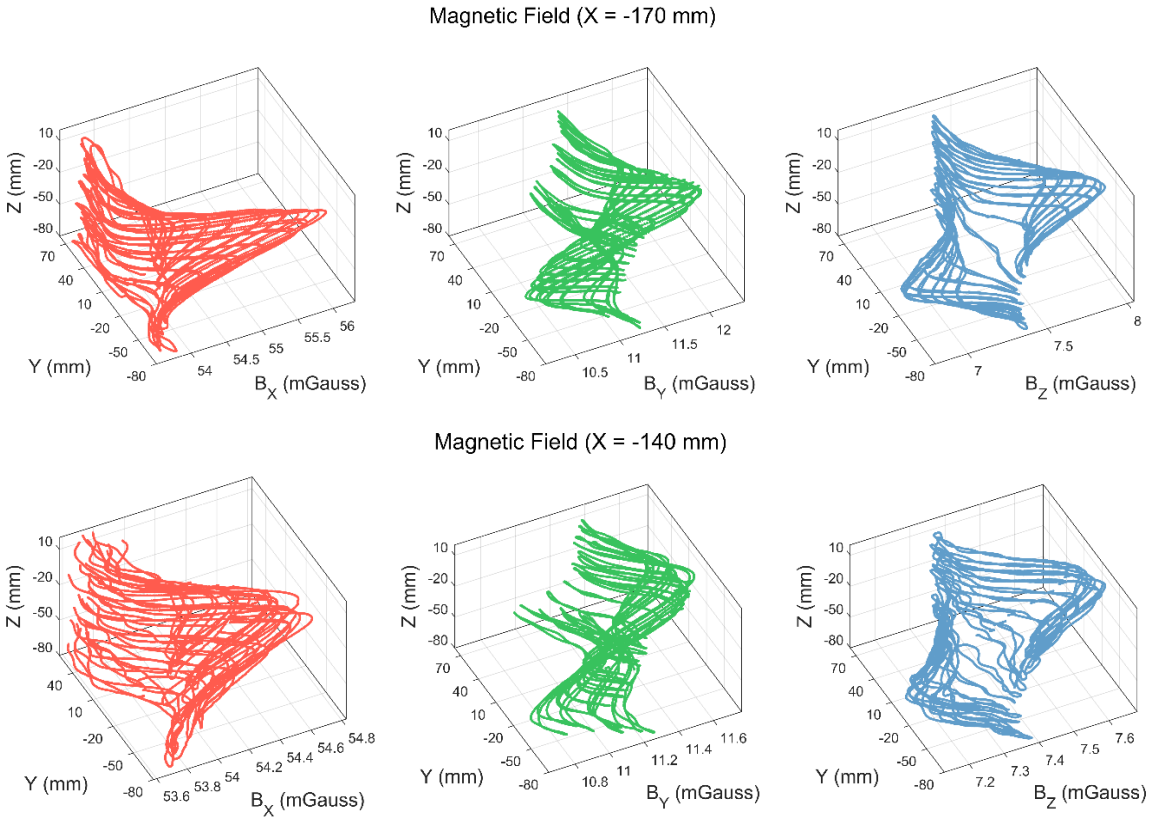

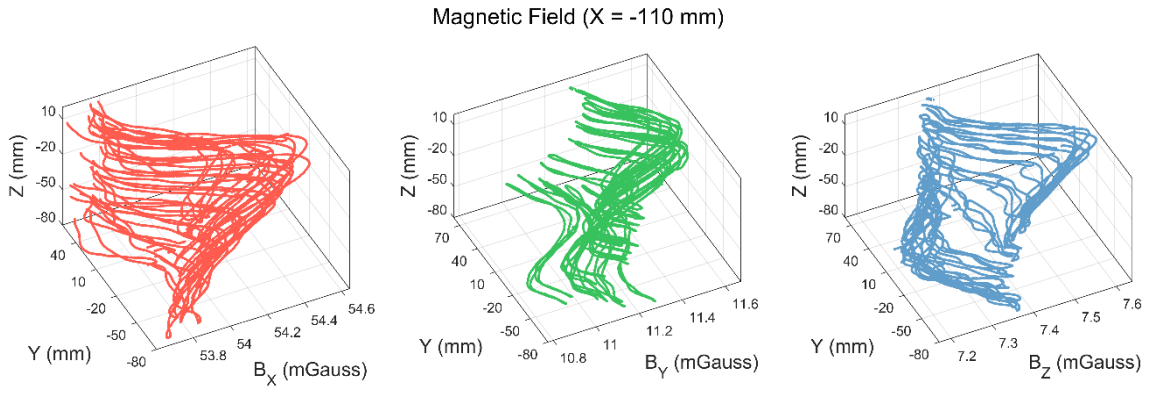

Figure 5-12 Magnetic field response on vertical planes (parallel to *yz*-plane).

For the magnetic field response on horizontal planes, B_y takes the same form for all three horizontal sample planes at z = 0, z = -30, and z = -60 mm. Along y-axis, B_y varies in a sinusoidal-wave trend. Along x-axis, B_y monotonically increases for the region with y < -30 mm, and decreases for the region with y > -30 mm. The transition point at y = -30 mm is exactly the location of the magnetic sensor. B_x varies in a single-peak pattern along y-axis for all three horizontal planes. However, B_x monotonically increases along x-axis on the plane z = 0 mm, and decreases along x-axis on the plane z = -30 mm and z = -60 mm. on the plane z = 0 mm, B_z varies in a single-peak pattern along y-axis, and decreases monotonically along x-axis. The variation of B_z on the plane z = -60 mm is in the opposite trend of that on the plane z = 0 mm, with the single-valley pattern along y-axis and monotonic increase along x-axis. The variation of B_z on the plane z = -30 mm is only significant in the region near the magnetic sensor and it is flooded with noise away from the sensor.

The response of three magnetic field components are almost in the same pattern for all three vertical planes. The variation of B_x is in the single-peak pattern along both y- and z-axis. Both B_y and B_z shows one peak and one valley. The peak and valley of B_y are distributed along y-axis while the peak and valley of B_z are distributed along z-axis. It is also observed that the magnitude of magnetic field response for B_x, B_y, and B_z decreases as the mu-metal moves far away from magnetic sensors along x-axis.

5.4.3 Position Estimation of Robot Insertion

To achieve ultrasound imaging of the heart, the TEE probe is inserted through the esophagus and the ultrasound transducer is controlled and maneuvered to have an optimal view of the heart. In this section, experiments are performed to test the position estimation performance of the mu-metal based 3-D positioning system for the motion of robot insertion. Experiments involving robot maneuver are shown in the next section.

Three trajectories of robot insertion along *y*-axis at x = -165 mm, x = -155 mm, and x = -145 mm are experimentally tested. Each trajectory is approximately a line with a length of about 80 mm. Two methods of position estimation, i.e. direction position prediction using ANN (ANN) and particle filter with ANN measurement model (PF-ANN), are compared. The position estimation results using the two methods are shown Figure 5-13 to Figure 5-18. For each case, 3-D view, *xy* view and *yz* view are presented and an error plot is shown with position errors in *x*-, y-, and z-axis and the total Euclidean error (i.e. $e_P = \sqrt{e_X^2 + e_Y^2 + e_Z^2}$).

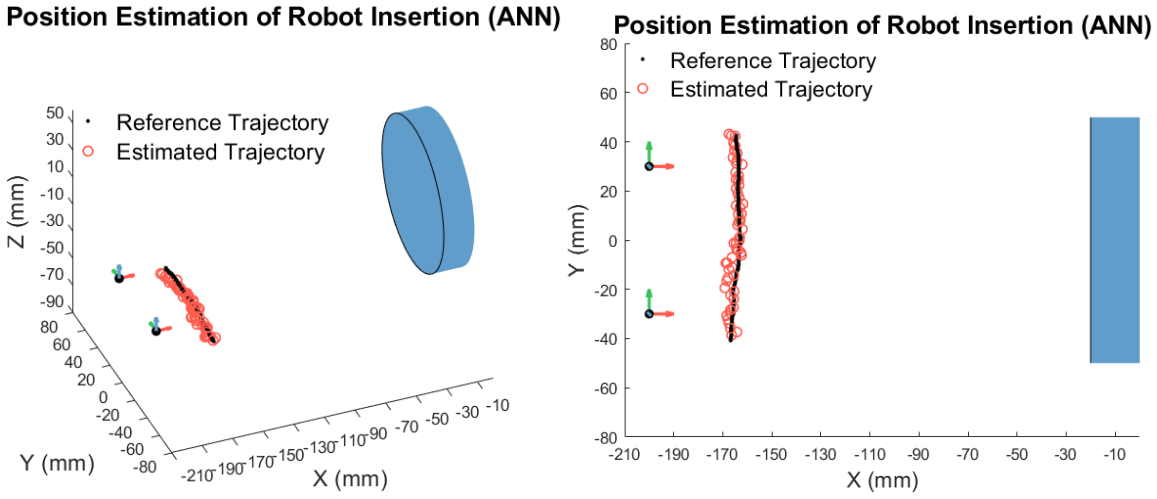

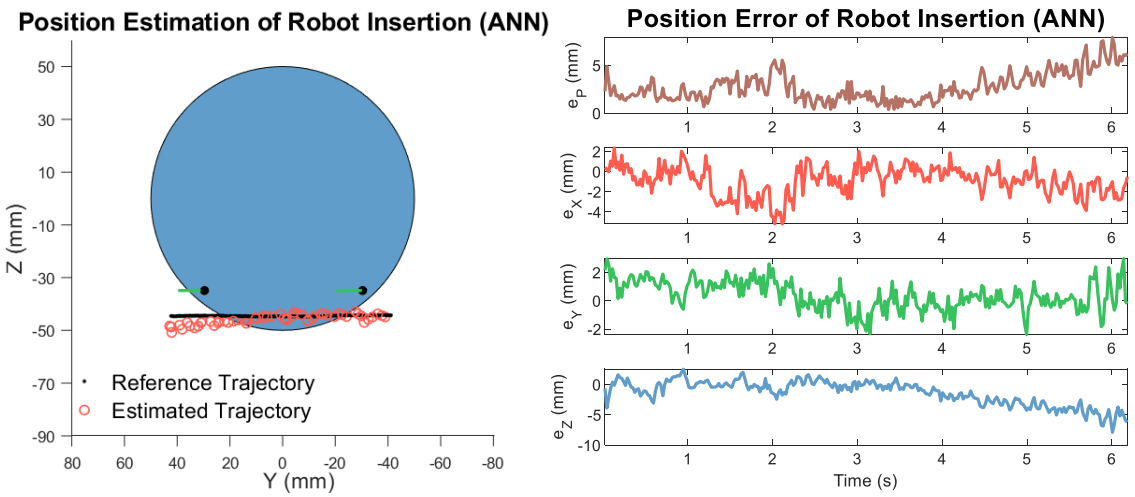

Figure 5-13 Position estimation for robot insertion using ANN at x = -165 mm.

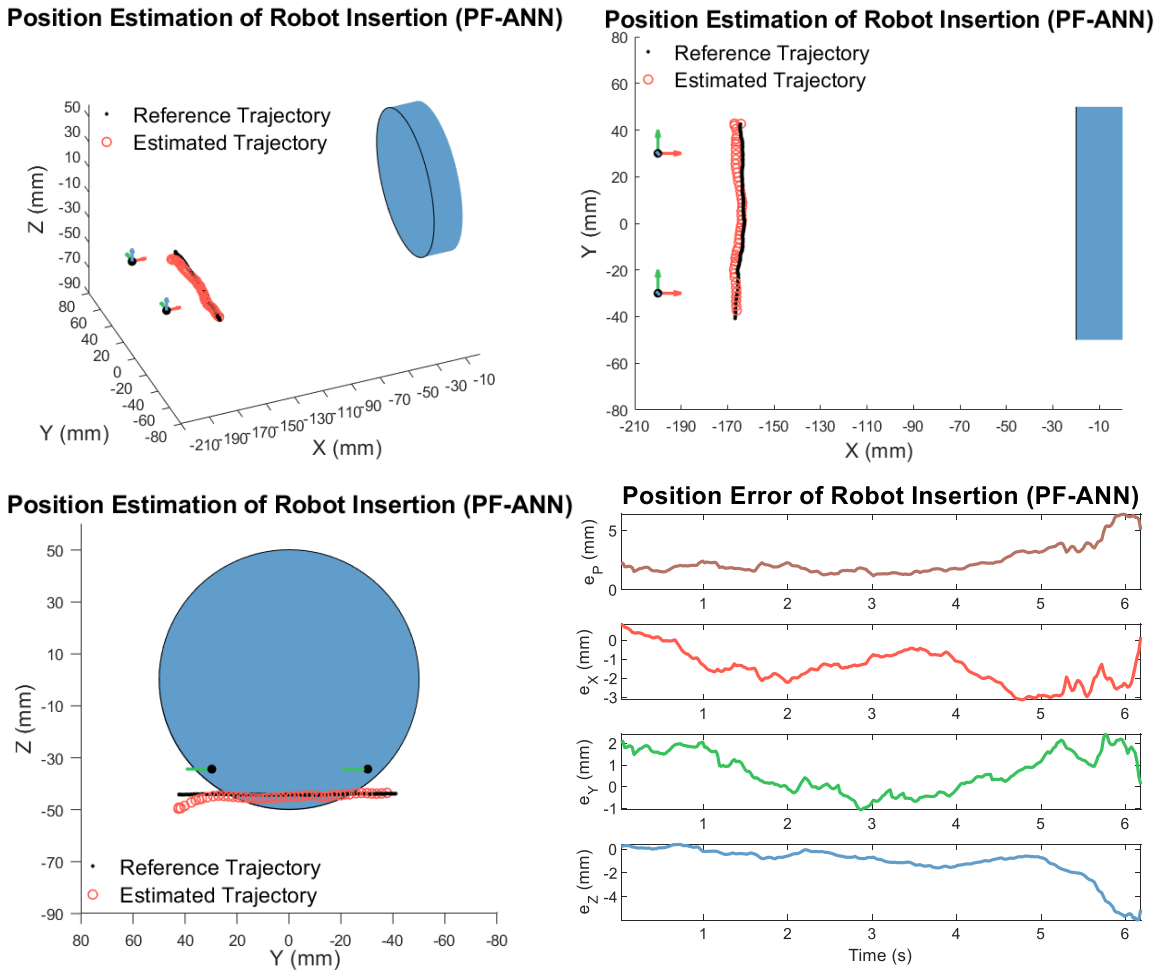

Figure 5-14 Position estimation for robot insertion using PF-ANN at x = -165 mm.

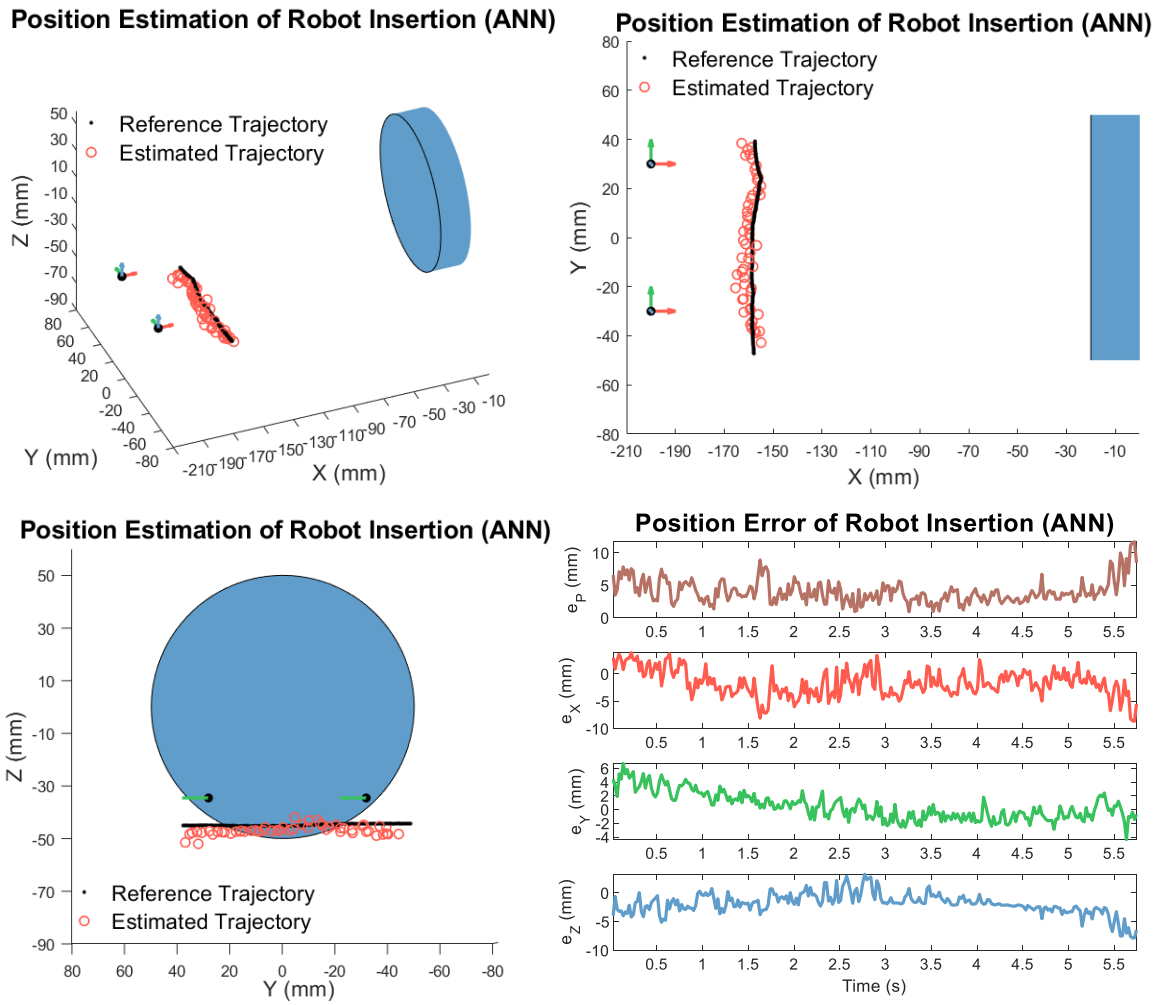

Figure 5-15 Position estimation for robot insertion using ANN at x = -155 mm.

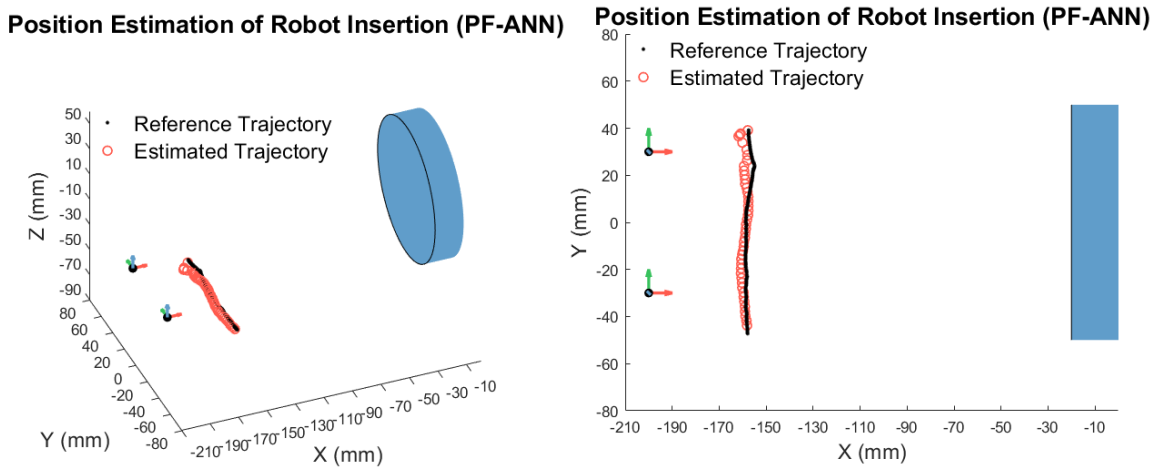

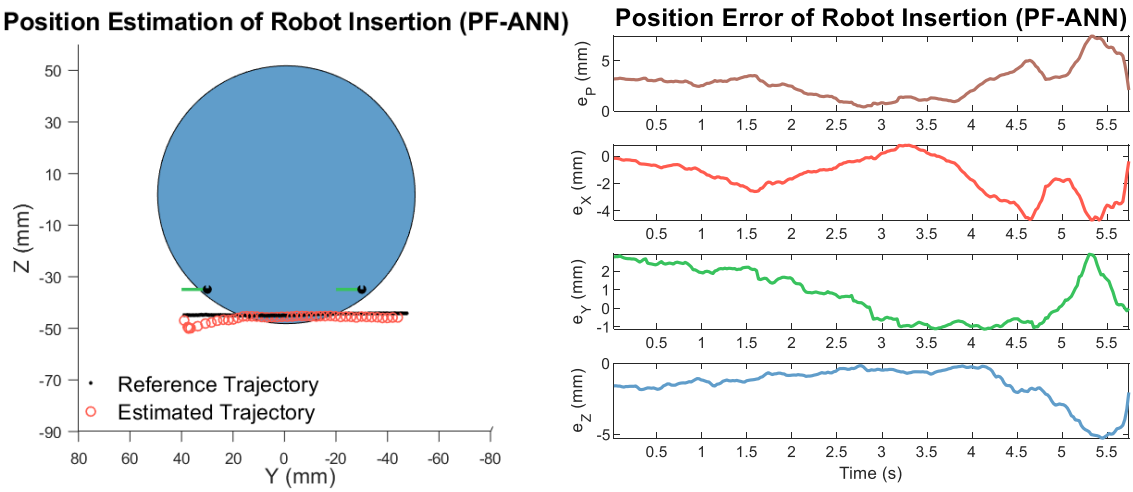

Figure 5-16 Position estimation for robot insertion using PF-ANN at x = -155 mm.

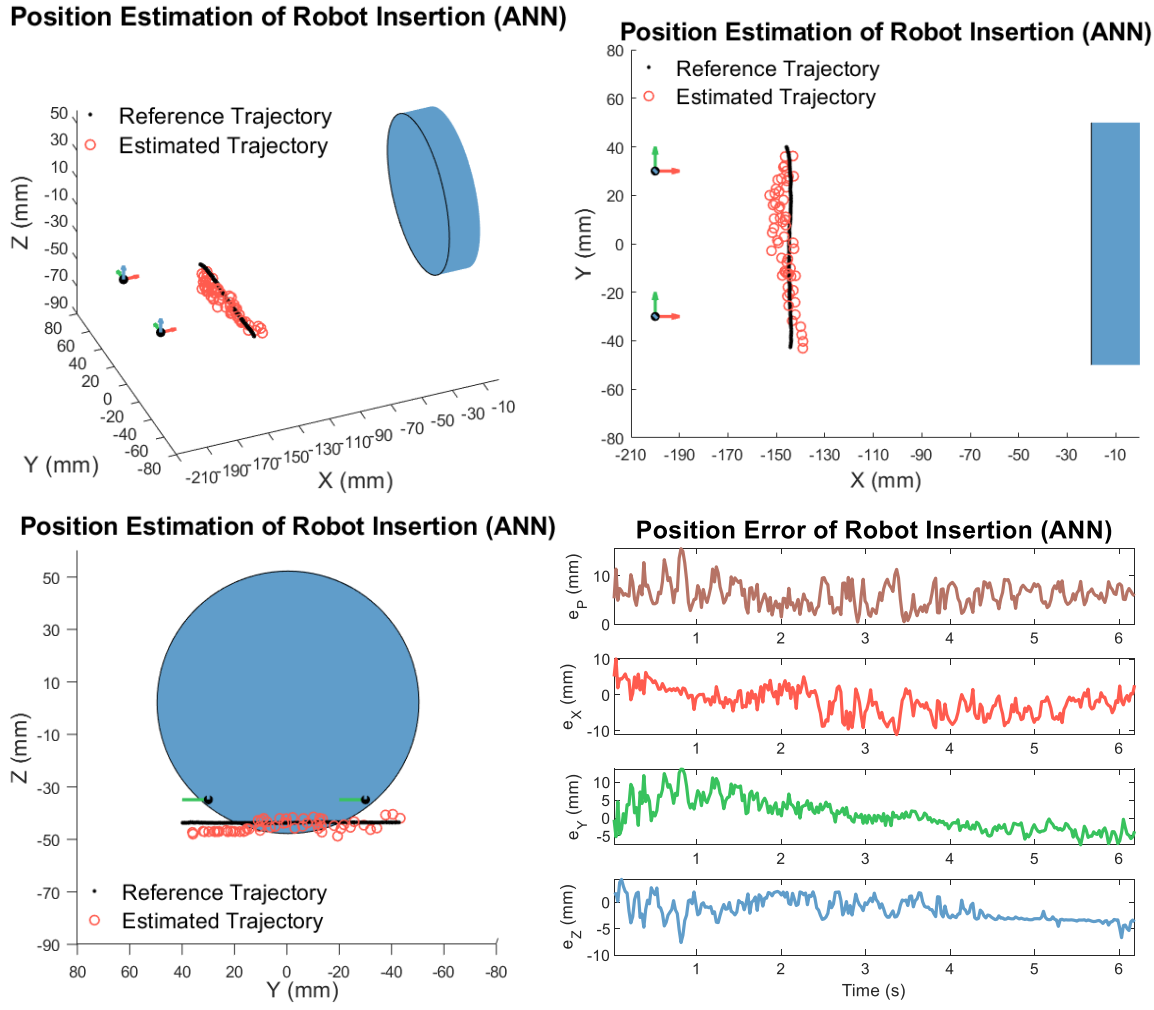

Figure 5-17 Position estimation for robot insertion using ANN at x = -145 mm.

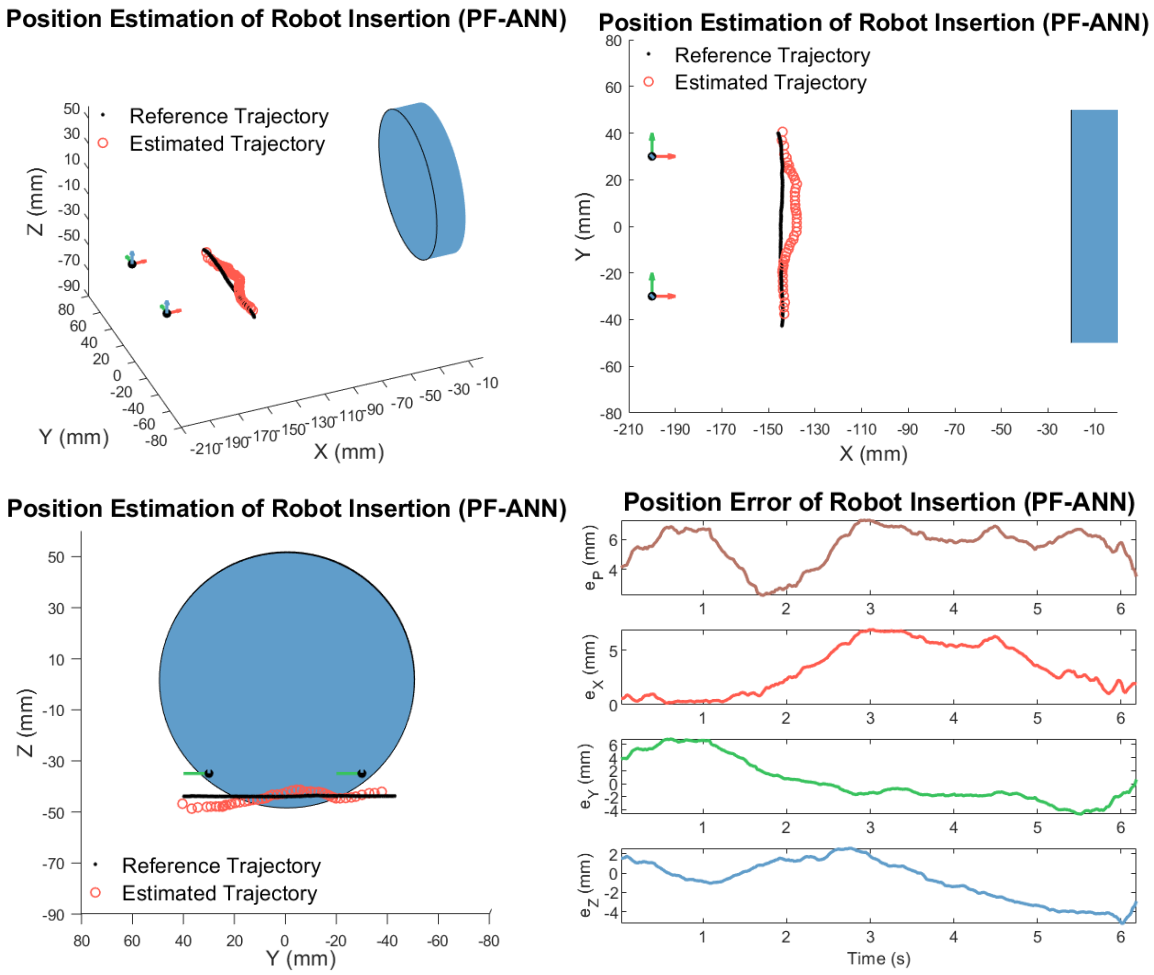

Figure 5-18 Position estimation for robot insertion using PF-ANN at x = -145 mm.

It is observed that the estimated position generally follows the reference true position well for all cases. The position estimation error become larger as the mu-metal moves in the region further from the magnetic sensors due to the impaired magnetic sensitivity as shown in Figure 5-11. Fusion of a constant-velocity kinematic model using a particle filter effectively suppresses the measurement noise, resulting in smoother position estimates. The error statistics are summarized in Table 5-1 and plotted in Figure 5-19. For position estimation using direct ANN prediction, both the maximum error and RMS error is nearly doubled when the x-axis position of robot insertion changes from -165 mm to -145 mm. For position estimation using PF-ANN, the maximum error is limited to the level of about 7 mm even at x = -145 mm. The RMS error of PF-ANN ranges from 2.71 mm to 5.71 mm for the three tested trajectories, which are consistently smaller than those obtained using

direct ANN prediction.

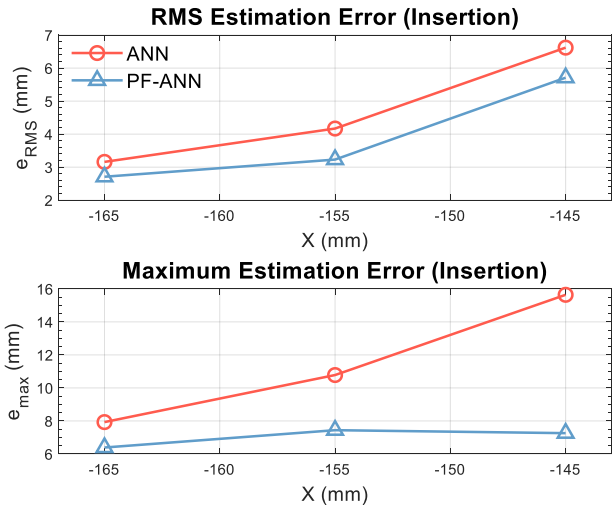

Figure 5-19 Error plot of position estimation for robot insertion.

Table 5-1 3-D position estimation error for robot insertion

Trajectory	Max. Error (mm)		RMS Error (mm)	
	ANN	PF-ANN	ANN	PF-ANN
x = -165 mm	7.93	6.39	3.16	2.71
x = -155 mm	10.78	7.44	4.17	3.23
x = -145 mm	15.64	7.26	6.62	5.71

5.4.4 Position Estimation of Robot Maneuver

In automatic trans-esophageal ultrasound imaging, the TEE probe is inserted by the robot to the rough location and then it is maneuvered to finely adjust the position such that a pre-planned optimal view of the heart is obtained. The sophisticated robot maneuver is enabled by bi-directional bending of the distal section of the probe through tendon/cable actuation. The robot maneuver of bi-directional bending in experimental validation of the mu-metal based 3-D positioning system is illustrated in Figure 5-20, where both the schematics and real pictures of the robot at the same position are shown. In schematics, the big red dots represent the joint around which the distal segment (shown as blue dashed lines) rotates. The red triangle marks the current position of the robot tip corresponding to the position shown in real pictures. In this section, pure pitch motion (vertical bending) and

pure yaw motion (horizontal bending) are implemented for experiments of 3-D position estimation, though any 3-D trajectory on a sphere can be achieved by proper control of both bending angles.

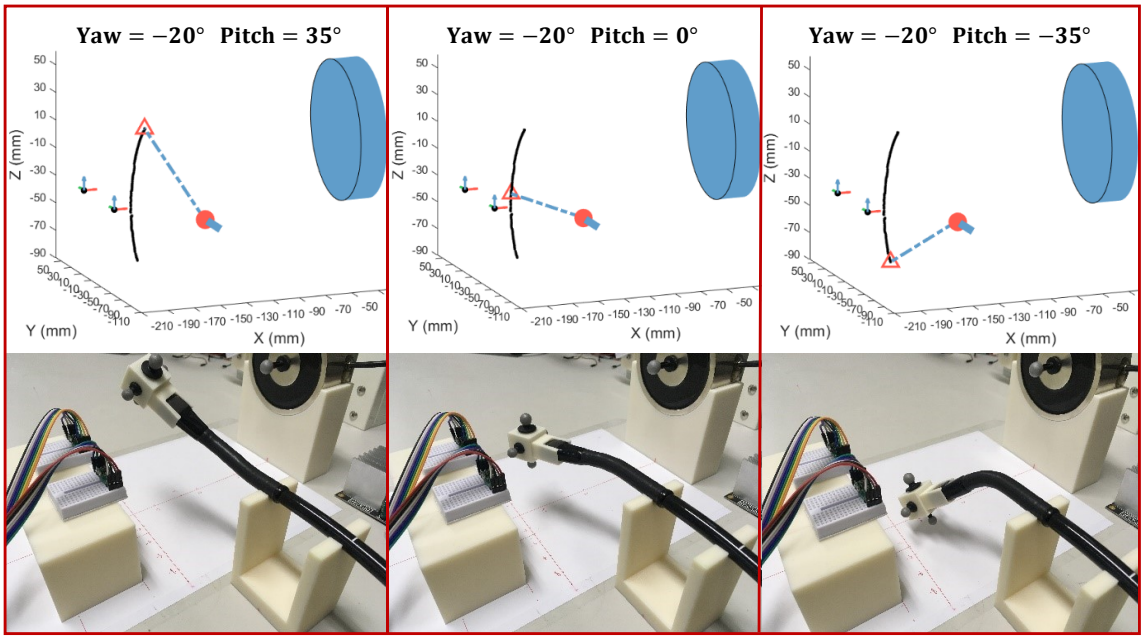

(a)

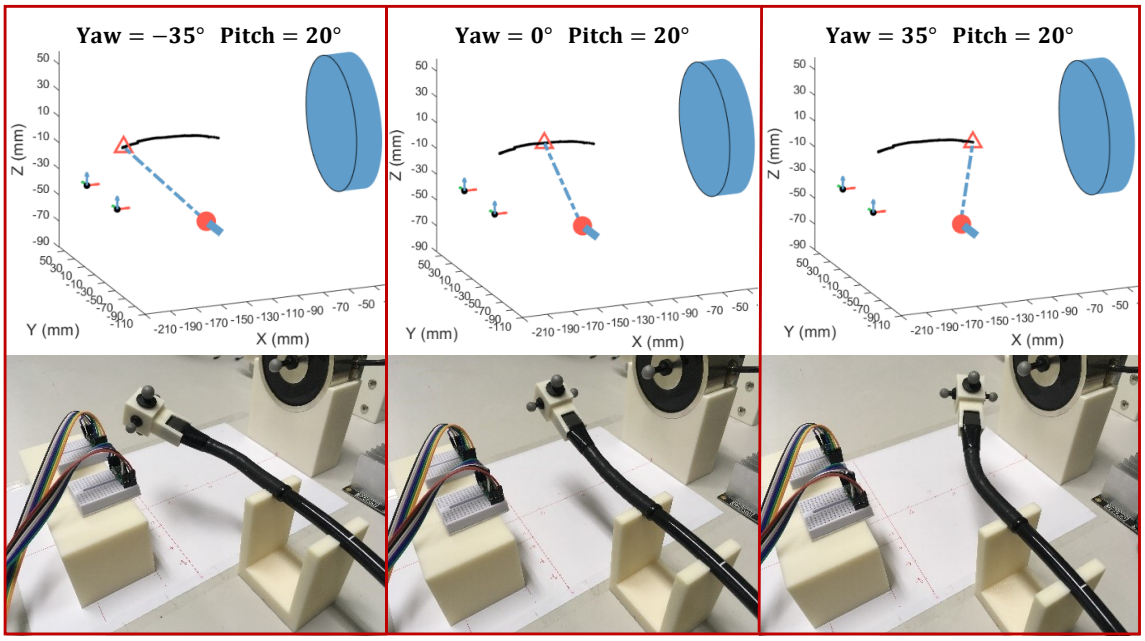

(b)

Figure 5-20 Illustration of robot maneuver. (a) Pitch motion. (b) Yaw motion.

To accommodate the bending maneuver of the robot, bending trajectories are used for calibration of the ANN measurement model as shown in Figure 5-21. It is shown that the training trajectories of pitch and yaw motion at different angles forms a partial sphere. Position estimation is also performed with a set of test trajectories of pitch and yaw motion on this partial sphere.

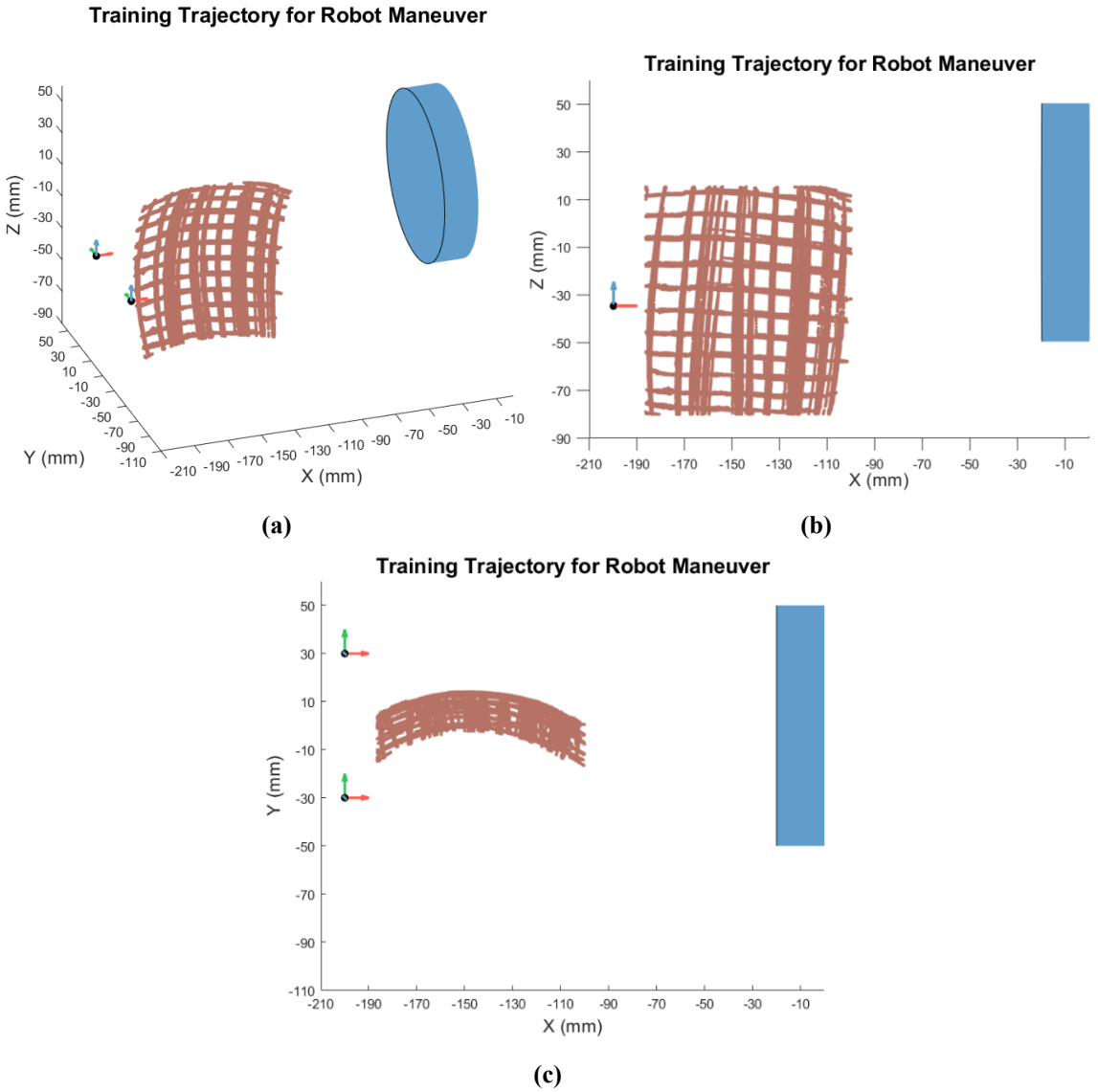

Figure 5-21 Bending trajectory for calibration of magnetic measurement model for 3-D positioning in robot maneuver. (a) 3-D view. (b) *xz*-view. (c) *xy*-view.

The position estimation for robot maneuver is also performed using both direct ANN prediction and particle filter with an ANN measurement model. The position estimation

results for the yaw motion of the robot at position z = 0 mm, z = -30 mm and z = -45 mm are shown in Figure 5-22 to Figure 5-27. For each case, a 3-D view, a *xy* view and a *xz* view are provided and the estimation error over time is plotted. Note that the yaw motion for all cases starts from the position near magnetic sensors and moves towards the electromagnet.

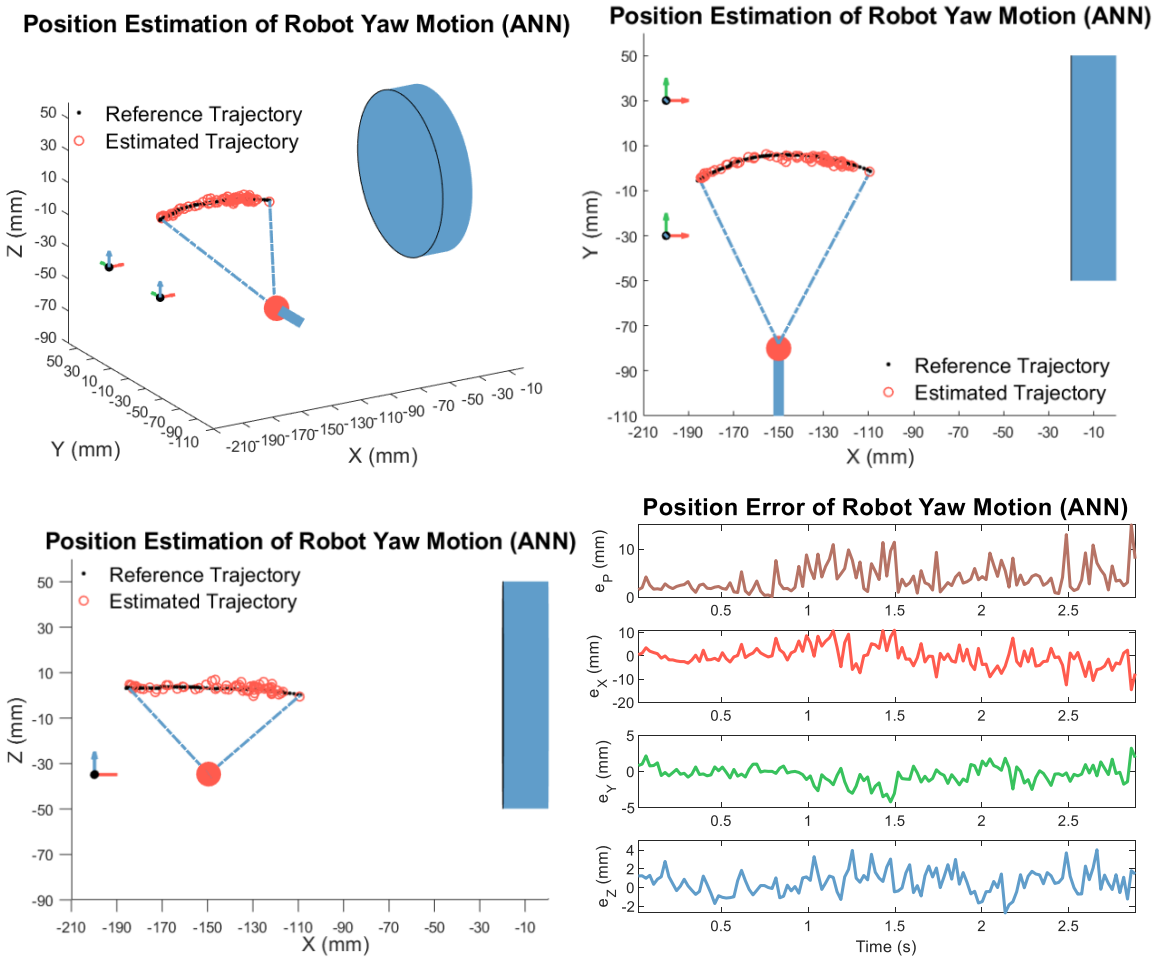

Figure 5-22 Position estimation for robot maneuver with yaw motion using ANN at z = 0 mm.

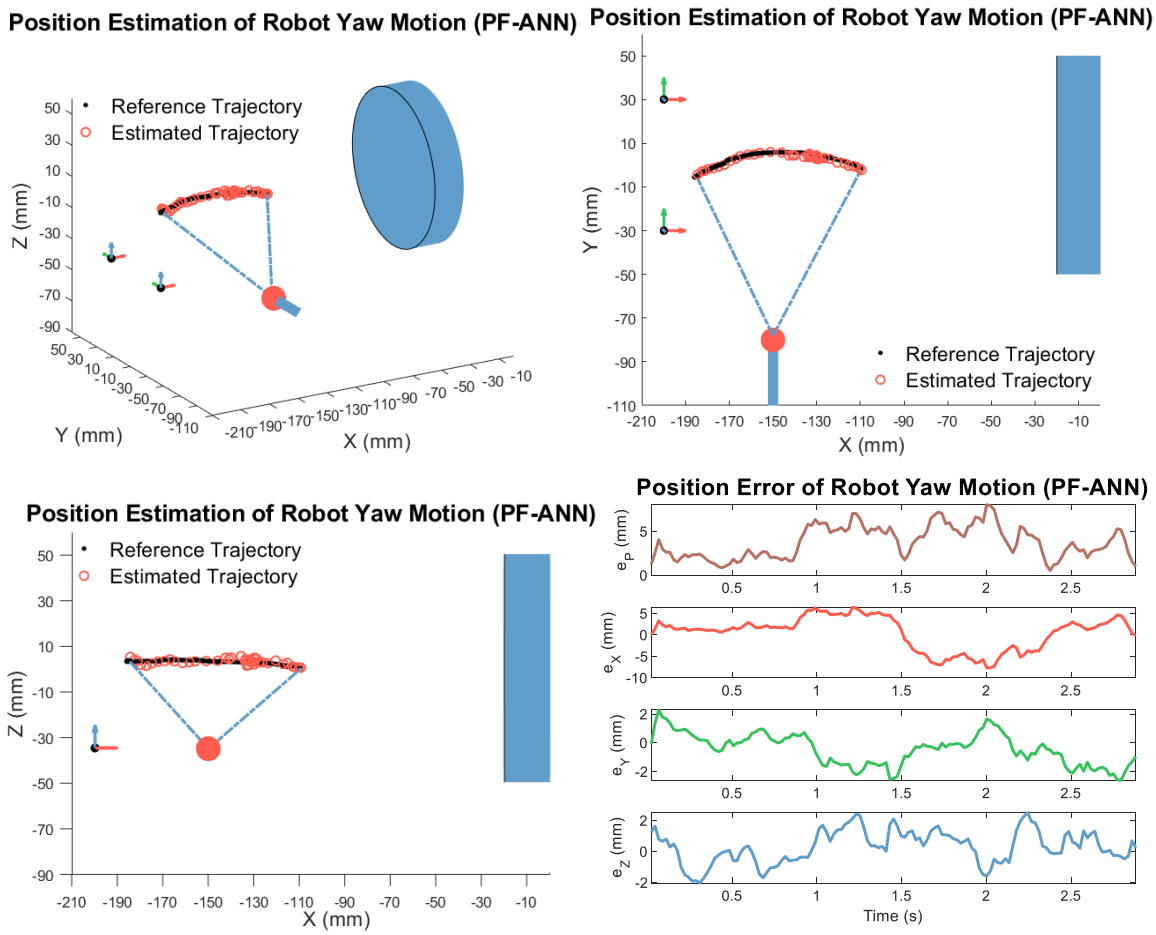

Figure 5-23 Position estimation for robot maneuver with yaw motion using PF-ANN at $z = 0$ mm.

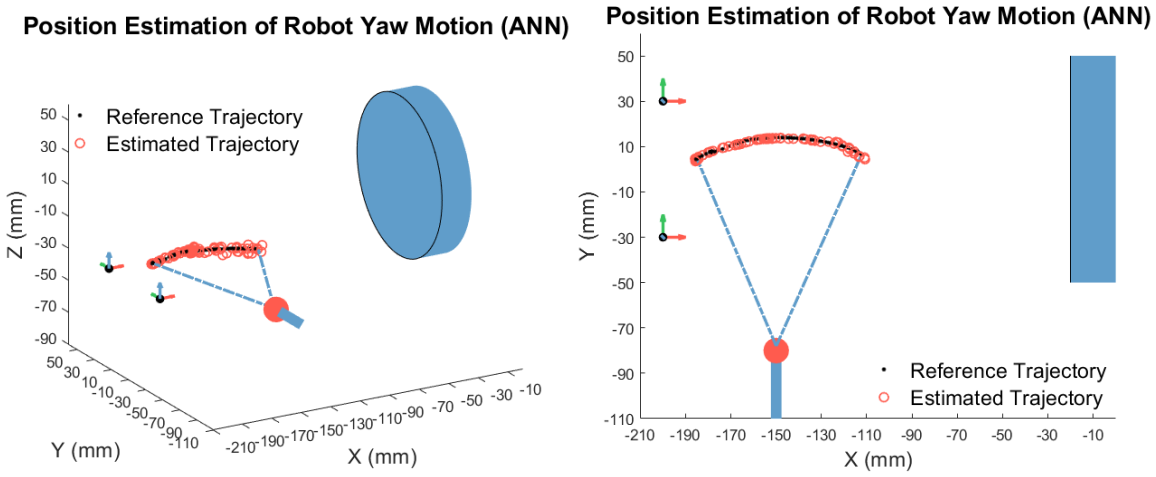

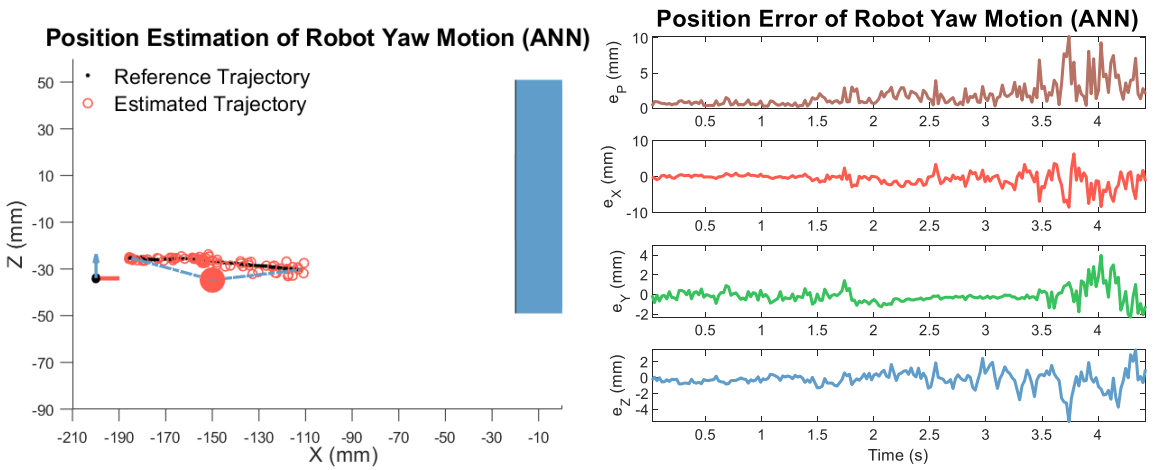

Figure 5-24 Position estimation for robot maneuver with yaw motion using ANN at z = -30 mm.

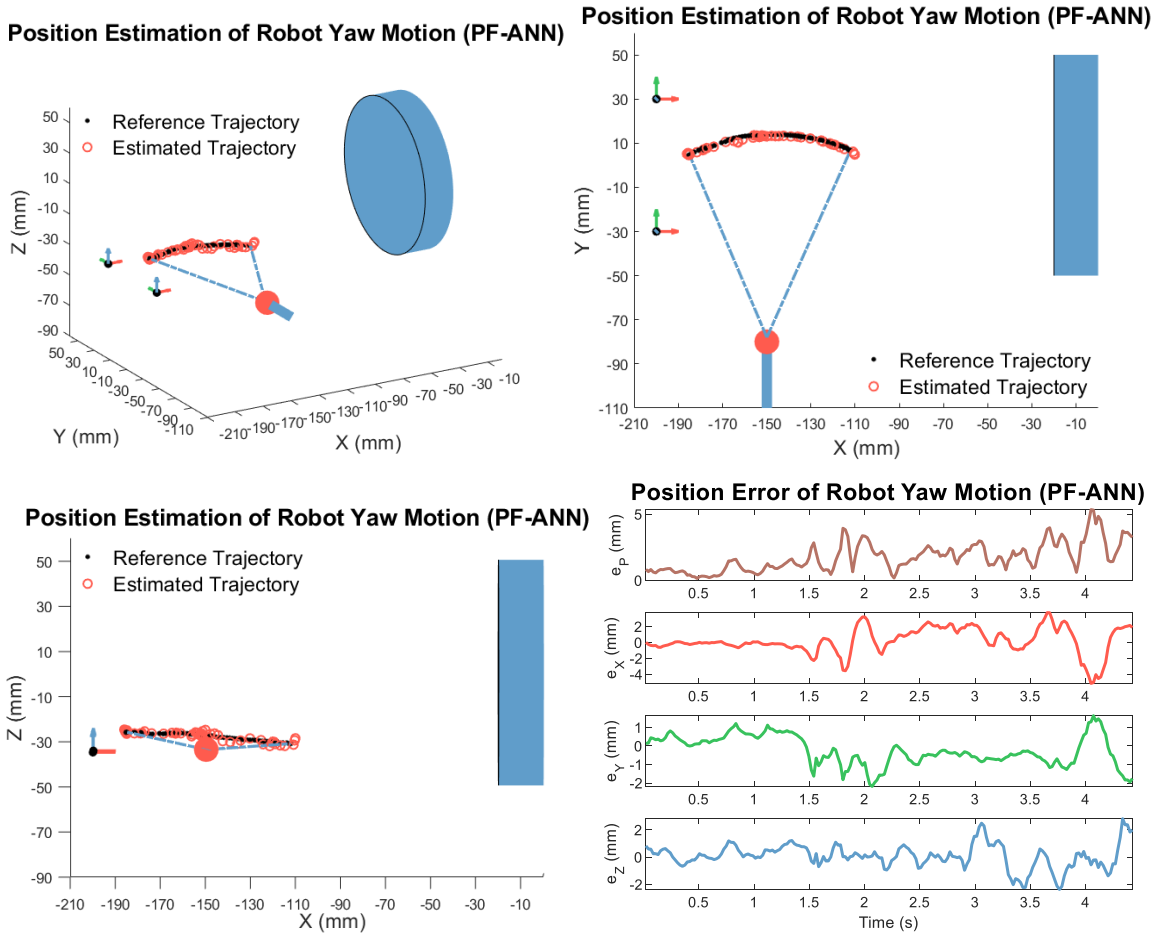

Figure 5-25 Position estimation for robot maneuver with yaw motion using PF-ANN at z = -30 mm.

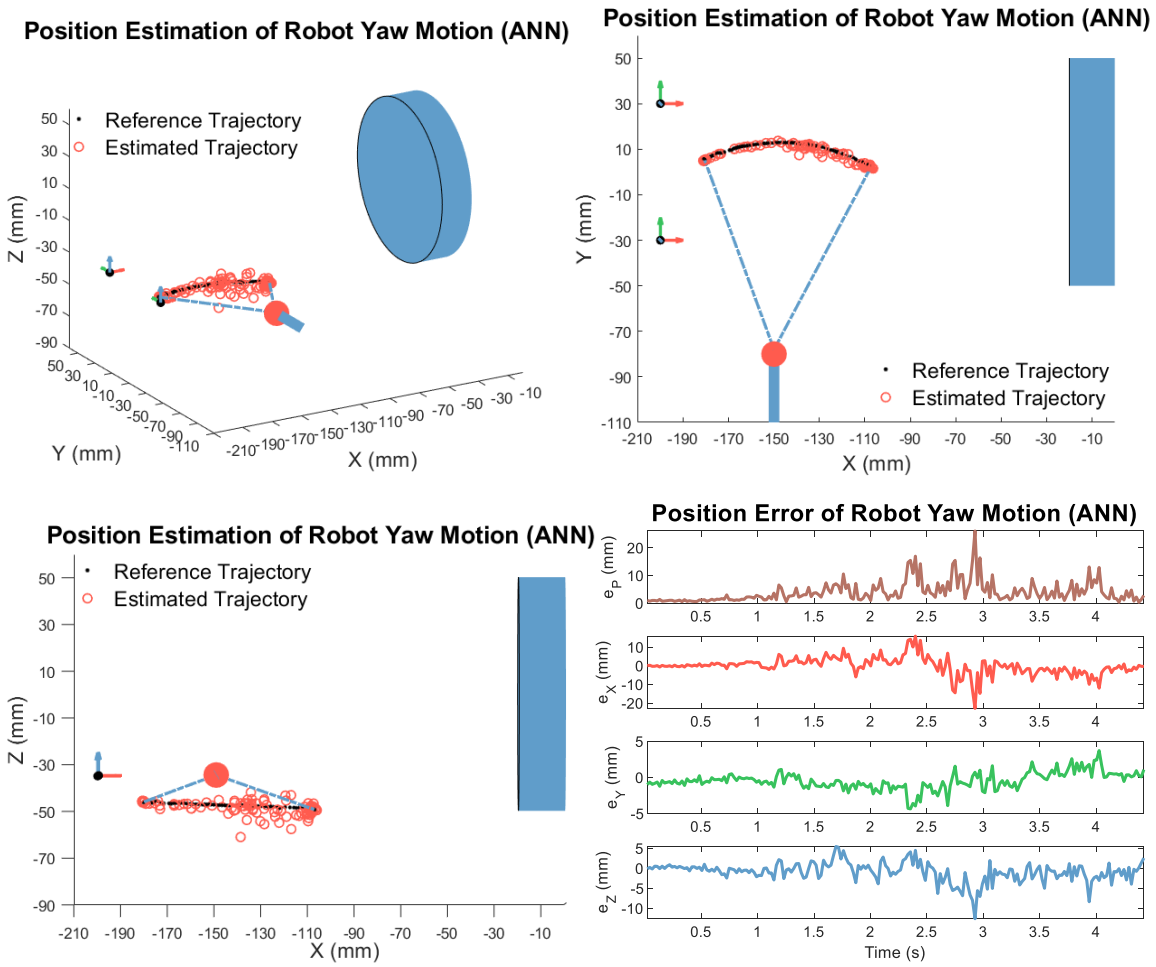

Figure 5-26 Position estimation for robot maneuver with yaw motion using ANN at z = -45 mm.

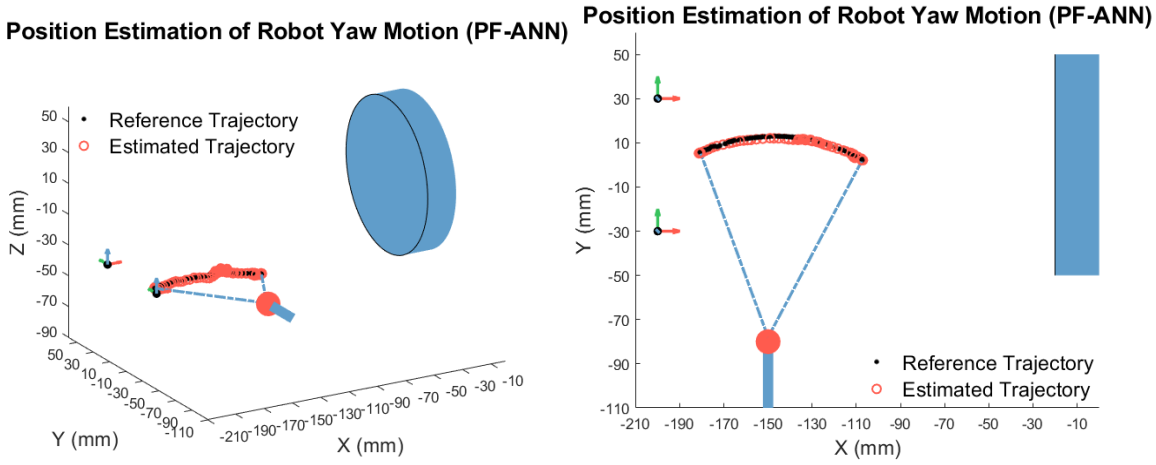

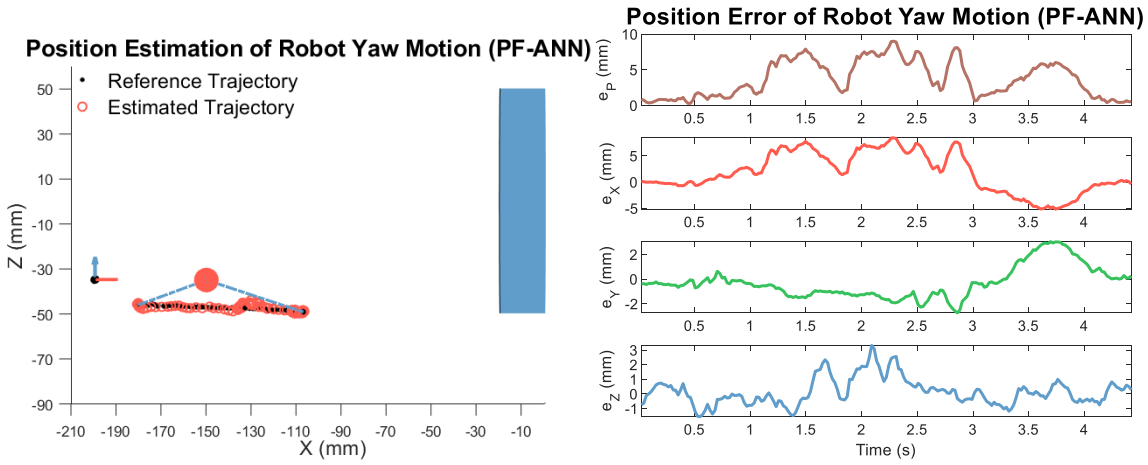

Figure 5-27 Position estimation for robot maneuver with yaw motion using PF-ANN at z = -45 mm.

It is observed that position estimates obtained from the mu-metal based 3-D positioning system generally follows the reference trajectory well for all cases. Position estimation for yaw motion at z = -30 mm gives the smallest error among the three trajectories. The particle filter successfully eliminates the error spikes and improves the estimation accuracy. For each case, the position estimation deteriorates as the robot tip bends towards the electromagnet due to decreased magnetic sensitivity in x-axis direction as illustrated in Figure 5-11. The position estimation error statistics for the robot yaw motion in the range of z = -60 ~ 10 mm are summarized in Table 5-2 and the error plot is given in Figure 5-28. It is noted that the position estimation error of PF-ANN is consistently lower than that of direct ANN prediction. Both the RMS error and maximum error increases as the robot tip moves too high or too low in z-axis direction. The RMS error of PF-ANN is below 4 mm in the range of z = -40 ~ 0 mm and the maximum error is bounded within 10 mm in the range of z = -45 ~ 10 mm, which is satisfactory for positioning of the ultrasound transducer in an automatic TEE procedure.

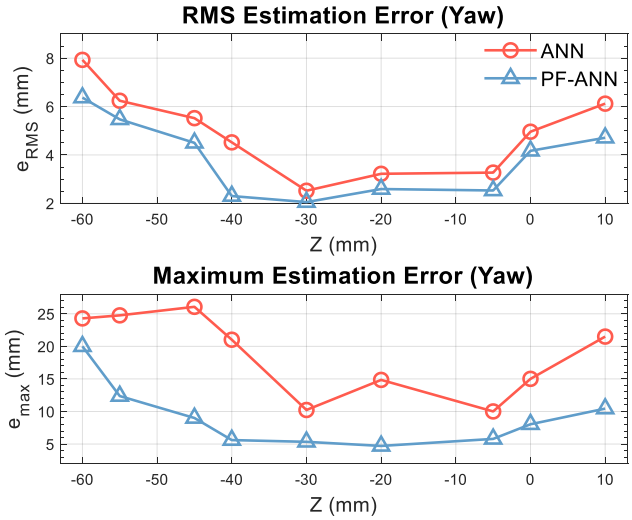

Figure 5-28 Error plot of position estimation for robot maneuver with yaw motion.

Table 5-2 3-D position estimation error for robot maneuver with yaw motion

Trajectory	Max. Error (mm)		RMS Error (mm)	
	ANN	PF-ANN	ANN	PF-ANN
z = 10 mm	21.50	10.44	6.12	4.71
z = 0 mm	15.01	8.04	4.96	4.17
z = -5 mm	10.01	5.79	3.27	2.53
z = -20 mm	14.85	4.71	3.22	2.59
z = -30 mm	10.23	5.34	2.52	2.05
z = -40 mm	21.02	5.61	4.52	2.30
z = -45 mm	26.07	9.00	5.52	4.50
z = -55 mm	24.76	12.37	6.24	5.47
z = -60 mm	24.29	20.01	7.93	6.37

The position estimation results for the pitch motion of the robot at position x = -185 mm, z = -150 mm and z = -110 mm are shown in Figure 5-29 to Figure 5-34. For each case, a 3-D view, a yz view and a xz view are provided and the estimation error over time is plotted. Note that the pitch motion for all cases is in the negative z-axis direction (i.e. top-down direction).

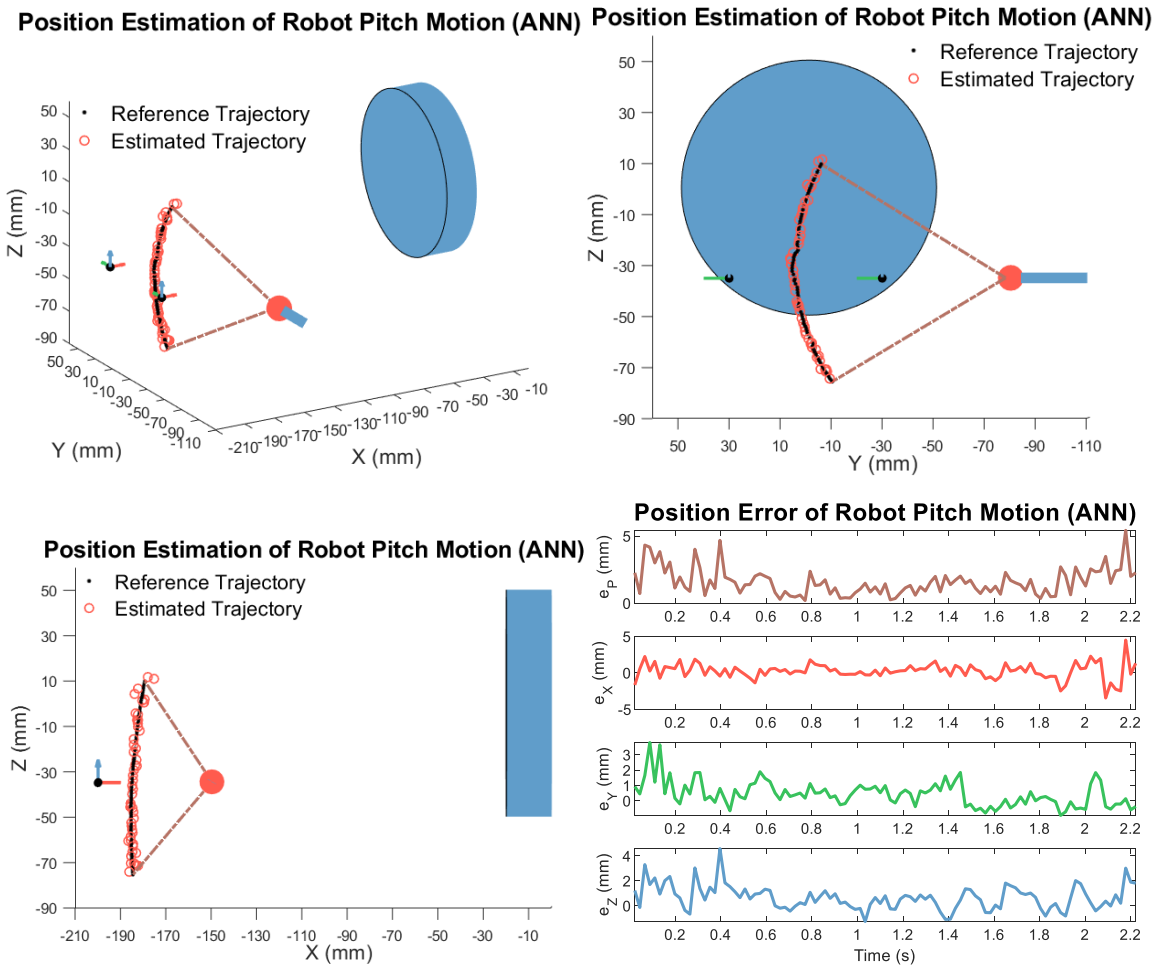

Figure 5-29 Position estimation for robot maneuver with pitch motion using ANN at x = -185 mm.

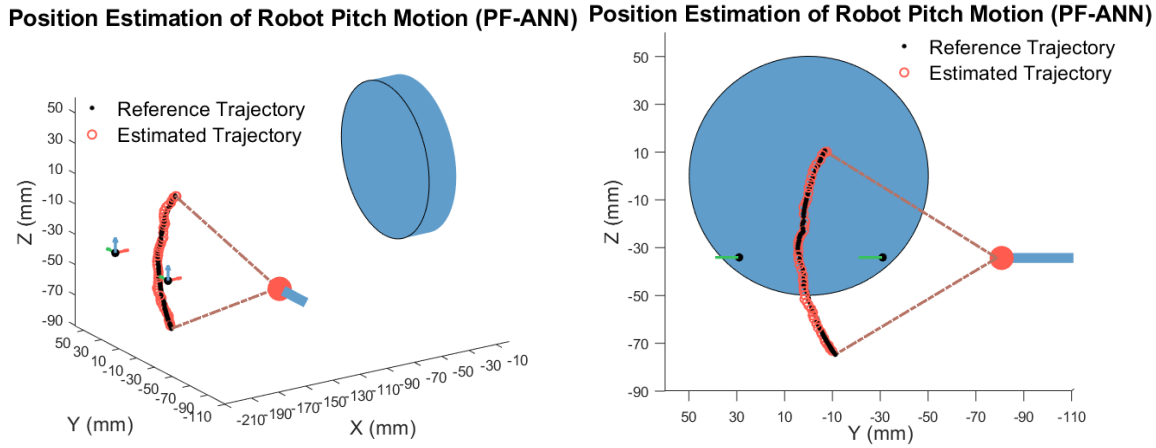

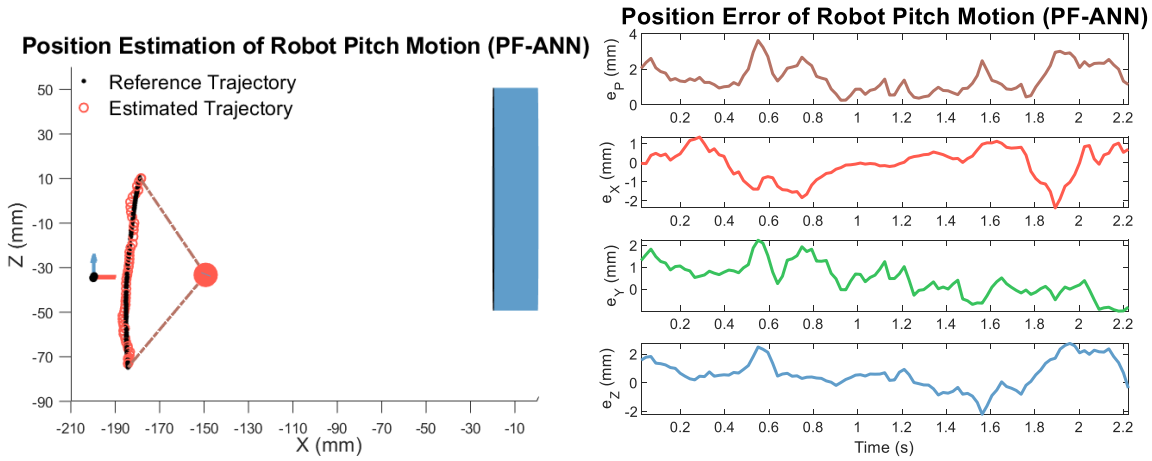

Figure 5-30 Position estimation for robot maneuver with pitch motion using PF-ANN at x = -185 mm.

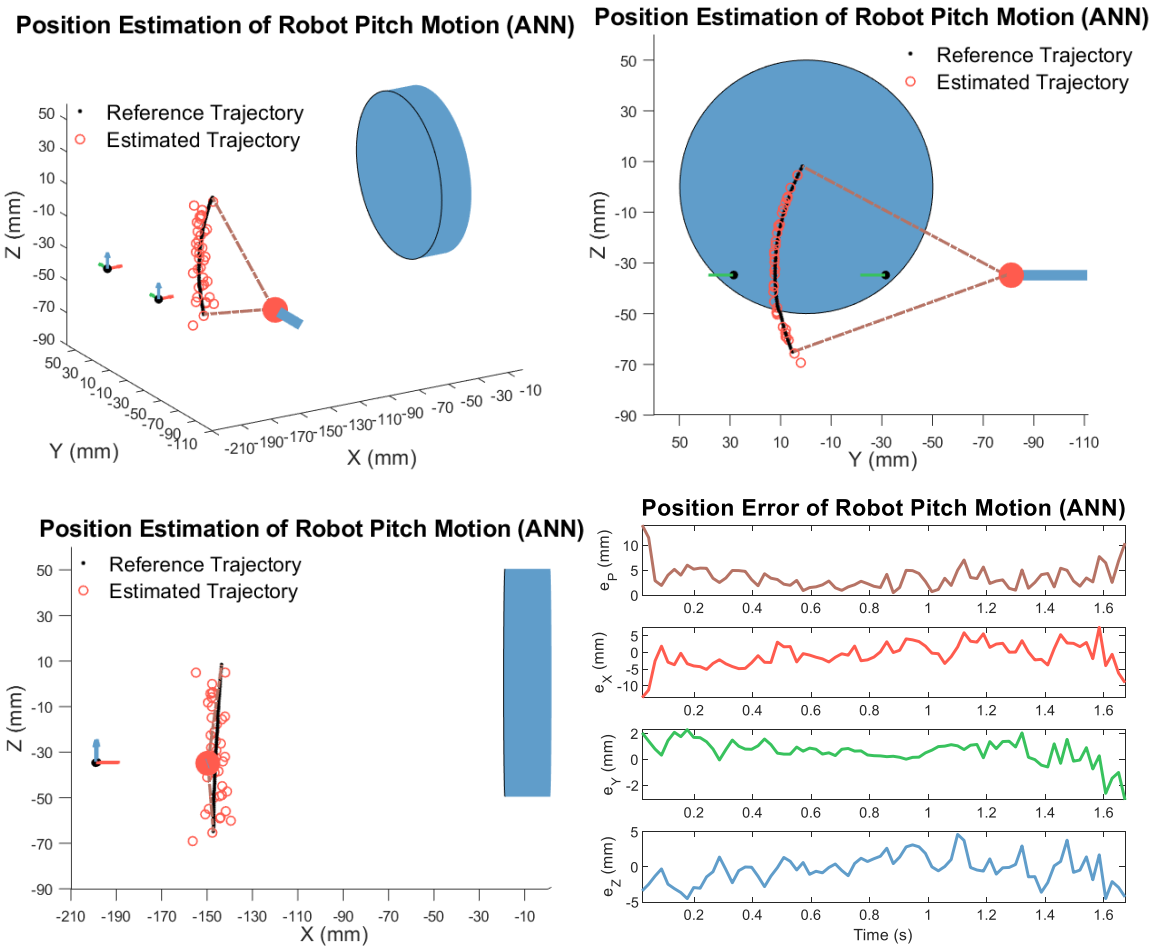

Figure 5-31 Position estimation for robot maneuver with pitch motion using ANN at x = -150 mm.

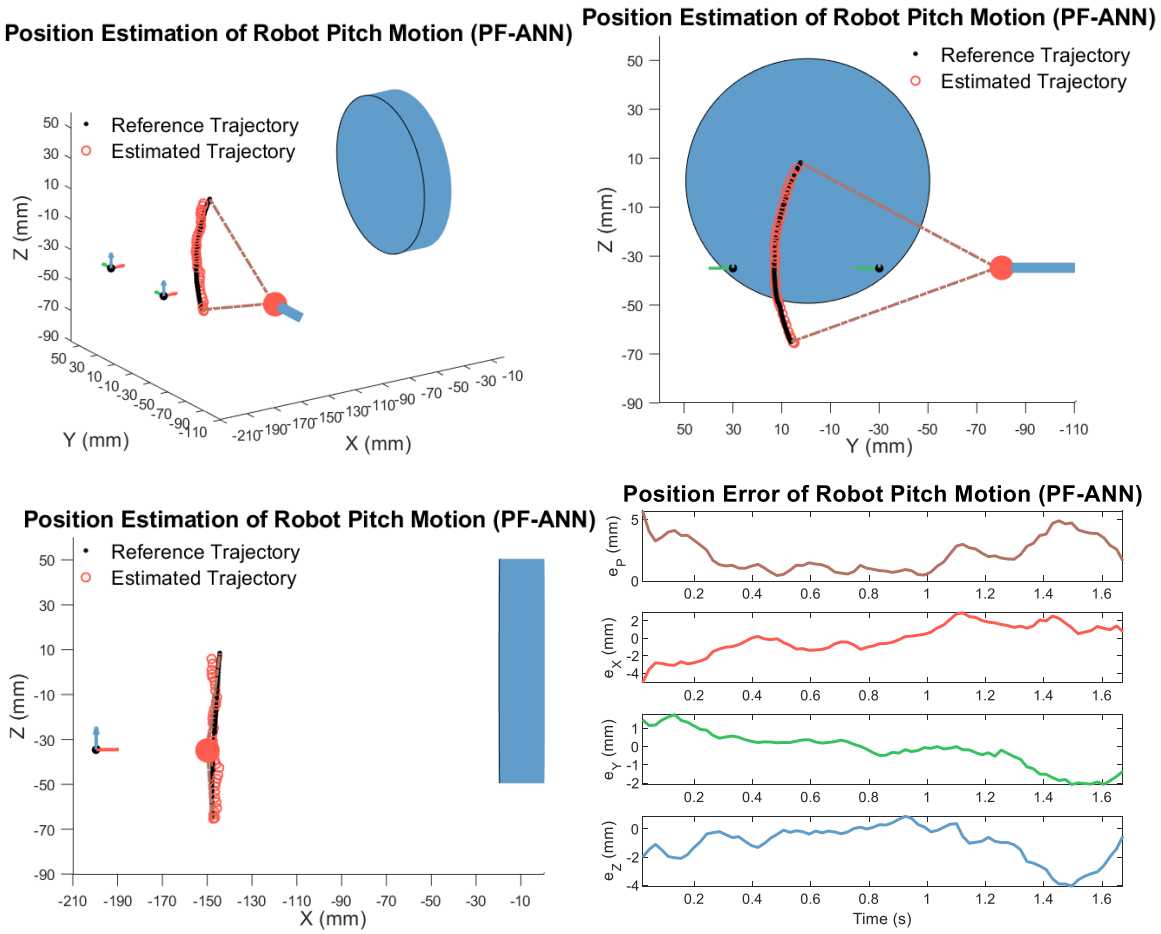

Figure 5-32 Position estimation for robot maneuver with pitch motion using PF-ANN at x = -150 mm.

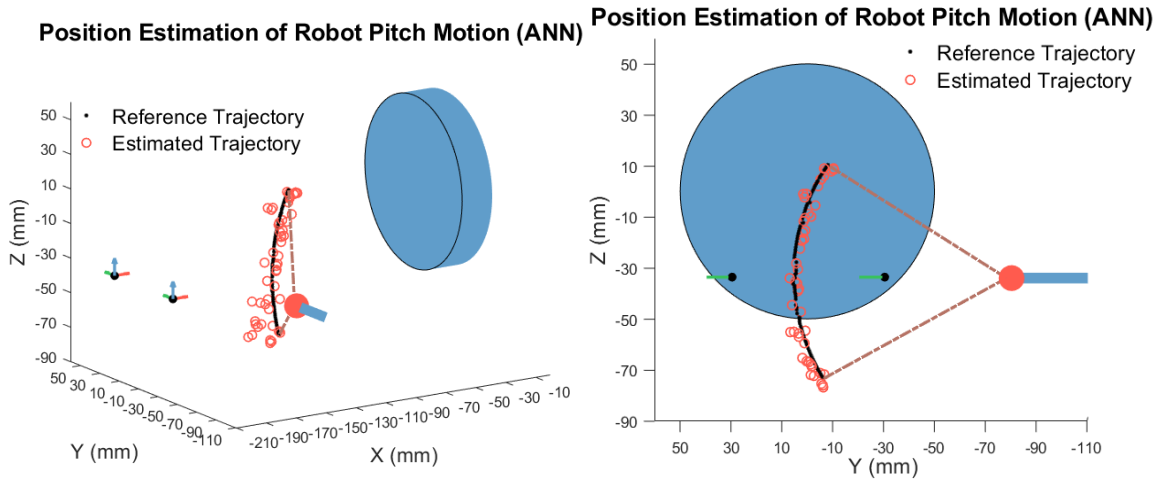

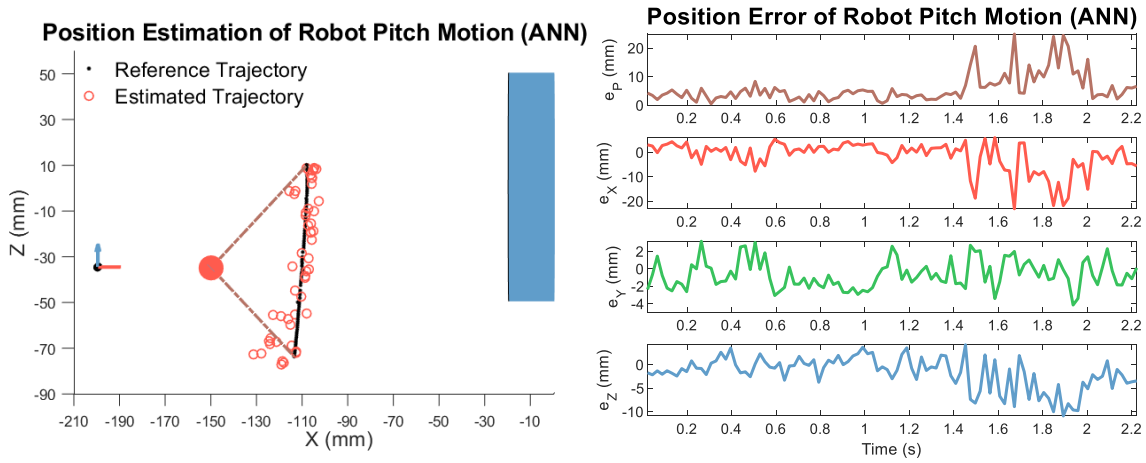

Figure 5-33 Position estimation for robot maneuver with pitch motion using ANN at x = -110 mm.

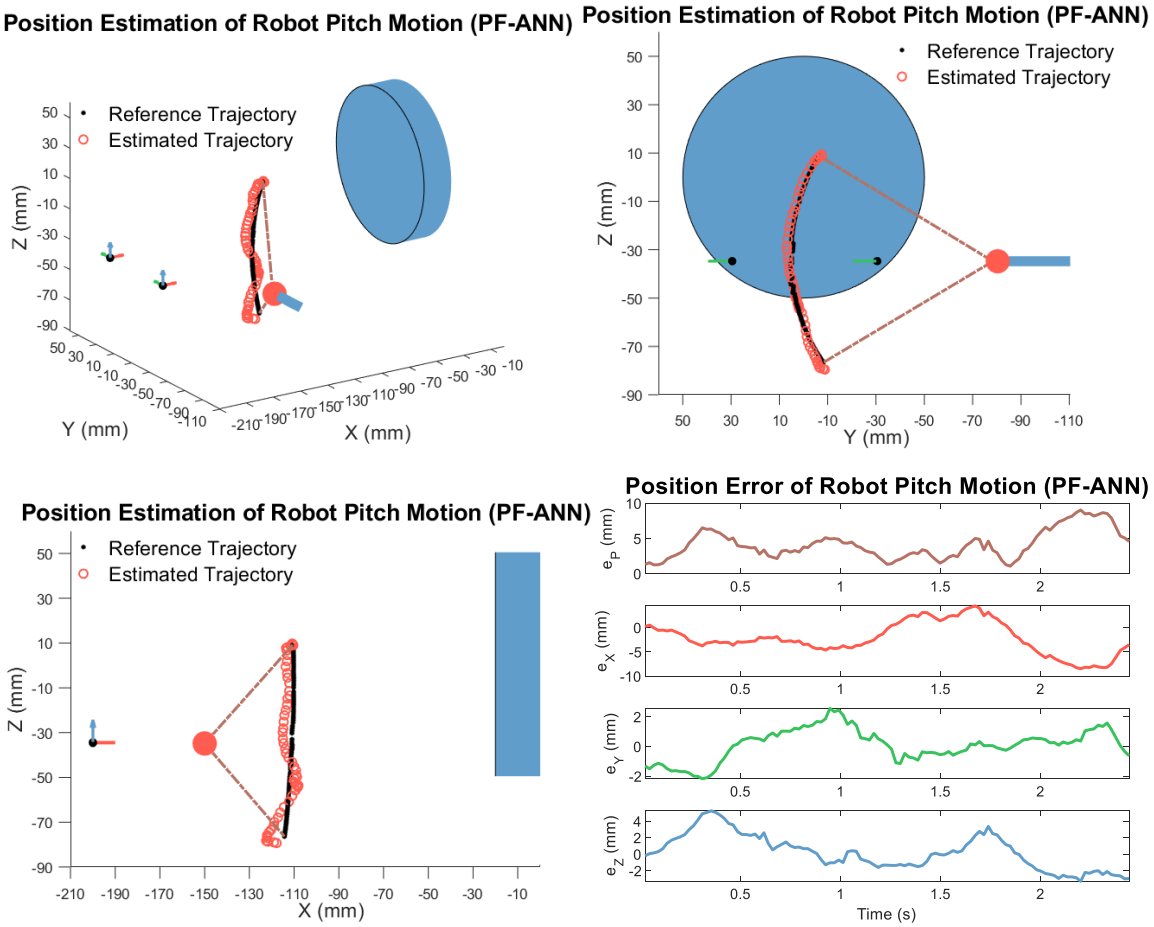

Figure 5-34 Position estimation for robot maneuver with pitch motion using PF-ANN at x = -110 mm.

The 3-D position of the robot end-effector in pitch motion is effectively estimated using

the mu-metal 3-D positioning system without large deviation or divergence. The particle filter again effectively suppresses the error spikes that appears in the direct ANN position prediction, thus reducing the maximum error of position estimation. The position error increases as the pitch motion is implemented further from magnetic sensors and this increase of error is especially significant in *x*-axis. For example, it is noted that the position error in *y*-axis and *z*-axis is much smaller than that in *x*-axis at $x = -110$ mm. This is because the magnetic sensitivity in *x*-axis decreases significantly as the mu-metal moves towards the electromagnet. This loss of magnetic sensitivity in *x*-axis in the region near the electromagnet restricts the effective region of 3-D positioning to the left-half space near magnetic sensors. The position estimation error statistics for the robot pitch motion in the range of $x = -185 \sim -100$ mm are summarized in Table 5-3Table 5-2 and the error plot is given in Figure 5-35. It is observed that both the maximum error and RMS error shows an increasing trend as the pitch motion is implemented further away from the magnetic sensors and towards the electromagnet in the positive *x*-axis direction, which can be explained by the magnetic sensitivity loss in *x*-axis in the near-electromagnet region. The position error of PF-ANN is consistently lower than that of ANN. The RMS error using PF-ANN is limited within 5 mm and the maximum error is bounded within 9 mm in the range of $x = -185 \sim -110$ mm, which meets the requirement of positioning accuracy in a robotic TEE procedure.

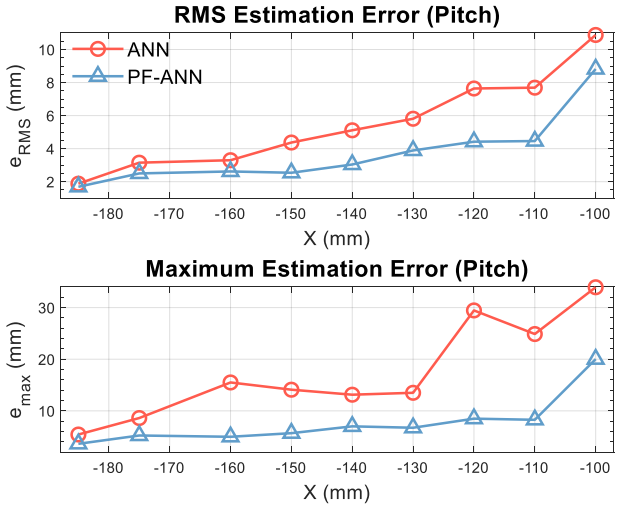

Figure 5-35 Error plot of position estimation for robot maneuver with pitch motion.

Table 5-3 3-D position estimation error for robot maneuver with pitch motion

Trajectory	Max. Error (mm)		RMS Error (mm)	
	ANN	PF-ANN	ANN	PF-ANN
x = -185 mm	5.42	3.62	1.88	1.69
x = -175 mm	8.61	5.23	3.15	2.50
x = -160 mm	15.50	4.98	3.30	2.62
x = -150 mm	14.10	5.68	4.37	2.54
x = -140 mm	13.13	7.00	5.11	3.04
x = -130 mm	13.50	6.73	5.81	3.89
x = -120 mm	29.45	8.49	7.64	4.42
x = -110 mm	24.88	8.27	7.69	4.46
x = -100 mm	33.94	20.02	10.88	8.82

5.4.5 Performance of Disturbance Rejection

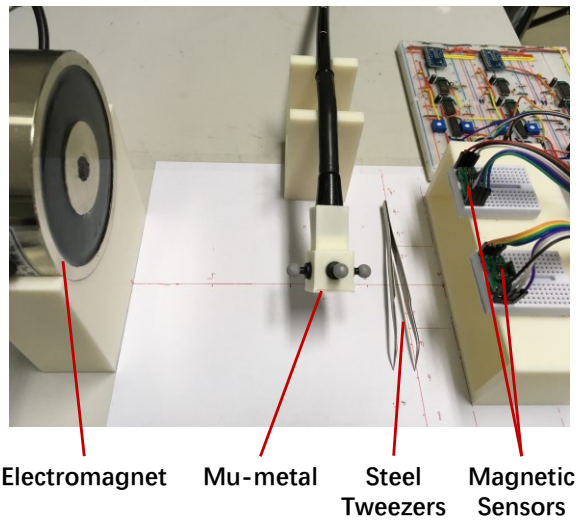

Figure 5-36 Introduction of steel tweezers as ferromagnetic disturbance.

It is claimed that the mu-metal based electromagnetic position estimation system is immune to ferromagnetic disturbance owing to the use of an alternating magnetic field at a certain high frequency generated by the electromagnet. In this section, as shown in Figure 5-36, steel tweezers are placed in the working region of the 3-D positioning system to validate the performance of ferromagnetic disturbance rejection. Figure 5-37 shows the

magnetic disturbance that the tweezers brings to the original magnetic field, where the shaded rectangle marks the time instant when the tweezers is placed in the vicinity of the magnetic sensors. The introduced magnetic field disturbance is about 22.7, 56.1, and 18.6 mGauss, in *x*-, *y*-, and *z*-axis, respectively. This disturbance is significant compared to the magnetic field variation caused by movement of mu-metal, which is under 2 mGauss in each axis as shown in Section 5.4.2.

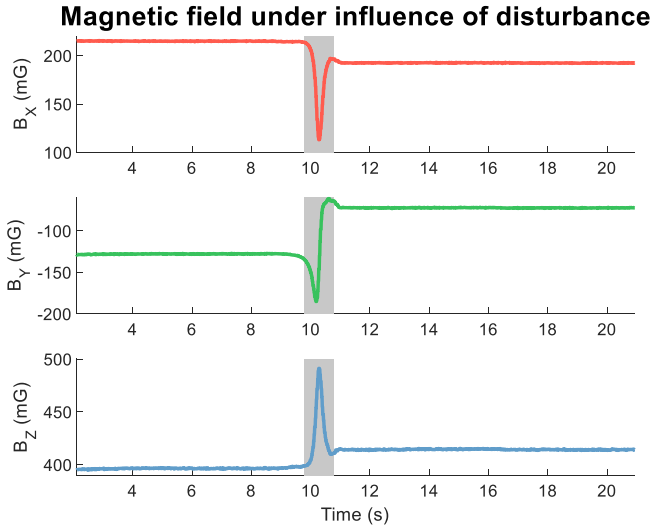

Figure 5-37 Magnetic field under ferromagnetic disturbance.

Two experiments with the same test trajectory of yaw motion, one with the disturbance and the other one without the disturbance, are conducted for comparison. The position estimation results of the two experiments are presented in Figure 5-38 and Figure 5-39. It is shown that the position is estimated well for both cases. The RMS error is 2.59 mm and 2.37 mm for the case without disturbance and with disturbance, respectively. The maximum error is 4.71 mm and 5.22 mm for the case without disturbance and with disturbance, respectively. Hence, there is no significant difference of position estimation performance no matter there is presence of a ferromagnetic object in the working region or not. Therefore, assisted by the alternating electromagnetic field and proper signal processing, the mu-metal based 3-D positioning system shows the potential for localization of flexible medical robots with steel surgical tools as sources of ferromagnetic disturbance.

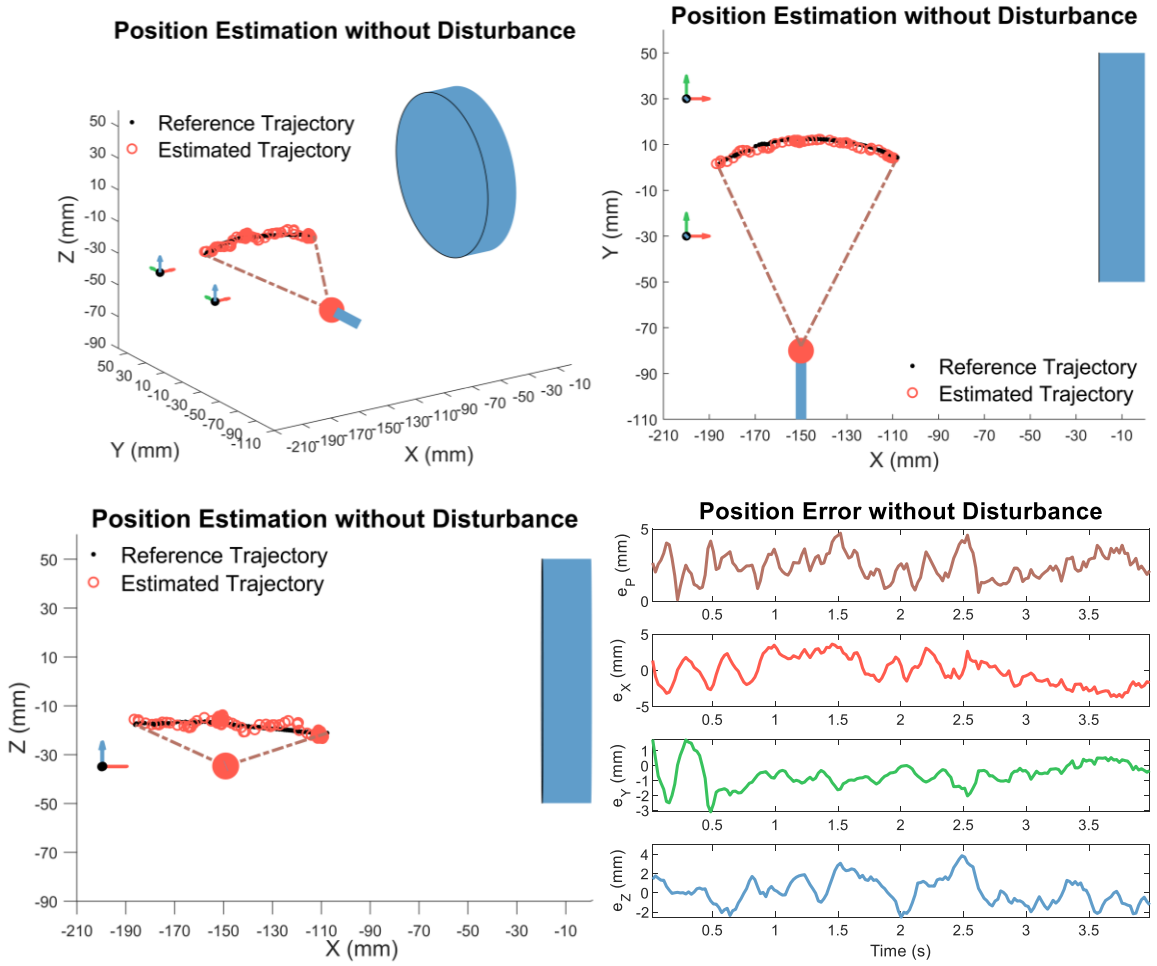

Figure 5-38 Position estimation results without ferromagnetic disturbance.

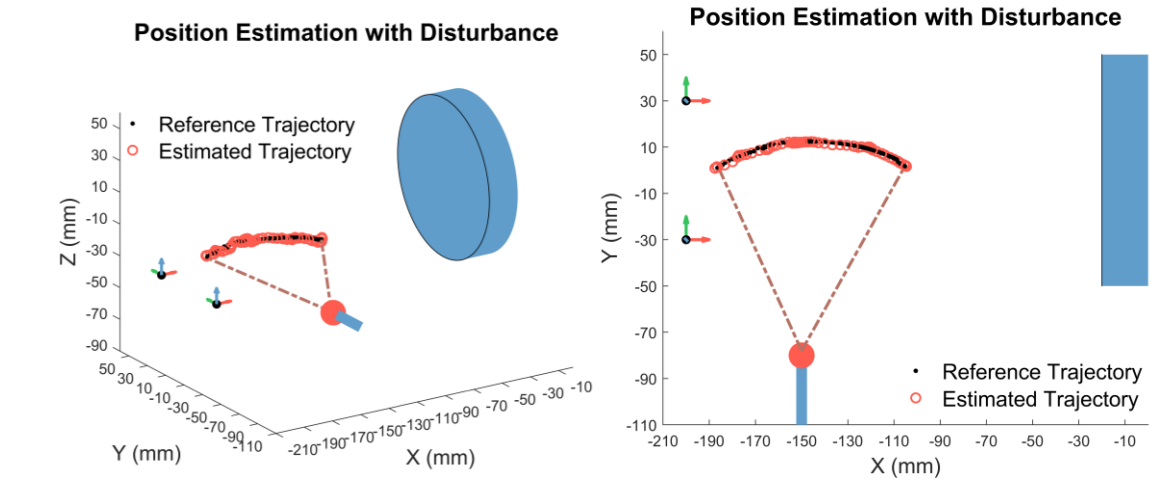

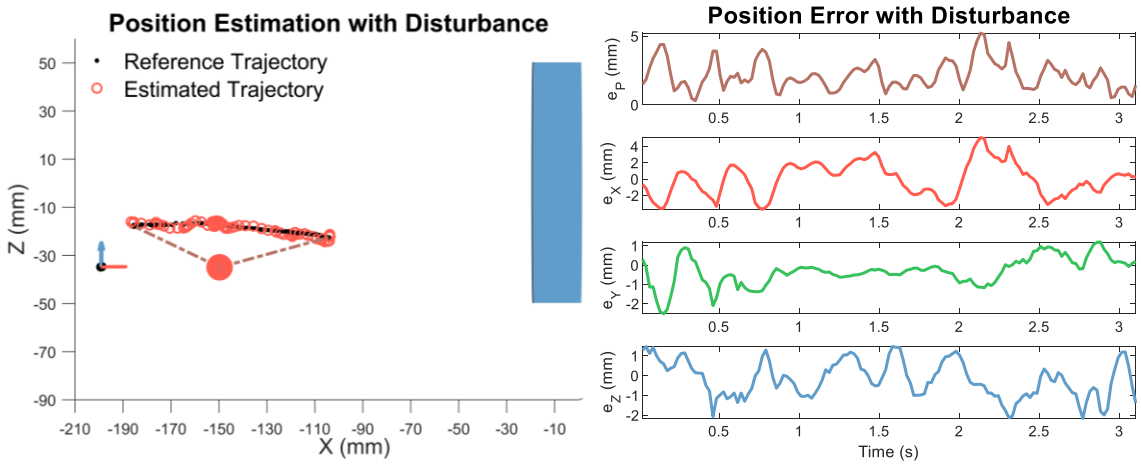

Figure 5-39 Position estimation results with ferromagnetic disturbance.

5.5 Conclusions

In this chapter, an electromagnetic 3-D positioning system based on high-magnetic-permeability materials (mu-metal) is developed to estimate the position of the end-effector in flexible transluminal medical robots or robotic endoscopic capsules. The 3-D positioning system consists of an external electromagnet as the magnetic source and multiple magnetic sensors located outside the human body, and a passive mu-metal element attached to any point of the robot whose position is of interest. The mu-metal is magnetized by the electromagnet differently at different locations, thus exerting magnetic field influence sensed by the magnetic sensors as it moves in the working region. Since only a piece of passive mu-metal is attached to the robot moving inside of the human body, there is no need of any wiring for power or signal transmission, which simplifies the system structure and enhances the robustness. In addition, the 3-D positioning system is based on magnetic field sensing, which does not require line-of-sight for position estimation. Though based on the magnetic-field-based sensing principle, the 3-D positioning system is immune to ferromagnetic disturbance due to the use of an alternating magnetic field at a specific high frequency generated by the electromagnet. The high-frequency magnetic field component is selectively extracted for position sensing while the ferromagnetic disturbance due to the presence or motion of nearby ferromagnetic objects, usually appearing as low-frequency component, is filtered out. The feature of immunity to ferromagnetic disturbance ensures

that the 3-D positioning system can be used for medical robots with surgical tools made of steel.

The developed mu-metal based 3-D positioning system is modeled and experimentally validated on a flexible trans-esophageal robot for ultrasound imaging of the heart. Two methods of position estimation, i.e. a direct ANN prediction and a particle filter with ANN measurement model, are implemented and compared. Experimental results show that the particle filter can effectively suppress the noise of position estimates, reducing the maximum estimation error. For the motion of robot insertion, the maximum position estimation error ranges from 6.39 mm to 7.44 mm and the RMS error ranges from 2.71 mm to 5.71 mm. For the bi-directional maneuver of the robot, the RMS error is under 5 mm and the maximum error is under 9 mm for a broad range of working region. The performance of ferromagnetic disturbance rejection is also experimentally validated for the 3-D positioning system, where no significant deterioration of position estimation is found in the presence of a disturbance source. Extensive experimental characterization indicates the capability and potential of the mu-metal based electromagnetic 3-D positioning system for the task of localization of medical robots moving inside the human body, which lays the foundation for autonomous navigation of medical robots and therefore promotes operation accuracy, efficiency, and consistency of surgical and diagnostic procedures.

Chapter 6

Conclusions

In this dissertation, a fundamentally new position sensing principle is proposed based on the use of passive high-magnetic-permeability metal (e.g. mu-metal) on the moving object and an alternating magnetic field generated by an external electromagnet. Because of the significantly higher magnetic permeability of mu-metal compared to that of the surrounding environment (e.g. air), the magnetic coupling between the stationary electromagnet and magnetic sensors varies as the mu-metal moves in the nearby space, resulting in the magnetic field variation at the location of magnetic sensors, from which the position of the moving mu-metal can be estimated. Since the high-magnetic-permeability metal is a passive component without the need for power supply, non-powered wireless position sensing is achieved. In addition, the proposed mu-metal based position estimation system has advantages of non-contacting operation, non-intrusive installation, and no need of line-of-sight access. Meanwhile, the selective measurement of the amplitude of alternating magnetic field removes any ambient low-frequency ferromagnetic disturbance that plagues most permanent magnet-based position sensing systems.

The newly developed position sensing principle based on high-magnetic-permeability materials is explored to address three real-world position estimation problems in this dissertation:

1) 1-D position estimation for linear actuators;

2) Angular position estimation for rotational joints;

3) 3-D position estimation for transluminal medical robots.

For each of the applications, the position sensing system is analytically or numerically modeled to reveal the underlying physics of the sensing principle and assist design of the position sensing system. A prototype of the position sensing system for each of the applications is developed. A signal processing scheme and related electronic circuits are designed to process the alternating magnetic field for ferromagnetic disturbance rejection. Since the magnetic measurement model is highly nonlinear, nonlinear state estimation algorithms are designed and implemented based on either stochastic filtering techniques or deterministic nonlinear observer design. Extensive experiments are conducted to validate the position estimation performance of the position sensing systems. The performance of ferromagnetic disturbance rejection is also evaluated experimentally for the position estimation systems.

First, the mu-metal based position sensing principle is applied to perform 1-D linear position estimation for non-ferrous hydraulic or pneumatic actuators on industrial machines or off-road vehicles. Conventional linear position sensors require either contacting operation (i.e. potentiometers and LVDTs) subject to wear and failure under fatigue loads or intrusive installation (magnetostrictive sensors) raising the total cost of the system. Permanent magnet-based position sensors, though free of the above problems, are subject to disturbance from surrounding ferromagnetic objects. The mu-metal based linear position sensor proposed in this dissertation is directly motivated by the need to develop a non-contacting, non-intrusive, easy to install, and low-cost position sensing solution immune to ferromagnetic disturbances for linear actuators. With only several pieces of passive mu-metal plates attached to the moving piston, and an electromagnet and magnetic sensors statically located on the cylinder of the actuator, the piston position can be estimated from the magnetic field variation induced by the motion of mu-metal using an extended Kalman filter fusing magnetic measurements and a constant-acceleration kinematic model. The linear position sensing system is analytically modeled to investigate the mechanism of position-dependent mu-metal magnetization and its resultant influence on the measured magnetic field. The maximum position estimation error is experimentally

shown to be approximately 1% over a measurement range of 10 cm. The measurement range can be extended to 20 cm and even longer by daisy-chained sensors. The linear position sensing system is also validated to reject ferromagnetic disturbances. This mu-metal based linear position sensor can potentially enable feedback control and autonomous operation in industrial machines and other applications with linear actuators. However, a limitation of the developed system is that it does work on ferrous actuators in which the mu-metal is completely enclosed in a ferrous body.

Before development of the above mu-metal based 1-D electromagnetic linear position sensing system, a precursor electromagnetic position sensing system is also investigated for its simple structure consisting of only an electromagnet on the stationary cylinder and magnetic sensors on the external end of the piston rod, without mu-metal involved. The spatial distribution of the magnetic field of the electromagnet is explored for position sensing. However, this system suffers from the drastic decrease of magnetic sensitivity as the sensors move far from the electromagnet, resulting in poor position estimates in the far-end region of the stroke. Therefore, an active position estimation system is developed based on varying the current input to the electromagnet along the stroke according to an off-line designed current profile. The current input is optimally controlled to increase as the magnetic sensor moves towards the low-sensitivity region far from the electromagnet, ensuring sufficient position estimation accuracy over the whole stroke length in an energy-efficient way. While the current control is based on following an optimal current profile as a function of piston position, the position itself is unknown and needs to be estimated from the magnetic field from the electromagnet, which depends on the current input to the electromagnet in return. The coupling between current control and position estimation poses a challenge for stabilizing the whole system. Hence, a nonlinear observer based on Lyapunov stability theory is designed to ensure both asymptotically stable position estimation as well as current control. The active position estimation system using the designed nonlinear observer is experimentally demonstrated to show a position estimation accuracy of 1% over the whole stroke length of 20 cm for a piston-cylinder system and a current tracking accuracy of 2%. This proposed active sensing scheme can also be generalized to 2-D and 3-D electromagnetic position estimation systems to improve

estimation accuracy, extend measurement range, or save energy consumption of the electromagnet.

A second application of the mu-metal based position sensing principle is angular position estimation for rotational mechanical joints. In this dissertation, the angle estimation for rotating joints on off-road vehicles such as track loaders and excavators is considered. Instead of being computed from the linear position of individual hydraulic actuators that might be too long or too expensive to measure, the end-effector position of the off-road vehicle can be alternatively determined from the angle of individual rotational joints. Two configurations of the mu-metal based angle sensing system are designed, i.e. the off-joint configuration and the on-joint configuration. In the off-joint configuration, the electromagnet and magnetic sensors are placed on one mechanical link while the mu-metal element is placed on another mechanical link connected to the first link by a common rotational joint, whose rotation makes the mu-metal pass by the nearby space between the electromagnet and magnetic sensors and exert magnetic influence for angle sensing. Several sensor placement schemes are designed and tested, in which the scheme with spatially separated dual sensors shows the best performance with the maximum sensing range with sufficient magnetic sensitivity. Experimental results show that the angle estimation error with the off-joint configuration is well under 1 degree for the measurement range of -60 ~ 60 degree. Though with high position estimation accuracy, the off-joint configuration fails to measure the angle of joints over the full range of 360 degrees. The on-joint configuration successfully solves this problem by attaching the mu-metal element right on the rotating shaft of the joint with the electromagnet and magnetic sensors placed nearby on the housing of the joint around the shaft. The key challenge of the on-joint configuration is to design an asymmetric geometry of the mu-metal element such that aperiodic magnetic field variation is achieved over the 360-degree measurement range for unique determination of the angle. Numerical modeling is employed to design the geometry of the mu-metal element and the arrow-shaped geometry is found to have the best performance. The maximum angle measurement error is 2 degrees for the on-joint configuration over the 360-degree measurement range. Both the on-joint and off-joint configuration are validated to be immune to ferromagnetic disturbances from a steel

wrench.

Finally, the mu-metal based electromagnetic position sensing principle is explored for the application of 3-D positioning of flexible transluminal medical robots or robotic endoscopic capsules, the position of which cannot be determined from individual joint or actuator positions due to their highly flexible and deformable structures and the resulting inaccurate kinematic model (continuum transluminal robots) or even non-existence of joints (untethered robotic capsules). Direct 3-D position measurement of the end-effector of transluminal medical robots or robotic capsules can enable real-time monitoring and autonomous navigation, by which operation accuracy, efficiency, and consistency are enhanced during minimally invasive surgical and diagnostic procedures. In this dissertation, the mu-metal based electromagnetic 3-D position estimation system is developed and validated specifically on a flexible trans-esophageal robot for ultrasound imaging of the heart. While the electromagnet and magnetic sensors are located outside of the human body, the mu-metal is attached to the robot tip with an ultrasound transducer that moves through the esophagus for imaging of the heart. The position of the ultrasound transducer can be estimated from the measured magnetic response caused by the magnetized mu-metal. Since the motion of the mu-metal happens in a 3-D space involving higher degrees of freedom, the magnetic response it creates is more complicated than that involved in 1-D linear or angular position estimation problems. Therefore, the highly nonlinear magnetic response to the 3-D position of the mu-metal is modeled using an artificial neural network and a particle filter is implemented to estimate the mu-metal position. Position estimation for two stages of robot motion, i.e. robot insertion and robot maneuver, are investigated in experiments. It is found that the RMS estimation error is under 5 mm and the maximum error is under 9 mm in the investigated working region, showing the potential of the mu-metal based 3-D positioning system to serve as a reference absolute localization system for the ultrasound probe. The mu-metal based 3-D positioning system is also validated to reject ferromagnetic disturbances, which is crucial for applications of medical robotics involving frequent presence of surgical tools made of ferromagnetic materials.

In summary, a novel electromagnetic position sensing principle based on the use of passive high-magnetic-permeability materials is proposed in this dissertation. Only the

passive high-permeability mu-metal is attached to the moving object whose position is to be estimated, resulting in a non-powered and wireless position sensing solution with advantages of non-contacting operation and non-intrusive installation. The selective measurement of an alternating magnetic field at a certain frequency makes the position sensing system immune to ferromagnetic disturbances. Based on the proposed mu-metal based position sensing principle, prototype position estimation systems are designed for both structured 1-D linear/angular position measurement for non-ferrous actuators, and free 3-D position measurement for applications of medical robotics, guided by analytical or numerical modeling of the magnetic sensing mechanisms. Extensive experiments are conducted to investigate the performance of position estimation, the results of which shed light on the potential use of the mu-metal based position sensing systems in real-world applications. In addition, an active sensing scheme for electromagnetic position estimation is proposed based on a nonlinear observer design, where a challenging coupled control and estimation problem is solved. The proposed active sensing framework can be applied to improve magnetic sensitivity, extend the sensing range and save energy costs of electromagnetic position sensing systems.

Bibliography

[1] L. Lacalle, A. Lamikiz, J. Sanchez, and I. Bustos, "Simultaneous measurement of forces and machine tool position for diagnostic of machining tests," *IEEE Trans. Instrum. Meas.,* vol. 54, no. 6, pp. 2329-2335, Dec. 2005.

[2] J. Du and M. J. Barth, "Next-generation automated vehicle location systems: positioning at the lane level," *IEEE Trans. Intell. Transp. Syst.*, vol. 9, no. 1, pp. 48–57, Mar. 2008.

[3] A. Giannitrapani, N. Ceccarelli, F. Scortecci, and A. Garulli, "Comparison of EKF and UKF for spacecraft localization via angle measurements," *IEEE Trans. Aerosp. Electron. Syst.*, vol. 47, no. 1, pp. 75–84, Jan. 2011.

[4] Z. Fan, G. Chen, J. Wang, and H. Liao, "Spatial position measurement system for surgical navigation using 3-D image marker-based tracking tools with compact volume," *IEEE Trans. Biomed. Eng.*, vol. 65, no. 2, pp. 378–389, Feb. 2018.

[5] Y. Kim, H. Y. Choi, Y. C. Lee, "Design and preliminary evaluation of high-temperature position sensors for aerospace applications," *IEEE Sensors J.*, vol. 14, no. 11, pp. 4018–4025, Nov. 2014.

[6] J. Cardillo and M. A. Sid-Ahmed, "3-D position sensing using a passive monocular vision system," *IEEE Trans. Pattern Anal. Mach. Intell.*, vol. 13, no. 8, pp. 809–813, Aug. 1991.

[7] J. Zhang, Z. Liu, Y. Gao, and G. Zhang, "Robust method for measuring the position and orientation of drogue based on stereo vision," *IEEE Trans. Ind. Electron.*, vol. 68, no. 5, pp. 4298–4308, May 2021.

[8] M. Li, F. Wei, Y. Li, S. Zhang, and G. Xu, "Three-dimensional pose estimation of infants lying supine using data from a Kinect sensor with low training cost," *IEEE Sensors J.*, vol. 21, no. 5, pp. 6904–6913, Mar. 2021.

[9] J. Lin, H. Ma, J. Cheng, P. Xu, and M. Meng, "A monocular target pose estimation system based on an infrared camera," in *2019 IEEE International Conference on*

Robotics and Biomimetics, Dali, China, Dec. 2019, pp. 1750–1755.

[10] Y.K. Kim, K.S. Kim, S. Kim, "A portable and remote 6-DoF pose sensor system with a long measurement range based on 1-D laser sensors," *IEEE Trans. Ind. Electron.*, vol. 62, no. 9, pp. 5722–5729, Sep. 2015.

[11] S. Pasinetti, M. M. Hassan, J. Eberhardt, M. Lancini, F. Docchio, and G. Sansoni, "Performance analysis of the PMD camboard Picoflexx time-of-fight camera for markerless motion capture applications," *IEEE Trans. Instrum. Meas.*, vol. 68, no. 11, pp. 4456–4471, Nov. 2019.

[12] Y. Kang, C. Roh, S. B. Suh, and B. Song, "A lidar-based decision-making method for road boundary detection using multiple Kalman filters," *IEEE Trans. Ind. Electron.*, vol. 59, no. 11, pp. 4360–4368, Nov. 2012.

[13] S. Paul, J. Chang, J. E. Fletcher, and S. Mukhopadhyay, "A novel high-resolution optical encoder with axially stacked coded disk for modular joints: physical modeling and experimental validation," *IEEE Sensors J.*, vol. 18, no. 14, pp. 6001–6008, Jul. 2018.

[14] P. Cheng, B. Oelmann, and F. Linnarsson, "A local positioning system for loader cranes based on wireless sensors – a feasibility study," *IEEE Trans. Instrum. Meas.*, vol. 60, no. 8, pp. 2881–2893, Aug. 2011.

[15] H. W. When and P. R. Belanger, "Ultrasound-based robot position estimation," *IEEE Trans. Robot. Autom.*, vol. 13, no. 5, pp. 682–692, Oct. 1997.

[16] S. Shin, M. H. Kim, and S. B. Choi, "Ultrasonic distance measurement method with crosstalk rejection at high measurement rate," *IEEE Trans. Instrum. Meas.*, vol. 68, no. 4, pp. 972–979, Apr. 2019.

[17] M. Sugimoto, N. Kanie, and S. Nakamura, "An accurate 3D localization technique using a single camera and ultrasound," in *2012 IEEE International Conference on Indoor Positioning and Indoor Navigation*, Sydney, NSW, Australia, Nov. 2012.

[18] C. Medina, J. C. Segura, and S. Holm, "Feasibility of ultrasound positioning based on signal strength," in *2012 IEEE International Conference on Indoor Positioning and Indoor Navigation*, Sydney, NSW, Australia, Nov. 2012.

[19] G. Paolini, D. Masotti, F. Antoniazzi, T. S. Cinotti, and A. Costanzo, "Fall detection

and 3D indoor localization by a custom RFID reader embedded in a smart e-health platform," *IEEE Trans. Microw. Theory Techn.*, vol. 67, no. 12, pp. 5329 – 5339, Dec. 2019.

[20] G. Bao, K. Pahlavan, and L. Mi, "Hybrid localization of microrobotic endoscopic capsule inside small intestine by data fusion of vision and RF sensors," *IEEE Sensors J.*, vol. 15, no. 5, pp. 2669–2678, May 2015.

[21] J. Hou, Y. Zhu, L. Zhang, Y. Fu, F. Zhao, L. Yang, G. Rong, "Design and implementation of a high resolution localization system for in-vivo capsule endoscopy," in *2009 8-th IEEE International Conference on Dependable, Automatic and Secure Computing*, Chengdu, China, Dec. 2009. pp. 209 – 214.

[22] B. D. Cullity and C. D. Graham, *Introduction to Magnetic Materials.* John Wiley & Sons, 2011.

[23] L. C. Boles and K. J. Lohmann, "True navigation and magnetic maps in spiny lobsters," *Nature,* vol. 421, pp. 60-63, 2003.

[24] K. J. Lohmann and C. M. Lohmann, "Detection of magnetic field intensity by sea turtles," *Nature,* vol. 380, pp. 5-61, 1996

[25] D. Gao, C. Wang, H. Zhu, "Geomagnetic/dead reckoning integrated navigation method considering geomagnetic error," in *2012 24th Chinese Control and Decision Conference*, Taiyuan, China, May 2009. pp. 3613 – 3616.

[26] S. Taghvaeeyan, R. Rajamani, "Use of vehicle magnetic signatures for position estimation," *Appl. Phys. Lett.*, Vol. 99, no. 13, Article 134101, 2011.

[27] S. Taghvaeeyan, R. Rajamani, "The development of vehicle position estimation algorithms based on the use of AMR sensors," *IEEE Trans. Intell. Transp. Syst.*, vol. 13, no. 4, pp.1845-1854, 2012.

[28] S. Taghvaeeyan, R. Rajamani, "Two-dimensional sensor system for automotive crash prediction," *IEEE Trans. Intell. Transp. Syst.*, vol. 15, no. 1, pp. 178-190, 2014.

[29] S. Taghvaeeyan, R. Rajamani, Z. Sun, "Non-intrusive piston position measurement system using magnetic field measurements," *IEEE Sensors J.,* vol. 13, no. 8, pp. 3106-3114, 2013.

[30] G. X. Liu, L. F. Shi, S. Chen, and Z. G. Wu, "Focusing matching localization method

based on indoor magnetic map," *IEEE Sensors J.,* vol. 20, no. 17, pp. 10012-10020, Sep. 2020.

[31] R. Madson and R. Rajamani, "Adaptive dipole model based disturbance compensation in nonlinear magnetic position systems," *IEEE/ASME Trans. Mechatronics.* vol. 22, no. 2, pp. 794 – 803, Apr. 2017.

[32] R. Madson and R. Rajamani, "Magnetic position estimation in ferromagnetic systems involving significant hysteresis," *IEEE/ASME Trans. Mechatronics.* vol. 23, no. 4, pp. 1555 – 1563, Jun. 2018.

[33] N. Sebkhi, N. Sahadat, S. Hersek, A. Bhavsar. S. Siahpoushan, M. Ghovanloo, and O. Inan, "A deep neural network-based permanent magnet localization for tongue tracking," *IEEE Sensors J.,* vol. 19, no. 20, pp. 9324-9331, Jun. 2019.

[34] D. Son, S. Yim, M. Sitti, "A 5-D localization method for a magnetically manipulated untethered robot using a 2-D array of Hall-effect sensors," *IEEE/ASME Trans. Mechatronics.* vol. 21, no. 2, pp. 708 – 716, Apr. 2016.

[35] C. R. Taylor, H. G. Abramson, H. M. Herr, "Low-latency tracking of multiple permanent magnets," *IEEE Sensors J.,* vol. 19, no. 23, pp. 11458-11468, Aug. 2019.

[36] W. Yang, C. Zhang, H. Dai, C. Hu, and X. Xia, "A novel wireless 5-D electromagnetic tracking system based on nine-channel sinusoidal signals," *IEEE/ASME Trans. Mechatronics.* vol. 26, no. 1, pp. 246 – 254, Feb. 2021.

[37] S. Song, Z. Li, H. Yu, H. Reng, "Electromagnetic positioning for tip tracking and shape sensing of flexible robots," *IEEE Sensors J.,* vol. 15, no. 8, pp. 4565 – 4575, Aug. 2015.

[38] S. Song, C. Hu, B. Li, X. Li, M. Meng, "An electromagnetic localization and orientation method based on rotating magnetic dipole," *IEEE Trans. Magn.,* vol. 49, no. 3, pp. 1274 – 1277, Mar. 2013.

[39] S. Song, H. Reng, H. Yu, "An improved magnetic tracking method using rotating uniaxial coil with sparse points and closed form analytic solution," *IEEE Sensors J.,* vol. 14, no. 10, pp. 3585 – 3592, Oct. 2014.

[40] S. B. Kim, J. Y. Soh, K. Y. Shin, J. H. Jeong, and S. H. Myung, "Magnetic shielding performance of thin metal sheets near power cables," *IEEE Trans. Magn.* vol. 46, no.

2, pp. 682 – 685, Feb. 2010.

[41] M. Zucca, M. Gamba, F. Fiorillo, "Open screens for local magnetic shielding at low frequencies," *IEEE Trans. Magn.* vol. 50, no. 11, Article No. 8500204, Nov. 2014.

[42] X. Sun, L. Jiang, P. Pong, "Magnetic flux concentration at micrometer scale," *Microelectronic Engineering*, vol. 111, pp. 77 – 81, 2013.

[43] S. Thrun, W. Burgard, and D. Fox, *Probabilistic robotics*. MIT Press, 2005.

[44] H. T. Sen and P. Kazanzides, "Particle filtering to improve the dynamic accuracy of electromagnetic tracking," in *2013 IEEE Conference on Sensors,* Baltimore, MD, USA, Nov. 2013.

[45] S. Boyd, L. El Ghaoui, E. Feron, and V. Balakrishnan, *Linear Matrix Inequalities in System and Control Theory*. Society for Industrial and Applied Mathematics, 1994.

[46] R. Rajamani, Y. Wang, G. D. Nelson, R. Madson, and A. Zemouche, "Observers with dual spatially separated sensors for enhanced estimation: industrial, automotive and biomedical applications," *IEEE Control Systems Magazine*, vol. 37, no. 3, pp. 42 – 58, May 2017.

[47] Y. Wang, R. Madson, R. Rajamani, "Magnetic sensor-based simultaneous state and parameter estimation using a nonlinear observer," *International Journal of Control*, vol. 92, no. 11, pp. 2639 – 2646, May 2018.

[48] R. Rajamani, W. Jeon, H. Movahedi, A. Zemouche, "On the need for switched-gain observers for non-monotonic nonlinear systems," *Automatica*, vol. 114, 108814, 2020.

[49] D.S. Nyce, *Linear Position Sensors*, John Wiley & Sons, ISBN 9780471474289, 2003.

[50] J. Fraden, *Handbook of Modern Sensors, Physics, Design and Applications*, 3rd Edition, Springer, ISBN 0-387-00750-4, 2003.

[51] E. Ramsden, *Hall-Effect Sensors: Theory and Application*. Boston, MA, USA: Newnes, 2011.

[52] X. Zhang, M. Mehrtash, andM. B. Khamesee, "Dual-axial motion control of a magnetic levitation system using Hall-effect sensors," *IEEE/ASME Trans. Mechatronics*, vol. 21, no. 2, pp. 1129–1139, Apr. 2016.

[53] D. J. Sadler and C. H. Ahn, "On-chip eddy current sensor for proximity sensing and crack detection," *Sens. Actuators A, Phys*., vol. 91, no. 3, pp. 340–345, Jul. 2001.

[54] C. Liu and G. Liu, "Field dynamic balancing for rigid rotor-AMB system in a magnetically suspended flywheel," *IEEE/ASME Trans. Mechatronics*, vol. 21, no. 2, pp. 1140–1150, Apr. 2016.

[55] O. Maier, M. Pfeiffer, and J. Wrede, "Development of a braking dynamics assistance system for electric bicycles: Design, implementation, and evaluation of road tests," *IEEE/ASME Trans. Mechatronics*, vol. 21, no. 3, pp. 1671–1679, Jun. 2016.

[56] S. Y. Yang, M. C. Lee, M. H. Lee, and S. Arimoto, "Measuring system for development of stroke-sensing cylinder for automatic excavator," *IEEE Trans. Ind. Electron.*, vol. 45, no. 3, pp. 376–384, Jun. 1998.

[57] B. Hebert, M. Brule, and L.-A. Dessaint, "A high efficiency interface for a biphase incremental encoder with error detection," *IEEE Trans. Ind. Electron.*, vol. 40, no. 1, pp. 155–156, Feb. 1993.

[58] S. Taghvaeeyan and R. Rajamani, "Nature-inspired position determination using inherent magnetic fields," *Technology*, vol. 2, no. 2, pp. 161–170, 2014.

[59] H. Knoepfel, *Magnetic Fields – A Comprehensive Theoretical Treatise for Practical Use*, ISBN 978-0471322054, John Wiley & Sons, 2008.

[60] M. L. Barton, "Loss calculation in laminated steel utilizing anisotropic magnetic permeability," *IEEE Trans. Power App. Syst*, vol. PAS-99, no. 3, pp. 1280-1287, 1980.

[61] X. R. Li and V. P. Jilkov, "Survey of maneuvering target tracking. Part I: dynamic models," *IEEE Trans. Aerosp. Electron. Syst.*, vol. 39, no. 4, pp. 1333–1364, Oct. 2003.

[62] D. Simon, *Optimal State Estimation: Kalman, H ∞ and Nonlinear Approaches*. Hoboken, NJ, USA: Wiley-Interscience, 2006.

[63] C. Leung, S. Huang, N. Kwok, G. Dissanayake, "Planning under uncertainty using model predictive control for information gathering," *Robotics and Autonomous Systems*, vol. 54, pp. 898 – 910, 2006.

[64] B. T. Hinson, M. K. Binder, and K. A. Morgansen, "Path planning to optimize observability in a planar uniform flow field", in *2013 American Control Conference*, Washington, DC, USA, Jun. 2013. pp. 1392 – 1399.

[65] M. Kelly, "An introduction to trajectory optimization: how to do your own direct collocation", *SIAM Review*, vol. 59, pp. 849-904, 2017.

[66] M. Kelly, “OptimTraj User’s Guide”, 2018. [Online]. Available: https://github.com/MatthewPeterKelly/OptimTraj/blob/master/docs/UsersGuide/OptimTraj_UsersGuide.pdf. [Accessed: 11-June-2021].

[67] 3Dbaza, “Robot manipulator.” [Online]. Available: https://3dbaza.com/robot-manipulator-125938. [Accessed: 11-June-2021].

[68] Steve Maxwell, “Everything you need to know about steering wheels.” [Online]. Available: https://www.familyhandyman.com/article/about-steering-wheels. [Accessed: 11-Jan-2021].

[69] tesa, “Paper production.” [Online]. Available: https://www.tesa.com/en-gb/industry/paper-print/market-segments/paper-production. [Accessed: 11-June-2021].

[70] CNH Industrial America LLC., “TV380 track loader.” [Online]. Available: https://www.casece.com/apac/en-anz/products/compact-track-loaders/compact-track-loaders/models/tv380. [Accessed: 11-June-2021].

[71] X. Zhang, E. Peltola, J. Mattila, “Angle estimation for robotic arms on floating based using low-cost IMUs,” in *2018 IEEE International Conference on Robotics and Automation*, Brisbane, Australia, May 2018. pp. 1458 – 1465.

[72] S. Wang, Z. Wu, D. Peng, S. Chen, Z. Zhang, and S. Liu, “Sensing mechanism of a rotary magnetic encoder based on time grating,” *IEEE Sensors J.,* vol. 18, no. 9, pp. 3677 – 3683, May 2018.

[73] *COMSOL Multiphysics Reference Manual*, COMSOL Multiphysics® v. 5.4. COMSOL AB, Stockholm, Sweden. 2020. [Online]. Available: https://doc.comsol.com/5.4/doc/com.comsol.help.comsol/COMSOL_ReferenceManual.pdf. [Accessed: 11-June-2021].

[74] K.-Y. Chen, S. Patel and S. Keller, “Finexus: Tracking precise motions of multiple fingertips using magnetic sensing,” in *2016 ACM CHI Conference on Human Factors in Computing Systems*, San Jose, California, USA, 2016. pp. 1504 – 1514.

[75] H. Mateen, M. R. Basar, A. U. Ahmed and M. Y. Ahmad, “Localization of wireless capsule endoscope: A systematic Review,” *IEEE Sensors J.,* vol. 17, no. 5, pp. 1197-1206, Mar. 2017.

[76] M. Allan, S. Ourselin, S. Thompson, D. J. Hawkes, J. Kelly and D. Stoyanov, "Toward detection and localization of instruments in minimally invasive surgery," *IEEE Trans. Biomed. Eng.,* vol. 60, no. 4, pp. 1050-1058, Apr. 2013.

[77] M. C. Vilas-Boas and J. P. S. Cunha, "Movement quantification in neurological diseases: methods and applications," *IEEE Rev. Biomed. Eng.,* vol. 9, pp. 15 – 29, 2016.

[78] C. Yang, G. Cheung, and V. Stankovic, "Estimating heart rate and rhythm via 3D motion tracking in depth video," *IEEE Trans. Multimedia,* vol. 19, no. 7, pp. 1625-1635, Jul. 2017.

[79] L. Bai, M. G. Pepper, Y. Yan, S. K. Spurgeon, M. Sakel, and M. Phillips, "Quantitative assessment of upper limb motion in neurorehabilitation utilizing inertial sensors," *IEEE Trans. Neural Systems and Rehabilitation Eng.,* vol. 23, no. 2, pp. 232 – 243, Mar. 2015.

[80] G. Ciuti, A. Menciassi, and P. Dario, "Capsule endoscopy: from current achievements to open challenges," *IEEE Rev. Biomed. Eng.,* vol. 4, pp. 59-72, 2011.

[81] T. Veiga, J. H. Chandler, P. Lloyd, G. Pittiglio, N. J. Wilkinson, A. K. Hoshiar, R. A. Harris, and P. Valdastri, "Challenges of continuum robots in clinical context: a review," *Progress in Biomedical Engineering*, vol. 2, 032003, 2020.

[82] Intuitive Surgical Inc., "Da Vinci robot." [Online]. Available: https://www.intuitive.com/en-us/about-us/press/press-resources. [Accessed: 11-June-2021].

[83] V. Vitiello, S. L. Lee, T. P. Cundy, and G. Z. Yang, "Emerging robotic platforms for minimally invasive surgery," *IEEE Rev. Biomed. Eng.,* vol. 6, pp. 111-126, 2013.

[84] H. Choi, H. S. Kwak, Y. A. Lim, H. J. Kim, "Surgical robot for single incision laparoscopic surgery," *IEEE Trans. Biomed. Eng.,* vol. 61, no. 9, pp. 2458 – 2466, Sep. 2014.

[85] F. Carpi, N. Kastelein, M. Talcott, and C. Pappone, "Magnetically controllable gastrointestinal steering of video capsules," *IEEE Trans. Biomed. Eng.,* vol. 58, no. 2, pp. 231 – 234, Feb. 2011.

[86] Y. Zhong, R. Du, P. W. Chiu, "Tadpole endoscope: a wireless micro robot fish for examining the entire gastrointestinal (GI) tract," *HKIE Transactions*, 2015.

[87] S. Wang, D. Singh, D. Johnson, K. Althoefer, K. Rhode, R. J. Housden, "Robotic ultrasound: view planning, tracking, and automatic acquisition of transesophageal echocardiography" *IEEE Robotics and Automation Magazine,* vol. 23, no. 4, pp. 118 – 127, Dec. 2016.

[88] S. Wang, J. Housden, D. Singh, K. Althoefer, K. Rhode, "Design, testing and modeling of a novel robotic system for trans-oesophageal ultrasound," *The International Journal of Medical Robotics and Computer Assisted Surgery*, vol. 12, no. 3, pp. 342 – 354, Jul. 2015.

[89] H. Reng and J. Sun, *Electromagnetic Actuation and Sensing in Medical Robotics*. Singapore: Springer, 2018.

[90] H. Demuth and M. Beale, "Neural network toolbox user's guide (version 4)", [Online]. Available: http://cda.psych.uiuc.edu/matlab_pdf/nnet.pdf. [Accessed: 11-June-2021].